Materials Under Extreme Conditions Series

Journal of Innovative Materials in Extreme Conditions

Volume 3

Technicum Scientific Publishing
Stuttgart, 2024

Bibliografische Information Der Deutschen Bibliothek

Die Deutsche Bibliothek verzeichnet diese Publikation in der Deutschen Nationalbibliografie; detaillierte bibliografische Daten sind im Internet über http://dnb.ddb.de abrufbar.

Bibliographic information published by Die Deutsche Bibliothek

Die Deutsche Bibliothek lists this publication in the Deutsche Nationalbibliografie; detailed bibliographic data are available on the Internet at http://dnb.ddb.de.

Editors:
Dr. rer. nat. Branko Matović
Dr. Vesna Maksimović
Dr. Ivana Cvijović-Alagić
Dr. rer. nat. Dejan Zagorac
Dr. Jelena Zagorac

Verlag / Publisher:
Technicum Scientific Publishing
Dachswaldweg 99, 70569 Stuttgart, Germany
Phone: +49 (0)177 241 4257
E-mail: contact@opentechnicum.com
Web: www.opentechnicum.com

ISBN: 978-3-9817635-4-6

Coverbild / Cover image: www.pixabay.com

Journal of Innovative Materials in Extreme Conditions

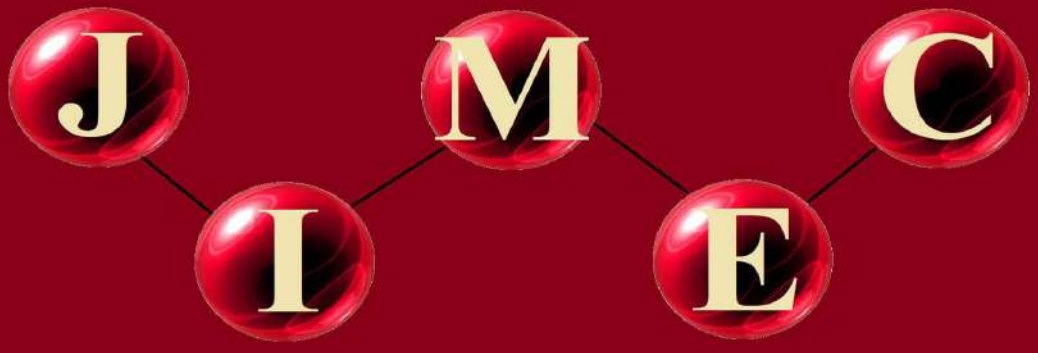

Volume 3, Issue 1, Year 2022

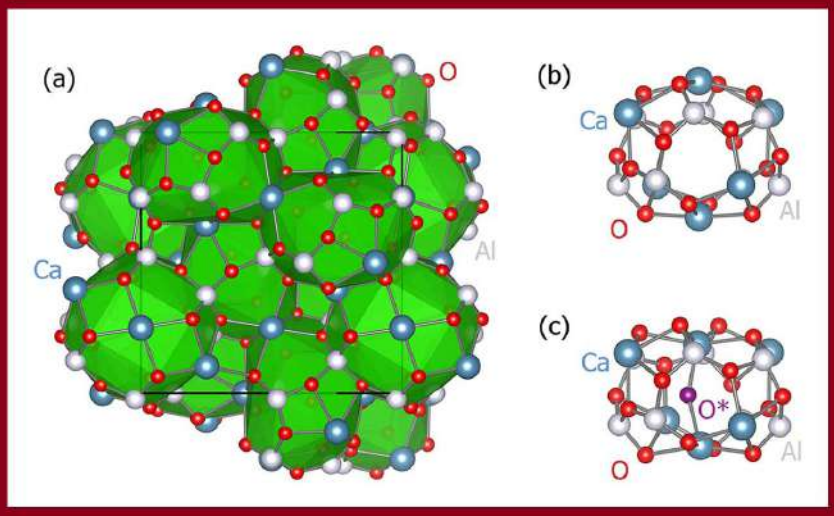

Published by:

SIM-EXTREME

Serbian Society for Innovative Materials in Extreme Conditions

Journal name

Journal of Innovative Materials in Extreme Conditions (*abbr*. JIMEC)

Publisher

Serbian Society for Innovative Materials in Extreme Conditions (SIM-EXTREME), Belgrade, Serbia.

Bibliographic Information

ISSN (Online) 2738-0882

Review Type

Single Blind Peer Review Process

No publication fees

Publication in the Journal is free for all authors and there are **no article processing charges.**

Open access statement

Editorial Board

Journal of Innovative Materials in Extreme Conditions (*abbr*. JIMEC)

Volume 3, Issue 1, Year 2022

Volume 3, year 2022

JIMEC: Table of Contents

Volume 3, Issue 1, Year 2022

Cover Picture

Mayenite structure: (a) C12A7 unit cell, consisting of 12 cages formed by Ca-Al-O framework, (b) Mayenite cage without extra-framework species, (c) Cage containing extra-framework O^{2-} ion (O*). Published in: Milan Pejić, Dejan Zagorac, Jelena Zagorac, Tamara Škundrić, Branko Matović, THEORETICAL STUDY OF GROUND STATE PROPERTIES OF Na^{+}, Cs^{+}, Mg^{2+} AND Ba^{2+} DOPED MAYENITE AND ITS ELECTRIDE FORMS UNDER EXTREME CONDITIONS, *Journal of Innovative Materials in Extreme Conditions*, **Vol. 3**, Issue 1, pages 30-42 (2022).

-Issue 1

Journal of Innovative Materials in Extreme Conditions
2022
Volume 3
Issue 1

EFFECT OF RECASTING ON THE STRUCTURE AND PROPERTIES OF COMMERCIAL Ni-Cr DENTAL ALLOY

Vesna Maksimović[1*], Aleksandra Čairović[2], Ivana Cvijović Alagić[1]
[1] Center of Excellence "CEXTREME LAB", Vinča Institute of Nuclear Sciences - National Institute of the Republic of Serbia, University of Belgrade, Mike Petrovića Alasa 12-14, 11001 Belgrade, Serbia
[2] Faculty of Dental Medicine, University of Belgrade, Rankeova 4, 11000 Belgrade, Serbia
Corresponding author: vesnam@vinca.rs*

Abstract: *The Ni-Cr dental alloys are among the oldest restorative materials used in dentistry. Reuse of previously melted and cast dental alloys is a routine procedure used in dental laboratories to reduce the cost of dental restorations. Continuous reuse of the commercial Ni-Cr dental alloys, such as Wirron 99, can change numerous properties of these materials, and therefore the present study was aimed to establish the outcome of several recasting cycles on the Wirron 99 alloy properties. Obtained results reveal that alloy recasting resulted in the appearance of typical dendritic microstructures where the chemical composition of dendritic and interdendritic regions differs. Moreover, the results of the present study showed that the number of recasting cycles has a significant effect on the alloy microstructure, structure, electrical conductivity, and hardness.*

Keywords**:** *Ni-Cr dental alloy, microstructure, electrical conductivity, micro- and macrohardness*

1. Introduction

Metallic materials (mainly alloys) are widely used in dental surgery for the production of most of the surgical instruments for face and jaw surgery, as well as in restorative dentistry, orthodontics, and dental prosthetics as a building material. Usage of dental alloys has a long tradition in restorative dentistry, but their application in the true sense of the word starts at the beginning of the 20th century with the introduction of the casting apparatus based on the centrifugal force principle [1,2]. The development of dental alloys followed the development of metallurgy with respect to the main requirements of metallic materials biomedical usage. Namely, one of the main requirements for dental metallic materials usage is high corrosion resistance of these materials in the human body environment, such as the oral cavity [1,3,4].

Dental casting alloys can be categorized in several different ways, but the classification system mostly used by dental practitioners is the American Dental Association (ADA) compositional classification system. The ADA classification system, established in the year 1984, classifies casting alloys into three main groups based on their wt.% compositions [1] as follows:

a. high-noble (HN) alloys with an overall noble metals content (sum of gold, palladium, and platinum content) of at least 60 wt.% and gold content of at least 40 wt.%,
b. noble (N) alloys with at least 25 wt.% of noble metals content with no specific requirements for gold content in the alloy composition, and
c. predominantly based (PB) alloys with less than 25 wt.% of noble metals content in the alloy composition with no additional compositional specifications.

Today's world market offers a large number of dental alloys while the modern dental industry strives to create new alloys that would be biocompatible and chemically resistant in a corrosive environment while possessing good mechanical properties. The ideal dental alloy does not exist in today's market since the dental alloy manufacturers are trying to produce an alloy for every budget [5,6]. In developed countries, such as the United States of America, European Union countries, and Japan, cast gold alloy and all-ceramic materials are the most commonly used in dental practice. On the other hand, in developing countries, the base alloys (Ni-Cr and Co-Cr alloys) and prefabricated stainless-steel crowns are the most prevalent types of used metallic dental materials [6]. It should be additionally emphasized that approximately 90% of all removable partial dentures used all over the world are nowadays cast from the non-precious alloys that contain Co, Cr, and Ni [7]. However, in

less economically developed countries (LEDCs), the reuse of previously melted and casted alloys is a routine procedure used in dental laboratories to further reduce the cost of dental restorations [8]. The available literature in this field [8-13] indicates that this procedure is widely used in everyday practice, despite the clinical suggestion that such a procedure should be avoided since the content of new and previously unused dental alloy in the overall dental alloy castings must be at least 50% in order to avoid an increase of the cytotoxicity of Co-Cr, Ni-Cr, and Au-Pt alloys [8]. Higher content of the already remelted alloy then suggested is however used in the case of the noble alloys [11,14-16], as well as in the case of the basic dental alloys [17-22]. The previous literature reports show that the chemical composition of the dental alloys changes with their repeated remelting and, as a consequence, reduction of the content of alloying elements, such as Ni, Cr, Cu, Sn, Zn, Cr, Ti [8,15], and Fe due to evaporation and oxidation [15], can be expected. Mentioned reduction of the content of these elements can significantly weaken the metal-ceramics bond [17]. Furthermore, it was also shown that the repeated remelting influences a change in the alloy grain size [11], the content of impurities and microporosity [11], and the change in microstructure and mechanical properties [8,11,23]. In general, new and reused dental alloys do not have the same composition, microstructure, physical and mechanical properties, color, corrosion resistance, ions release tendency, and most importantly, they do not have the same biological quality [24].

This study, therefore, aims to establish the outcome of repeated alloy recasting on the microstructure, structure, electrical conductivity, and hardness of commercially attainable nickel-chromium alloy, *i.e.* Wirron 99.

2. Experimental Procedures

Commercially available Ni-Cr-based dental alloy Wirron 99 (Bego, Germany) was used in this study. The alloy composition is shown in Table 1, as provided by the alloy manufacturer.

Table 1. Chemical composition of the commercial Wirron 99 alloy (in wt.%).

Alloy type	Ni	Cr	Mo	Nb	Si	Fe	Ce	C
Ni-Cr	65.00	22.50	9.50	1.00	1.00	0.50	0.50	0.02

Disk-shaped Wirron 99 samples with 6 mm in diameter and thickness of 1 mm were cast in an air atmosphere using the laboratory induction furnace at the Clinic for Dental Prosthetics of the Faculty of Dental Medicine, University of Belgrade. The casting of the alloy was performed at 1420 ^{o}C, according to the manufacturer's specifications. Alloy castings were examined after a different number of repeated casting cycles, *i.e.* first (sample W1), fourth (sample W4), and eighth (sample W8). Each casting cycle consisted of subsequent melting and casting sequences.

2.1 Microstructural characterization

For microstructural analysis, the casted alloy samples were wet ground and polished using the standard metallographic preparation procedure. Alloy samples were afterward cleaned with alcohol and distilled water and air-dried. The disc-shaped alloy castings were additionally etched using the etching solution that contains 10 ml HNO_3 and 40 ml HCl [25,26]. The polished and etched samples were observed under a Carl Zeiss Axiovert 25 light optical microscope (LOM) equipped with the digital Panasonic WV-CD50 camera, and an FEI Quanta 200 scanning electron microscope (SEM) equipped with an Oxford Instruments INCA X-sight energy dispersive spectroscope (EDS).

The x-ray diffraction (XRD) patterns were obtained from the mechanically polished alloy samples using a Siemens D5000 PC automatic diffractometer with Cu Kα radiation. The XRD patterns were recorded in the 2θ range from 40° to 80° with a scanning rate of 0.02°/s.

2.2 Hardness testing and electrical conductivity measurements

The macrohardness and microhardness measurements of the casted alloy samples were performed using a Buehler SemiMacro Vickers 1112 HV112 and a Buehler MicroMet 5101 Vickers

hardness tester with a load of 1 kgf (9.805 N) applied for 5 s and 25 gf (245.2 mN) applied for 10 s, respectively. Results were obtained as the average values of five consecutive measurements.

The electrical conductivity of the casted alloy samples was measured using a Forested SIGMATEST 2.069 conductivity meter [27]. A frequency of 960 kHz was applied during measurements due to the small sample thickness. Obtained results were presented as an average value of fifteen consecutive measurements.

3. Results and Discussion

Fig. 1(a-c) shows the typical dendritic microstructures of the recast Ni-Cr alloy samples. It is well known that a dendritic structure usually exhibits compositional variations, with the dendrite arms containing fewer alloying and impurity elements than interdendritic regions. Because of such compositional changes, the rate of etching at interdendritic regions differs from that at dendrite arms [15]. Microstructural changes, induced by an increase in the number of recasting cycles, could be observed in the alloy microstructure even at small magnification.

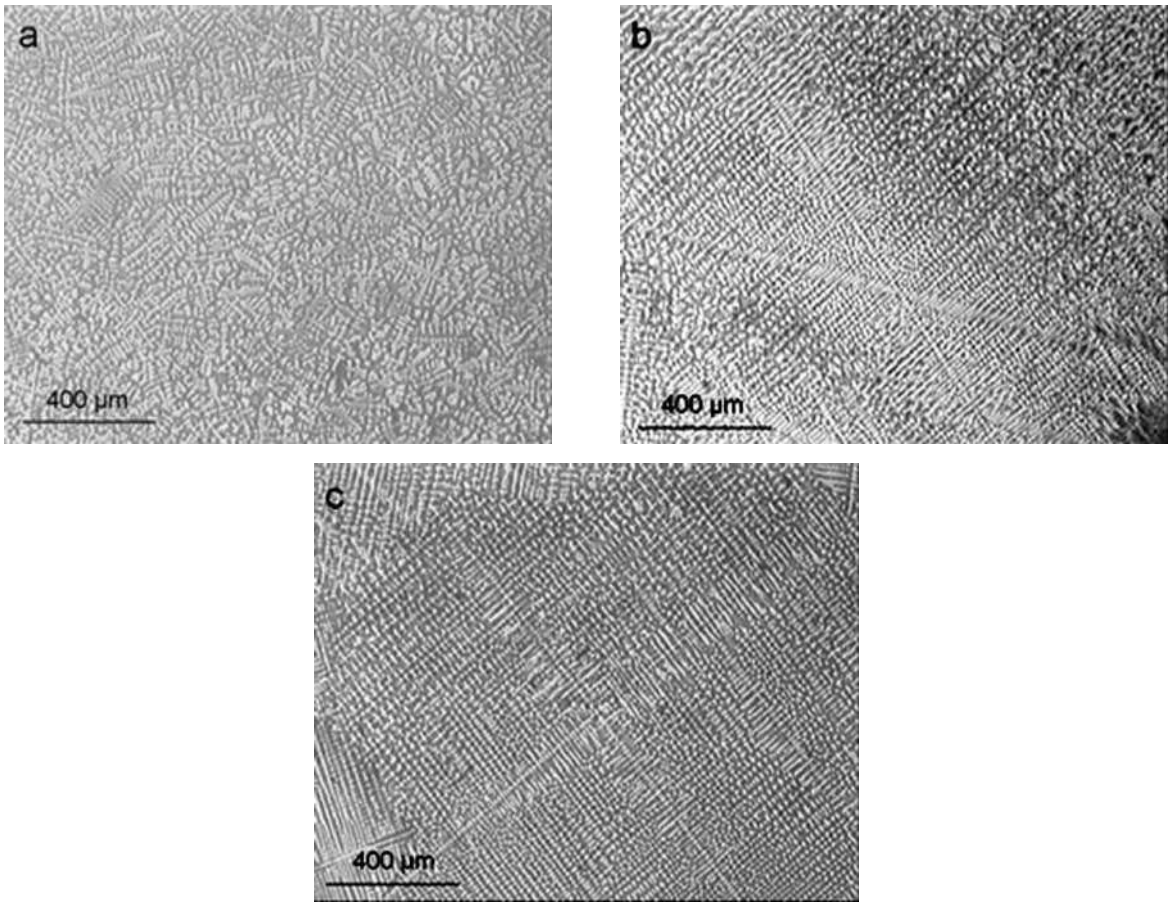

Figure 1. LOM micrographs showing the typical microstructure of Ni-Cr dental alloy after (a) first, (b) fourth, and (c) eighth recast cycle.

SEM microphotographs showing the microstructure of Ni-Cr alloy after the first, fourth, and eighth recast cycle are given in Fig. 2(a-c). The dendrite structure is clearly observed. With the increasing number of melting and casting sequences pronounced crystal segregation appears (Figs. 2b and 2c). In the complex system, such as dental Wirron 99 alloy, in addition to the solid solution, phases in the interdendritic region of irregular shape appeared. The presence of precipitates, which are probably Mo- and Nb-carbides, can also be observed along the grain boundaries [15].

EDS analysis of the dendritic and interdendritic regions did not indicate significant differences in the chemical composition between these zones, and because of that, a semi-quantitative surface analysis was performed. Based on the obtained EDS information, shown in Fig. 2(a-c),

variation of the primary elements (Ni, Cr, and Mo) content in the alloy was presented in Fig. 3. With an increase in the recasting cycle number, the content of Ni decreases from 65 wt.% up to approximately 60 wt.%. Quite the opposite trend was observed for the change in Mo content.

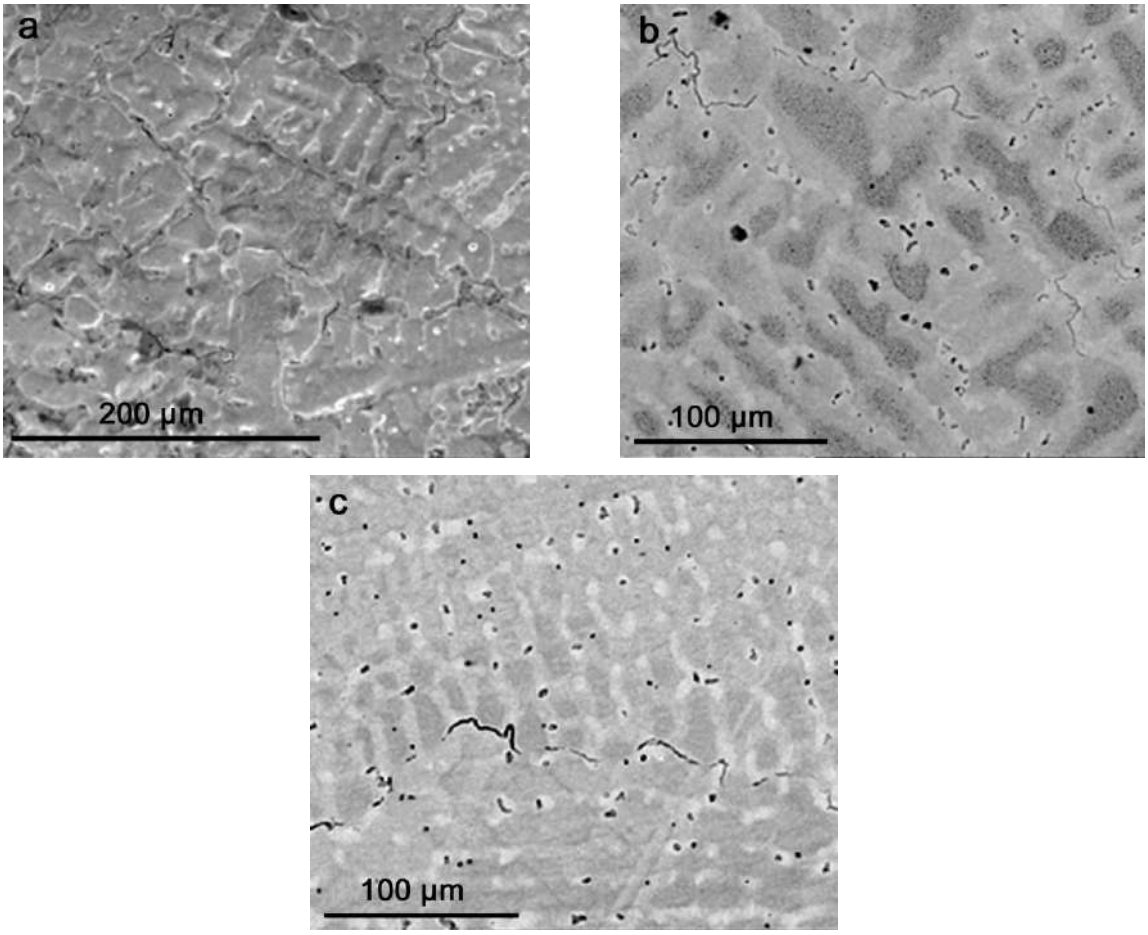

Figure 2. SEM micrographs showing the microstructure of Ni-Cr dental alloy after (a) first, (b) fourth, and (c) eighth recast cycle.

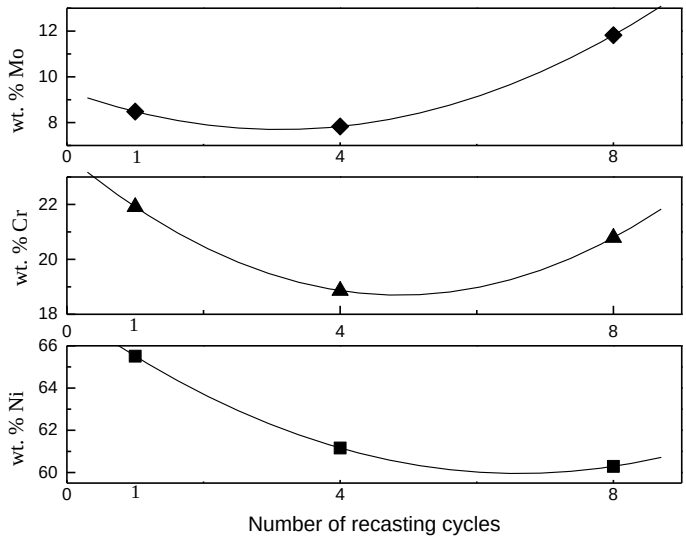

Figure 3. Variation of the primary elements (Ni, Co, Mo) content in the Wirron 99 alloy with an increase in the recasting cycle number.

XRD patterns of the Ni-Cr alloy after the first (W1), fourth (W4), and eighth (W8) melting and casting sequences are shown in Fig. 4. Only the characteristic peaks of α-Ni phase (■), as the Ni-rich solid solution with face-centered cubic (fcc) lattice, may be seen. With an increase in the number of repeated casting cycles, a change in the intensity of peaks from $(111)_{fcc}$, $(200)_{fcc}$, and $(220)_{fcc}$ planes can be observed. Moreover, the preferential orientation has changed from $(111)_{fcc}$ to $(200)_{fcc}$ planes. The reason for this behavior can be found in the alloy chemical composition variation during the successive melting and casting sequences, *i.e.* fitting alloying elements in precisely defined planes.

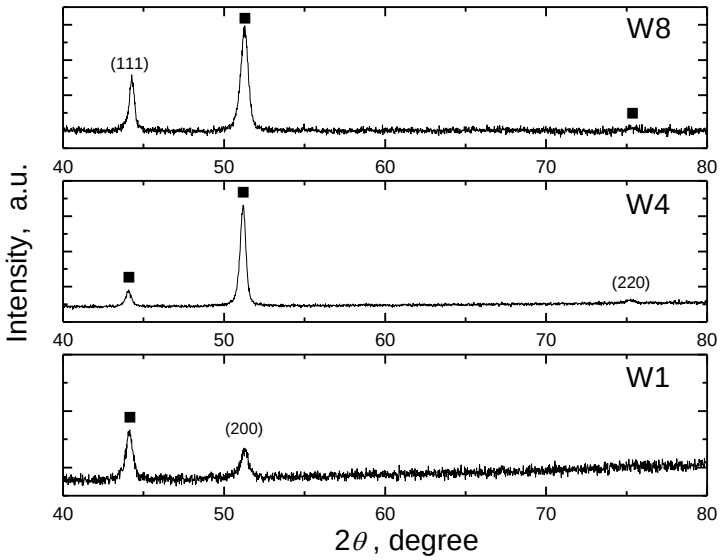

Figure 4. XRD patterns of the Ni-Cr dental alloy after (a) first (W1), (b) fourth (W4), and (c) eight (W8) recasting cycle.

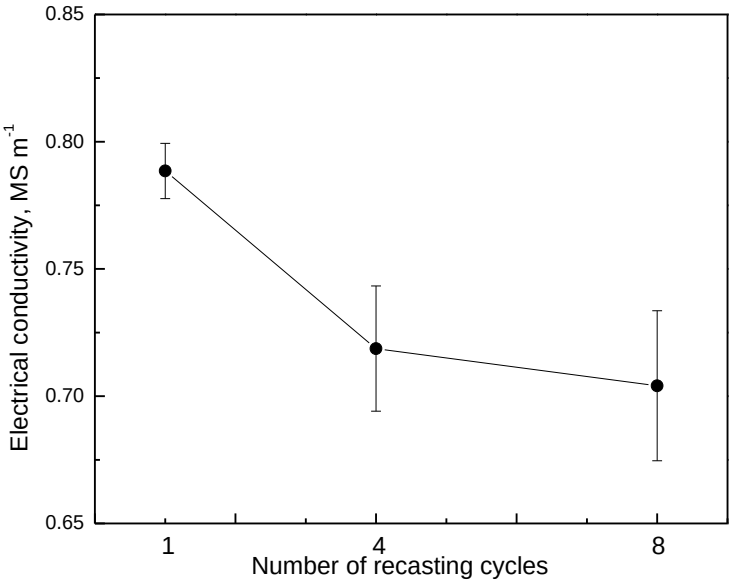

Figure 5. Electrical conductivity of multiple casting samples of the Ni-Cr dental alloy.

The information about the electrical conductivity of most of the materials used in dentistry is limited in the available literature. Starčuková et al. [5] reported that the difference in the electrical conductivity of 45 metallic dental materials is in the range from 0.8 MS m^{-1} to 9.41 MS m^{-1}. Based on their results, the Ni-Cr alloys are in the group of dental alloys with the lowest value of electrical conductivity ranging from 0.80 to 0.89 MS m^{-1}, and the Wirron 99 alloy has a value of 0.8 MS m^{-1}. The electrical conductivity of Ni-Cr alloys was found to be law and in the narrow range of 0.7-0.78 MS m^{-1}. The values of electrical conductivity of the recast samples of Ni-Cr-based dental alloy

indicate that when the number of recasting cycles increases the concentration of impurities, such as oxides, nitrides, and carbines, causes a decrease in electrical conductivity (Fig. 5). Furthermore, it was reported that several alloying elements in the Ni-Cr alloys (Mo, Nb, and Fe) can form oxides and nitrites at high temperatures with gases from the surrounding atmosphere that can alter the properties of these alloys [28].

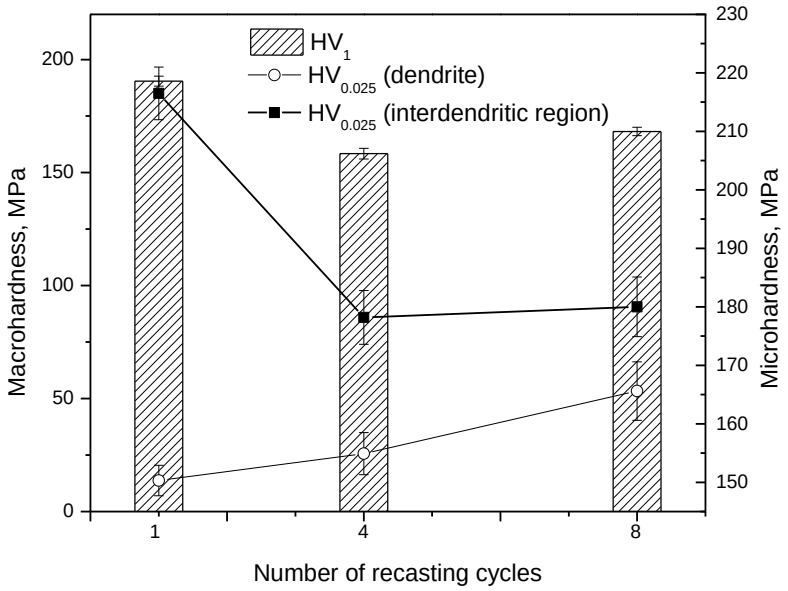

Figure 6. Effect of the recasting cycle number on the macrohardness and microhardness of dendritic and interdendritic regions in the Ni-Cr dental alloy.

The correlation between the number of recasting cycles and the macro- and microhardness of dendritic and interdendritic regions of the alloy is shown in Fig. 6. It can be noticed that with the recasting cycles number increase the macro- and microhardness of interdendritic regions decrease with a slight discrepancy observed for samples obtained after the fourth and eighth recasting. On the other hand, the microhardness of dendrites increases with the recasting cycle number increase. The microhardness of interdendritic regions is higher than that of dendritic areas. The difference between the microhardness of these two regions (dendritic and interdendritic) is decreased with an increase in the recasting cycle number and tends to equalize. The minor difference in the concentration of elements between these two zones is additionally confirmed by the slight difference in the level of microhardness that decreases in series 66→22→15 MPa with the recasting cycle number increase.

4. Conclusions

Commercially available Ni-Cr-based dental alloy Wirron 99 was investigated to determine the effect of multiple recasting processes on the alloy structure and properties. For this purpose, the number of recasting cycles was selected to be one, four, and eight. The alloy microstructural and structural alterations were examined in detail. All tested samples showed dendritic solidification microstructure that changes with the number of recasting cycles. An increase in the recasting cycle number resulted in a decrease in the interdendritic regions' hardness and an increase in the dendrites' hardness. The electrical conductivity of the recast Wirron 99 alloy decreased with an increase in the number of recasting cycles due to an increase in the impurities concentration.

Acknowledgments

This research was financially supported by the Ministry of Education, Science and Technological Development of the Republic of Serbia, grant number 451-03-68/2022-14/200017.

References

[1] Wataha, J.C., Messer, R.L., Casting alloys, *Dental Clinics of North America*, 48 (2004), pp. 499-512
[2] Anusavice, K.J., *Philips' Science of Dental Materials, 10ed*, W.B. Saunders Company, Pennsylvania, 1996, pp. 423-523
[3] Karimi, S., Nickchi, T., Alfantazi, A., Effect of bovine serum on the corrosion behavior of AISI 316L, Co-28Cr-6Mo, and Ti-6Al-4V alloys in phosphate buffered saline solutions, *Corrosion Science*, 53 (2011), pp. 3262-3272
[4] Karimi, S., Nickchi, T., Alfantazi, A., Long-term corrosion investigation of AISI 316L, Co-Cr-Mo, and Ti-6Al-4V alloys in simulated body solution, *Applied Surface Science*, 258 (2012), pp. 6087-6096
[5] Starčukova, J., Starčuk Jr. Z, Hubálková, H., Linetsky, I., Magnetic suspctibility and electrical conductivity of metallic dental materials and their impact on MR imaging artifacts, *Dental Materials*, 24 (2008), pp. 715-793
[6] Elshahawy W., Watanabe, I., Biocompatibility of dental alloys in dental fixed prosthodontics, *Tanta Dental Journal*, 11 (2014), pp. 150-159
[7] Sharma, M., Kumar, A.V.R., Singh, N., Adya, N., Saluja B., Electrochemical Corrosion Behavior of Dental/Implant Alloys in Artificial Saliva, *Journal of Materials Engineering and Performance*, 17 (2008), pp. 695-701
[8] Imirzalioglu, P., Alaaddinoglu E., Yilmaz, Z., Oduncuoglu, B., Yilmaz, B., Rosenstiel, S., Influence of recasting different types of dental alloys on gingival fibroblast cytotoxicity, *The Journal of Prosthetic Dentistry*, 107 (2012), pp. 24-33
[9] Ameer, M.A., Khamis, E., Al-Motlaq, M., Electrohemical behavior of recasting Ni-Cr and Co-Cr non-precious dental alloys, *Corrosion Science*, 46 (2004), pp. 2825-2836
[10] Nakhaei, M.R., Ghanbarzadeh, J., Goharian, R, The Effect of Recast Base metal Alloys on Crown's Marginal Accuracy, *Journal of Medical Science*, 8 (2008), pp. 599-602
[11] Maksimović, V.M., Čairović, A.D., Pantić, J.R, Cvijović-Alagić, I.Lj. The Recasting Effect of the High Gold Dental Alloy Properties, *Journal of Mining and Metallurgy - Section B. Metallurgy*, 51 (2015), pp. 55-59
[12] Čairović, A., Djordjević, I., Bulatović, M., Mojić, M., Momčilović, M., Stošić-Grujić, S., Maksimović, V., Maksimović-Ivanić, D., Mijatović, S., Stamenković, D., In Vitro assessment of Ni-Cr and Co-Cr dental alloys upon recasting: Cellular Compatibility, *Digest Journal of Nanometerials and Biostructure*, 8 (2013), pp. 877-886
[13] Chandra, T.S., Kumar, N.S., Kumari, B.K., Evaluation cytotoxicity of recycled Ni-Cr dental casting alloys: An in vitro study, *Trends in Biomaterials and Artificial Organs*, 25 (2011), pp. 51-59
[14] Stamenković, D.S., Čairović, A., Čolić, M., Rudolf, R., Radović, K., Đorđevic, I. The effect of repeated casting on biocompatibility of a dental gold alloy, *Acta Veterinaria-Beograd*, 59 (2009), pp. 641-652
[15] Vaillant-Corroy, A.S., Corne P., De March, P., Fleutot, S., Cleymand, F., Influence of recasting on the quality of dental alloys: A systematic review, *Journal of Prosthetic Dentistry*, 114 (2015), pp. 205-211
[16] Fitzpatrick, B.J., Brockhurst, P., Gullotta, E., Determination of gold alloy loss during the production of cast dental restorations, *Australian Dental Journal*, 43 (1998), pp. 417-421
[17] Madani, A.S., Rokni, S.R., Mohammadi, A., Bahrami, M., The effect of recasting on bond strength between porcelain and base-metal alloys, *Journal of Prosthodontics*, 20 (2011), pp. 190-194
[18] Al-Hiyasat, A.S., Darmani, H., The effects of recasting on the cytotoxicity of base metal alloys, *Journal of Prosthetic Dentistry*, 93 (2005), pp. 158-163
[19] Jabbar, M.A.A., Comparative study of the corrosion behavior between casting and recasting of the three types of non-precious alloys, *Journal of Baghdad College of Dentistry*, 20 (2008), pp. 14-19
[20] Palaskar, J., Nadgir, D.V., Shah, I., Effect of recasting of nickel-chromium alloy on it porosity, *Contemporary Clinical Dentristy*, 1 (2010), pp. 237-242
[21] Ozyegin, L.S., Tuncer, R., Avci, E., Hardness, behavior and metal surface evaluation of recasting non-precious dental alloys, *Key Engineering Materials*, 330-332 (2007), pp. 1425-1428

[22] Palaskar, J., Nadgir, D.V., Shah, I., Effect of recasting of nickel-chromium alloy on its hardness, *International Journal of Dental Clinics*, 2 (2010), pp. 8-11
[23] Peraire, M., Martinez-Gomis, J., Anglada, J.M., Bizar, J., Salsench, J., Gil, F.J, Effect of recasting on the chemical composition, microstructure, microhardness and ion release of 3 dental casting alloys and titanium, *International Journal of Prosthodontics*, 20 (2007), pp. 286-288
[24] Bandela, V., Kanaparthi, S., Effect of Recasting on the Quality of Dental Alloys: A Review, *International Medical Journal*, 28 (2021), pp. 115-117
[25] Qiu J, Yu W-Q., Zhang F-Q., Smales R.J., Zhang Y-L., Lu C-H., Corrosion behaviour and surface analysis of a Co–Cr and two Ni–Cr dental alloys before and after simulated porcelain firing, *European Journal of Oral Science*, 119 (2011), pp. 93–101
[26] Lin, H-Y., Bowers, B., Wolan, J.T., Cai, Z., Bumgardner, J.D., Metallurgical, surface, and corrosion analysis of Ni-Cr dental casting alloys before and after porcelain firing, *Dental Materials*, 3 (2008), pp. 378-385
[27] Maksimović,V.M, Stoiljković, M.M., Čairović, A.G, Some consequences of repeated casting of Co-Cr dental alloy, *Journal of the Serbian Chemical Society*, 81 (2016), pp. 1307-1319
[28] Bauer, J.R. de O., Loguercio, A.D., Reis, A., Filho, L.E.R., Microhardness of Ni-Cr alloys under different casting conditions, *Brazilian Oral Research*, 20 (2006), pp. 40-46

Journal of Innovative Materials in Extreme Conditions
2022
Volume 3
Issue 1

DFT STUDY OF THE Cr_2SiN_4 UNDER EXTREME PRESSURE CONDITIONS

Tamara Škundrić[1,2,3]* Dejan Zagorac[1,2], Milan Pejić[1,2], Jelena Zagorac[1,2] Branko Matović[1,2]

[1] Institute of Nuclear Sciences "Vinča", University of Belgrade, Belgrade, Serbia
[2] Centre of Excellence "CextremeLab", Centre for synthesis, processing, and characterization of materials for application in extreme conditions, Belgrade, Serbia
[3] Department of Chemistry, Faculty of Science and Mathematics, University of Niš, 18000 Niš, Serbia

Corresponding author: tamara.skundric@vin.bg.ac.rs*

Abstract: Recently predicted Cr_2SiN_4 phases have been further investigated using *ab initio* methods to explore their behavior under extreme conditions of pressure. Thermodynamic functions for several different modifications have been calculated for the pressure range from 0 to 10 GPa using the GGA-PBE functional. Detailed analysis of the mechanical properties under pressure has been performed using the CRYSTAL solid-state quantum-chemical program. The change in volume, energy, and bulk modulus with pressure elevation has been discussed for each of the phases investigated within this study. The highest value of bulk modulus is found in the equilibrium spinel type modification showing the highest capacity of resistance to volume change under pressure. As this material could potentially have a very wide industrial and technological application, these findings could be of great importance as they provide more insight into this novel Cr_2SiN_4 compound, and especially its behaviour in the extreme environment.

Keywords**:** *DFT, Cr_2SiN_4, extreme pressures, high temperature, structure prediction, theoretical methods, Cr-Si-N*

1. Introduction

Various equipment faces severe damage during usage, especially those operating in harsh conditions such as the marine environment. To extend the lifetime of such equipment, protective coatings are urgently needed [1]. Protective hard coatings are used to reduce friction and wear of various tools and to improve the corrosion and oxidation resistance of mechanical parts and die-casting molds [2]. Transition metal nitride (TM-N) coatings have been widely used as protective methods [3] and CrN coatings are among the most widely used due to their high hardness, excellent toughness, preferable adhesion, and excellent anti-corrosive properties [4]. Besides the fact that this coating is distinguished as a very stable coating with a vast application, the research on the addition of alloying elements is thriving in order to additionally enhance its features as a protective coating [5-13].

There is a number of studies indicating that introduction of a third element, like silicon, in the Cr-N complex significantly improves its performance [14-18]. The CrSiN coating is composed of two phases: the nanocrystalline CrN that is embedded in the Si_3N_4 amorphous matrix [4, 13, 15, 17, 19], but it appears that silicon content leads to the change in the microstructure of these CrSiN films [20]. Besides the improvement of hardness and wear resistance, silicon content increase has a certain lubrication effect as well. Due to the silicon increase, the particles change from triangle to circle with a distribution that tends to be uniform so the crystal structure of the coating is also changed, and the density increases [21]. The increase of Si content in CrSiN coatings has been also considered to have a critical impact on the rise in hardness [4, 15], and Young's modulus [18]. However, it has been recorded that after reaching a maximum in hardness, a further rise in silicon content can lead to a sharp decrease in hardness [13, 15, 21], which is believed to be associated with the increase in volume fraction of amorphous Si_3N_4 phase [13, 15]. The structure of the CrSiN coating also changes from crystalline to amorphous with the silicon increase [22, 23]. Rising silicon content led to a reduced friction coefficient [15] and wear rate and this is considered to be associated with the formation of the amorphous oxide layer as a consequence of the tribochemical reaction that occurs in

the wear contact area [24]. The reaction that takes place between the interfaces generates $Si(OH)_4$ which has a lubricating effect that is thought to have led to the lower friction coefficient [14].

Because of its excellent properties, CrSiN can be used in many cyclic and repeated load applications [25] (such as high-speed cutting, wood machining applications, hydraulic piston pump, valve, gear, shaft, and propeller) [1, 14, 26] as corrosion-resistant coatings in the marine environment [27] and as a protective coating for die casting molds. Also, CrSiN can be used in environmentally friendly, clean, low-cost water-based lubricating systems [24], thus replacing traditional oil-based ones in modern machines. As many applications require materials capable of operating under extreme conditions, there is a rising trend in research of innovative materials sustainable in different extreme environments. Materials can behave in unexpected ways when placed in extreme environments, thus it is necessary to understand the forces that affect materials' behavior.

From the theoretical aspect, energy landscape investigation refer to the isolated system that has no interaction with the environment, but that changes drastically when exploring materials in extreme conditions where the interaction with the environment must be taken into account [28]. Within this study, we investigated the bulk Cr_2SiN_4, to find candidate structures possible to be observed at extreme conditions of temperature and pressure. We have performed global explorations of the energy landscape of the bulk Cr_2SiN_4 using simulated annealing with an empirical potential [29, 30], combined with data mining [31, 32] and the Primitive Cell approach for Atom Exchange (PCAE) method [33, 34]. *Ab initio* structural refinement confirmed several structure candidates on both the GGA-PBE and the LDA-PZ levels of calculation, and their behavior under extreme conditions has been further investigated in this study.

2. Computational details

Ab initio calculations of the structural and mechanical properties in the high-pressure regime were performed using the CRYSTAL17 code [35, 36], which is based on linear combinations of atomic orbitals (LCAO). Local optimizations are performed on the density functional theory level using the Generalized Gradient Approximation (GGA) with the Perdew–Burke–Ernzerhof (PBE) functional [37]. An all-electron basis set based on Gaussian-type orbitals was employed in the case of chromium (Cr_86-411d41G_catti_1995) [38, 39], silicon (Si_86-311G**_pascale_2005) [40, 41], and nitrogen (N_6-21G*_dovesi_1990) [42, 43]. *Ab initio* simulation of elastic properties of crystalline materials under pressure has been performed with the solid-state quantum-chemical program CRYSTAL [44]. Results of successful calculations applied previously are discussed in refs. [45-49] and are highly important in the exploration of energy landscapes under extreme conditions [28, 50, 51]. KPLOT code [52] was used for the crystallographic analysis, while visualization of the structures has been done by VESTA software [53].

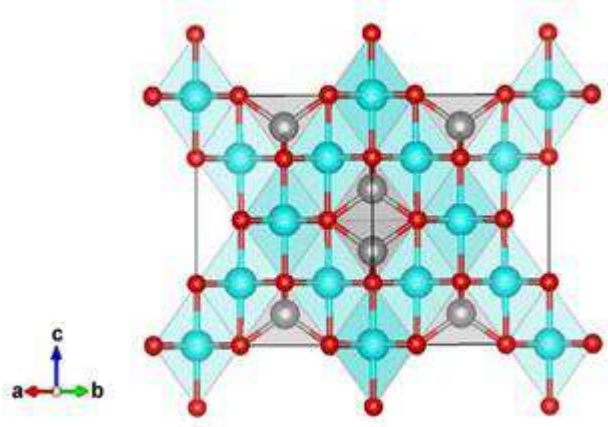

Figure 1. Visualization of the Al_2MgO_4-spinel-type in space group *Fd-3m* (no. 227) appearing as the equilibrium Cr_2SiN_4 modification. Blue, grey and red spheres denote Cr, Si and N atoms, respectively.

3. Results and Discussion

Generated from the DM-based searches the Al_2MgO_4-spinel-type modification [54, 55], is the lowest one in the calculated total energy at both the GGA-PBE and the LDA-PZ level of calculation. It represents the global minimum for the whole energy landscape including the structures obtained from the GO and the PCAE method calculations. It crystallizes in the space group *Fd-3m* (no. 227) with unit cell parameters a = 7.88 Å at the GGA-PBE level of calculation [56] and is visualized in Figure 1a. This Al_2MgO_4-spinel-type modification remains the global minimum when structure optimizations of the candidates are performed on the DFT-LDA level [56]. Volume change, thermodynamic functions, and bulk modulus calculated for the Al_2MgO_4-spinel phase in the pressure range from 0 – 10 GPa using the third-order Birch-Murnaghan isothermal equation of state are presented in Table 1. *Ab initio* calculations were performed using the GGA-PBE functional.

Table 1. Thermodynamic functions obtained with third-order Birch-Murnaghan isothermal equation of state for the Al_2MgO_4-spinel-type of structure for pressures up to 10 GPa. Calculations were performed using GGA-PBE functional. V = Volume, P = Pressure, E = Total energy, G = Gibbs free energy, B = Bulk modulus.

V (A^3)	P (GPa)	E (a.u.)	G (a.u.)	B (GPa)
122.05	0.00	-5193.506	-5193.506	368.23
121.68	1.11	-5193.506	-5193.475	372.68
121.32	2.22	-5193.506	-5193.444	377.12
120.96	3.33	-5193.506	-5193.414	381.54
120.61	4.45	-5193.506	-5193.383	385.95
120.27	5.56	-5193.505	-5193.352	390.35
119.93	6.67	-5193.505	-5193.322	394.73
119.59	7.78	-5193.504	-5193.291	399.11
119.26	8.89	-5193.504	-5193.261	403.47
118.94	10.00	-5193.503	-5193.230	407.83

From the calculated results one can observe that with the respective pressure increase, bulk modulus (B) gradually increases from 368.23 GPa, and at a pressure of 10 GPa reaches a value of 407.83 GPa which represents the highest value of all of the investigated phases at the extreme conditions within this system of interest. At the same time, there is a gradual decrease in the volume (V) of the unit cell with pressure elevation. We note a monotonous increase of the Gibbs free energy (G) with pressure increase, while minute energy differences are observed in the calculated total energies (E).

We have further investigated Cr_2SiN_4 modifications appearing under extreme conditions. At first, we have investigated the structure generated from the global optimization method denoted as β-Cr_2SiN_4-type modification that crystallizes in space group *P-1* (no. 2) with unit cell parameters a = 7.28, b = 7.79, c = 2.74 Å, α = 93.66, β = 82.48, and γ= 120.64, computed with the GGA-PBE functional [56]. The structure is presented in Figure 2a, and within this monoclinic phase, chromium is six-fold coordinated by nitrogen forming two different CrN_6 octahedra. The whole structure resembles zeolite as face-connected CrN_6 octahedra incline to each other thus forming a void in the center of the structure. Structure denoted as γ-Cr_2SiN_4-type was generated using the PCAE method and it structurally differentiates from the phase used as a starting structure in the Si_3N_4 system. It crystallizes in space group *Cc* (no. 9) with unit cell parameters a = 5.62, b = 8.96, c = 5.36 Å, and β = 117.93, and the structure is visualized in Figure 2b. Another monoclinic structure from the global optimization search is referred as δ-Cr_2SiN_4-type and is presented in Figure 2c. It appears in space group *P21/m* (no. 11) with unit cell parameters a= 6.21, b = 3.82, c = 5.54 Å, and β = 116.24, calculated with the GGA-PBE functional.

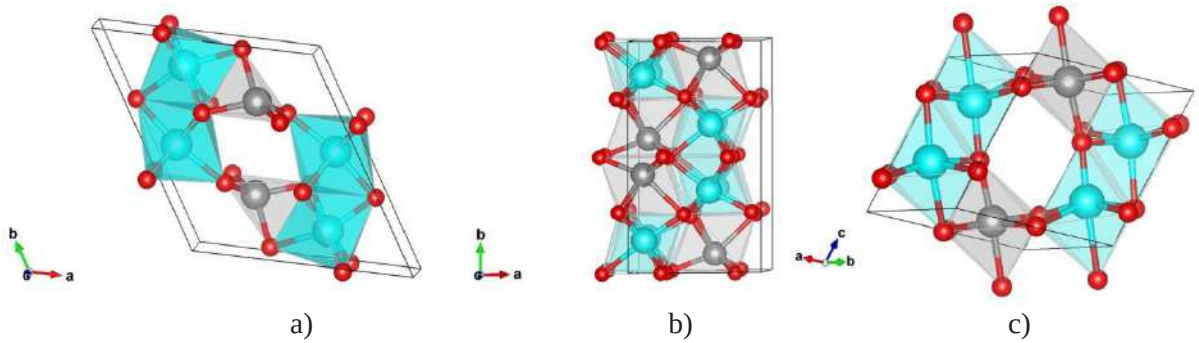

a) b) c)

Figure 2. Visualization of the: a) β-Cr_2SiN_4-type in space group *P-1* (no. 2); b) γ-Cr_2SiN_4-type in space group *Cc* (no. 9); c) δ-Cr_2SiN_4-type in space group *P21/m* (no. 11). Blue, grey and red spheres denote Cr, Si and N atoms, respectively.

The behavior of the β- and the γ-Cr_2SiN_4 structures under extreme conditions is investigated and presented in Table 2. At first, we note that the initial volume of the β-phase is much larger than the equilibrium spinel modification, while γ-phase appears to have smaller volumes than the spinel modification. There is also a slight increase in total energy and Gibbs free energy with increasing pressure as in the previous case. Resistance to the volume change under pressure, presented with the bulk modulus (B) [57], and the calculated values using the GGA-PBE functional for these modifications are given in Table 2. The smallest value of bulk modulus of these three phases explored is found in β-Cr_2SiN_4-type modification with starting value of 166.28 GPa up to 262.79 GPa (at the applied pressure of 10 GPa). In the following γ-Cr_2SiN_4-type modification the largest jump in value from 236.96 GPa to 356.95 GPa has been observed, which is in both cases different and smaller than the Al_2MgO_4-spinel-type of structure (368.23-407.83 GPa).

In the case of the δ-Cr_2SiN_4 structure type, high-pressure calculations up to 10 GPa are presented in Table 3. We note that the δ-Cr_2SiN_4 modification appears at the lowest volumes, however, with bulk modulus much higher than the previous β- and the γ-Cr_2SiN_4 modifications. The calculated value of B with the increase of pressure goes from 296.30-342.89 GPa, which is closer to the spinel phase. In all of the examined Cr_2SiN_4 phases so far, with the first increase in pressure of 1.11 GPa, a rapid increase in bulk modulus is observed, which is necessarily accompanied by a slight decrease in volume. This trend continues for the whole investigated pressure range, however, the increase in bulk modulus is slightly smaller for each subsequent rise in pressure.

Table 2. Thermodynamic functions obtained with third-order Birch-Murnaghan isothermal equation of state for a) the β-Cr_2SiN_4 type; b) the γ-Cr_2SiN_4 type of structure for pressures up to 10 GPa. Calculations were performed using GGA-PBE functional. V = Volume, P = Pressure, E = Total energy, G = Gibbs free energy, B = Bulk modulus.

a)

V (A^3)	P (GPa)	E (a.u.)	G (a.u.)	B (GPa)
134.01	0.00	-5193.437	-5193.437	166.28
133.15	1.11	-5193.437	-5193.403	179.68
132.36	2.22	-5193.437	-5193.369	192.59
131.62	3.33	-5193.436	-5193.335	205.07
130.93	4.45	-5193.436	-5193.302	217.18
130.28	5.56	-5193.435	-5193.269	228.98
129.67	6.67	-5193.434	-5193.236	240.49
129.08	7.78	-5193.433	-5193.203	251.75
128.53	8.89	-5193.432	-5193.170	262.79
128.00	10.00	-5193.431	-5193.137	273.62

b)

V (A^3)	P (GPa)	E (a.u.)	G (a.u.)	B (GPa)
119.23	0.00	-5193.435	-5193.435	236.93
118.69	1.11	-5193.435	-5193.404	251.71
118.18	2.22	-5193.434	-5193.374	266.03
117.70	3.33	-5193.434	-5193.344	279.93
117.24	4.45	-5193.434	-5193.314	293.48
116.81	5.56	-5193.433	-5193.284	306.70
116.40	6.67	-5193.433	-5193.255	319.63
116.00	7.78	-5193.432	-5193.225	332.31
115.62	8.89	-5193.431	-5193.195	344.74
115.25	10.00	-5193.430	-5193.166	356.95

Table 3. Thermodynamic functions obtained with third-order Birch-Murnaghan isothermal equation of state for the δ-Cr_2SiN_4 structure type for pressures up to 10 GPa. Calculations were performed using GGA-PBE functional. V = Volume, P = Pressure, E = Total energy, G = Gibbs free energy, B = Bulk modulus.

V (A^3)	P (GPa)	E (a.u.)	G (a.u.)	B (GPa)
117.86	0.00	-5193.419	-5193.419	296.30
117.42	1.11	-5193.419	-5193.389	301.55
116.99	2.22	-5193.419	-5193.359	306.79
116.57	3.33	-5193.419	-5193.329	312.00
116.16	4.45	-5193.418	-5193.300	317.19
115.76	5.56	-5193.418	-5193.270	322.37
115.36	6.67	-5193.417	-5193.241	327.52
114.97	7.78	-5193.416	-5193.211	332.66
114.59	8.89	-5193.416	-5193.182	337.78
114.22	10.00	-5193.415	-5193.153	342.89

Next, we have explored the structures appearing in the most extreme conditions, and the first of investigated structures, $TiMn_2O_4$-type [58] modification is presented in Figure 3a. This tetragonal structure obtained from the data-mining search appears in space group *P4322* (no. 95) with unit cell parameters a= 5.64 and c = 7.74 Å. Another structure generated from the global optimization search is denoted as ε-Cr_2SiN_4-type and it crystallizes in space group *P21/m* (no. 11). This monoclinic structure is visualized in Figure 3b with unit cell parameters a = 5.09, b = 2.89, c = 8.90 Å, and ε = 90.20. Within this structure, chromium is 6-fold coordinated by nitrogen thus forming an octahedral environment. The final analyzed structure, Mg_2SiO_4(Forsterite)-type [59] is a structure generated from a data-mining search and is presented in Figure 3c. It appears in space group *Pnma* (no. 62) with unit cell parameters a = 9.42, b = 5.45, and c = 4.82 Å. Within this orthorhombic structure, chromium is in 6-fold coordination by nitrogen, however forming two different octahedra.

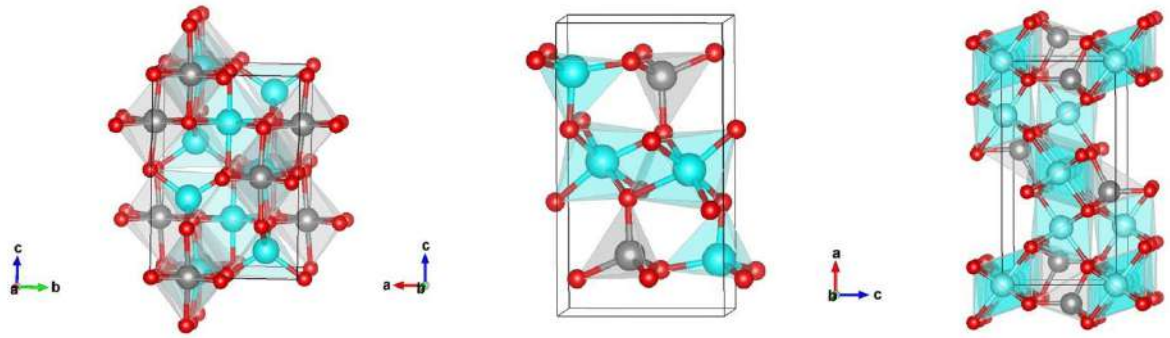

a) b) c)

Figure 3. Visualization of the: a) $TiMn_2O_4$-type in space group *P4322* (no. 95); b) ε-Cr_2SiN_4-type in space group *P21/m* (no. 11); c) Mg_2SiO_4(Forsterite)-type in space group *Pnma* (no. 62). Blue, grey and red spheres denote Cr, Si and N atoms, respectively.

The behaviour of the $TiMn_2O_4$-type and the ε-Cr_2SiN_4-type modification that appear in most extreme conditions is investigated and the results are presented in Table 4. Firstly, one can observe that the initial volume of the $TiMn_2O_4$-type modification is very similar to the equilibrium spinel type, while the ε-Cr_2SiN_4-type modification has a much larger initial volume, close to the β-Cr_2SiN_4-type modification. However, in both cases, there is a gradual decrease in volume with a pressure increase. As in previous cases, we also note a slight increase in total energy and Gibbs free energy with pressure addition. The resistance to the volume change under pressure for these phases is calculated

using the GGA-PBE functional and the results are presented in Table 4. In the case of $TiMn_2O_4$-type modification, the value of bulk modulus is almost the same as in the β-Cr_2SiN_4-type modification, but with the applied pressure of 10 GPa reaches a much smaller value of 187,42 GPa. The other one, ε-Cr_2SiN_4-type modification has a much smaller value of bulk modulus of 148,92 GPa, but compared to the previous phase larger jump in value has been observed (reaching 236,44 GPa at a pressure of 10 GPa).

For the last one of these investigated phases, Mg_2SiO_4(Forsterite)-type modification, high-pressure calculations up to 10 GPa are presented in Table 5. Compared to the previous investigated phase, the initial volume of 124,24 A^3 is much smaller and quite similar to the $TiMn_2O_4$-type modification. As in the previous phases, a gradual decrease in volume with pressure elevation has been observed. Calculated results indicate that pressure increase also led to the increase in Gibbs free energy, but a minute energy difference in total energy has also been noted (Table 5). The calculated value of bulk modulus (B) of 128,46 GPa for this modification, with an increase in pressure up to 10 GPa reaches a value of 161,51 GPa which represents the smallest value of bulk modulus of all of the investigated phases.

Table 4. Thermodynamic functions obtained with third-order Birch-Murnaghan isothermal equation of state for a) the $TiMn_2O_4$ type; b) ε-Cr_2SiN_4 type of structure for pressures up to 10 GPa. Calculations were performed using GGA-PBE functional. V = Volume, P = Pressure, E = Total energy, G = Gibbs free energy, B = Bulk modulus.

a)

V (A^3)	P (GPa)	E (a.u.)	G (a.u.)	B (GPa)
123.04	0.00	-5193.412	-5193.412	166.78
122.64	1.11	-5193.412	-5193.381	169.10
122.24	2.22	-5193.412	-5193.350	171.41
121.84	3.33	-5193.412	-5193.319	173.72
121.46	4.45	-5193.412	-5193.288	176.02
121.08	5.56	-5193.411	-5193.257	178.31
120.70	6.67	-5193.411	-5193.226	180.60
120.34	7.78	-5193.410	-5193.195	182.88
119.97	8.89	-5193.409	-5193.165	185.15
119.62	10.00	-5193.409	-5193.134	187.42

b)

V (A^3)	P (GPa)	E (a.u.)	G (a.u.)	B (GPa)
132.13	0.00	-5193.414	-5193.414	148.12
131.17	1.11	-5193.414	-5193.381	158.88
130.29	2.22	-5193.414	-5193.347	169.33
129.46	3.33	-5193.413	-5193.314	179.52
128.68	4.45	-5193.413	-5193.281	189.46
127.95	5.56	-5193.412	-5193.249	199.20
127.26	6.67	-5193.411	-5193.216	208.75
126.59	7.78	-5193.410	-5193.184	218.13
125.96	8.89	-5193.409	-5193.152	227.35
125.36	10.00	-5193.407	-5193.120	236.44

Table 5. Thermodynamic functions obtained with third-order Birch-Murnaghan isothermal equation of state for the Mg_2SiO_4 structure type for pressures up to 10 GPa. Calculations were performed using GGA-PBE functional. V = Volume, P = Pressure, E = Total energy, G = Gibbs free energy, B = Bulk modulus.

V (A^3)	P (GPa)	E (a.u.)	G (a.u.)	B (GPa)
124.24	0.00	-5193.402	-5193.402	128.46
123.71	1.11	-5193.402	-5193.371	132.25
123.20	2.22	-5193.402	-5193.339	136.01
122.70	3.33	-5193.402	-5193.308	139.74
122.22	4.45	-5193.401	-5193.277	143.43
121.76	5.56	-5193.401	-5193.246	147.10
121.30	6.67	-5193.400	-5193.215	150.74
120.86	7.78	-5193.400	-5193.184	154.35
120.43	8.89	-5193.399	-5193.153	157.94
120.02	10.00	-5193.398	-5193.123	161.51

4. Conclusion

The exploration of the energy landscape of the Cr_2SiN_4 system generated a number of structure candidates using a combination of global optimization (GO), data-mining (DM), and the Primitive Cell approach for Atom Exchange (PCAE) method. After full structural optimization on the ab initio level using the GGA-PBE and LDA-PZ functionals, several structures have been confirmed. Within this study, we have investigated the behavior of Cr_2SiN_4 under high pressure using quantum mechanical calculations. Thermodynamic functions for the selected modifications have been computed using the GGA-PBE functional. In all of the investigated phases, a gradual decrease in the unit cell parameters and corresponding volumes under pressure has been observed. There is also a minute change in total energy and a gradual increase in Gibbs free energy when pressure is applied. A rising trend in bulk modulus with the pressure elevation is detected in all phases under investigation. The largest initial value of bulk modulus of 368,23 GPa has been observed in the equilibrium spinel type modification, and at a pressure of 10 GPa it reaches a value of 407,83 GPa, thus it has the highest capacity of resistance to the volume change under pressure. The smallest initial value of bulk modulus (128,46 GPa) is found in one of the phases that appears in the most extreme conditions, Mg_2SiO_4-type modification, reaching only 161,51 GPa with pressure elevation up to 10 GPa. These findings are important for the future synthesis and development of new Cr-Si-N materials with enhanced properties under extreme conditions.

Acknowledgments

This research was financially supported by the Ministry of Education, Science, and Technological Development of the Republic of Serbia (Grant No. 1702201).

References

[1] Y. Benlatreche, C. Nouveau, H. Aknouche, L. Imhoff, N. Martin, J. Gavoille, C. Rousselot, J.Y. Rauch, D. Pilloud, Physical and mechanical properties of CrAlN and CrSiN ternary systems for wood machining applications, *Plasma Processes and Polymers*, 6 (2009) S113-S117.
[2] Y. Iwasaki, Y. Mizuno, T. Nakayama, T. Suzuki, Preparation of Cr–Si–N–O thin films epitaxially grown on MgO substrates by pulsed laser deposition, *Vacuum*, 179 (2020) 109498.
[3] F. Ge, T. Shao, C. Jia, P. Li, F. Huang, Tribological behaviors of a magnetron sputtered CrSiN coating under ambient air and wet environments, *Surface and Coatings Technology*, 332 (2017) 304-311.
[4] H. Wang, Y. Ye, Y. Wang, Structure, corrosion, and tribological properties of CrSiN coatings with various Si contents in 3.5% NaCl solution, *Surface and Interface Analysis*, 50 (2018) 471-479.
[5] D. Mercs, N. Bonasso, S. Naamane, J.-M. Bordes, C. Coddet, Mechanical and tribological properties of Cr–N and Cr–SI–N coatings reactively sputter deposited, *Surface and Coatings Technology*, 200 (2005) 403-407.
[6] J.W. Kim, K.H. Kim, D. Lee, J. Moore, Study on high-temperature oxidation behaviors of Cr–Si–N films, *Surface and Coatings Technology*, 200 (2006) 6702-6705.
[7] H.N. Shah, R. Jayaganthan, D. Kaur, Influence of reactive gas and temperature on structural properties of magnetron sputtered CrSiN coatings, *Applied surface science*, 257 (2011) 5535-5543.
[8] P. Wo, P. Munroe, Z. Li, Z.-T. Jiang, Z. Xie, Z. Zhou, K. Li, Factors governing the mechanical behaviour of CrSiN coatings: Combined nanoindentation testing and transmission electron microscopy, *Materials Science and Engineering: A*, 534 (2012) 297-308.
[9] K. Bobzin, N. Bagcivan, P. Immich, S. Bolz, R. Cremer, T. Leyendecker, Mechanical properties and oxidation behaviour of (Al, Cr) N and (Al, Cr, Si) N coatings for cutting tools deposited by HPPMS, *Thin Solid Films*, 517 (2008) 1251-1256.
[10] S. Vepřek, New development in superhard coatings: the superhard nanocrystalline-amorphous composites, *Thin Solid Films*, 317 (1998) 449-454.

[11] J. Morgiel, J. Grzonka, R. Mania, S. Zimowski, J.L. Labar, Z. Fogarassy, Relation between microstructure and hardness of nano-composite CrN/Si3N4 coatings obtained using CrSi single target magnetron system, *Vacuum*, 90 (2013) 170-175.
[12] E. Martinez, R. Sanjines, A. Karimi, J. Esteve, F. Lévy, Mechanical properties of nanocomposite and multilayered Cr–Si–N sputtered thin films, *Surface and Coatings Technology*, 180 (2004) 570-574.
[13] J.H. Park, W.S. Chung, Y.-R. Cho, K.H. Kim, Synthesis and mechanical properties of Cr–Si–N coatings deposited by a hybrid system of arc ion plating and sputtering techniques, *Surface and Coatings Technology*, 188 (2004) 425-430.
[14] S. Lei, Y.-r. Zhang, Y.-x. Wang, J.-l. Li, X. Jiang, J.-m. Chen, Corrosion and wear behaviors of PVD CrN and CrSiN coatings in seawater, *Transactions of nonferrous metals society of China*, 26 (2016) 175-184.
[15] L. Huang, C. Zou, W. Xie, F. Peng, L. Shao, Influence of Si contents on the microstructure, mechanical and tribological properties of Cr–Si–N coatings, *Ceramics International*, 42 (2016) 5062-5067.
[16] A. Thobor-Keck, F. Lapostolle, A. Dehlinger, D. Pilloud, J. Pierson, C. Coddet, Influence of silicon addition on the oxidation resistance of CrN coatings, *Surface and Coatings Technology*, 200 (2005) 264-268.
[17] H.-H. Lin, C.-C. Chou, J.-W. Lee, Tribological properties of Cr–Si–N nanocomposite film adherent silicon under various environments, *Thin Solid Films*, 518 (2010) 7509-7514.
[18] H.N. Shah, R. Jayaganthan, A.C. Pandey, Nanoindentation study of magnetron-sputtered CrN and CrSiN coatings, *Materials & Design*, 32 (2011) 2628-2634.
[19] G. Kim, B. Kim, S. Lee, High-speed wear behaviors of CrSiN coatings for the industrial applications of water hydraulics, *Surface and Coatings Technology*, 200 (2005) 1814-1818.
[20] H. Lee, W. Jung, J. Han, S. Seo, J. Kim, Y. Bae, The synthesis of CrSiN film deposited using magnetron sputtering system, *Surface and Coatings Technology*, 200 (2005) 1026-1030.
[21] S. Lu, Y. Wang, P. Gaoand, D. Meng, Effect of Si Content on structure and friction and wear properties of CrSiN coatings, *IOP Conference Series: Earth and Environmental Science, IOP Publishing*, 2020, pp. 022028.
[22] X.M. Xu, H. Zhang, F.F. Luo, Z.H. Zhou, S.W. Duo, The properties of CrSiN coatings of different Si content, *Applied Mechanics and Materials, Trans Tech Pub*l, 2014, pp. 4323-4326.
[23] Q.M. Wang, K.H. Kim, Microstructural control of Cr–Si–N films by a hybrid arc ion plating and magnetron sputtering process, *Acta Materialia*, 57 (2009) 4974-4987.
[24] Z. Geng, H. Wang, C. Wang, L. Wang, G. Zhang, Effect of Si content on the tribological properties of CrSiN films in air and water environments, *Tribology International*, 79 (2014) 140-150.
[25] K. Khlifi, N. Barhoumi, H. Dhiflaoui, A. Ben Cheikh Larbi, Fatigue behaviour and mechanical properties of PVD CrSiN coating using cyclic nanoindentation, *Tribology-Materials, Surfaces & Interfaces*, 15 (2021) 252-257.
[26] S.-Y. Lee, Y.-S. Hong, Effect of CrSiN thin film coating on the improvement of the low-speed torque efficiency of a hydraulic piston pump, *Surface and Coatings Technology*, 202 (2007) 1129-1134.
[27] T. Shao, F. Ge, C. Pei, F. Huang, D. Sun, S. Zhang, Effects of Si content on Tribo-corrosion behavior of Cr1-xSixN coatings prepared via magnetron sputtering, *Surface and Coatings Technology*, 356 (2018) 11-18.
[28] J.C. Schön, Energy Landscape Concepts for Chemical Systems under Extreme Conditions, *Journal of Innovative Materials in Extreme Condition*s, 2 (2021) 5-57.
[29] D. Zagorac, J.C. Schön, V.I. Pentin, M. Jansen, Structure prediction and energy landscape exploration in the zinc oxide system, *Processing and Application of Ceramics*, 5 (2011) 73-78.
[30] D. Zagorac, J. Schön, J. Zagorac, M. Jansen, Prediction of structure candidates for zinc oxide as a function of pressure and investigation of their electronic properties, *Physical Review B*, 89 (2014) 075201.
[31] D. Zagorac, J.C. Schön, M. Jansen, Identification of promising chemical systems for the synthesis of new materials structure types: An ab initio minimization data mining approach, *Processing and Application of Ceramics*, 7 (2013) 37-41.
[32] J. Zagorac, D. Zagorac, A. Zarubica, J.C. Schon, K. Djuris, B. Matovic, Prediction of possible CaMnO3 modifications using an ab initio minimization data-mining approach, *Acta Crystallographica Section B*, 70 (2014) 809-819.

[33] D. Zagorac, J. Zagorac, J.C. Schön, N. Stojanović, B. Matović, ZnO/ZnS (hetero) structures: ab initio investigations of polytypic behavior of mixed ZnO and ZnS compounds, *Acta Crystallographica Section B: Structural Science, Crystal Engineering and Materials*, 74 (2018) 628-642.
[34] D. Zagorac, J. Zagorac, M. Pejić, B. Matović, J.C. Schön, Band Gap Engineering of Newly Discovered ZnO/ZnS Polytypic Nanomaterials, *Nanomaterials*, 12 (2022) 1595.
[35] R. Dovesi, A. Erba, R. Orlando, C.M. Zicovich-Wilson, B. Civalleri, L. Maschio, M. Rérat, S. Casassa, J. Baima, S. Salustro, Quantum-mechanical condensed matter simulations with CRYSTAL, *Wiley Interdisciplinary Reviews: Computational Molecular Science*, 8 (2018) e1360.
[36] R. Dovesi, F. Pascale, B. Civalleri, K. Doll, N.M. Harrison, I. Bush, P. D'arco, Y. Noël, M. Rérat, P. Carbonniere, The CRYSTAL code, 1976–2020 and beyond, a long story, *The Journal of Chemical Physics*, 152 (2020) 204111.
[37] J.P. Perdew, K. Burke, M. Ernzerhof, Generalized gradient approximation made simple, *Physical review letters*, 77 (1996) 3865.
[38] M. Catti, G. Sandrone, G. Valerio, R. Dovesi, Electronic, magnetic and crystal structure of Cr2O3 by theoretical methods, *Journal of Physics and Chemistry of Solids*, 57 (1996) 1735-1741.
[39] E. Ruiz, M. Llunell, P. Alemany, Calculation of exchange coupling constants in solid state transition metal compounds using localized atomic orbital basis sets, *Journal of Solid State Chemistry*, 176 (2003) 400-411.
[40] F. Pascale, C.M. Zicovich-Wilson, R. Orlando, C. Roetti, P. Ugliengo, R. Dovesi, Vibration frequencies of Mg3Al2Si3O12 pyrope. An ab initio study with the CRYSTAL code, *The Journal of Physical Chemistry B*, 109 (2005) 6146-6152.
[41] Y. Noel, M. Catti, P. D'Arco, R. Dovesi, The vibrational frequencies of forsterite Mg2SiO4: an all-electron ab initio study with the CRYSTAL code, *Physics and Chemistry of Minerals*, 33 (2006) 383-393.
[42] R. Dovesi, M. Causa', R. Orlando, C. Roetti, V. Saunders, A binitio approach to molecular crystals: A periodic Hartree–Fock study of crystalline urea, *The Journal of Chemical Physics*, 92 (1990) 7402-7411.
[43] D. Zagorac, J. Zagorac, M. Djukic, D. Jordanov, B. Matović, Theoretical study of AlN mechanical behaviour under high pressure regime, *Theoretical and Applied Fracture Mechanics*, 103 (2019) 102289.
[44] A. Erba, A. Mahmoud, D. Belmonte, R. Dovesi, High pressure elastic properties of minerals from ab initio simulations: The case of pyrope, grossular and andradite silicate garnets, *The Journal of chemical physics*, 140 (2014) 124703.
[45] T. Škundrić, B. Matović, A. Zarubica, J. Zagorac, P. Tatarko, D. Zagorac, Structure Prediction and Mechanical Properties of Silicon Hexaboride on Ab Initio Level, *Materials*, 14 (2021) 7887.
[46] J. Zagorac, D. Zagorac, B. Babić, T. Prikhna, B. Matović, Effect of aluminum addition on the structure and electronic properties of boron nitride, *Journal of Solid State Chemistry*, 311 (2022) 123153.
[47] D. Jovanović, J.B. Zagorac, B. Matović, A.R. Zarubica, D. Zagorac, Structural, electronic and mechanical properties of superhard B4C from first principles, *Journal of Innovative Materials in Extreme Conditions*, 1 (2020) 19-27.
[48] J.B. Zagorac, B. Matović, M. Pejić, K. Milutinović, D. Zagorac, Crystal structure and properties of theoretically predicted AlB12, *Journal of Innovative Materials in Extreme Conditions*, 1 (2020) 28-36.
[49] J.B. Zagorac, D. Zagorac, D. Jovanović, M. Pejić, T. Škundrić, B. Matović, Ab Initio Investigations and Behaviour of the α-Ce2ON2 Phase in the Extreme Pressure Conditions, *Journal of Innovative Materials in Extreme Conditions*, 2 (2021) 36-43.
[50] K. Hari Kumar, S. Sridar, Calphad Modelling of Ceramic Systems, *Journal of Innovative Materials in Extreme Conditions*, 2 (2021) 25-35.
[51] D. Zagorac, J.C. Schön, Energy landscapes of pure and doped ZnO: From bulk crystals to nanostructures, *Frontiers of Nanoscience*, Elsevier2022, pp. 151-193.
[52] R. Hundt, KPLOT: A Program for Plotting and Analysing Crystal Structures, Technicum Scientific Publishing: Stuttgart, Germany, (2016).
[53] K. Momma, F. Izumi, VESTA: a three-dimensional visualization system for electronic and structural analysis, *Journal of Applied Crystallography*, 41 (2008) 653-658.
[54] T. Yamanaka, Y. Takéuchi, Order-disorder transition in MgAl2O4 spinel at high temperatures up to 1700 C, *Zeitschrift für Kristallographie-Crystalline Materials*, 165 (1983) 65-78.

[55] P. Kroll, Pathways to metastable nitride structures, *Journal of Solid State Chemistry*, 176 (2003) 530-537.
[56] T. Škundrić, D. Zagorac, J.C. Schön, M. Pejić, B. Matović, Crystal Structure Prediction of the Novel Cr2SiN4 Compound via Global Optimization, Data Mining, and the PCAE Method, *Crystals*, 11 (2021) 891.
[57] E. Ziambaras, E. Schröder, Theory for structure and bulk modulus determination, *Physical Review B*, 68 (2003) 064112.
[58] E. Bertaut, H. Vincent, Etude par diffraction neutronique de la forme ordonnee de l'orthotitanate de manganese-structure cristalline et structure magnetique, *Solid State Communications*, 6 (1968) 269-275.
[59] J.R. Smyth, R.M. Hazen, The crystal structures of forsterite and hortonolite at several temperatures up to 900 C, *American Mineralogist: Journal of Earth and Planetary Materials*, 58 (1973) 588-593.

Journal of Innovative Materials in Extreme Conditions
2022
Volume 3
Issue 1

THEORETICAL MODIFICATIONS OF SCANDIUM OXYCHLORIDE IN EXTREME CONDITIONS AS AN EXAMPLE OF RARE EARTH COMPOUNDS

Dejan Zagorac[1,2*], Matej Fonović[3], Jelena Zagorac[1,2], Milan Pejić[1,2], J. Christian Schön[4]

[1] Institute of Nuclear Sciences "Vinča", University of Belgrade, Belgrade, Serbia
[2] Centre of Excellence "CextremeLab", Centre for synthesis, processing, and characterization of materials for application in extreme conditions, Belgrade, Serbia
[3] Faculty of Engineering, University of Rijeka-RiTeh, Rijeka, Croatia
[4]Max Planck Institute for Solid State Research, Stuttgart, Germany

Corresponding author: dzagorac@vin.bg.ac.rs*

Abstract: *Theoretical modifications of ScOCl at extreme thermodynamic conditions have been identified and are studied as an example of rare earth element (RRE) compounds. Global optimizations with empirical potentials and local optimizations on the ab initio level were performed, leading to the identification of four new structure candidates on the energy landscape that are expected to be relevant under extreme conditions. The structural, as well as electronic properties of these polymorphs, have been investigated and compared with the modifications of the structure under standard conditions. Such theoretical explorations are very important since literature data regarding ScOCl is rather scarce, although ScOCl and the rare-earth elements (REEs) in general have a wide range of applications; for example, scandium is used in solid oxide fuel cells and could be used for potential future applications in photocatalysis or electronic devices, while oxyhalides of transition metals and REEs exhibit interesting magnetic and electronic properties.*

Keywords: ScOCl, Scandium oxychloride, *Ab initio*, DFT, high temperature, ScClO, structure prediction

1. Introduction

The rare-earth elements (REEs) share many comparable chemical and physical properties due to their similar electron configuration; in particular, the atoms of the REEs have the same number of electrons in the outer valence shell (e.g. Sc-$3d^1 4s^2$, Y-$4d^1 5s^2$ and La-$5d^1 6s^2$). Unlike Sc and Y, La and the lanthanides (Ce-Lu) have an additional 4f orbital that fills up before the $5d^1 6s^2$ shell. The most common and stable oxidation state of the REEs is +3, however, other oxidation states may occur, such as +2 (in case of Sm, Eu, and Yb) and +4 (in case of Ce, Pr and Tb) [1,2]. Hence, these chemical elements are highly electropositive and mostly form ionic compounds. Another similarity among the REEs is the so-called lanthanide contraction, where the ionic radius of the rare earth cations decreases (except for Sc and Y) with an increasing atomic number [2]. For example, the cation radius decreases approximately by one-fourth from La^{3+} to Lu^{3+} [2, 3]. Thus, it follows that chemical similarities, in particular the oxidation states and the ionic radii of the REEs, permit easy replacement of one REE by another one in various crystal structures. Besides resulting in very similar crystal structures for the REE compounds, this leads to the occurrence of numerous REEs within a single mineral, with a broad dispersion of the REEs in the earth's upper continental crust [4]. In particular, this suggests that if an REE compound is observed with a particular crystal structure for one REE, one can expect that this structure should also be feasible in an analogous compound with another REE. As commonly observed in the literature, the REEs can be divided into two distinct groups: (i) heavy rare-earth elements (HREEs) consisting of Gd to Lu including Y along with Sc, and (ii) light rare-earth elements (LREEs) consisting of La to Eu. The REEs are not found in their pure state in nature, but rather occur in a wide spectrum of about 250 different minerals species, such as carbonates, silicates, oxides, fluorides, phosphates, borates, arsenates, sulfates, vanadates and tantalates, and others [5, 6]. Some examples of minerals and their associated chemical composition are given in Table 1. [5, 6, 7]

Table 1. Selected minerals and their composition of the rare-earth elements (REEs).

Rare-earth mineral type		Chemical composition
Oxides	Cerianite	$(Ce^{4+},Th^{4+})O_2$
	Loparite	$(Ce,Na,Ca)(Ti,Nb)O_3$
	Hibonite	$(Ca,Ce)(Al,Ti,Mg)_{12}O_{19}$
Phosphates	Monazite	$(Ce,La,Nd,Th)PO_4$
	Xenotime	$(Y,Th,U,Dy,Yb,Er,Gd)PO_4$
	Pretulite	$Sc(PO_4)$
Carbonates	Bastnaesite	$(Ce,La)(CO_3)F$
	Synchysite	$Ca(Ce,La)(CO_3)_2F$
	Lanthanite	$(Ca,La)_2(CO_3)_3\cdot 8H_2O$
Silicates	Jervisite	$(Na, Ca, Fe^{2+})(Sc, Mg, Fe^{2+})Si_2O_6$
	Bazzite	$Be_3(Sc,Al)_2Si_6O_{18}$
	Stillwellite	$CeBSiO_5$
Fluorides	Fluocerite	$(Ce,La)F_3$
	Gagarinite	$NaCaY(F,Cl)_6$
	Tveitite	$(Y, Na)_6Ca_6Ca_6(Ca,Na)F_{42}$
Borates	Braitschite	$(Ca,Na_2)_7CeB_{22}O_{43}\cdot 7H2O$
Sulfates	Chukhrovite	$Ca_3(Y,Ce)(AlF_6)_2(SO_4)(OH)_6$
Arsenates	Chernovite	$Y(AsO_4)$
Tantalates	Polycrase	$(Y,Ca,Ce,U,Th)(Ti,Nb,Ta)_2O_6$
	Formanite	$YTaO_4$
Vanadates	Yttrium vanadate	YVO_4

The REEs form tens of thousands of compounds due to their high affinity toward oxygen and other chemical elements such as nitrogen, carbon, hydrogen, fluoride, and many other non-metals, including some metals, such as Be, Mg, Tc, Re and Mn [8]. Oxides of the REEs make the largest group of inorganic compounds with the typically stable R_2O_3 (R = rare earth element) stoichiometry (e.g. Sc_2O_3, Y_2O_3, etc…) [8]. Furthermore, since some lanthanoids have additional valence states (see above) other stoichiometries may occur too (e.g. Tb_4O_7 or EuO). [8]. At room temperature, all RREs form sesquioxides and they can exist in 5 different crystal structures [9]. These oxides are mostly used as a refractory material. Nevertheless, some oxides can be used for other applications; for example, Y_2O_3 can be added to the ZrO_2 host lattice in order to stabilize the cubic form of the ZrO_2 ceramics [10]. In the cases of Ce, Pr, and Tb, tetravalent or nearly tetravalent compounds may form (e.g., Tb_4O_7 Pr_6O_{11} or CeO_2) [11]. For instance, CeO_2 is used as a catalytic converter for environmentally unfriendly exhaust gases in the automotive industry [12].

In almost all REE compounds, NaCl-type structures have been shown to exist with typical RO (R= rare earth element) stoichiometry. A typical stable representative of such a structure is binary EuO [13]. Other NaCl-type structures of the REE compounds can be stabilized by adding carbon and/or nitrogen [14]. On top of that, the REEs can form high-order chemical compounds with other metal oxides, leading to the formation of perovskite and garnet structures [15]. Chemical compounds with the perovskite structure (e.g., $LaGaO_3$) can be used as superconductors, insulators, catalysts, or magnets. [15] Furthermore, garnet structures (e.g., $Y_3Fe_5O_{12}$) are much more complex compounds than perovskites and such compounds can find their application as electrical insulators, as well as materials with magnetic properties [16]. Hydrides of the REEs usually form nonstoichiometric chemical compounds which can crystallize in different crystal structures [17]. Regarding the halides (iodine, chlorine, bromine and fluorine) there are three major stoichiometries in the respective REE compounds, known as trihalides, tetrahalides and reduced halides [18]. Besides that, REEs can also form numerous intermetallic compounds, which nowadays play an important role in the development of materials for magnetic and electrical applications [19]. For instance, $LaNi_5$ is the main constituent in the Ni-metal hydride (Ni-MH) rechargeable batteries [20]. A so-called neodymium permanent

magnet composed of Nd, Fe, and B to form the $Nd_2Fe_{14}B$ tetragonal crystal structure is one of the strongest magnets known today [21].

Scandium (Sc) with the atomic number Z=21 is the first transition chemical element located in group 3 of the periodic table of elements, and it is classified as a rare earth element. Even though scandium, a lightweight chemical element, and by its nature, very similar to aluminum, has a high melting point and low toxicity, it is still commonly regarded as a non-essential element [22]. Up to now, the most important use of scandium is as an alloying element in aluminum-based alloys, since this leads to an increase in material strength including ductility and improves fatigue properties by forming very fine, coherent intermetallic Al_3Sc precipitates in the microstructure [23]. Nowadays scandium is also used in solid oxide fuel cells as a stabilizing agent for zirconia-based electrolyte materials in order to improve performance and/or reduce the operating temperature of the fuel cell [24]. However, we note that oxyhalides of transition metals and REEs exhibit interesting magnetic and electronic properties [25, 26], and thus analogous compounds of scandium might show potential for future applications in photocatalysis or electronic devices. One possible candidate in this regard is scandium oxychloride; however, there are not many studies about ScOCl available in the literature. Recently we have investigated the energy landscape of ScOCl at standard conditions using a multi-methodological approach [27], and in the current study, we will focus on the theoretical modifications that are specifically expected to be capable of existence in extreme environments. Here, we note that it is known from the literature that lanthanide oxyfluorides, oxychlorides, oxybromides, and oxyiodides provide a great diversity of structure types and accessible polymorphs, especially as metastable phases. [28] Such metastable structures can be accessed through e.g. quenching of structures accessed by application of temperature and/or pressure. [27-33]

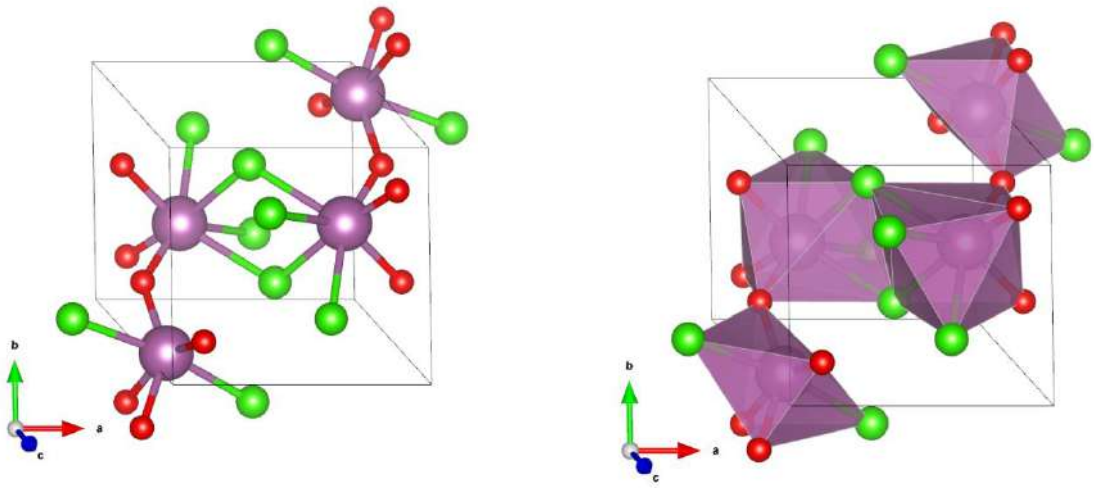

Figure 1. Visualization of the scandium oxychloride modification ScOCl-*et-1* in space group *P-1* (no. 2), presented with and without coordination polyhedra. Purple, green and red spheres denote Sc, Cl and O atoms, respectively.

2. Computational details

A search for structure candidates that might exist in extreme conditions has been performed for the ScOCl system, via the exploration of the energetically higher-lying minima on the energy landscape of ScOCl.[29-32] The general approach of finding structure candidates has been successfully applied previously [27] and consists of a combination of global optimization on the empirical level, and local optimization on the *ab initio* level, [34-36] but where we now focus on local minima with moderately high energies and/or high densities. Global Optimization (GO) of the energy landscape in the ScOCl system was performed using simulated annealing [37] combined with periodic stochastic minimizations, implemented in the G42+ code [38], where an empirical two-body potential consisting of Lennard-Jones and exponentially damped Coulomb terms were employed. [39,40] The

structure candidates obtained were analyzed using the SFND,[41] RGS, [42] and CMPZ [43] algorithms implemented in the KPLOT software. [44] Finally, promising structure candidates in the appropriate energy range were locally optimized on the *ab initio* level. The *ab initio* calculations and minimizations were performed using the CRYSTAL17 program, [45,46] employing analytical gradients with respect to atom positions and cell parameters. [47-49] Density functional theory (DFT) calculations were performed, using the local density approximation (LDA) with the correlation functional by Perdew and Zunger (PZ). [50] All-electron basis sets (AEBS) were used; for scandium, an Sc_864-11G*_harrison_2006 basis set as in refs. [51,52], for oxygen, a modified O_8-411_towler_1994 basis set as in refs. [53-55], and for chlorine, a Cl_86-311G_apra_1993 all-electron basis set as in refs. [56], respectively.

3. Results and Discussion

3.1. Candidates for modifications at extreme conditions

At standard conditions, the thermodynamically stable modification of scandium oxychloride (α-ScOCl) is found in the orthorhombic crystal structure with *Pmmn* (no. 59) space group at ambient conditions. [57-61] The equilibrium structure of ScOCl consists of layers of edge-connected ScO_4Cl_2 octahedra where all O-Cl and O-O edges are shared with neighboring octahedra. The oxygen anions reside within ScOCl layers while the Cl anions of each layer point outwards, resulting in van der Waals-type interactions between layers. In addition, several other modifications (β-, γ-, and δ-ScOCl) are expected to be capable of existing as metastable phases under standard conditions, exhibiting space groups *P4/nmm*, *P42/m* and *C2/m*, respectively. [27] In this study, however, the focus is on possible modifications of ScOCl under extreme conditions. As a result of global optimization with their energies after *ab initio* relaxations, the four most relevant structure candidates on the EL at extreme conditions were identified. Their structural information, atom-atom distances, and computed total energies are presented in Table 1.

Table 1. Modification, space group, unit cell parameters (Å), atomic positions, bond lengths and computed total energies (Eh) for the predicted ScOCl structures at extreme conditions, labeled "ScOCl-extreme-type" (ScOCl-*et*-1, ScOCl-*et*-2, ScOCl-*et*-3, ScOCl-*et*-4, in short). The DFT calculations were performed using the LDA-PZ functional.

Modification and space group	Cell parameters (Å) and atomic positions	Bond length (Å)	Total energy (E_h)
ScOCl-*et*-1 *P*-1 (no. 2)	*a* = 6.08, *b* = 5.57, *c* = 6.23, *α* = 109.06, *β* = 73.02, *γ* = 90.84 Sc 0.2400 0.4292 0.3012 Sc 0.0469 0.0462 0.7571 O 0.8988 0.7934 0.9286 O 0.0270 0.2649 0.5314 Cl 0.3625 0.7495 0.0750 Cl 0.4309 0.7761 0.5770	Sc-O 1 x 1.9530 Sc-O 1 x 2.0758 Sc-O 1 x 2.1357 Sc-Cl 1 x 2.5919 Sc-Cl 1 x 2.6389 Sc-Cl 1 x 2.7219 Sc-Cl 1 x 2.7501 Mean: 2.4096 Sc-O 1 x 1.9916 Sc-O 1 x 2.0790 Sc-O 1 x 2.1676 Sc-O 1 x 2.2020 Sc-Cl 1 x 2.5243 Sc-Cl 1 x 2.5389 Mean: 2.2506	-2584.9237
ScOCl-*et*-2 *Imma* (no.74)	*a* = 3.95, *b* = 5.04, *c* = 11.05	Sc-O 2 x 1.9971 Sc-O 1 x 1.9962	-2584.9205

	Sc 1/2 1/4 0.1457 O 0 1/4 0.1737 Cl 1/2 1/4 0.9039	Sc-Cl 2 x 2.5814 Sc-Cl 1 x 2.6730 Mean: 2.3043	
ScOCl-*et*-3 *Pnma* (no. 62)	*a* = 9.16, *b* = 3.69, *c* = 5.90 Sc 0.5735 1/4 0.8203 O 0.0828 3/4 0.5581 Cl 0.6491 3/4 0.4586	Sc-O 2 x 1.9806 Sc-O 1 x 2.0053 Sc-Cl 2 x 2.9037 Sc-Cl 1 x 2.6689 Sc-Cl 1 x 2.6200 Mean: 2.4375	-2584.9161
ScOCl-*et*-4 *Imma* (no. 74)	*a* = 5.02, *b* = 6.21, *c* = 10.76 Sc 0 1/4 0.5952 O 0 0 1/2 Cl 0 1/4 0.8422	Sc-O 2 x 1.8603 Sc-Cl 2 x 2.5982 Sc-Cl 1 x 2.6569 Mean: 2.3148	-2584.8509

The ScOCl-*et*-1 modification has the lowest energy but the least symmetry of the candidates expected to be relevant in extreme environments (Table 1). ScOCl-*et*-1 crystallizes in the triclinic lattice with space group *P-1* (no. 2) and cell parameters a = 6.08 Å, b = 5.57 Å, c = 6.23 Å, α = 109.06 °, β = 73.02 °, γ = 90.84 °. The ScOCl-*et*-1 has a complex structure comprised of 6-fold coordination (strongly distorted octahedra which are corner connected) and 7-fold coordination (forming edge-connected polyhedra) of Sc atoms by Cl and O atoms, within the structure (Figure 1). In particular, the coordination of the scandium atom by oxygen atoms in the distorted octahedra is four (Sc-O 1 x 1.9916 Å, Sc-O 1 x 2.0790 Å, Sc-O 1 x 2.1676 Å, Sc-O 1 x 2.2020 Å) while the coordination of the scandium atom by chlorine atoms is two (Sc-Cl 1 x 2.5243 Å, Sc-Cl 1 x 2.5389 Å). In the case of the 7-corner polyhedra, scandium atoms are surrounded by three oxygen atoms (Sc-O 1 x 1.9530 Å, Sc-O 1 x 2.0758 Å, Sc-O 1 x 2.1357 Å), and four chlorine atoms (Sc-Cl 1 x 2.5919 Å, Sc-Cl 1 x 2.6389 Å, Sc-Cl 1 x 2.7219 Å, Sc-Cl 1 x 2.7501 Å). The mean cation-anion distance in the octahedra is 2.2506 Å, while the 7-corner polyhedra have a slightly larger average cation-anion distance of 2.4096 Å (Table 1).

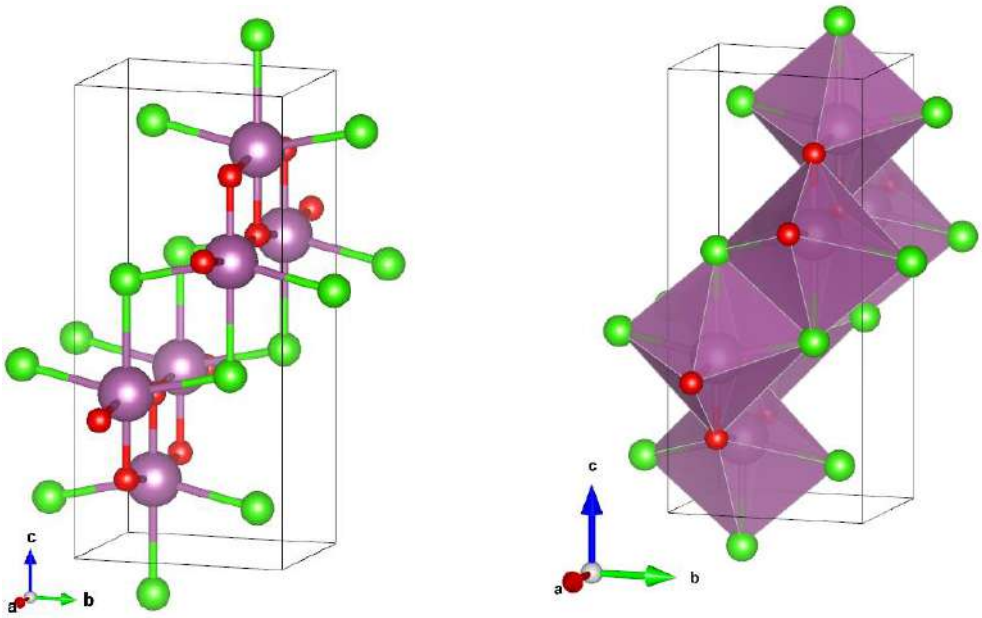

Figure 2. Visualization of the scandium oxychloride modification ScOCl-*et*-2 in space group *Imma* (no. 74), presented with and without coordination polyhedra. Purple, green and red spheres denote Sc, Cl and O atoms, respectively.

Figure 2 shows the ScOCl-*et*-2 phase that might be relevant at high temperatures (Tables 1 and 2). Although this structure has higher energy than ScOCl-*et*-1, it crystallizes with a higher (orthorhombic) symmetry, *Imma* (no. 74) space group with a = 3.95 Å, b = 5.04 Å and c = 11.05 Å. In the ScOCl-*et*-2 structure, we find a 6-fold coordination (CN=6) of Sc atoms by Cl and O atoms, forming corner and edge-connected octahedra (Figure 2). In these approximate octahedra, the scandium atoms have 3 oxygen atoms (CN=3, Sc-O 2 x 1.9971 Å, Sc-O 1 x 1.9962 Å), and three chlorine atoms (CN=3, Sc-Cl 2 x 2.5814 Å, Sc-Cl 1 x 2.6730 Å) as first neighbors, with a mean cation-anion distance of 2.3043 Å (Table 1). If we compare this structure to the ScOCl-*et*-1 modification, we note that the 6-fold coordination in the latter case is a highly deformed octahedral environment with CN = 4+2, while the ScOCl-*et*-2 phase exhibits ordered octahedra with coordination CN = 3+3. We note that the ScOCl-*et*-2 modification shows some similarity with the anatase structure in TiO_2 [62,63] and anatase was recently found in the ternary TiOS system [64].

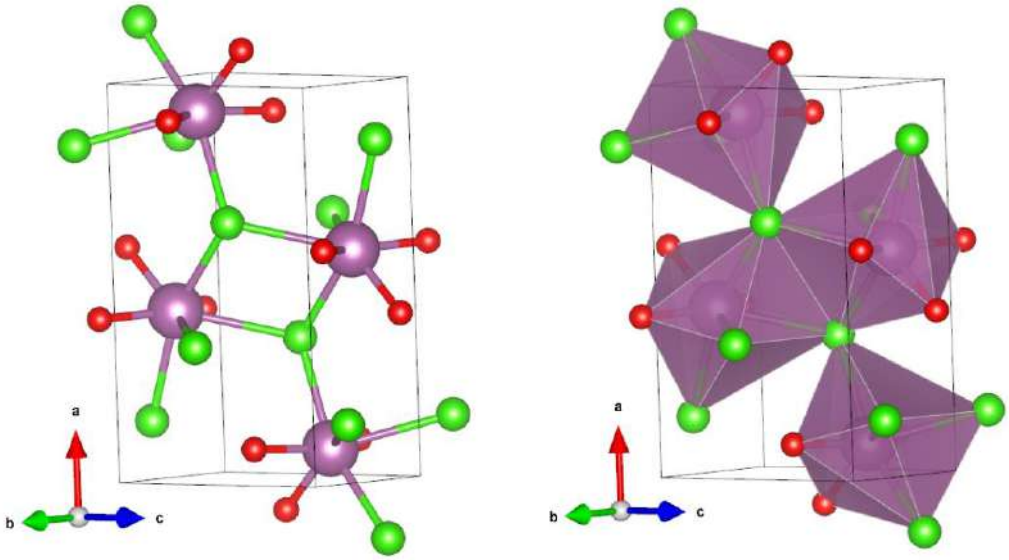

Figure 3. Visualization of the scandium oxychloride modification ScOCl-*et*-3 in space group *Pnma* (no. 62), presented with and without coordination polyhedra. Purple, green and red spheres denote Sc, Cl and O atoms, respectively.

The ScOCl-*et*-3 modification crystalizes in the orthorhombic lattice with *Pnma* (no. 62) space group and cell parameters *a* = 9.16 Å, *b* = 3.69 Å and *c* = 5.90 Å. ScOCl-*et*-3 shows a 7-fold coordination (CN=7) of Sc atoms by Cl and O atoms, forming corner and edge-connected polyhedra within the structure (Figure 3). Furthermore, the scandium atoms have three oxygen atoms (Sc-O 2 x 1.9806 Å, Sc-O 1 x 2.0053 Å) and four chlorine atoms (CN=4, Sc-Cl 2 x 2.9037 Å, Sc-Cl 1 x 2.6689 Å, Sc-Cl 1 x 2.6200 Å) as neighbors, with a mean cation-anion distance of 2.4375 Å (Table 1). When comparing the structures of ScOCl-*et*-3 and ScOCl-*et*-1, we note similar coordination polyhedra where the Sc atoms are surrounded by 3 O atoms and 4 Cl atoms (CN= 3+4). Moreover, an orthorhombic *Pnma* structure has been synthesized as a metastable variant under elevated temperature and pressure conditions for lanthanide oxyfluorides [65,66], which indicates that the analogous ScOCl-*et*-3 modification might be synthetically accessible.

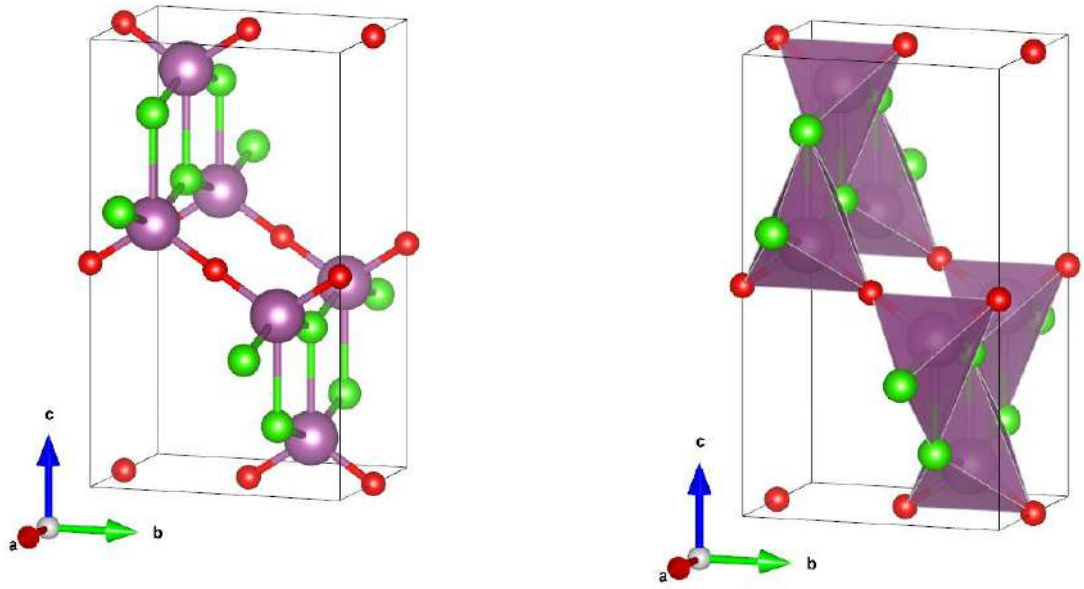

Figure 4. Visualization of the scandium oxychloride modification appearing ScOCl-*et*-4 in space group *Imma* (no. 74), presented with and without coordination polyhedra. Purple, green and red spheres denote Sc, Cl and O atoms, respectively.

Finally, we present the ScOCl-*et*-4 structure (Figure 4). Interestingly, this structure is also found in space group *Imma* (no. 74), like the ScOCl-*et*-2 modification. However, these structures significantly differ both energetically and structurally (Tables 1 and 2, Figures 2 and 4). The unit cell parameters of ScOCl-*et*-2 are a = 3.95 Å, b = 5.04 Å and c = 11.05 Å, while those of ScOCl-*et*-4 are a = 5.02 Å, b = 6.21 Å and c = 10.76 Å, respectively, and the atom positions are also quite different. In addition, the ScOCl-*et*-4 structure shows a unique 5-fold coordination of the Sc atoms by O and Cl atoms, forming monocapped tetrahedra (Sc-O 2 x 1.8603 Å, Sc-Cl 2 x 2.5982 Å, Sc-Cl 1 x 2.6569 Å) and a mean cation-anion distance of 2.3148 Å. Since analogous metastable orthorhombic structures have been stabilized under extreme conditions for several Ln-oxyfluorides (except for Ce, Pm, and Tm) [65,66], and have also been observed as a result of deviations from the 1:1:1 stoichiometry in F-rich oxyfluorides [67,68], it might well be possible to synthesize yet another orthorhombic metastable modification at extreme conditions, in this case for ScOCl.

3.2. Band gap calculations

Table 2. Compared total energies and band gap values for the experimentally known and the predicted ScOCl structures, at standard and extreme conditions. The DFT calculations were performed using the LDA-PZ functional.

Theoretical model	Total energy (Eh)	Band gap (eV)	Theoretical model	Total energy (E_h)	Band gap (eV)
α-ScOCl (FeOCl type)	-2584.9514	4.40	ScOCl-*et*-1	-2584.9237	3.84
β-ScOCl (PbClF type)	-2584.9480	4.36	ScOCl-*et*-2 (anatase-like)	-2584.9205	4.47
γ-ScOCl	-2584.9420	4.58	ScOCl-*et*-3	-2584.9161	4.69
δ-ScOCl	-2584.9351	4.63	ScOCl-*et*-4	-2584.8509	4.60

In order to explore the potential of the ScOCl system for applications, the electronic properties and size of the band gap of the predicted theoretical modifications of ScOCl under extreme conditions were investigated and compared to the modifications found at standard conditions (Table 2). The DFT calculations were performed using the same LDA-PZ functional as in the structural relaxations. The computed band gap of 4.40 eV for the α-ScOCl modification is in agreement with previous theoretical work (GGA 4.06 eV, GGA+U 6.00 eV, HSE06 6.26 eV [69]). We note that this is the first band gap calculation of all other ScOCl phases, showing a great diversity among the proposed modifications and highlighting the possibilities for fine-tuning electronic properties in the ScOCl system. Especially important is the ScOCl-*et*-1 modification which shows a band gap of only 3.84 eV, i.e., a reduction of about 15% compared to the α-ScOCl phase, which could dramatically change the electronic properties of ScOCl material.

4. Conclusion

We have explored the possibility of the existence of scandium oxychloride modifications under extreme conditions, using global optimization with empirical potentials and local optimization on the *ab initio* level. The four structure candidates on the energy landscape expected to be most relevant in extreme conditions were identified. Among these, the ScOCl-*et*-1 modification has the lowest energy but also the lowest symmetry, crystallizing in a triclinic space group, while the other 3 phases exhibit an orthorhombic symmetry, where especially ScOCl-*et*-2 and ScOCl-*et*-4 show very regular octahedral and monocapped tetrahedral coordination polyhedra around the scandium atoms.

Moreover, the size of the band gap was computed for all predicted ScOCl structures, including the band gaps for those modifications found at standard conditions in earlier work. The results show that there is a great diversity in the electronic properties of ScOCl, with particularly interesting ones for the hypothetical modifications expected to be important under extreme conditions. The discovery of these new modifications for extreme conditions and their eventual synthesis might have possible applications in solid oxide fuel cells, photocatalysis, or electronic devices.

Acknowledgments

This research was financially supported by the Ministry of Education, Science, and Technological Development of the Republic of Serbia (Grant No. 1702201). The authors thank Prof. R. Dovesi, Prof. K. Doll, and Crystal Solutions for software support.

References

[1] V. Balaram, Rare earth elements: A review of applications, occurrence, exploration, analysis, recycling, and environmental impact, *Geosci. Front.* 10 (2019), 1285-1303.
[2] G. R. Choppin, E. N. Rizkalla, *Handbook on the Physics and Chemistry of the Rare Earths*, Vol 18, Elsevier, Amsterdam, 1994, p. 562.
[3] R. D. Shannon, Revised effective ionic radii and systematic studies of interatomic distances in halides and chalcogenides, *Acta. Crystallogr Sect*. A 32 (1976) 751767.
[4] S. B. Castor, J. B. Hedrick, *Rare earth elements*, in J. E. Kogel, N. C. Trivedi, J. M. Barker, and S. T. Krukowski, eds., Industrial minerals & rocks—Commodities, markets, and uses (7th ed.), Society for Mining, Metallurgy, and Exploration, Inc. Littleton, Colorado, 2006, p. 769
[5] Y. Kanazawa and M. Kamitani, Rare Earth Minerals and Resources in the World, *J. Alloy Compd.*, vol. 408–412 (2006), 1339-1343.
[6] R. K. Jyothi, *Rare-Earth Metal Recovery for Green Technologies*, Springer, Cham, Switzerland, 2020, p.13
[7] D. Qi, *Hydrometallurgy of Rare Earths: Separation and Extraction*, Elsevier, Amsterdam, 2018, p. 148
[8] D. A. Atwood: *The Rare Earth Elements: Fundamentals and Applications*, Wiley, Chichester UK, 2013, p. 248

[9] M. Zinkevich, Thermodynamics of rare earth sesquioxides, *Prog. Mater. Sci.* Vol. 52, (2007), 597
[10] A. Rittidech, R. Somrit, T. Tunkasiri, Effect of adding Y2O3 on structural and mechanical properties of Al2O3–ZrO2 ceramics, *Ceram. Int.* Vol. 39, 2013, 433
[11] Ž. Mesíková, P. Šulcová, M. Trojan, Synthesis and description of SrSn0.6Ln0.4O3 perovskite pigments, *J. Therm. Anal. Calorim.* Vol. 91, (2007), 163
[12] Y. Gao, W. Wang, S. Chang, W. Huang, Morphology Effect of CeO2 Support in the Preparation, Metal–Support Interaction, and Catalytic Performance of Pt/CeO2 Catalysts, *ChemCatChem*, Vol. 5, (2013), 3610
[13] L. Petit, Z. Szotek, M. Lüders, W. M. Temmerman, A. Svane, First-principles study of valence and structural transitions in EuO under pressure, *Phys. Rev. B*, Vol. 90, (2014), 035110
[14] S. Wada, Interference of spin-, charge- and orbital degrees of freedom in low-carrier rare earth compounds, investigated by NMR, *Phys. B: Condens. Matter*, Vol. 378–380, (2006) 369.
[15] Q. Zhang Z. Gao, X. Sh, C. Zhang, K. Liu, J. Zhang, L.Zhou. C. Ma, Y. Du, Recent advances on rare earths in solid lithium ion conductors, *J. Rare Earths*, Vol. 39, 2021, 1-10.
[16] F. Yang, P. C, Hammel, FMR-driven spin pumping in Y3Fe5O12-based structures, *J. Phys. D: Appl. Phys*, Vol. 51, (2018), 253001
[17] G. G. Libowitz, Nonstoichiometry in chemical compounds, *Prog. Solid. State Ch.* Vol. 2, 1965, 216-264.
[18] W.-X. Ji, W. Xu, Y. Xiao, S.-G. Wang, Does the 4f-shell contribute to bonding in tetravalent lanthanide halides?, J. *Chem. Phys.* Vol. 141, (2014), 244316
[19] B. Y. Kotur, Crystal chemistry of ternary intermetallic compounds of scandium with transition metals and carbon, silicon or germanium, *J. Alloys Compd.* Vol. 219, (1995), 88-92.
[20] K. Pandey, A. Srivastava, O. N. Srivastava, Improvement in hydrogen storage capacity in through substitution of Ni by Fe, *Int. J. Hydrog. Energy*, Vol. 32, (2007), 2461
[21] D. Givord, H. S. Li, J. M. Moreau, Magnetic properties and crystal structure of Nd2Fe14B, *Solid State Commun.* Vol. 50, (1984), 497
[22] W. Wang, Y. Pranolo, C. Y. Cheng, Metallurgical processes for scandium recovery from various resources: A review, *Hydrometallurgy*, Vol. 108, 2011, 100-108.
[23] E. A. Marquis, D. N. Seidman, Nanoscale structural evolution of Al3Sc precipitates in Al(Sc) alloys, *Acta Mater.* Vol. 49, (2001), 1909-1919.
[24] N. Kim, C. H. Hsieh, J. F. Stebbins, Scandium Coordination in Solid Oxides and Stabilized Zirconia: 45Sc NMR, *Chem. Mater.* Vol. 18, (2006), 3855-3859.
[25] G. Caimi, L. Degiorgi, N. N. Kovaleva, P. Lemmens, F. C. Chou, Infrared optical properties of the spin-12 quantum magnet TiOCl, *Phys. Rev. B* 69, (2004), 125108.
[26] A. C. Komarek, T. Taetz, M. T. Fernández-Díaz, D. M. Trots, A. Möller, M. Braden, Strong magnetoelastic coupling in VOCl: Neutron and synchrotron powder x-ray diffraction study, *Phys. Rev. B*, 79, (2009), 104425.
[27] D. Zagorac, J. Zagorac, M. Fonović, M. Pejić, J. C. Schön, Computational discovery of new modifications in scandium oxychloride (ScOCl) using a multi-methodological approach, *Zeitschrift für Anorganische and Allgemeine Chemie*, (2022) https://doi.org/10.1002/zaac.202200198.
[28] M. Udayakantha, P. Schofield, G.R. Waetzig, S. Banerjee, A full palette: Crystal chemistry, polymorphism, synthetic strategies, and functional applications of lanthanide oxyhalides, *Journal of Solid State Chemistry*, 270 (2019) 569-592.
[29] Schön, J. C. Energy Landscape Concepts for Chemical Systems under Extreme Conditions. *Journal of Innovative Materials in Extreme Conditions* 2, (2021), 5-57.
[30] Zagorac, J.B.; Zagorac, D.; Jovanović, D.; Pejić, M.; Škundrić, T.; Matović, B. Ab Initio Investigations and Behaviour of the α-Ce2ON2 Phase in the Extreme Pressure Conditions. *Journal of Innovative Materials in Extreme Conditions* 2, (2021), 36-43.
[31] Hari Kumar, K.; Sridar, S. Calphad Modelling of Ceramic Systems. *Journal of Innovative Materials in Extreme Conditions* 2, (2021), 25-35
[32] D. Zagorac, J. Zagorac, Advanced semiconductors under extreme pressure conditions, in: S.J. Ikhmayies (Ed.) Advanced Semiconductors, Springer 2022.
[33] A. Parija, G. R. Waetzig, J. L. Andrews, and S. Banerjee, Traversing Energy Landscapes Away from Equilibrium: Strategies for Accessing and Utilizing Metastable Phase Space, *Journal of Physical Chemistry C*, 122 (2018) 45, 25709–25728.

[34] J. Zagorac, J. C. Schön, B. Matović, T. Škundrić, D. Zagorac, Predicting Feasible Modifications of Ce2ON2 Using a Combination of Global Optimization and Data Mining, *Journal of Phase Equilibria and Diffusion*, 41 (2020), 538-549.
[35] T. Škundrić, D. Zagorac, J. C. Schön, M. Pejić, B. Matović, Crystal Structure Prediction of the Novel Cr2SiN4 Compound via Global Optimization, Data Mining, and the PCAE Method, *Crystals*, 11 (2021) 891.
[36] D. Zagorac, J. Zagorac, J. C. Schön, N. Stojanovic, B. Matovic, ZnO/ZnS (hetero)structures: ab initio investigations of polytypic behavior of mixed ZnO and ZnS compounds, *Acta Crystallographica Section B*, 74 (2018) 628-642.
[37] S. Kirkpatrick, C.D. Gelatt, M.P. Vecchi, Optimization by Simulated Annealing, *Science*, 220 (1983) 671-680.
[38] J. C. Schön, Nanomaterials - What energy landscapes can tell us, *Processing and Application of Ceramics*, 9 (2015) 157-168.
[39] J. C. Schön, M. Jansen, Determination of candidate structures for simple ionic compounds through cell optimisation, *Computational Materials Science*, 4 (1995) 43-58.
[40] D. Zagorac, J. C. Schön, Chapter 8 - Energy landscapes of pure and doped ZnO: from bulk crystals to nanostructures, in: D.J. Wales (Ed.) *Frontiers of Nanoscience*, Elsevier2022, pp. 151-193.
[41] R. Hundt, J. C. Schön, A. Hannemann, M. Jansen, Determination of symmetries and idealized cell parameters for simulated structures, *Journal of Applied Crystallography*, 32 (1999) 413-416.
[42] A. Hannemann, R. Hundt, J. C. Schön, M. Jansen, A New Algorithm for Space-Group Determination, *Journal of Applied Crystallography*, 31 (1998) 922-928.
[43] R. Hundt, J. C. Schön, M. Jansen, CMPZ - an algorithm for the efficient comparison of periodic structures, *Journal of Applied Crystallography*, 39 (2006) 6-16.
[44] R. Hundt, KPLOT: A Program for Plotting and Analysing Crystal Structures, Technicum Scientific Publishing, Stuttgart, 2016.
[45] R. Dovesi, A. Erba, R. Orlando, C. M. Zicovich-Wilson, B. Civalleri, L. Maschio, M. Rérat, S. Casassa, J. Baima, S. Salustro, B. Kirtman, Quantum-mechanical condensed matter simulations with CRYSTAL, *WIREs Computational Molecular Science*, 8 (2018) e1360.
[46] R. Dovesi, F. Pascale, B. Civalleri, K. Doll, N.M. Harrison, I. Bush, P. D'Arco, Y. Noël, M. Rérat, P. Carbonnière, M. Causà, S. Salustro, V. Lacivita, B. Kirtman, A.M. Ferrari, F.S. Gentile, J. Baima, M. Ferrero, R. Demichelis, M.D.L. Pierre, The CRYSTAL code, 1976–2020 and beyond, a long story, *The Journal of Chemical Physics*, 152 (2020) 204111.
[47] K. Doll, V.R. Saunders, N.M. Harrison, Analytical Hartree–Fock gradients for periodic systems, *International Journal of Quantum Chemistry*, 82 (2001) 1-13.
[48] K. Doll, Analytical stress tensor and pressure calculations with the CRYSTAL code, *Molecular Physics*, 108 (2010) 223-227.
[49] B. Civalleri, P. D'Arco, R. Orlando, V.R. Saunders, R. Dovesi, Hartree–Fock geometry optimisation of periodic systems with the Crystal code, *Chemical Physics Letters*, 348 (2001) 131-138.
[50] J. P. Perdew, A. Zunger, Self-interaction correction to density-functional approximations for many-electron systems, *Physical Review B*, 23 (1981) 5048-5079.
[51] L. Ge, J. H. Jefferson, B. Montanari, N. M. Harrison, D. G. Pettifor, G.A.D. Briggs, Effects of Doping on Electronic Structure and Correlations in Carbon Peapods, *ACS Nano*, 3 (2009) 1069-1076.
[52] R. Dovesi, V. R. Saunders, C. Roetti, R. Orlando, C. M. Zicovich-Wilson, F. Pascale, B. Civalleri, K. Doll, N. M. Harrison, I. J. Bush, P. D'Arco, M. Llunell, M. Causà, Y. Noël, L. Maschio, A. Erba, M. Rerat, S. Casassa, CRYSTAL17 User's Manual University of Torino, Torino, Italy, 2017.
[53] M. D. Towler, N. L. Allan, N.M. Harrison, V. R. Saunders, W. C. Mackrodt, E. Aprà, Ab initio study of MnO and NiO, *Physical Review B*, 50 (1994) 5041-5054.
[54] D. Zagorac, J. Zagorac, M. Pejić, B. Matović, J. C. Schön, Band Gap Engineering of Newly Discovered ZnO/ZnS Polytypic Nanomaterials, *Nanomaterials*, 12 (2022) 1595.
[55] J. Zagorac, D. Jovanovic, T. Volkov-Husovic, B. Matovic, D. Zagorac, Structure prediction, high pressure effect and properties investigation of superhard B6O, *Modelling and Simulation in Materials Science and Engineering*, 28, (2020), 035004.

[56] E. Apra, M. Causa, M. Prencipe, R. Dovesi, V. R. Saunders, On the structural properties of NaCl: an ab initio study of the B1-B2 phase transition, *Journal of Physics: Condensed Matter*, 5 (1993) 2969-2976.
[57] L. Jongen, G. Meyer, Scandium(III) oxide bromide, ScOBr, *Acta Crystallographica Section E*, 61 (2005) i153-i154.
[58] W. Li, N. Miao, J. Zhou, Z. Sun, Pressure-mediated structural phase transitions and ultrawide indirect–direct bandgaps in novel rare-earth oxyhalides, *Journal of Materials Chemistry C*, 9 (2021) 547-554.
[59] E. Garcia, J.D. Corbett, J.E. Ford, W.J. Vary, Low-temperature routes to new structures for yttrium, holmium, erbium, and thulium oxychlorides, *Inorganic Chemistry*, 24 (1985) 494-498.
[60] L.H. Brixner, J.F. Ackerman, C.M. Foris, Rare earth fluorescence in some LnOCl type hosts, *Journal of Luminescence*, 26 (1981) 1-19.
[61] P. Javadian, T.K. Nielsen, D.B. Ravnsbæk, L.H. Jepsen, M. Polanski, T. Plocinski, I. Kunce, F. Besenbacher, J. Bystrzycki, T.R. Jensen, Scandium functionalized carbon aerogel: Synthesis of nanoparticles and structure of a new ScOCl and properties of NaAlH4 as a function of pore size, *Journal of Solid State Chemistry*, 231 (2015) 190-197.
[62] Horn, M.; Schwerdtfeger, C.F.; Meagher, E.P. Refinement of the structure of anatase at several temperatures, *Zeitschrift fuer Kristallographie* ,136 (1972) 273-281.
[63] Weirich, T.E.; Winterer, M.; Seifried, S.; Mayer, J. Structure of nanocrystalline anatase solved and refined from electron powder data, *Acta Crystallographica, Section A: Foundations of Crystallography*, 58 (2002) 308-315.
[64] Jovanović, D., Zagorac, D., Matović, B., Zarubica, A. and Zagorac, J., Anion substitution and influence of sulfur on the crystal structures, phase transitions, and electronic properties of mixed TiO2/TiS2 compounds. *Acta Crystallographica, Section B: Structural Science, Crystal Engineering and Materials*, 77 (2021) 833-847.
[65] E.I. Tonkov, High Pressure Phase Transformations: A Handbook, *Gordon and Breach Science Publishers*, (1992).
[66] S. Wang, R. Deng, H. Guo, S. Song, F. Cao, X. Li, S. Su, H. Zhang, Lanthanide doped Y6O5F8/YF3 microcrystals: phase-tunable synthesis and bright white up conversion photoluminescence properties, *Dalton Trans.*, 39 (38) (2010) 9153–9158.
[67] A.W. Mann, D.J.M. Bevan, Intermediate fluorite-related phases in the Y203-YF3 system-examples of one-dimensional ordered intergrowth, *J. Solid State Chem.*, 5 (1972) 410–418.
[68] T. Wen, W. Luo, Y. Wang, M. Zhang, Y. Guo, J. Yuan, J. Ju, Y. Wang, F. Liao, B. Yang, Multicolour and up-conversion fluorescence of lanthanide doped Vernier phase yttrium oxyfluoride nanocrystals, *J. Mater. Chem. C*, 1 (10) (2013) 1995–2001.
[69] W. Li, N. Miao, J. Zhou, Z. Sun, Pressure-mediated structural phase transitions and ultrawide indirect–direct bandgaps in novel rare-earth oxyhalides, *J. Mater. Chem. C*, 9 (2021) 547-554.

Journal of Innovative Materials in Extreme Conditions
2022
Volume 3
Issue 1

THEORETICAL STUDY OF GROUND STATE PROPERTIES OF Na^+, Cs^+, Mg^{2+} AND Ba^{2+} DOPED MAYENITE AND ITS ELECTRIDE FORMS UNDER EXTREME CONDITIONS

Milan Pejić[1,2,3*], Dejan Zagorac[1,2], Jelena Zagorac[1,2], Tamara Škundrić[1,2,4], Branko Matović[1,2]

[1] Institute of Nuclear Sciences "Vinča", University of Belgrade, Belgrade, Serbia
[2] Centre of Excellence "CextremeLab", Centre for synthesis, processing and characterization of materials for application in the extreme conditions, Belgrade, Serbia
[3] Department of Physics, Faculty of Physics, University of Belgrade, Belgrade, Serbia
[4] Department of Chemistry, Faculty of Science and Mathematics, University of Niš, Niš, Serbia
Corresponding author: milan.pejic@vinca.rs*

Abstract: *Calculations of band structure and electronic density distribution near Fermi energy have been performed for complex nanoporous oxide mayenite $12CaO{\cdot}7Al_2O_3$ (C12A7) on the ab initio level. The electronic structure of mayenite doped with selected cations from the 1st and 2nd group of the periodic table of elements (Na^+, Cs^+, Mg^{2+}, and Ba^{2+}) have also been calculated in order to estimate the effect of cationic doping on structural, electronic, and optical properties of mayenite. Partial and complete substitution of the interstitial oxygen anions (there are two O^{2-} anions per unit cell) with electrons (e^- "doping") is also considered in ab initio calculations to observe differences in electronic structure (such as band gap and Fermi level) during the transition from insulator (regular mayenite crystal with O^{2-} anions in interstitial places) to electride.*

Keywords: mayenite, DFT, ab-initio, electronic band structure, cation doping, electride, transparent conductors.

1. Introduction

Mayenite ($12CaO{\cdot}7Al_2O_3$, $Ca_{12}Al_{14}O_{33}$, C12A7 or C12A7:$(O^{2-})_2$) belongs to a group of calcium aluminates, a range of minerals obtained, by heating calcium oxide and aluminium oxide together at high temperatures, or recently in various ways, from solution-derived precursors to plasma arc melting.[1-8] It crystallizes with a body-centered cubic crystal structure belonging to the space group No. 220, *I43d*, with a unit cell of about 12 Å and with Z=2 (two formula units per unit cell).[9-11] It is comprised of nano-pores and polyhedra that form cages (similar to zeolites) which are approximately 4-5Å in diameter.

The unit cell of C12A7 consists of 12 cages formed by the Ca-Al-O framework, which include 24 Ca, 28 Al and 64 O atoms, while the remaining two oxygen anions are randomly distributed within the cages as extra-framework ions (see Figure 1). Cages with different S4 symmetry axes (S_{4x}, S_{4y}, and S_{4z}), which pass through two Ca (axial) atoms, are connected via large windows formed by a shared Ca-Al-O framework. This means that in the C12A7 unit cell structure, two oxygen ions occupy two of the twelve cages, which are also responsible for the high oxygen ion conductivity found in mayenite.[12] The structure is known as a host material to a variety of anionic species such as O^-, O^{2-}, e^-, OH^-, H^-, F^-, and

Cl^-. [12-16] On the other hand, there has been a plethora of studies on the cationic doping of C12A7 $(Ca_{24}Al_{28}O_{64})^{4+}$, where substitutional cation is located on the Ca^{2+} or Al^{3+} site.[12, 17-19] Doping affects emissive, optical, and chemical properties of mayenite where an important role is played by the structure-property relationships while cationic dopants have strong impacts on the electronic properties and structural distortions.[12, 20]

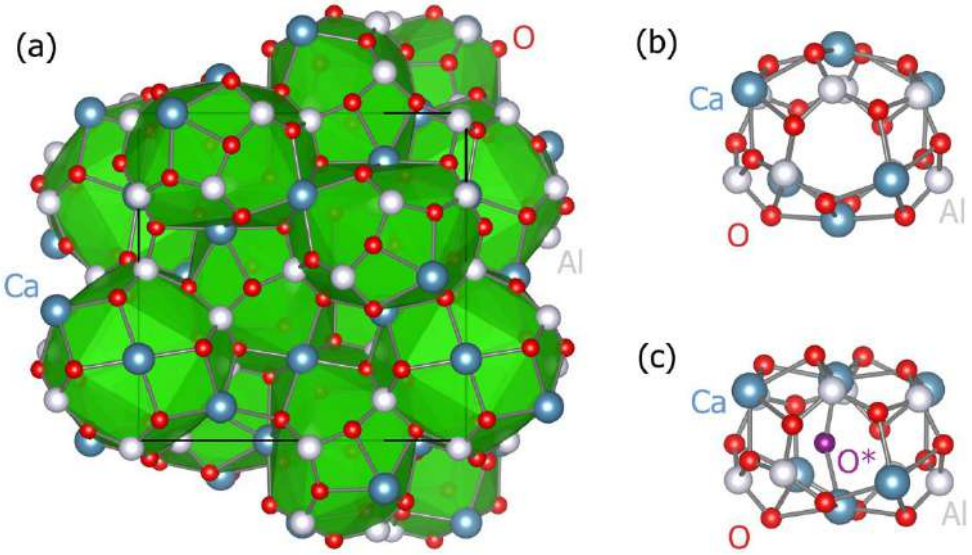

Figure 1. Mayenite structure: (a) C12A7 unit cell, consisting of 12 cages formed by Ca-Al-O framework, (b) Mayenite cage without extra-framework species, (c) Cage containing extra-framework O^{2-} ion (O*).

Many of mayenite's properties that are uncharacteristic to $CaO\text{-}Al_2O_3$ systems are the result of its unusual structure.[21] It has a melting point of 1415°C, and its "electride"[22] (mayenite with all interstitial O^{2-} ions substituted with electrons, which then serve as anions) state can be also regarded as a chemically and thermally stable structure.[15] Varying the electron concentration in the electride form of mayenite can be used to make it optically transparent and electrically conductive material.[23] Conductivity and thermodynamic stability of anion-substituted[20, 24] and cation-substituted[12, 25] mayenite are also being studied recently. There are many other applications of mayenite ranging from catalysts, batteries, hydrogen storage, and transportation to environmental applications, cement, ceramic, and bio-materials.[12, 20, 26-30]

Theoretical modeling of C12A7 and its modifications represents a formidable challenge in the search for novel transparent conducting oxides, catalysts, anion conductors, etc. because of the size of the unit cell and random arrangement of extra-framework species. The purpose of this work is to generate structural models of chosen cation-doped bulk C12A7 structures and analyze their electronic properties using quantum-mechanical simulations based on density-functional theory (DFT). Moreover, this study investigates the behavior of mayenite structure at extreme conditions as a function of the size, charge, and position of the doped cation.

2. Details of the Calculations

Our general approach to the investigation of advanced materials as the effect of anion/cation substitution is given elsewhere [31-36]. Similarly, the effect of extreme conditions on structural and electronic properties, as well as the structure-property relationship has been studied previously[37-44] and is of great importance. In this study, structural and electronic properties of mayenite (C12A7 or C12A7:$(O^{2-})_2$), Na-doped Mayenite (C12A7+Na or C12A7:$(O^{2-})_2$(Na)), Mg-doped (C12A7+Mg or C12A7:$(O^{2-})_2$(Mg)), Cs-doped (C12A7+Cs or C12A7:$(O^{2-})_2$(Cs)) and Ba-doped (C12A7+Ba or C12A7:$(O^{2-})_2$(Ba)) structures (C12A7+X represents two mayenite formula units doped with one X cation), as well as partial (C12A7:$(O^{2-})(e^-)_2$) and complete mayenite electride (C12A7:$(e^-)_4$), are analyzed using quantum-mechanical simulations based on density-functional theory (DFT).

Generalized Gradient Approximation (GGA) with the PBE (Perdew, Burke, and Ernzerhof) functional,[45] as implemented in VASP[46, 47] and Quantum Espresso (QE)[48, 49] simulation package were used in the calculations. Plane-wave basis set with 50 Ry (550 eV) kinetic energy cut-off for wavefunctions, 500 Ry cut-off for charge density and potential, and 4 x 4 x 4 Monkhorst-Pack grids for k-point sampling were used. The structures were fully optimized using both VASP and QE software packages, while the electronic properties were calculated using the QE code. Visualization of the structures and cages was done by VESTA software.[50]

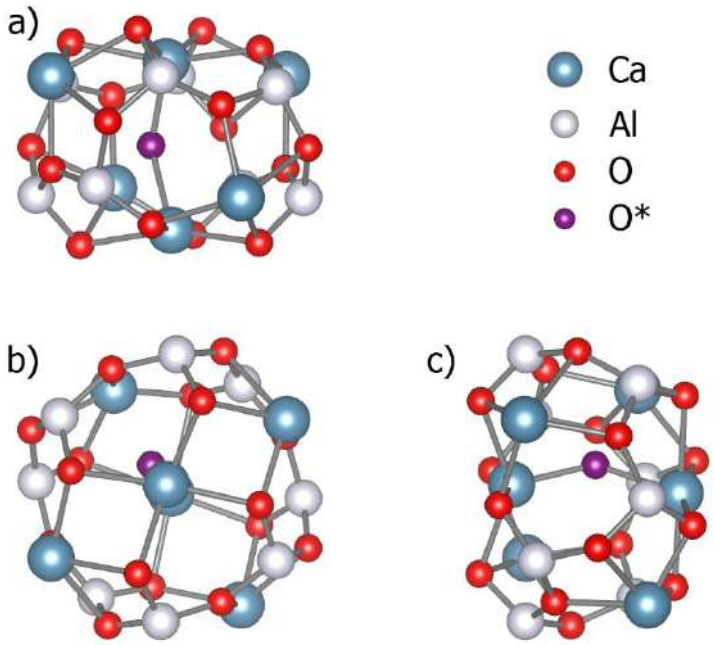

Figure 2. Mayenite C12A7:$(O^{2-})_2$ cage with extra-framework O^{2-} anion structure: (a) front, (b) top, and (c) side view. Calculations performed using GGA-PBE functional.

3. Results and Discussion

3a. Structure properties

The ground state of mayenite C12A7 cages with extra-framework O^{2-} anion structure obtained by DFT calculations is shown in Figure 2. Structural relaxation of the structure using GGA-PBE functional resulted in the unit cell of a=12.065 Å (Table 1). Present

calculations with O^{2-} anion placed in an empty cage is in good agreement with already existing experimental and theoretical results.[9, 21, 22, 51-57] In the following, we investigate the influence of cation doping on the mayenite C12A7 structure. In particular, this was performed by doping C12A7+X (X = Mg, Na, Ba, Cs), where dopant cations are initially incorporated inside the various position of the empty cage or in the framework as an extra-framework species (Figure 1b), pushing the mayenite cage to the extreme boundaries. Thus, each C12A7+X (X = Mg, Na, Ba, Cs) cation doped calculation consists of nine empty mayenite cages (cage without extra-framework species, Figure 1b), one previously "empty" cage that is filled with doped X atom (X = Mg, Na, Ba, Cs), and two already existing interstitial oxygen anions inside two other cages (Figure 1c), making in total twelve mayenite C12A7 cages.

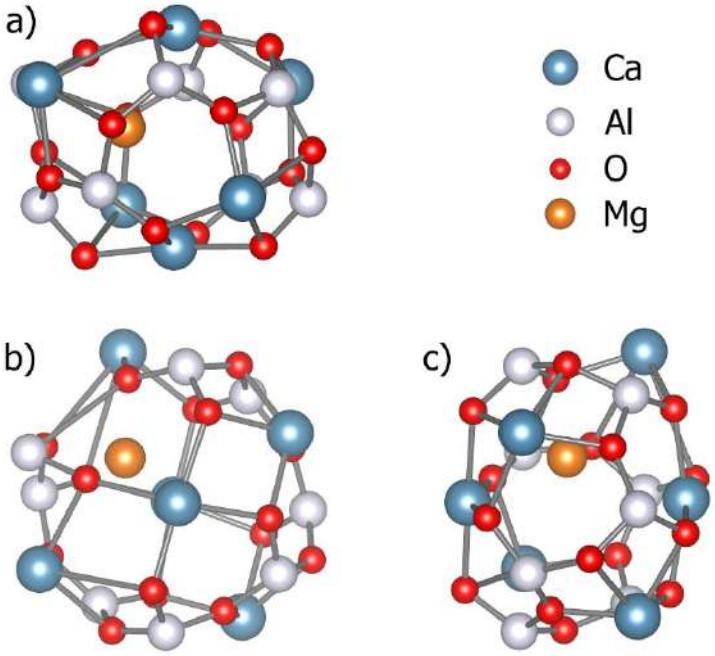

Figure 3. Mg-doped mayenite C12A7:$(O^{2-})_2$(Mg) cage with extra-framework Mg cation structure: (a) front, (b) top, and (c) side view. Calculations performed using GGA-PBE functional.

Firstly, we have investigated an Mg^{2+} cation doping on C12A7:$(O^{2-})_2$ mayenite structure. The resulting Mg-doped mayenite C12A7:$(O^{2-})_2$(Mg) cage with extra-framework Mg cation structure calculated using GGA-PBE is shown in Figure 3. The Mg atom has the same oxidation number as Ca^{2+} and it is its closely related element from the Group 2A (or IIA) of the periodic table (the alkaline earth metals), but the ionic radius is much smaller than calcium (Ca).[58] Interestingly, the ground state structure is achieved with dopant Mg cations incorporated inside the cages, even when Mg atoms were placed at Ca cation sites in the C12A7 framework (Figure 3). The calculated unit cell of a = 12.088 Å and volume V = 1766.14 $Å^3$ are larger than the undoped C12A7:$(O^{2-})_2$ mayenite structure (Table 1).

The influence of the Na cation doping on the C12A7:$(O^{2-})_2$ mayenite structure has been investigated in the next phase of the study. Figure 4 shows the Na-doped mayenite C12A7:$(O^{2-})_2$(Na) cage with extra-framework Na cation structure calculated using GGA-PBE functional. The sodium (Na) atom has an oxidation number of +1 and comes from Group 1 elements (alkali metals) of the periodic table, differently from calcium atoms. On the other hand, the ionic radius of the Na cation is very close to calcium,[58] while sodium and

magnesium are members of the s-block of the third period of the periodic table. The computed unit cell of a = 12.090 Å and volume V = 1767.08 $Å^3$ is just a bit larger than the Mg-doped mayenite C12A7:$(O^{2-})_2$(Mg) cage structure (Table 1). As previously observed, the ground state is achieved with dopant Na cations incorporated inside the cages as extra-framework species (Figure 4).

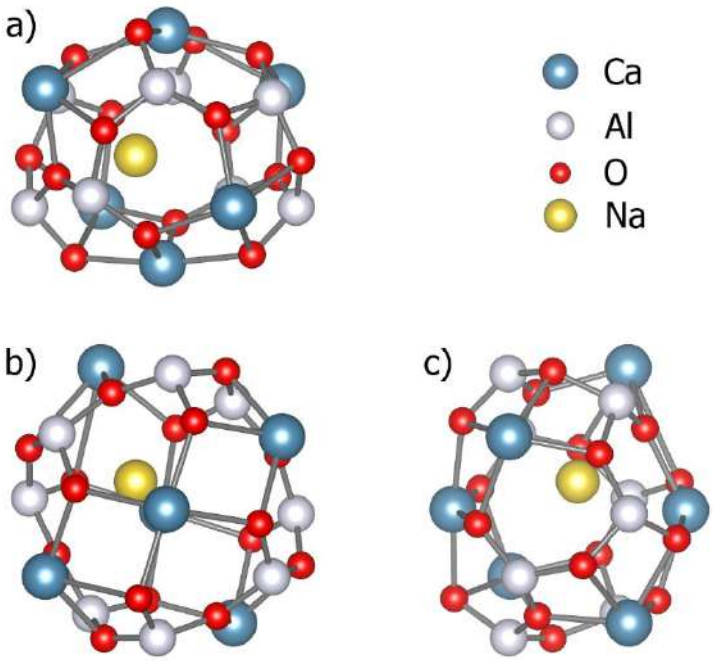

Figure 4. Na-doped mayenite C12A7:$(O^{2-})_2$(Na) cage with extra-framework Na cation structure: (a) front, (b) top, and (c) side view. Calculations performed using GGA-PBE functional.

In the case of the barium (Ba) cation doping on C12A7:$(O^{2-})_2$ mayenite structure, Figure 5 shows the resulting Ba-doped mayenite C12A7:$(O^{2-})_2$(Na) cage with extra-framework Ba cation structure calculated using GGA-PBE functional. The Ba atom has the same oxidation number as Ca^{2+} and it is also a closely related element from the Group 2A (or IIA) of the periodic table (as is the magnesium atom). However, the ionic radius of the Ba cation is much larger compared to calcium (Ca) and especially the Mg cation.[58] The calculated cell parameter of a = 12.116 Å and volume of V = 1778.74 $Å^3$ is larger than undoped and Mg-doped mayenite C12A7:$(O^{2-})_2$(Mg) cage structure (Table 1), as expected. Still, even with incorporating a much larger Ba atom, the ground state is achieved with dopant Ba cations inside the cages as extra-framework species as previously observed (Figure 5).

Finally, the influence of the cesium cation doping on C12A7:$(O^{2-})_2$ mayenite structure has been investigated in great detail. Figure 6 shows the cesium (Cs) cation doping on C12A7:$(O^{2-})_2$ mayenite structure, resulting in C12A7:$(O^{2-})_2$(Cs) cage with extra-framework Cs cation structure calculated using GGA-PBE functional. The cesium cation has an oxidation number +1 and comes from Group 1 elements of the periodic table (same as Na), different than that of the calcium atoms. Moreover, Cs atoms are the largest with the highest ionic radii, compared to Ca or any of the other dopant atoms.[58] Still, DFT calculations show that the calculated cell parameter of a = 12.111 Å and volume of V = 1776.24$Å^3$ are a bit smaller than Ba-doped mayenite C12A7:$(O^{2-})_2$(Ba) cage structure (Table 1). By

incorporating even larger Cs atoms with a different charge, the ground state is achieved with dopant Cs cations inside the cages as extra-framework species as in all previous cases (Figure 6).

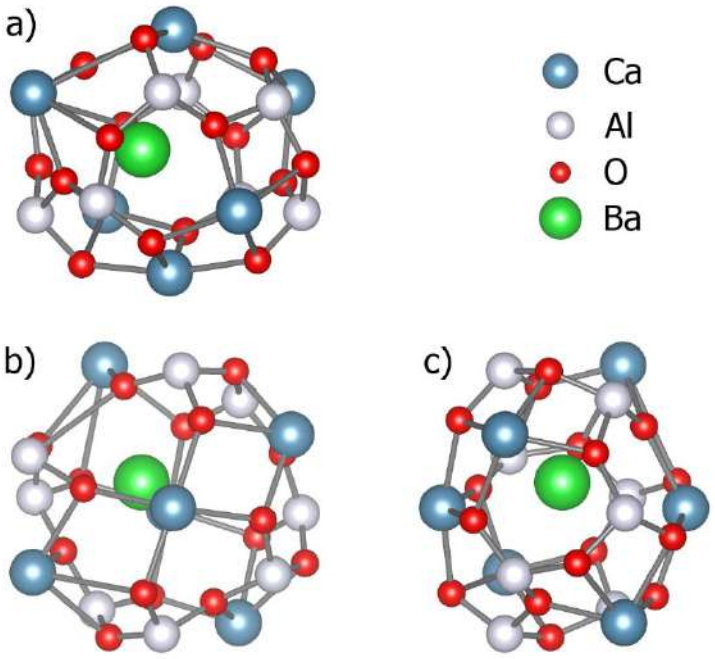

Figure 5. Ba-doped mayenite C12A7:$(O^{2-})_2$(Ba) cage with extra-framework Ba cation structure: (a) front, (b) top, and (c) side view. Calculations performed using GGA-PBE functional.

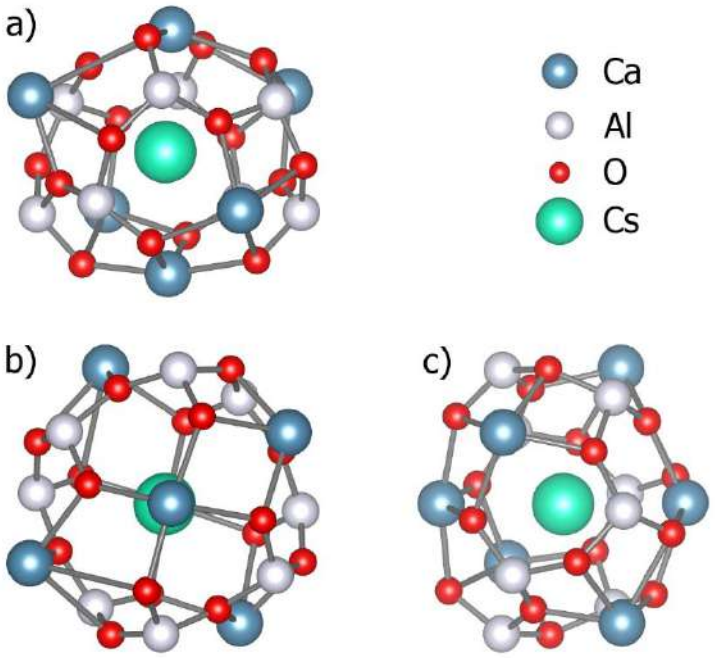

Figure 6. Cs-doped mayenite C12A7:$(O^{2-})_2$(Cs) cage with extra-framework Cs cation structure: (a) front, (b) top, and (c) side view. Calculations performed using GGA-PBE functional.

In summary, for all cation-doped configurations, C12A7+X, the ground state is achieved with dopant cations incorporated inside the cages as extra-framework species, along with two already existing interstitial oxygen anions inside two other cages (Figures 3-6). Having a cation at the interstitial ion place, as expected, deforms the cage in the opposite way the anion does. All cation-doped cages are elongated in the axial Ca-Ca direction, with the Mg-containing cage exhibiting the smallest change compared to the oxygen-containing cage, as well as compared to the cage without extra-framework species. Cages that have Ba and Cs as extra-framework species exhibit the largest elongation along the axial Ca-Ca direction. Theoretical models of all doped mayenite structures show that the basic structure of the lattice framework remains unchanged.

Table 1. Mayenite and Na-, Mg-, Cs-, and Ba-doped mayenite structure parameters calculated using GGA-PBE functional.

Structure	a [Å]	V [Å^3]	Density [g/cm^3]	Ca-Ca distance* [Å]	Ca-X-Ca angle [°]
C12A7:$(O^{2-})_2$	12.065	1756.15	2.62	4.26	141.3
C12A7:$(O^{2-})_2$(Mg)	12.088	1766.14	2.63	5.54	116.7
C12A7:$(O^{2-})_2$(Na)	12.090	1767.08	2.63	5.92	141.8
C12A7:$(O^{2-})_2$(Ba)	12.116	1778.74	2.72	6.20	144.4
C12A7:$(O^{2-})_2$(Cs)	12.111	1776.24	2.72	6.22	175.8

* Axial Ca-Ca distance in the cages containing interstitial atoms (O, Na, Mg, Cs or Ba). Ca-Ca distance in cages without interstitial atoms (empty cages) ranges from ~5.6Å to ~5.9Å.

3b. Electronic properties

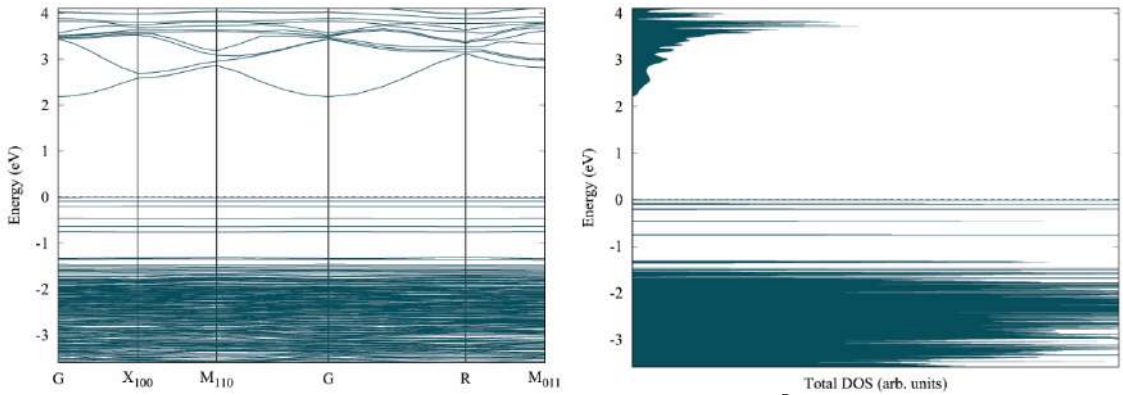

Figure 7. Electronic band structure and DOS for C12A7:$(O^{2-})_2$ mayenite calculated using GGA-PBE functional.

In order to investigate the electronic properties of doped mayenite structures, we have performed electronic band structure and Density of States (DOS) calculations. Figure 7 shows the electronic band structure and DOS for undoped C12A7:$(O^{2-})_2$ mayenite calculated

using GGA-PBE functional. Our results show the existence of the direct band gap for insulator-type mayenite structure ($C12A7:(O^{2-})_2$) of the order of 2 eV in agreement with previous experimental and theoretical studies. [9, 21, 22, 51-57] In addition, we have computed the total DOS for $C12A7:(O^{2-})(e^-)_2$ partial electride and $C12A7:(e^-)_4$ electride shown in Figure 8. The DOS calculations show that both electride mayenite structures appear to have a metallic character.

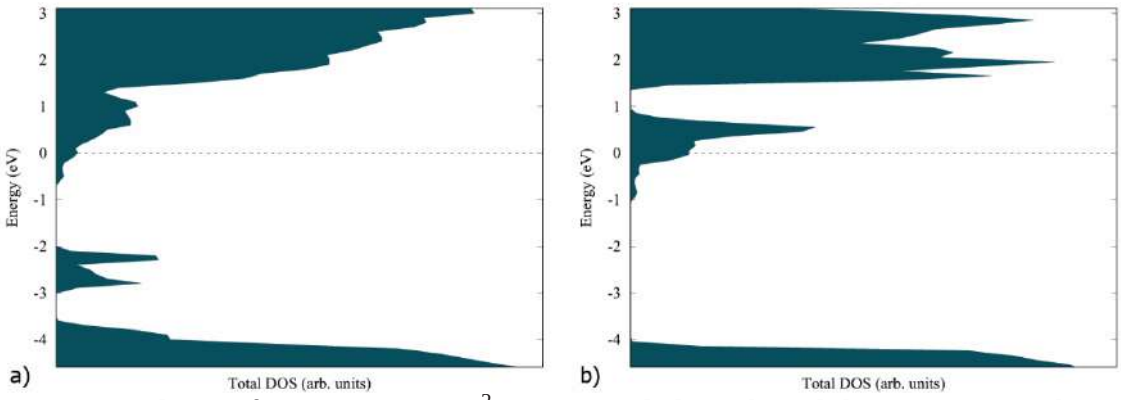

Figure 8. Total DOS for: (a) $C12A7:(O^{2-})(e^-)_2$ partial electride and (b) $C12A7:(e^-)_4$ electride.

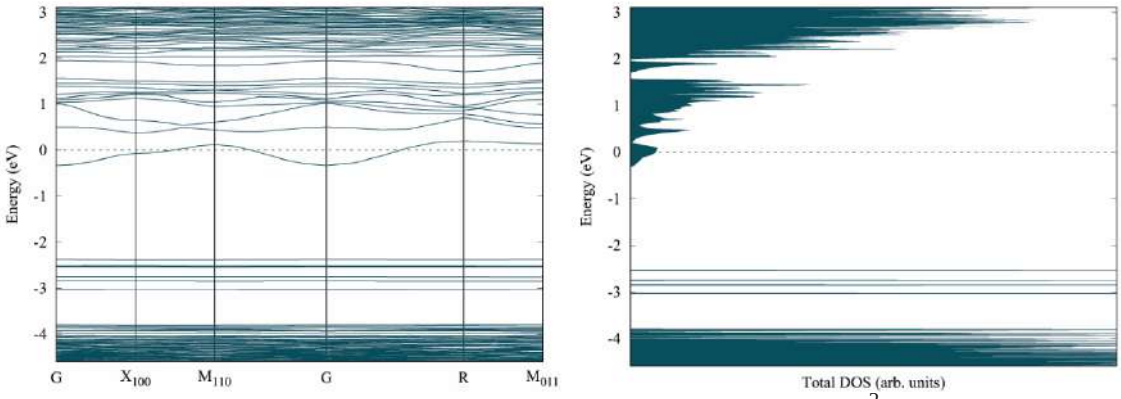

Figure 9. Electronic band structure and DOS for Na doped $C12A7:(O^{2-})_2(Na)$ mayenite.

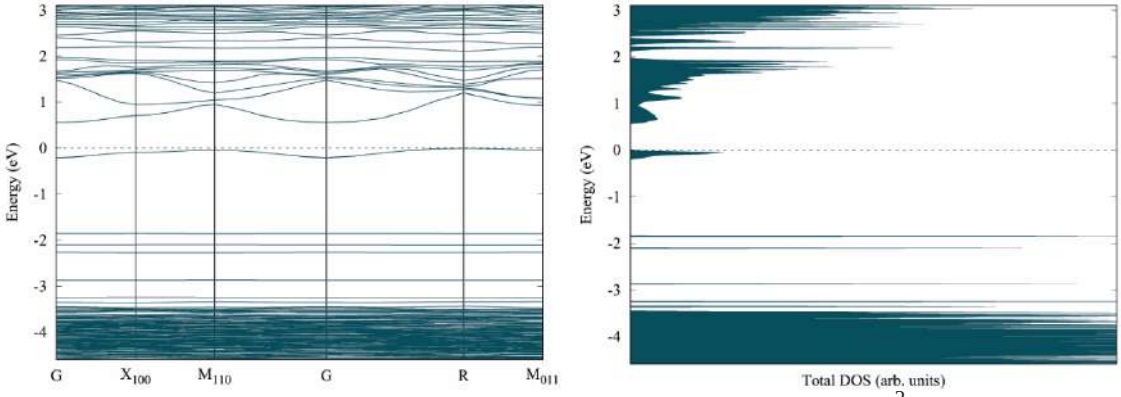

Figure 10. Electronic band structure and DOS for Mg-doped $C12A7:(O^{2-})_2(Mg)$ mayenite.

To investigate the potassium cation-doped mayenite structure, we have computed the electronic band structure and DOS for Na-doped $C12A7:(O^{2-})_2(Na)$ mayenite. It shows that

when the C12A7:$(O^{2-})_2$ mayenite structure is doped with potassium cation within the cage, it appears to be semi-metallic, resembling the electride in Figure 8. On the other hand, when the C12A7:$(O^{2-})_2$ mayenite structure is doped with Mg cation inside the cage (Figure 10), it appears to be semiconducting (similar to the undoped mayenite in Figure 7). Still, the electronic band structure and DOS for Mg-doped C12A7:$(O^{2-})_2$(Mg) mayenite (Figure 10) are showing a much smaller band gap compared to the undoped mayenite (of the order of 0.6 eV).

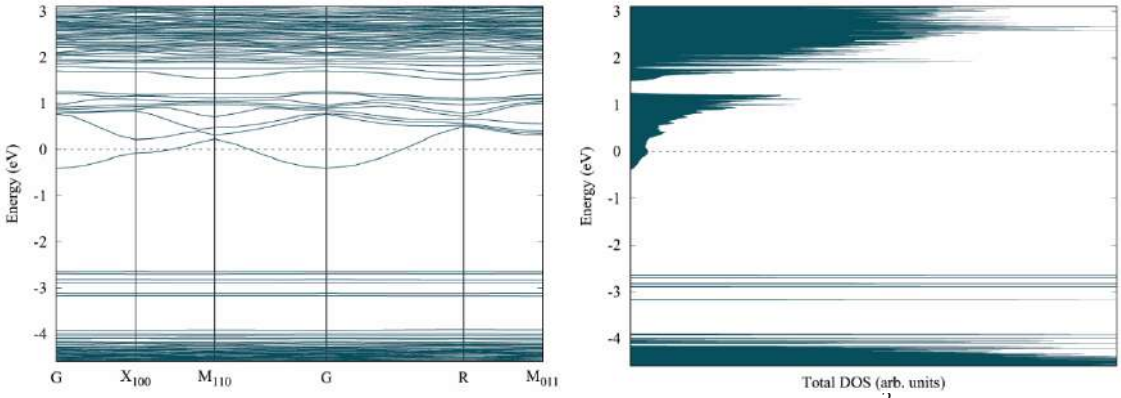

Figure 11. Electronic band structure and DOS for Cs doped C12A7:$(O^{2-})_2$(Cs) mayenite.

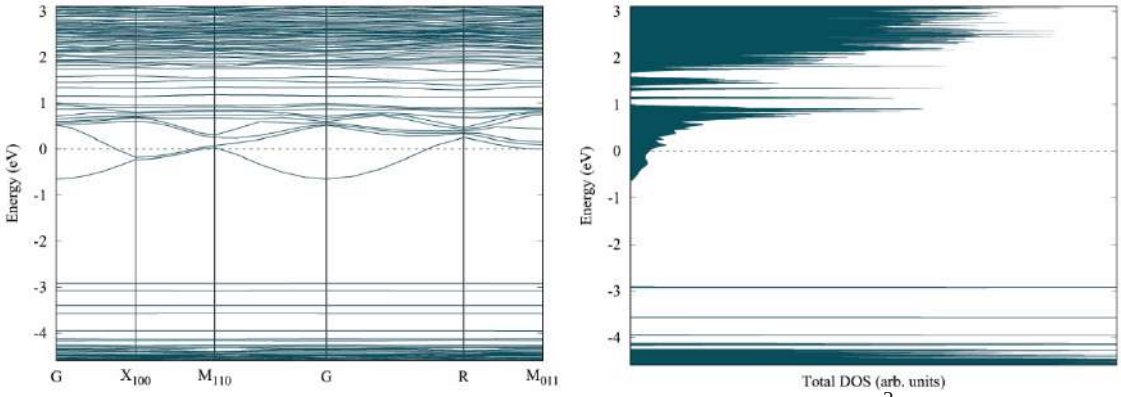

Figure 12. Electronic band structure and DOS for Ba doped C12A7:$(O^{2-})_2$(Ba) mayenite.

Figure 11 shows the electronic band structure and DOS for Cs-doped C12A7:$(O^{2-})_2$(Cs) mayenite computed using GGA-PBE functional. It shows that Cs-doped mayenite appears to be semi-metallic, similar to Na-doped C12A7:$(O^{2-})_2$(Na) mayenite (Figure 9). The electronic band structure and DOS for Ba-doped C12A7:$(O^{2-})_2$(Ba) mayenite is shown in Figure 12. It appears that Ba-doped mayenite exhibits metallic behavior, different from all other dopant cations. The density of states shows a moderately dispersed band at the bottom of the conduction band (similar to the electride DOS). A moderately dispersed band at the bottom of the conduction band which is also separated from the valence band by a large fundamental band gap should favor transparent conducting behavior. To summarize, there is a great diversity of electronic properties of C12A7:$(O^{2-})_2$ mayenite structures, depending on the selection of doping cations.

4. Conclusion

Cationic dopants have strong impacts on electronic properties, and structural distortions. This study investigates the behavior of mayenite structure under extreme conditions as a function of size, charge, and position of the doping cations (Na^{+}, Cs^{+}, Mg^{2+}, and Ba^{2+}). The electron doping increases mayenite electrical conductivity compared to the base mayenite (C12A7:$(O^{2-})_2$). A similar effect is obtained by cationic doping with all chosen cations. While doping (both electronic and cationic) increases conductivity, it also increases the concentration of electrons at the bottom of the conduction band, which leads to stronger optical absorption due to interband transition. There is a trade-off between higher conductivity and transparency in mayenite. Calculations show that C12A7+X (possibly with different cation concentrations) are good candidates for transparent conducting oxides as well as tunable band-gap semiconductors.

Acknowledgments

This research was financially supported by the Ministry of Education, Science, and Technological Development of the Republic of Serbia (Grant No. 1702201).

References

[1] D. Jiang, Z. Zhao, S. Mu, V. Phaneuf, J. Tong, Simple and Efficient Fabrication of Mayenite Electrides from a Solution-Derived Precursor, *Inorganic Chemistry*, 56 (2017) 11702-11709.
[2] K. Berent, S. Komarek, R. Lach, W. Pyda, The Effect of Calcination Temperature on the Structure and Performance of Nanocrystalline Mayenite Powders, *Materials*, 12 (2019) 3476.
[3] F. Li, X. Zhang, H. Liu, Calciothermic synthesis of inorganic [Ca24Al28O64]4+(4e−) electride from solid-derived precursor, *Vacuum*, 169 (2019) 108880.
[4] T. Johnson, E.W. Awin, M.D. Prekajski-Đorđević, B. Matović, R. Kumar, Metal-Like Thermal Conductivity Possessed By Atmosphere Assisted Synthesis, *Journal of Innovative Materials in Extreme Conditions*, 1 (2020) 7-11.
[5] A.V. Kapishnikov, R.M. Kenzhin, A.P. Koskin, A.M. Volodin, P.V. Geydt, Mayenite Synthesis from Hydroxide Precursors: Structure Formation and Active Sites on Its Surface, *Materials*, 15 (2022) 778.
[6] B. Matović, M. Prekajski, J. Pantić, T. Bräuniger, M. Rosić, D. Zagorac, D. Milivojević, Synthesis and densification of single-phase mayenite (C12A7), *Journal of the European Ceramic Society*, 36 (2016) 4237-4241.
[7] S. Weber, S. Schäfer, M. Saccoccio, K. Seidel, H. Kohlmann, R. Gläser, S.A. Schunk, Mayenite-based electride C12A7e−: an innovative synthetic method via plasma arc melting, *Materials Chemistry Frontiers*, 5 (2021) 1301-1314.
[8] E.V. Ilyina, A.F. Bedilo, S.V. Cherepanova, Y.Y. Gerus, E.I. Shuvarakova, A.A. Vedyagin, Aerogel synthesis of calcium aluminates with varied stoichiometry, *Journal of Sol-Gel Science and Technology*, (2022).
[9] L. Palacios, Á.G. De La Torre, S. Bruque, J.L. García-Muñoz, S. García-Granda, D. Sheptyakov, M.A.G. Aranda, Crystal Structures and in-Situ Formation Study of Mayenite Electrides, *Inorganic Chemistry*, 46 (2007) 4167-4176.
[10] T. Sakakura, K. Tanaka, Y. Takenaka, S. Matsuishi, H. Hosono, S. Kishimoto, Determination of the local structure of a cage with an oxygen ion in Ca12Al14O33, *Acta Crystallographica Section B*, 67 (2011) 193-204.

[11] F. Gfeller, 7. Mayenite Ca12Al14O32[X2−]: From minerals to the first stable electride crystals, in: A. Thomas, D. Rosa Micaela (Eds.) *Highlights in Mineralogical Crystallography*, De Gruyter (O), Berlin, München, Boston, 2015, pp. 169-196.
[12] J. R. Salasin, C. Rawn, Structure Property Relationships and Cationic Doping in [Ca24Al28O64]4+ Framework: A Review, *Crystals*, 7 (2017) 143.
[13] J. JEEVARATNAM, F.P. GLASSER, L.S.D. GLASSER, Anion Substitution and Structure of 12CaO·7A122O, *Journal of the American Ceramic Socie*ty, 47 (1964) 105-106.
[14] K. Hayashi, M. Hirano, S. Matsuishi, H. Hosono, Microporous Crystal 12CaO·7Al2O3 Encaging Abundant O- Radicals, *Journal of the American Chemical Society*, 124 (2002) 738-739.
[15] S. Matsuishi, Y. Toda, M. Miyakawa, K. Hayashi, T. Kamiya, M. Hirano, I. Tanaka, H. Hosono, High-Density Electron Anions in a Nanoporous Single Crystal: $[Ca_{24}Al_{28}O_{64}]4^{+}(4e^{-})$, *Science*, 301 (2003) 626-629.
[16] V.I. Zaikovskii, A.M. Volodin, V.O. Stoyanovskii, S.V. Cherepanova, A.A. Vedyagin, Effect of carbon coating on spontaneous C12A7 whisker formation, *Applied Surface Science*, 444 (2018) 336-338.
[17] B. Matović, M.G. Nikolić, M.D. Prekajski-Đorđević, S. Dmitrović, J.M. Luković, J. Maletaškić, B. Jelenković, Luminescence Properties Of Eu3+ Doped Mayenite Under High Pressure, *Journal of Innovative Materials in Extreme Conditions*, 1 (2020) 12-18.
[18] Y. Lv, Y. Sun, J. Xu, X. Xu, A.J. Fernández-Carrión, T. Wei, H. Yi, X. Kuang, Phase Evolution, Electrical Properties, and Conduction Mechanism of Ca12Al14–xGaxO33 ($0 \leq x \leq 14$) Ceramics Synthesized by a Glass Crystallization Method, *Inorganic Chemistry*, 60 (2021) 2446-2456.
[19] K. Hayashi, N. Ueda, S. Matsuishi, M. Hirano, T. Kamiya, H. Hosono, Solid State Syntheses of 12SrO·7Al2O3 and Formation of High Density Oxygen Radical Anions, O^{-} and O^{2-}, *Chemistry of Materials*, 20 (2008) 5987-5996.
[20] H. Visbal, T. Omura, K. Nagashima, T. Itoh, T. Ohwaki, H. Imai, T. Ishigaki, A. Maeno, K. Suzuki, H. Kaji, K. Hirao, Exploring the capability of mayenite (12CaO·7Al2O3) as hydrogen storage material, *Scientific Reports*, 11 (2021) 6278.
[21] P.V. Sushko, A.L. Shluger, M. Hirano, H. Hosono, From Insulator to Electride: A Theoretical Model of Nanoporous Oxide 12CaO·7Al2O3, *Journal of the American Chemical Society*, 129 (2007) 942-951.
[22] Z. Li, J. Yang, J.G. Hou, Q. Zhu, Is Mayenite without Clathrated Oxygen an Inorganic Electride?, *Angewandte Chemie International Edition*, 43 (2004) 6479-6482.
[23] K. Hayashi, S. Matsuishi, T. Kamiya, M. Hirano, H. Hosono, Light-induced conversion of an insulating refractory oxide into a persistent electronic conductor, *Nature*, 419 (2002) 462-465.
[24] J.-P. Eufinger, A. Schmidt, M. Lerch, J. Janek, Novel anion conductors – conductivity, thermodynamic stability and hydration of anion-substituted mayenite-type cage compounds C12A7:X (X = O, OH, Cl, F, CN, S, N), *Physical Chemistry Chemical Physics*, 17 (2015) 6844-6857.
[25] K. Khan, A.k. Tareen, U. Khan, A. Nairan, S. Elshahat, N. Muhammad, M. Saeed, A. Yadav, L. Bibbò, Z. Ouyang, Single step synthesis of highly conductive room-temperature stable cation-substituted mayenite electride target and thin film, *Scientific Reports*, 9 (2019) 4967.
[26] A. Intiso, F. Rossi, A. Proto, R. Cucciniello, The fascinating world of mayenite (Ca12Al14O33) and its derivatives, Rendiconti Lincei. *Scienze Fisiche e Naturali*, 32 (2021) 699-708.
[27] K. Fang, J. Zhao, D. Wang, H. Wang, Z. Dong, Use of ladle furnace slag as supplementary cementitious material before and after modification by rapid air cooling: A comparative study of influence on the properties of blended cement paste, *Construction and Building Materials*, 314 (2022) 125434.
[28] J.G. Miranda-Hernández, C.O. González-Morán, H. Herrera-Hernández, E.H. Sánchez, J.d.J.A. Flores-Cuautle, M. Ortega-Avilés, Sea snail shells for synthesis of ceramic compounds reinforced with metallic oxide: Microstructural, mechanical and electrical behavior, *Materials Today Communications*, 28 (2021) 102656.
[29] E. Temeche, Solid Electrolytes Derived From Precursors and Liquid-Feed Flame Spray Pyrolysis Nano-Powders Enabling Assembly of All-Solid-State-Batteries, *Materials Science and Engineerin*g, University of Michigan, Michigan, USA, 2021.
[30] W. Langlar, A. Aeimbhu, P. Limsuwan, C. Ruttanapun, Microwave-assisted biosynthesis of C12A7 nanopowders from Aloe Vera leaf extract, *J. Ceram. Soc. Jpn*., 128 (2020) 322-328.

[31] D. Zagorac, J. Zagorac, M. Pejić, B. Matović, J.C. Schön, Band Gap Engineering of Newly Discovered ZnO/ZnS Polytypic Nanomaterials, *Nanomaterials*, 12 (2022) 1595.
[32] D. Jovanovic, D. Zagorac, B. Matovic, A. Zarubica, J. Zagorac, Anion substitution and influence of sulfur on the crystal structures, phase transitions, and electronic properties of mixed TiO2/TiS2 compounds, *Acta Crystallographica Section B: Structural Science, Crystal Engineering and Materials*, 77 (2021) 833-847.
[33] J. Zagorac, D. Zagorac, B. Babić, T. Prikhna, B. Matović, Effect of aluminum addition on the structure and electronic properties of boron nitride, *Journal of Solid State Chemistry*, 311 (2022) 123153.
[34] D. Fischer, D. Zagorac, J.C. Schön, The presence of superoxide ions and related dioxygen species in zinc oxide—A structural characterization by in situ Raman spectroscopy, J. Raman Spectrosc., accepted for publication, (2022).
[35] D. Zagorac, J. Zagorac, M. Fonović, T. Prikhna, B. Matović, Novel boron-rich aluminum nitride advanced ceramic materials, International Journal of *Applied Ceramic Technology*, (2022), 1-16.
[36] D. Zagorac, J.C. Schön, Chapter 8 - Energy landscapes of pure and doped ZnO: from bulk crystals to nanostructures, in: D.J. Wales (Ed.) *Frontiers of Nanoscience*, Elsevier (2022), 151-193.
[37] D. Zagorac, J. Zagorac, K. Doll, M. Čebela, B. Matović, Extreme pressure conditions of bas based materials: Detailed study of structural changes, band gap engineering, elastic constants and mechanical properties, *Processing and Application of Ceramics* 13 (2019) 401-410.
[38] D. Jovanović, J. Zagorac, B. Matović, A. Zarubica, D. Zagorac, Structural, electronic and mechanical properties of superhard B_4C from first principles, *Journal of Innovative Materials in Extreme Conditions*, 1 (2020) 12-18.
[39] J. Zagorac, D. Zagorac, D. Jovanović, M. Pejić, T. Škundrić, B. Matović, Ab initio investigations and behaviour of the α-Ce_2ON_2 phase in the extreme pressure conditions, *Journal of Innovative Materials in Extreme Conditions*, 2 (2021) 36-43.
[40] K. Hari Kumar, S. Sridar, Calphad Modelling of Ceramic Systems, *Journal of Innovative Materials in Extreme Conditions*, 2 (2021) 25-35.
[41] J. Zagorac, D. Zagorac, D. Jovanović, M. Pejić, T. Škundrić, B. Matović, Ab Initio Investigations and Behaviour of the α-Ce2ON2 Phase in the Extreme Pressure Conditions, *Journal of Innovative Materials in Extreme Conditions* 2, (2021) 36-43.
[42] D. Zagorac, K. Doll, J.C. Schön, M. Jansen, Ab initio structure prediction for lead sulfide at standard and elevated pressures, *Physical Review B*, 84 (2011) 045206.
[43] J.C. Schön, Energy Landscape Concepts for Chemical Systems under Extreme Conditions, *Journal of Innovative Materials in Extreme Conditions* 2(2021) 5-57.
[44] D. Zagorac, J. Zagorac, Advanced Semiconductors under Extreme Pressure Conditions, in: S.J. Ikhmayies (Ed.) *Advanced Semiconductors*, Springer2022.
[45] J.P. Perdew, K. Burke, M. Ernzerhof, Generalized Gradient Approximation Made Simple, *Physical Review Letters*, 77 (1996) 3865-3868.
[46] G. Kresse, J. Hafner, Ab initio molecular dynamics for liquid metals, *Physical Review B*, 47 (1993) 558-561.
[47] G. Kresse, J. Furthmüller, Efficient iterative schemes for ab initio total-energy calculations using a plane-wave basis set, *Physical Review B*, 54 (1996) 11169-11186.
[48] P. Giannozzi, S. Baroni, N. Bonini, M. Calandra, R. Car, C. Cavazzoni, D. Ceresoli, G.L. Chiarotti, M. Cococcioni, I. Dabo, A. Dal Corso, S. de Gironcoli, S. Fabris, G. Fratesi, R. Gebauer, U. Gerstmann, C. Gougoussis, A. Kokalj, M. Lazzeri, L. Martin-Samos, N. Marzari, F. Mauri, R. Mazzarello, S. Paolini, A. Pasquarello, L. Paulatto, C. Sbraccia, S. Scandolo, G. Sclauzero, A.P. Seitsonen, A. Smogunov, P. Umari, R.M. Wentzcovitch, QUANTUM ESPRESSO: a modular and open-source software project for quantum simulations of materials, *Journal of Physics: Condensed Matter*, 21 (2009) 395502.
[49] P. Giannozzi, O. Andreussi, T. Brumme, O. Bunau, M. Buongiorno Nardelli, M. Calandra, R. Car, C. Cavazzoni, D. Ceresoli, M. Cococcioni, N. Colonna, I. Carnimeo, A. Dal Corso, S. de Gironcoli, P. Delugas, R.A. DiStasio, A. Ferretti, A. Floris, G. Fratesi, G. Fugallo, R. Gebauer, U. Gerstmann, F. Giustino, T. Gorni, J. Jia, M. Kawamura, H.Y. Ko, A. Kokalj, E. Küçükbenli, M. Lazzeri, M. Marsili, N. Marzari, F. Mauri, N.L. Nguyen, H.V. Nguyen, A. Otero-de-la-Roza, L. Paulatto, S. Poncé, D. Rocca, R. Sabatini, B. Santra, M. Schlipf, A.P. Seitsonen, A. Smogunov, I.

Timrov, T. Thonhauser, P. Umari, N. Vast, X. Wu, S. Baroni, Advanced capabilities for materials modelling with Quantum ESPRESSO, *Journal of Physics: Condensed Matter*, 29 (2017) 465901.
[50] K. Momma, F. Izumi, VESTA 3 for three-dimensional visualization of crystal, volumetric and morphology data, *Journal of Applied Crystallography*, 44 (2011) 1272-1276.
[51] P. V. Sushko, A.L. Shluger, Y. Toda, M. Hirano, H. Hosono, Models of stoichiometric and oxygen-deficient surfaces of subnanoporous $12CaOx7Al_2O_3$, *Proceedings of the Royal Society A: Mathematical, Physical and Engineering Sciences*, 467 (2011) 2066-2083.
[52] N. Kuganathan, H. Hosono, A.L. Shluger, P.V. Sushko, Enhanced N2 Dissociation on Ru-Loaded Inorganic Electride, *Journal of the American Chemical Society*, 136 (2014) 2216-2219.
[53] A. Schmidt, M. Lerch, J.-P. Eufinger, J. Janek, I. Tranca, M.M. Islam, T. Bredow, R. Dolle, H.-D. Wiemhöfer, H. Boysen, M. Hölzel, Chlorine ion mobility in Cl-mayenite (Ca12Al14O32Cl2): An investigation combining high-temperature neutron powder diffraction, impedance spectroscopy and quantum-chemical calculations, *Solid State Ionics*, 254 (2014) 48-58.
[54] X. Zhang, Y. Wang, H. Wang, Q. Cui, C. Wang, Y. Ma, G. Zou, Pressure-induced amorphization in mayenite (12CaO·7Al2O3), *The Journal of Chemical Physics*, 135 (2011) 094506.
[55] L. Palacios, A. Cabeza, S. Bruque, S. García-Granda, M.A.G. Aranda, Structure and Electrons in Mayenite Electrides, *Inorganic Chemistry*, 47 (2008) 2661-2667.
[56] H. Boysen, M. Lerch, A. Stys, A. Senyshyn, Structure and oxygen mobility in mayenite (Ca12Al14O33): a high-temperature neutron powder diffraction study, *Acta Crystallographica Section B*, 63 (2007) 675-682.
[57] N. Takatoshi, H. Katsuro, K. Yoshiki, K. Toshio, H. Masahiro, T. Masaki, H. Hideo, Anion Incorporation-induced Cage Deformation in 12CaO·7Al2O3 Crystal, *Chemistry Letters*, 36 (2007) 902-903.
[58] R.D. Shannon, Revised effective ionic radii and systematic studies of interatomic distances in halides and chalcogenides, *Acta Crystallographica Section A*, 32 (1976) 751-767.

Journal of Innovative Materials in Extreme Conditions

Volume 3, Issue 2, Year 2022

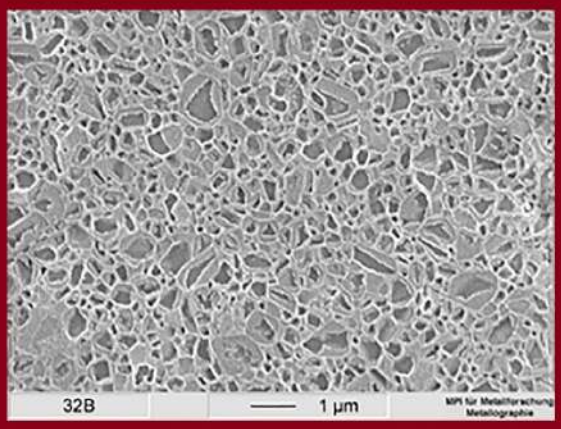

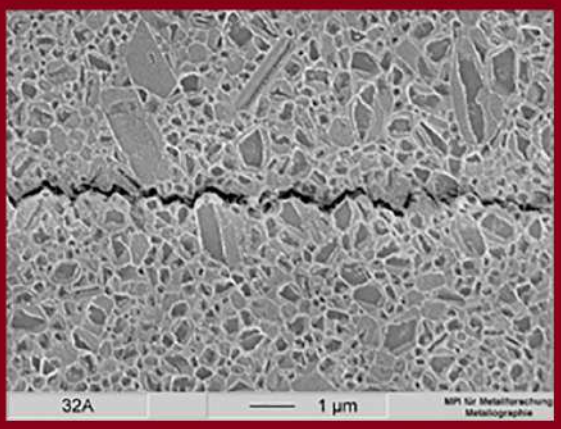

Published by:

SIM-EXTREME

Serbian Society for Innovative Materials in Extreme Conditions

Journal of Innovative Materials in Extreme Conditions (*abbr*. JIMEC)

Volume 3, Issue 2, Year 2022

Volume 3, year 2022

JIMEC: Table of Contents

Volume 3, Issue 2, Year 2022

Cover Picture

Microstructure and crack path in Si_3N_4 ceramic sintered with 15 wt.% of $LiAlSiO_4$ additive at 1500 ºC for 8 h. Published in: Branko Matović, PROCESSING AND PROPERTIES OF SILICON NITRIDE CERAMICS: REVIEW. *Journal of Innovative Materials in Extreme Conditions*, **Vol. 3**, Issue 2, pages 43-117, 2022.

-Issue 2

Journal of Innovative Materials in Extreme Conditions
2022
Volume 3
Issue 2

PROCESSING AND PROPERTIES OF SILICON NITRIDE CERAMICS: A REVIEW

Branko Matović [1,2*]

[1] *Department of Materials Science, Vinča Institute of Nuclear Sciences – National Institute of the Republic of Serbia, University of Belgrade, Belgrade, Serbia*
[2] *Center of Excellence "Center for Synthesis, Processing, and Characterization of Materials for Application in the Extreme Conditions – CextremeLab", Vinča Institute of Nuclear Sciences – National Institute of the Republic of Serbia, University of Belgrade, Belgrade, Serbia*
Corresponding author: mato@vinca.rs*

Abstract: *The progress in monolithic Si_3N_4 as well as Si_3N_4/Si_3N_4 composites (seeded materials) for structural applications is reviewed. The conventional processing involving the powder synthesis, densification, phase transformation and microstructure design is discussed. Special attention is paid to basic theory of liquid phase sintering due to the complexity and difficulty in understanding consolidation of Si_3N_4 powders. The mechanical properties of the resulting Si_3N_4 based ceramics and their industrial applications are summarized. A key factor for the future development in the field of conventionally processed Si_3N_4 ceramics is given.*

Keywords**:** *structural ceramics, monolithic Si_3N_4, Si_3N_4/Si_3N_4 composites, powders processing*

1. Introduction

Silicon nitride (Si_3N_4) has been studied extensively during the last 50 years. Si_3N_4 based ceramics were found to possess promising thermal and mechanical properties at high temperatures since 1955 [1]. As reaction bonding was the only method to fabricate Si_3N_4 ceramics at that time, the products were not completely dense. For an optimum utilization of the inherent good properties of Si_3N_4, the powders must be fully densified to compacts [2]. High density materials were first obtained early in the 1960s by hot-pressing with small amounts of various oxide and nitride additives [3]. However, only simple shapes could be fabricated by this process. In the beginning of the 1970s research focused on the applications of Si_3N_4 as a structural material for gas turbines [4]. As a result pressureless [5] and gas pressure sintering [6] techniques were developed. This made possible the fabrication of components having high density and complex shape. During the past 30 years, many different aspects have been explored, such as the fundamental properties of Si_3N_4, powder production, porous and dense Si_3N_4 and amorphous thin films for applications in electronics. It was found that Si_3N_4 possesses a unique combination of properties, such as high strength at ambient and high temperatures, good thermal shock resistance due to a low coefficient of thermal expansion, relatively good resistance to oxidation compared to other high-temperature structural materials, high wear resistance and high thermal conductivity. In addition, the density of Si_3N_4 is only about 40% of superalloys. This combination of properties makes it possible for Si_3N_4 to replace metallic components that are conventionally used as structural materials.

During investigations on the sintering of Si_3N_4, it was also found that some oxides can be dissolved into Si_3N_4 grains [7, 8]. Thus, the resulting material is not pure silicon nitride anymore. “Silicon nitride ceramics” is thus a general name for multicomponent mixtures or alloys of Si_3N_4. The solid solutions with Al_2O_3 have been referred to as Sialons. The creep and corrosion resistance of high density Sialon was envisaged to be higher than that of sintered Si_3N_4 ceramics because of the reduction or elimination of the grain boundary phase [9] which could be aspired to with these materials.

Si-N bonds are predominantly covalent and this is the source of the excellent intrinsic properties of silicon nitride ceramics. However, due to the high degree of covalent bonding, it is very difficult to sinter these materials to full density. As a consequence, several alternative techniques have been developed to improve the densification of Si_3N_4 based ceramics [10]. Fully dense Si_3N_4 can be produced by the addition of densification additives that allow liquid phase sintering (LPS). A wide range of sintering additives for Si_3N_4 have been explored to date [2, 11]. Since the densification rate is strongly related to the type and amount of sintering additives, as are the microstructure development and the thermal and mechanical properties of sintered bodies, there is considerable effort to find and optimize sintering aids for high performance Si_3N_4 materials.

In spite of their excellent properties and great potential, the application of Si_3N_4 based ceramics is still limited. The main reasons for this are the high cost of raw materials, *i.e.* Si_3N_4 and the sintering additives, in addition to the production process being cost-intensive [12]. In general, high-quality Si_3N_4 grades are used in combination with rare-earth oxides (RE_2O_3 with e.g., RE=Y, Ce, Yb, Lu) [2], which are not only expensive but require high sintering temperatures. Therefore, there is an ongoing search for a production process that utilizes low-cost Si_3N_4 powder and sintering additives, which are equally cheap and enable attainment of lower sintering temperatures. Recently, more attention has been given to low-temperature sintering of Si_3N_4 ceramics with the aim of reducing manufacturing costs [13, 14].

1.1 Crystal structure of silicon nitride

Silicon nitride exists in three crystallographic modifications designated as the α, β and γ phases. While the α and β modifications can be produced under normal nitrogen pressure and have great importance in the production of advanced ceramics, the recently discovered γ-Si_3N_4 can be formed only at extremely high pressures [16] and has no practical use yet.

In a simple chemical picture, chemical bonding in α- and β-Si_3N_4 are due to the overlap of the sp^3 hybrid orbitals of silicon atoms with the sp^2 hybrid orbitals of the nitrogen atoms. Each nitrogen atom has a remaining *p* atomic orbital which is nonbonding and occupied by a lone pair of electrons [17, 18].

The basic unit of Si_3N_4 is the SiN_4 tetrahedron. A silicon atom is at the centre of a tetrahedron, with four nitrogen atoms at each corner. The SiN_4 tetrahedra are joined by sharing corners in such a manner that each nitrogen atom is common to three tetrahedra. Thus nitrogen has three silicon atoms as neighbors [9]. The structural difference between α- and β-Si_3N_4 can be explained by different arrangements of Si-N layers. The basic units are linked together to form puckered six-membered rings which surround large holes. These basal planes form the building blocks for the structures of α and β-Si_3N_4. The α-Si_3N_4 structure is formed by stacking the basal planes in the ABCDABCD... order, and β-Si_3N_4 is constructed of basal planes stacked in the ABAB... sequence [19]. The AB layer is the same in α-Si_3N_4 and β- Si_3N_4, and the CD layer in α-Si_3N_4 is related to the AB layer of β-Si_3N_4 by a *c*-glide plane. Regarding the unit cell dimensions, α- and β-Si_3N_4 structures are related by $a_\alpha \approx a_\beta$ (Table 1). The β-Si_3N_4 structure exhibits channels parallel to the c-axis which are about 0.15 nm in diameter enabling higher diffusion coefficients of ions compared to the α-structure. These channels are changed into voids with seven nearest neighbouring nitrogen atoms in α-Si_3N_4. The α- and β-forms have trigonal and hexagonal symmetry. The relevant crystallographic data are listed in Table 1.

Table 1. Crystal structure and lattice parameters of Si_3N_4 modifications.

Modification	***α-Si_3N_4***	***β-Si_3N_4***	***γ-Si_3N_4***
Space group	P31c	$P6_3$ or $P6_3/m$	Fd3m
Lattice parameter a (nm) c (nm)	 0.7818(3) 0.5591(4)	 0.7595(1) 0.29023(6)	 0.7738

The α-structure belongs to the space group P31c, with 28 atoms per units cell (Fig. 1). Its lattice parameters are very sensitive to the oxygen content dissolved in the structure. This was the reason why it was assumed that α-Si_3N_4 is an oxynitride with an oxide content of 0.9-1.48 wt% corresponding to the compositions [21]: $Si_{11.5}N_{15}O_{0.5}$ and $Si_{11.5}Si_2N_{15}O_{0.5}$. In these formulas some N atoms were replaced with O atoms and other N sites remained vacant.

However, more detailed investigations showed that the oxygen content was less than that required by the formulas given above [22]. Although oxygen is capable of replacing nitrogen in some sites, it is not needed to form the α-structure. A refinement of the crystal structure of an α-Si_3N_4 single crystal produced by a chemical vapour deposition process clearly demonstrated that the bond length and site occupancy data do not indicate any oxygen in the structure [23].

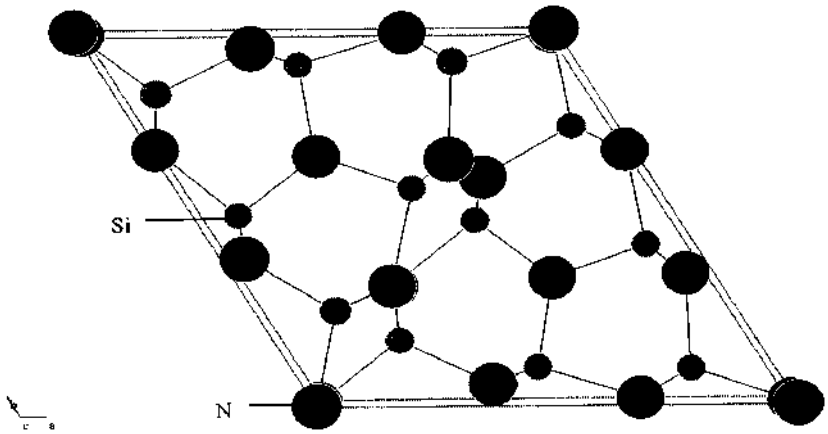

Figure 1. Crystal structure of trigonal α-Si_3N_4 [2].

The atomic arrangement of the β-form is derived from the structure of the mineral phenacite ($BeSi_2O_4$), with the oxygen atoms being replaced by nitrogen and the beryllium atoms by silicon [24]. The unit cell of β-Si_3N_4 consists of Si_6N_8 units (Fig. 2). While the literature values of the structural parameters of this modification do not differ remarkably, the real space group, whether centrosymmetric ($P6_3/m$) or acentric ($P6_3$), is still under debate [25]. In the structure of space group $P6_3/m$, the silicon and nitrogen atoms lie in mirror planes at z=1/4 and z=3/4, normal to the c-axis [26]. In the case of the acentric space group, the nitrogen atoms are slightly displaced from the mirror planes [27].

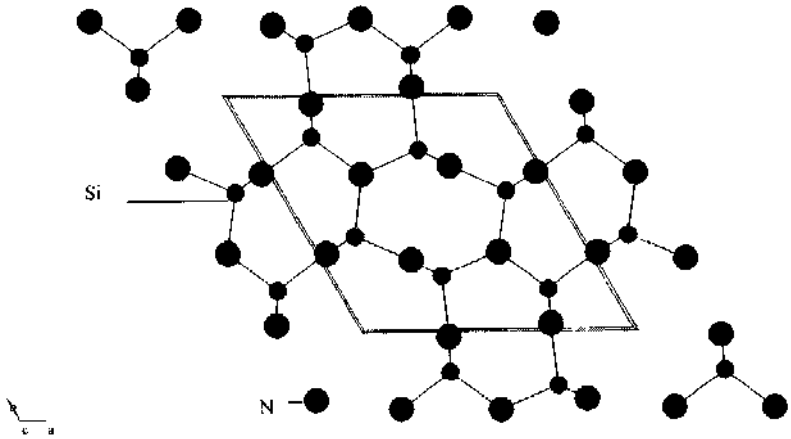

Figure 2. Crystal structure of hexagonal β-Si_3N_4 [2].

During heating above 1400°C, the α-phase irreversibly transforms to the β-phase. β-Si_3N_4 is the thermodynamically more stable phase at all temperatures and hence the transformation from β- to α-phase is not possible [28]. The transformation is a reconstructive process involving the breaking and reconstruction/formation of six Si-N bonds in each unit cell. This transformation mechanism can proceed only in the presence of liquid phases, which lower the activation energy for transformation. The value for the activation energy in the presence of the liquid phase is about 405 kJ/mol^{-1} which is close to the Si-N bond energy (435 kJ/mol^{-1}) [29].

The recently discovered γ-modification has a cubic structure, similar to the spinel structure [30]. One silicon atom is coordinated tetrahedrally by four nitrogen atoms and two silicon atoms have octahedral coordination by (six) nitrogen atoms (Fig. 3.). This atomic arrangement results in a density of 3.75 g cm^{-3}, which is larger than that of α- and β-Si_3N_4 (3.19 g cm^{-3}). In addition, the cubic modification has a hardness of 35.5 GPa, which is larger than that of stishovite, a high pressure phase

of SiO_2 (33 GPa) and significantly higher than the hardness of α- and β-Si_3N_4. Thus, the γ-modification is the third hardest material after diamond and cubic boron nitride [29].

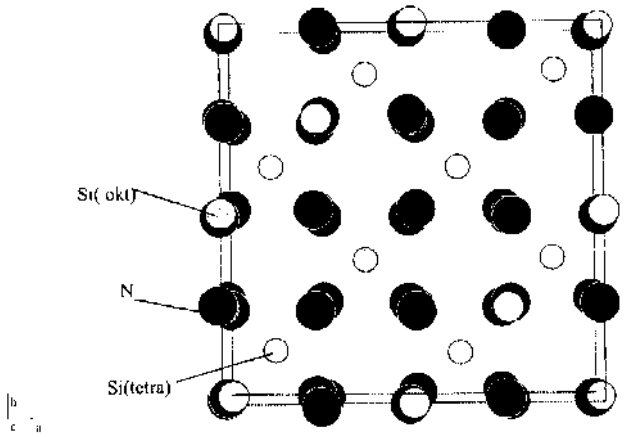

Figure 3. Crystal structure of γ-Si_3N_4 [2].

Silicon and Si_3N_4 have a high affinity to oxygen. Since the dimensions of the SiN_4 tetrahedron are very similar to those of SiO_4 [30], some oxynitrides exist consisting of both, SiO_4 and SiN_4 tetrahedra. The most common oxynitride is built up of SiN_3O tetrahedra which are linked together to form a three-dimensional network with the formula Si_2N_2O. Moreover, silicon and oxygen atoms in β-Si_3N_4 can be replaced by Al and O atoms to form the so-called Sialons with the formula $Si_{6-z}Al_zN_{8-z}O_z$, since the unit cell contains two Si_3N_4 units. The number of replaced Al and O atoms is represented by the "z" value which can be varied continuously from zero to about 4.2 [31, 32]. The Si_3N_4 ceramics with "z" values ≥ 0.5 belong to the group of extended β-Si_3N_4 solid solutions (β_{SS}) and all others with "z" values ≤ 0.5 belong to group of low β-Si_3N_4 solid solutions [2]. Similar extended solid solutions can be formed with the addition of BeO or BeN [33]. However, these solid solutions (SiBeON) have no practical use due to the toxicity of Be.

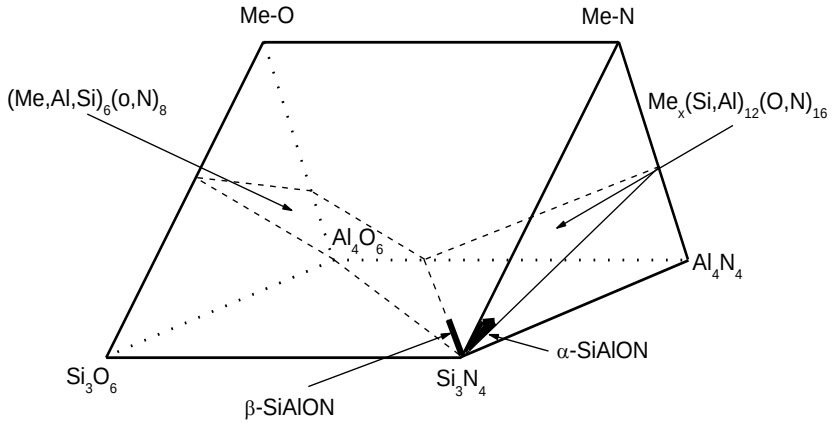

Figure 4. Phase relationship in the M-Si-Al-N-O system [36].

α-Si_3N_4 has an empty position with a coordination number of eight (7+1), which can be partially occupied by ions with an atomic radius of about 0.1 nm. Occupation of the void position causes a stabilization of the metastable α-Si_3N_4. The cations, which can be incorporated in the αphase, are Li^+, Mg^{+2}, Ca^{+2}, Y^{+3} and lanthanides with Z ≥ 60 [34]. Additionally, Al and O to obtain must replace Si and N to obtain electroneutrality. The resulting α-solid solutions are the so-called α-Sialons with the formula $M_xSi_{12-m-n}Al_{m+n}N_{16-n}O_n$, where *m* represents the number of (Si-N) bonds in α-

Si_3N_4 which are replaced by (Al-N) bonds, *n* is the number of (Si-N) bonds that are replaced by (Al-O) bonds, and *x* equals *m* divided by the valence of the M cation. The charge discrepancy is compensated by M cations occupying the interstices in the (Si,Al)-(O,N) network. Thus, α-Sialon can be regarded as a substitutional-interstitial solid solution. The parameter "x" has a minimum value 0.33 for trivalent cations and 0.3 for divalent cations since there is a miscibility gap between α-Si_3N_4 and α-SiAlON, and the value of x cannot exceed 2 as there are only two interstitial sites in the unit cell [35]. Since the substitution range of α-solid solutions is smaller than for β solutions, the formation of single phase α-Sialon is rather difficult. Deviations from the stoichiometry lead to the simultaneous formation of β-solid solutions. The relationship between α- and β-Sialon is given in Fig. 4.

An important feature of the SiAlON system is that the α- to β-SiAlON phase transformation is fully reversible [37]. The α-phase is more stable at lower temperatures and can accommodate metal oxides [38]. During the α- to β-SiAlON transformation metal oxides are rejected to the intergranular regions according to the following equation:

α-SiAlON ⇔ β-SiAlON + M-oxides rich intergranular liquid (1.1)

Additionally, the phase composition can be controlled by heat treatment procedures.

1.2 Preparative routes for silicon nitride powders

Since the occurrence of Si_3N_4 as a mineral in nature is very rare [39], all silicon nitride-based ceramics must be produced synthetically. There are many different production routes for Si_3N_4 powders:

— direct nitridation of silicon,
— carbothermic reduction of silica,
— diimide synthesis,
— vapor phase synthesis,
— plasma chemical synthesis,
— pyrolyses of silicon organic compounds, and
— laser induced reactions.

All of these routes are based on four different chemical processes (Table 2) [40]. However, only direct nitridation of silicon and diimide synthesis techniques are commercially viable processes [41].

Table 2. Production of Si_3N_4 powders.

Method	***Chemical process***
direct nitridation	$3\ Si + 2\ N_2 \Rightarrow Si_3N_4$
carbothermal nitridation	$3\ SiO_2 + 6\ C + 2\ N_2 \Rightarrow Si_3N_4 + 6\ CO\uparrow$
diimide synthesis	$SiCl_4 + 6\ NH_3 \Rightarrow Si(NH)_2 + 4\ NH_4Cl\uparrow$ $3\ Si(NH)_2 \Rightarrow Si_3N_4 + 2\ NH_3\uparrow$
vapor phase synthesis	$3\ SiCl_4 + 4\ NH_3 \Rightarrow Si_3N_4 + 12\ HCl\uparrow$

The reaction conditions may be adjusted to provide powders of different crystallinity, α/β ratio, morphology, particle size, particle size distribution and impurities. Typical chemical analysis data and properties for commercial silicon nitride powders synthesized by different techniques as mentioned above are given in Table 3.

The direct nitridation of silicon is performed in an atmosphere of N_2, N_2/H_2 or NH_3 at temperatures above 1100 °C but below the melting point of silicon (1410 °C). The α-phase of silicon nitride is the major product. Since the β-modification appears only in the presence of a liquid phase, β-Si_3N_4 formation is favored either by the presence of impurity elements, which are able to form low-melting eutectics, or by nitridation above the melting point of silicon [42]. This reaction is highly

exothermic and it is extremely difficult to control the temperature using raw silicon. The heat of reaction can be used for the self-propagating synthesis of Si_3N_4 [43]. However, because of the uncontrolled reaction and a significant amount of β-phase in the product, the self-propagation method can not be used for the production of high quality Si_3N_4 powders. The process finally results in Si_3N_4 lumps which are then crushed and milled. The quality of the final product depends on the purity of the raw material, the milling procedure after nitridation and additional chemical purification of the powder. The direct nitridation method can be carried out by a plasma chemical reaction, where temperatures on the order of 5750°C are reached. The time of reaction is very short; resulting in a high amount of amorphous Si_3N_4 and nano-crystallites of the α- and β-phases (about 20 nm). The grain size can be increased to 100 nm by an additional heat treatment process [44].

Table 3. Typical properties of Si_3N_4 powders produced by various processing techniques.

Technique	***Direct nitridation of silicon***	***Vapor phase synthesis***	***Carbothermal nitridation***	***Diimide synthesis***
Specific surface area, ($g\ cm^{-2}$)	8-25	3.7	4.8	10
Oxygen content, (wt %)	1.0-2.0	1.0	1.6	1.4
Carbon content, (wt %)	0.1-0.4	-	0.9-1.1	0.1
Metallic impurities, (wt %) Σ Fe, Al, Ca	0.07-0.15	0.03	0.06	0.005
Crystallinity, (%)	100	60	100	100
α/(α + β), (%)	95	95	95	85
Morphology	equiaxed	equiaxed + rod-like	equiaxed + rod-like	equiaxed

Carbothermal nitridation was the earliest method to be used for Si_3N_4 production [45]. The process involves the nitridation of carbon and silica precursor powder mixtures in a flowing nitrogen atmosphere at temperatures in the range from 1400 up to 1500 °C. Nowadays, it is the most promising candidate for obtaining a large variety of non-oxides products with important technical uses [46-49]. This reaction offers the possibility of an economically attractive production route from naturally occurring materials.

The overall reaction (Table 3) proceeds *via* a number of intermediate reactions. The first step involves the generation of SiO (gas) by the reduction of silica by carbon:

$$SiO_2 + C \rightarrow SiO(g) + CO(g) \quad (1.2)$$

The CO produced in Eq. (1.2) is also capable of reducing further silica through the following reaction:

$$SiO_2 + CO \rightarrow SiO(g) + CO_2 \quad (1.3)$$

The carbon within the system can in turn reduce the CO_2 thereby regenerating CO as given by Eq. (1.4):

$$C + CO_2 \rightarrow 2CO \quad (1.4)$$

The SiO(g) produced by Eq. (1.2) or (1.3) reacts with N_2 to form Si_3N_4 according to the reactions given by Eqs. (1.5) and (1.6):

$$3SiO + 3C + 2N_2 \rightarrow Si_3N_4 + 3CO \quad (1.5)$$

$$3SiO + 3CO + 2N_2 \rightarrow Si_3N_4 + 3CO_2 \quad (1.6)$$

Many authors have studied the formation of non-oxide powders from the minerals such as different types of clays; sepiolite and from aluminosilicates and bauxite. Among the raw materials that may be used for non-oxides production diatomaceous earth has some advantages such as high specific surface area, high silica content and low price.

Diatomaceous earth is a natural occurring mineral compound from microscopic skeletal remains of unicellular algae-like plants called diatoms. As living plants diatoms weave microscopic shells from the silica, however as they die, deposits are formed and fossilized. Diatom particles have pitted surface area that it is several times greater than any other natural compound with the same particle size. The surfaces of diatom fructules possess fine pores with dimensions ranging from the micro scale to the nanometer scale. Such high surface area and siliceous composition can be used as Si precursor for the synthesis of different types of non-oxide powders by carbothermal reduction-nitridation (CRN) by mixing with one of reducing agents.

The characteristics of the Si_3N_4 powders resulting from carbothermic reduction depend on many factors namely the C/SiO_2 ratio, the nitrogen flow rate, reaction temperature, particle size and specific surface area of silica and carbon and the impurities present.

1.2.1 Carbonitriding reactions of diatomaceous earth

The raw material used was a diatomaceous earth from the Serbia. The carbon black with a specific surface area BET = $46 m^2 \cdot g^{-1}$ and 99% purity was used as reducing agent. The diatomaceous earth was previously acid treated with HCl solution of 1 mol/dm^3 concentration in order to remove iron oxide from material. The chemical composition of as-resived and chemically treated samples are done by wet chemical methods (Table 4). Mixtures with different C/SiO_2 ratio were homogenized by vibro-milling in the presence of distilled water. The green bodies were heated at temperatures between 1200 and 1500 °C in an alumina reactor with controlled nitrogen flow. The nitrogen gas used contained less than 5 ppm O_2 and H_2O. In all experiments a N_2 flow of 0.5 $l \cdot min^{-1}$ was used. The heating of the alumina reactor was carried out in a furnace with SiC heating element. Temperature was measured with Pt-(Pt-10 wt.%Rh) thermocouple (± 5 °C). The nitrogen flow was kept during cooling until 200 °C.

Table 4. Chemical composition of as-received diatomaceous earth and chemically treated diatomite.

Sample	***SiO_2***	***Al_2O_3***	***Fe_2O_3***	***CaO***	***MgO***	***K_2O***	***Na_2O***	***L.O.I. (1000 ℃)***
As-received	73.68	12.28	3.29	0.72	0.44	1.01	0.12	8.26
Chem. treated	76.58	11.34	1.72	1.22	0.44	0.9	0.11	7.13

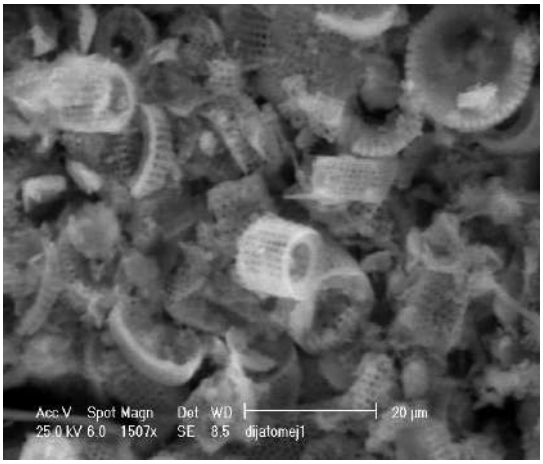

Figure 5. SEM image of as-received diatomaceous earth.

According to the shape and morphology as received raw material belongs to Aulacoseira type of diatoms (Fig. 5). Diatom particles possess pitted surface area with fine pores with dimensions ranging from the micro scale to the nanometer scale. Its XRD pattern shows that the main mineralogical component is crysaballite (SiO_2) accompanied by amorphous phase.

Chemical composition shows that diatomaceous earth is mainly composed of SiO_2 and important quantities of Al_2O_3. Also the other impurities such as Na_2O, K_2O, Fe_2O_3 are present. However, it is known that the Na_2O and K_2O are largely lost at the carbothermal reduction stage. In the other side, it would be expected that the Fe_2O_3 would be reduced to Fe or on iron silicides (FeSi), but small quantities of iron has been shown to help initialize nitridation [50]. Thus, the phase relation during carbonitriding reaction of diatomaceous earth (mixture of silica and alumina) may be derivate from the quaternary system Si-Al-O-N (Fig. 6).

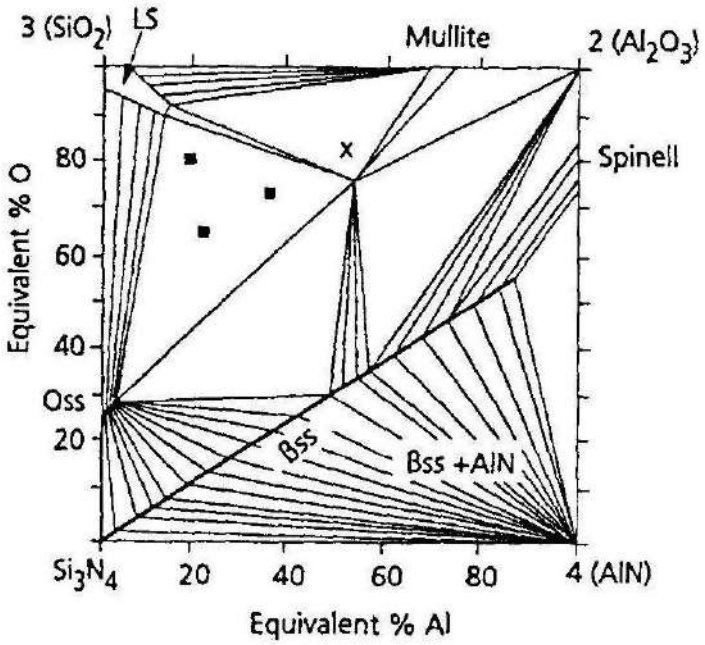

Figure 6. Phase diagram of the quaternary Si-Al-O-N system [51].

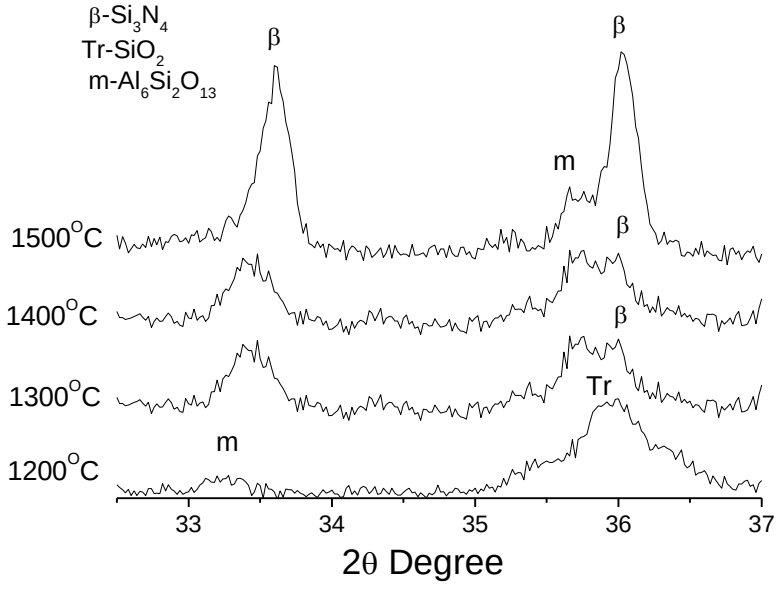

Figure 7. XRD patterns after different heat treatments of mixture of carbon block and silica with molar ratio 3.

Thus, the overall reaction may be represented by the equation (1.7) [51]:

$$\underset{\text{A}}{[Si_mAl_nO_6]} + xC + (x/3)\cdot N_2 \Rightarrow \underset{\text{B}}{[Si_mAl_nO_{6-x}N_{2x/3}]} + xCO \quad (1.7)$$

where A and B points belong to the Si-Al-O-N diagram. Point A is on the line SiO_2-$3SiO_2 2Al_2O_3$-Al_2O_3 and point B is in the interior of the Si-Al-O-N diagram and it can be monophase or multiphase zone.

From the chemical composition of the diatocemous earth with the constant Si/Al ratio, the line passes through a few single phase zones as well as equilibrium regions of two phases. Starting from the point on the axis SiO_2-$3Al_2O_3$-$2SiO_2$-Al_2O_3, the phase equilibrium line passes by the single phase zone of the O-Sialons, by the the part with an equilibrium of O-Sialons and β-Sialons, by the single phase region of β-Sialons and finally line reaches a point where there is mixture of Si_3N_4 and AlN (Fig. 7).

Table 5 shows the evolution of the crystalline phases formed as a function of the reaction temperature. At low temperature (1200 °C) there were three phases: crystobalite (SiO_2), mulite ($3Al_2O_3 2SiO_2$) and Si_2N_2O (sinonite). Crystobalite is the principal phase, however, this phase tends to decrease with increasing of temperature. This behavior results from the mulite and Si_2N_2O formation.

Table 5. The phase evolution of the crystalline phases after heat treatment at 1200 °C to 1500 °C for 4 h.

Sample C/SiO_2 mol ratio	*Reaction temparture (°C)*	*Crystalline phases*
3	1200	SiO_2, mullite, Si_2N_2O
3	1300	SiO_2, mullite, Si_2N_2O
3	1400	Si_3N_4, Si_2N_2O, SiO_2, mullite
3	1500	Si_3N_4, SiO_2, mulite
4	1200	SiO_2, mulite, Si_2N_2O
4	1300	SiO_2, Si_3N_4, Si_2N_2O
4	1400	Si_3N_4, SiO_2, sialon
4	1500	sialon, Si_3N_4, SiO_2
5	1200	SiO_2, mulite, Si_2N_2O
5	1300	SiO_2, Si_3N_4, Si_2N_2O
5	1400	Si_3N_4, SiO_2, sialon
5	1500	sialon , Si_3N_4, SiO_2

Mullite is formed by recrystalization of starting diatomeus earth through direct reaction between SiO_2 and Al_2O_3 (Eq. (1.8)):

$$2\ SiO_2 + 3\ Al_2O_3 \rightarrow 3Al_2O_3 2SiO_2 \quad (1.8)$$

The reaction (1.8) explains the appearance of mullite, which increases at 1300 and 1400 °C and then disappeared at 1500 °C. Since mullite is coming from diatomeus earth recristalization, it is highly reactive in the formation of nitrogenous phases.

The formation of Si_2N_2O is based on the reaction :

$$3\ Si + SiO_2 + 2\ N_2 \rightarrow 2\ Si_2N_2O \quad (1.9)$$

which involves vapor phase formed of SiO and N_2 and yields a powderous Si_2N_2O. Appearing of Si_2N_2O phase indicates that prior the reaction (1.9) the carbothermal-reduction of SiO_2 occurred according the reactions (1.10) and (1.11):

$$SiO_2 + C \rightarrow SiO + CO \quad (1.10)$$

$$2\ SiO \rightarrow Si + SiO_2 \quad (1.11)$$

The XRD pattern shows remarkable broadening of the diffraction lines in the regions around 33-34° and 35-37° 2θ, which can be associated with the phase, β-Si_3N_4. This indicates that nucleation and crystallization of β-Si_3N_4 takes place at 1300°C. However, with increasing C/SiO_2 ratio β-Si_3N_4 tends to disappear when temperature increase (Fig. 8). In samples with C/SiO_2 ratio 4 and 5, respectively, the principal phase is β′-sialon. As mention before, these coincidences with disappearing mullite, what indicates that mullite has a main role in β′-sialon formation. This can be explained by reduction of mullite. The Al_2O_3 from mullite can be reduced to AlN which will be dissolved in β-Si_3N_4 according to the following equation:

$$0.5z\ Al_2O_3 + (2\text{-}0.25z)\ Si_3N_4 \rightarrow Si_{6-z}Al_zN_{8-z}O_z + 0.25z\ SiO_2 \quad (1.12)$$

where "z" represents the number of replaced Al an O ions, respectevily. Increasing C/SiO_2 ratio means more contact points between C and Al_2O_3 resulting in more reduced amount of Al_2O_3. The total amount of dissolved AlN is higher and as a consequence, the amount of the β′-sialon is higher.

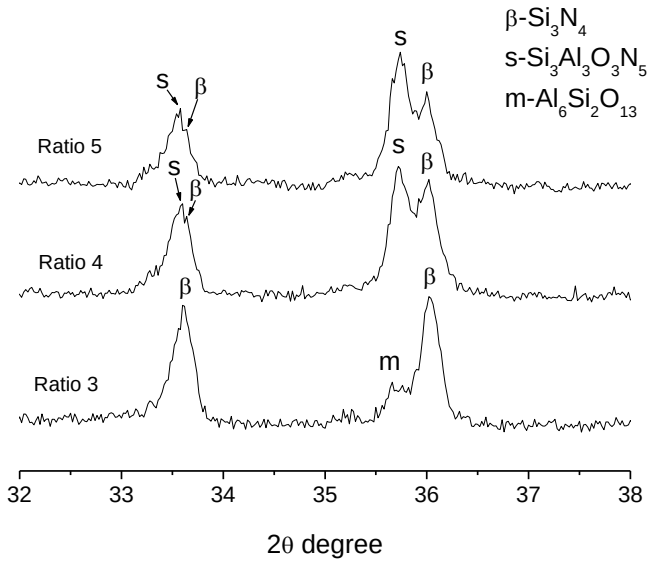

Figure 8. XRD patterns of the reaction products with different molar ratio of carbon block and silica, after heat treatment at 1500 °C.

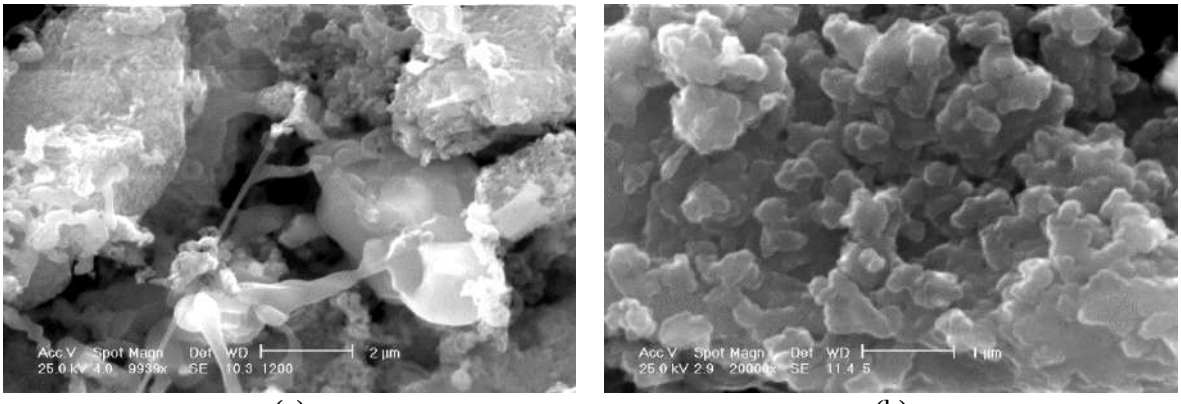

(a) (b)

Figure 9. SEM micrograph of powders obtained at lower temperature – 1200 °C (a) and at higher temperature – 1500 °C (b) for 4 h with molar ratio (C/SiO_2) = 4.

The morphology of powder obtained at low temperature shows that these products retain characteristic of some fragments of original diatomite (Fig. 9a). However, at higher temperatures the micrographs of the powder is completely different (Fig. 9b), these particles exhibit polygonal habitus, which is characteristic of hexagonal sialon and silicon nitride crystals.

1.2.2 Summary

It has been demonstrated that carbonitriding of diatomaceous earth leads to the formation of phases of the Si-Al-O-N system. The reaction products depend of the reaction temperature and carbon/ silicon ratio, where many intermediate compounds appear in small quantities. At low temperature the reaction products are mixture of different oxides and Si_2N_2O with morphology that retain some features of starting diatomite. Powders obtained at higher temperature are the mixture of sialon and silicon nitride with well-defined crystal geometry. Increasing carbon/silicon ratio, the amount of sialon increase compared to silicon nitride.

1.2.3 Diimide thermal decomposition

The diimide thermal decomposition fabrication process comprises three major steps: (a) diimide synthesis, (b) diimide thermal decomposition and (c) crystallization. In the first step, silicon tetrachloride ($SiCl_4$) and ammonia (NH_3) are made to react by liquid phase surface reaction or vapor phase reaction to synthesize silicon diimide ($Si(NH)_2$) and ammonium chloride (NH_4Cl). In the following step the $Si(NH)_2$ is thermally decomposed at a temperature of about 1000 °C to obtain an amorphous silicon nitride powder. During the final step, the amorphous powder is crystallized in a temperature range of 1300-1500 °C to form the α-Si_3N_4 powder [52]. This powder is characterized by sub-micron equiaxed particles containing a large amount of α-phase.

1.2.4.Vapor phase synthesis

The vapor phase synthesis takes place between different gaseous species in the temperature range from 800 °C up to 1400 °C. Usually, the starting materials are $SiCl_4$ and ammonia which react to form amorphous Si_3N_4. Crystallization of the amorphous powder is carried out at temperatures 1300-1500 °C. Deagglomeration is also a necessary step to be carried out. Synthesis of powders by lasers is a useful technique for making nano-size (10-100 nm) powders starting from gaseous or volatile mixtures [53] and is based on the absorption of infrared laser energy (10.6 μm wavelength for CO_2 laser) which is converted into vibrational modes of the reactant gases that produce very high temperatures (above 1000 °C) for a short total reaction time (0.1 s or less). These conditions are necessary for the initiation of a chemical reaction the final result of which is the formation of the powder. Due to the coherent nature of the laser source, a well-localized reaction zone can be defined. The grown particles have a spherical morphology, small size; narrow size distribution and their stoichiometry can be precisely controlled by adjusting the main process parameters such as laser intensity, pressure in the reaction cell, reactant flow rates, reaction gas ratio and temperature of the reaction [54]. All these powders are useful in structural ceramic applications.

1.3 Processing techniques of silicon nitride ceramics

The high degree of covalent bonding makes it very difficult to produce pure dense Si_3N_4 ceramics by classical sintering (simple heating of powder compacts). The main reason for this is that the diffusion of silicon (at 1400 °C $D_{Si} \approx 0.5 \times 10^{-19}$ $m^2 \cdot s^{-1}$) and nitrogen (at 1400 °C $D_N \approx 6.8 \times 10^{-10}$ $m^2 \cdot s^{-1}$) in the volume or at the grain boundaries of Si_3N_4 is extremely slow [10]. As densification by sintering requires mass transport via volume or grain boundary diffusion and since such diffusion is a thermally activated process, a higher sintering temperature would result in a highly dense material [49]. However, at high temperatures Si_3N_4 starts to dissociate [50]. Therefore, sintering additives are utilized as a possibility to promote liquid phase sintering and thus enhance volume or grain boundary diffusion. As a consequence, many different sintering techniques have been developed:

— Reaction bonding RBSN

— Hot pressing HPSN
— Hot-isostatic pressing HIPSN
— Gas-pressure sintering GPSN
— Pressureless sintering SSN

One common densification method is the nitridation of silicon compacts, leading to reaction-bonded silicon nitride (RBSN) materials. By this method, complex shapes can be produced using various ceramic forming methods (slip casting, injection molding, die pressing, isostatic pressing) with low costs. However, the process leads to a material of limited density (about 70-88%) resulting in poor mechanical properties. Because of the residual porosity the strength of RBSN is relatively low. Furthermore, the pore structure leads to high oxidation rates and to small erosion resistance [42, 51]. Thus, low densities and pore structure limit the range of possible applications of RBSN materials. Hot-pressing of pure silicon nitride powder at high temperatures does not result in full density and leads to the production of porous materials with properties similar to those of RBSN [52]. In spite of this, the first dense Si_3N_4 ceramic was that accomplished by hot pressing Si_3N_4 powders containing MgO as sintering additive [3]. Such kind of hot-pressed Si_3N_4 ceramics (HPSN) is a high strength material, which can be used at temperatures up to 1000°C without a decrease in strength. Because of high cost and difficulties to machine the components, hot-pressing, today, has limited use for the production of simple shaped parts and low quantities.

Another method is to apply isostatic pressure instead of uniaxial pressure, i.e. hot-isostatic pressing (HIPSN). During this process a high gas pressure is applied to consolidate a powder compact or to remove the residual porosity from presintered bodies. The uniform manner of applying the high pressure results in fully isotropic material properties. The possibility to use much higher pressures than in uniaxial hot-pressing leads to an enhancement in the densification of the products. Thus, fully dense ceramic parts can be produced from powders of lower sintering activity and with smaller amounts of additives as compared with unaxial hot pressing. Three different routes are used in order to produce fully dense ceramics by the HIP technique: (a) HIP densification of Si_3N_4 powder compacts, (b) HIP densification of reaction bonded Si_3N_4 and (c) HIP densification of normal sintered Si_3N_4. All these techniques lead to materials which combine excellent mechanical and thermo-mechanical properties. The main disadvantage of this method is its high cost. The most common sintering/densification method for high-strength Si_3N_4 ceramics is gas pressure sintering (GPSN). This method allows sintering of complex-shaped parts with medium cost. However, the most economical method is to sinter Si_3N_4 powder compacts with additive under 0.1 MPa N_2 at 1700°C-1800 °C, *i.e.* pressureless or normal sintering (SSN). The powder mixtures (Si_3N_4 plus additives) are compacted to required shapes by various shaping methods. Complex-shaped components of dense Si_3N_4, which require little machining, remain after sintering. Because the highest sintering temperature is restricted by thermal dissociation of Si_3N_4 [53], relatively large amounts of additives are necessary to fabricate high-density materials.

2. Sintering

2.1 Basic theory of liquid phase sintering

Liquid phase sintering (LPS) is the sintering process in which a part of the material being sintered is in the liquid state. This is a conventional technique, that has been used to manufacture ceramics for many centuries [54]. LPS is important for systems which are difficult to densify by solid state sintering, *i.e.* ceramics that possess a high degree of covalent bonding (e.g. Si_3N_4 and SiC). The liquid is normally produced from a mixture of at least two powders, a major component and an additive. On heating of the mixture, the additive melts or reacts with a small part of the major component to form a eutectic. The amount of liquid produced at the sintering temperature is usually maintained in the range of 5-15 vol.%. In most systems, the liquid does not change its volume. Due to persistence of the liquid throughout the sintering process, this condition is referred to as persistent liquid-phase sintering. In other systems, the liquid may be present over a major part of the sintering process and then disappears by different ways:

1. incorporation into the solid phase (formation of a solid solution),
2. crystallization of the liquid or devitrification of glassy phase, and
3. evaporation.

All these situations are referred to as transient liquid-phase sintering. Transient LPS is a very important technique in the sintering of Si_3N_4 with additives for producing dense Si_3N_4 based ceramics.

2.1.1 Factors controlling liquid phase sintering

Liquids with a low surface tension readily wet solids, giving rise to small contact angles, while liquids with a high surface tension show poor wetting, forming larger contact angles (Fig. 10).

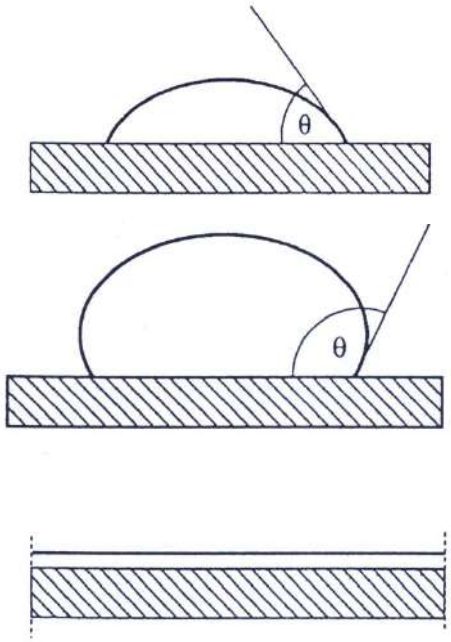

Figure 10. Wetting behavior between a liquid and a solid.

At the molecular level, if the cohesion between the liquid molecules is smaller than the adhesion between the liquid and solid, the liquid has a tendency to wet the solid. The degree of wetting is quantified by the equilibrium contact angle that forms between the liquid and the solid and is defined in Fig. 11.

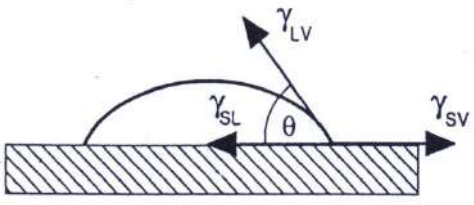

Figure 11. Equilibrium contact angle between a liquid and a solid.

If the energies of the liquid/vapor, solid/vapor and solid/liquid interfaces are γ_{lv}, γ_{sv} and γ_{sl} respectively, then a simple balance of forces indicates equilibrium according to the equation given below:

$$\gamma_{sv} = \gamma_{sl} + \gamma_{lv} \cdot \cos\theta \quad (2.1)$$

Hence, higher values of γ_{sv} and lower values of γ_{sl} and/or γ_{lv} promote wetting. This equation, derived by Young and Dupre [55], shows that a necessary condition for liquid-phase sintering to

occur is that the contact angle must lie between 0 and 90° (to stay consistent with the drawings). For higher contact angles (>π/2), the liquid will bead up in the pores and the sintering can occur only by the solid-state mechanism. The contact angle also has an important effect on the magnitude and nature of the capillary forces exerted by the liquid on the solid grains [56].

The other necessary condition for LPS is that the liquid distributes itself to cover the surfaces of the particulate solids. The complete penetration and separation of the grain boundary by the liquid depends on the dihedral angle which is defined as the angle between the solid/liquid interfaces as sketched in Fig. 12 :

$$\gamma_{gb} = 2\,\gamma_{sl} \cos(\psi/2) \qquad (2.2)$$

The grain boundary energy (γ_{gb}) must be less than twice the solid/liquid surface energy γ_{sl} [57]. Thus, high values of γ_{gb} and low values of γ_{sl} are desirable. The microstructural features obtained for various values of the dihedral angle are listed in Table 6. For $\psi = 0$, the liquid completely penetrates the grain boundaries and no solid/solid contact exists. As ψ increases, the penetration of the liquid phase between the grains decreases and the number of solid/solid contacts increases.

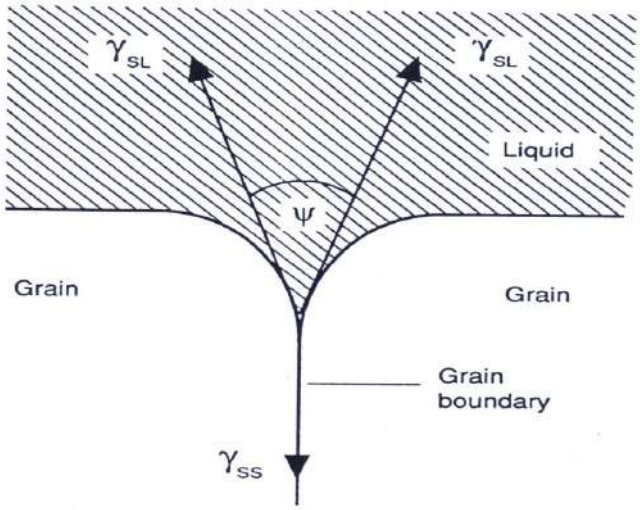

Figure 12. Equilibrium dihedral angle between a grain and the liquid phase.

Table 6. Microstructural features of liquid-phase sintering as a function of dihedral angles (ψ).

Dihedral angle (ψ)	***Microstructure***
0°	isolated grains separated by liquid phase
0-60°	partial penetration of grain boundaries by liquid along the three-grain edges
60-120°	isolated pockets of liquid at extended four-grains junctions
≥ 120°	isolated liquid phase at four grain junctions

Surface tension between solids and liquids generates capillary forces, which may give rise to very strong attractive forces among neighboring grains. The contact stress that is generated upon grain impingement, in combination with the lubricating potential of the liquid, enhances the dissolution of solids leading to rapid particle rearrangement and densification. The main processing parameters, such as particle size, green density, sintering temperatures, time and atmosphere, have large effects on the material characteristics obtained by liquid-phase sintering. All of these factors contribute to the complexity and difficulty in understanding liquid-phase sintering mechanisms.

2.1.2 Basic mechanisms of liquid-phase sintering

The plausible mechanisms for liquid-phase sintering have been described in detail by Kingery [58, 59], Petzow et al. [60] and German [61]. In order to understand these mechanisms, a number of experimental and theoretical investigations were made. All of them come to the same conclusion that

the LPS process occurs in three stages, so that there is some degree of overlapping between the theories. Classically, the following sequence of sintering stages is considered to be prevailing:

1. Particle rearrangement,
2. Solution-reprecipitation, and
3. Solid-state or skeleton sintering.

2.1.2.1 Particle rearrangement

Rearrangement is the dominant process in the first stage. After a liquid has been formed within the powder compact, rapid densification occurs, due to liquid capillary forces via the movement of the solid particles from their initial positions towards an arrangement of random dense packing and a higher degree of space filling. Rearrangement is also an effective densification phenomenon during the whole shrinkage period, even during solid state sintering [62].

This process is rapid. However, except for large liquid contents, it cannot lead to complete densification. Many parameters, such as the amount of liquid, its viscosity, green density, wetting, sintering temperature etc. strongly affect this stage. Kingery's model gives an empirical approach in which the rate of densification corresponds approximately to the viscous flow and follows a relation as given below:

$$\Delta L/L_0 \approx 1/3\ \Delta V/V_0 \approx t^{1+y} \quad (2.3)$$

where ΔL is the change in length and L_0 the original length, ΔV and V_o correspond to the change in volume and initial volume respectively. The exponent $1+y$ is slightly greater than unity due to the fact that pore sizes decrease and the driving force increases during the process, while at the same time t, the resistance to rearrangement, increases from the initially pure viscous flow. There are other approaches to analyzing the rearrangement during liquid-phase sintering, such as analysis of the capillary forces between particles separated by a liquid layer. All of these models are quite complex and calculations are very cumbersome.

2.1.2.2 Solution-reprecipitation

In the second stage, the rearrangement efficiency decreases significantly and the solution-precipitation process becomes dominant. Capillary forces generate a difference in the chemical potential at the points of contact between grains when compared to the areas that are not in contact. This chemical potential gradient induces the dissolution of atoms at the contact points and their reprecipitation away from the contact areas, which leads to shrinkage and densification. The necessary condition for the process to occur would be a finite solubility of the solid in the liquid and good wetting ability of the liquid. In addition to densification, coarsening can occur simultaneously by the dissolution of the smaller particles and their reprecipitation on the larger particles. The dissolution and reprecipitation of dissolved materials contributes to the microstructural development, shape accommodation and grain growth.

There are two theories explaining the evolution of densification during liquid phase sintering, namely the contact flattening theory and the pore filling theory. The fundamental difference between these theories lies in whether the grain shape is changed or not during densification of the powder compact. Kingery [58] proposed that shrinkage and hence densification is achieved by the matter transport from the contact area between grains to the off-contact neck region, analogous to solid-state sintering. The contact regions between particles become flat. This process results in a continuous change in grain shape, until there is a complete elimination of the pores. A number of investigations were confirmed this theory [59, 63, 64, 65, 66].

Another mechanism of densification has been proposed according to microstructural observations [67]. In this model, an isolated pore was eliminated by the instantaneous filling with liquid [68, 69]. Upon prolonged sintering, the liquid pocket is eliminated by microstructural homogenization due to material deposition of the grains at the concave surfaces and growth toward the liquid pocket center. Once the pore filling occurs, the grains grow into the liquid pocket, resulting in microstructural homogenization [70, 71, 72]. This solution-precipitation process is the classic Ostwald ripening process [73]. Dissolution of the small grains and precipitation away from the

contact points causes the centers of the larger grains to approach each other, resulting in shrinkage. Ostwald ripening is thought to accompany the densification process.

2.1.2.3 Solid-state or skeleton sintering

The last stage is referred to as solid-state controlled sintering. The overall shrinkage or densification rates are significantly reduced due to formation of a rigid skeleton that inhibits further rearrangement [74, 75]. Coarsening is the dominant process. The three stages of liquid-phase sintering are sketched as a sintering curve in Fig. 13.

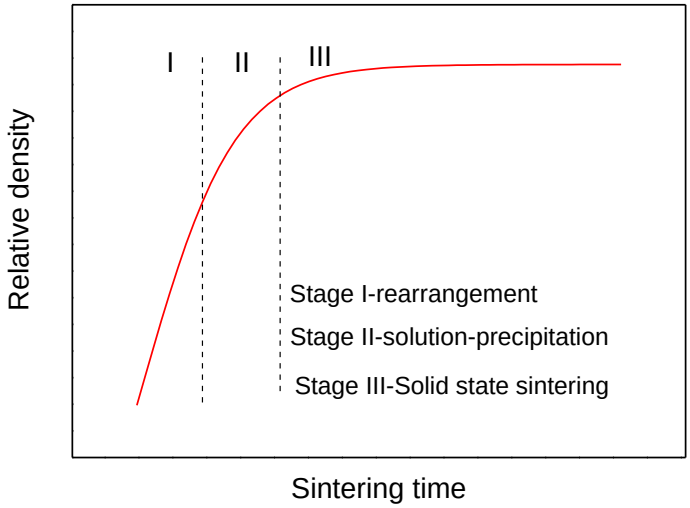

Figure 13. Schematic diagram illustrating the three stages of liquid-phase sintering on a typical sintering curve.

Particle rearrangement is the process occurring the fastest on a time scale of minutes [76]. The solution-reprecipitation process and skeleton sintering depend on diffusion through the liquid and solid, respectively, and hence, are slower in comparison to I stage (particle rearrangement).

2.3 Consolidation of Si_3N_4 powders

The mechanical properties and reliability of the Si_3N_4-based ceramics are strongly dependent on their density and microstructure. However, densification of pure Si_3N_4 powder compacts is inhibited by the strongly covalent character of the Si–N bond, which results in an extremely low self-diffusivity of Si_3N_4. Therefore, sinking Si_3N_4 ceramics to full density requires the presence of sintering additives to form a eutectic melt (liquid phase sintering). The liquid acts as a mass transport medium during densification.

After sintering, upon cooling, the liquid forms grain boundary phases which are either amorphous or crystalline depending on the type and concentration of additives. The introduction of sintering additives is a critical step in the production process. Inhomogenities introduced at this stage remain inside the material and degrade the mechanical properties and reliability of Si_3N_4 based ceramics. It is important to find powder processing routes able to produce high homogenity in powder premixes/mixtures in order to produce materials with optimum properties.

Various preparation routes for engineering ceramics powders have been used. The best results are obtained by chemical routes, but this method is more costly in terms of industrial manufacturing than conventional milling techniques. Milling is the most common and industrially preferred method of adding and mixing the additives with the matrix.

The effects of different types of homogenization procedures (ball milling, attrition milling and vibratory milling) on the properties of Si_3N_4 powder and sintered bodies are described in detail in the following text.

2.3.1 Experimental methodology for powders processing

Usually, starting material used to fabricate green bodies is commercial Si_3N_4 powder. The low cost powder has advantage due to price of final products. Typical chemical analysis of low cost powders and its characteristic impurity contents are given in Table 7.

Table 7. Characteristic of initial powder.

N	>38.5 wt.%
Si free	<0.5 wt.%
SiC	<0.4 wt.%
Al	<0.1 wt.%
Fe	<0.04 wt.%
Ca	<0.02 wt.%
O	≈0.5 wt.%
$\alpha/(\alpha+\beta) - Si_3N_4$	0.8
Specific surface area (m^2/g)	3.2
Density (g/cm^3)	3.2
Mean particle size, d_{50} (μm)	1.7

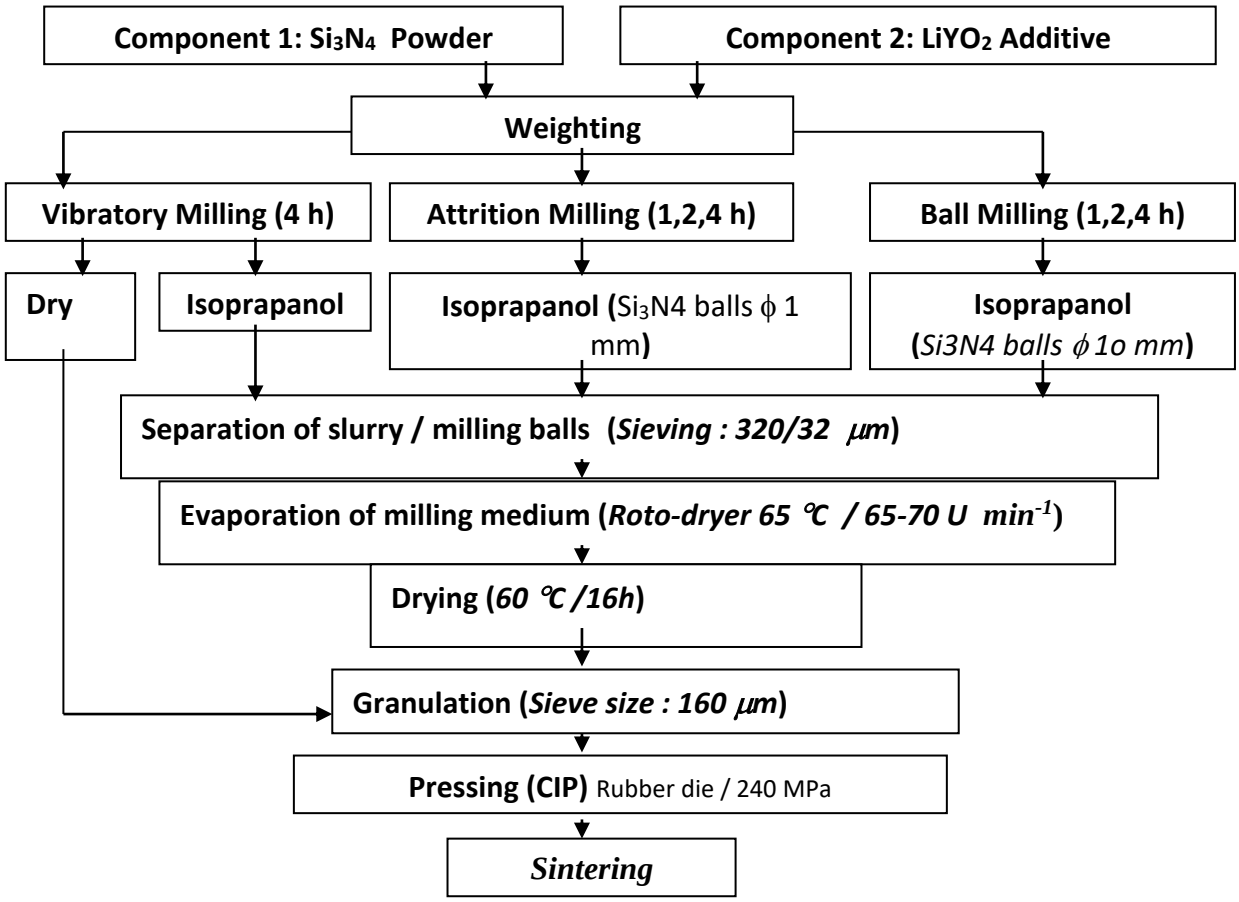

Figure 14. Schematic diagram of sample preparation method.

In this case additive was the $LiYO_2$ compound synthesized by mixing as-received Y_2O_3 and Li_2CO_3 powders, and calcining at 1400 °C for 4h. Powder mixtures were prepared by vibratory milling, ball milling and attrition milling in isopropanol with Si_3N_4 milling media for different times.

One probe was mixed in a vibratory mill without any fluid media. The slurry was separated from the milling media in a rotating vacuum evaporator. Completely dried powders were obtained after 16 h at 65 °C in a drying oven. They were subsequently sieved to obtained granules with a maximum size of 160 μm. Green body compaction was done by cold isostatic pressing at 240 MPa. The preparation method is schematically represented in Fig. 14. The obtained mixtures were characterized for their particle size distribution (laser granulometry) and specific surface area (N_2 adsorption isotherms, BET). For the determination of oxygen contents, a gas analyser (type TC 436, Leco Instruments) was used. Microstructures of as-received and sintered samples were examined by scanning electron microscopy (SEM). Backscattering imaging of elemental yttrium with the SEM was used to examine the homogeneity of the additive distribution in the green compacts. For this purpose the green compacts (10 mm in diameter) were formed via isostatic pressing of different powder mixtures and coated with carbon to make their surfaces electrically conductive.

2.3.2 Results and discussion

Powders with favorable pressing and sintering characteristics are distinguished by: high percentage of the α-Si_3N_4 phase (>90%), high surface area, narrow particle size range, low content of impurities (Fe, C, Al, Ca, O) and equi-axed grain morphology [6]. In contrast, as- received powder is a coarse grained powder with a broad particle size distribution. Fig. 15 depicts the powder morphology. Equiaxed, rod-like and a few needle-shaped particles can be clearly identified. The presence of these particles leads to decreasing compressibility and hence to low green density. The starting material could be pressed to only about 50% of the theoretical density. This powder morphology is connected with a low specific surface area and with low oxygen content (Table 8).

According to above criteria, used powder is not considered to be a good sinterable powder. However, during the homogenization by milling several processes are occurring simultaneously. The surface of the powder increases owing to the deglomeration and to the grinding of the crystallites. As a result, the oxygen content increases. We shall examine below whether used powder can be converted into a sinterable powder by mixing/milling processing.

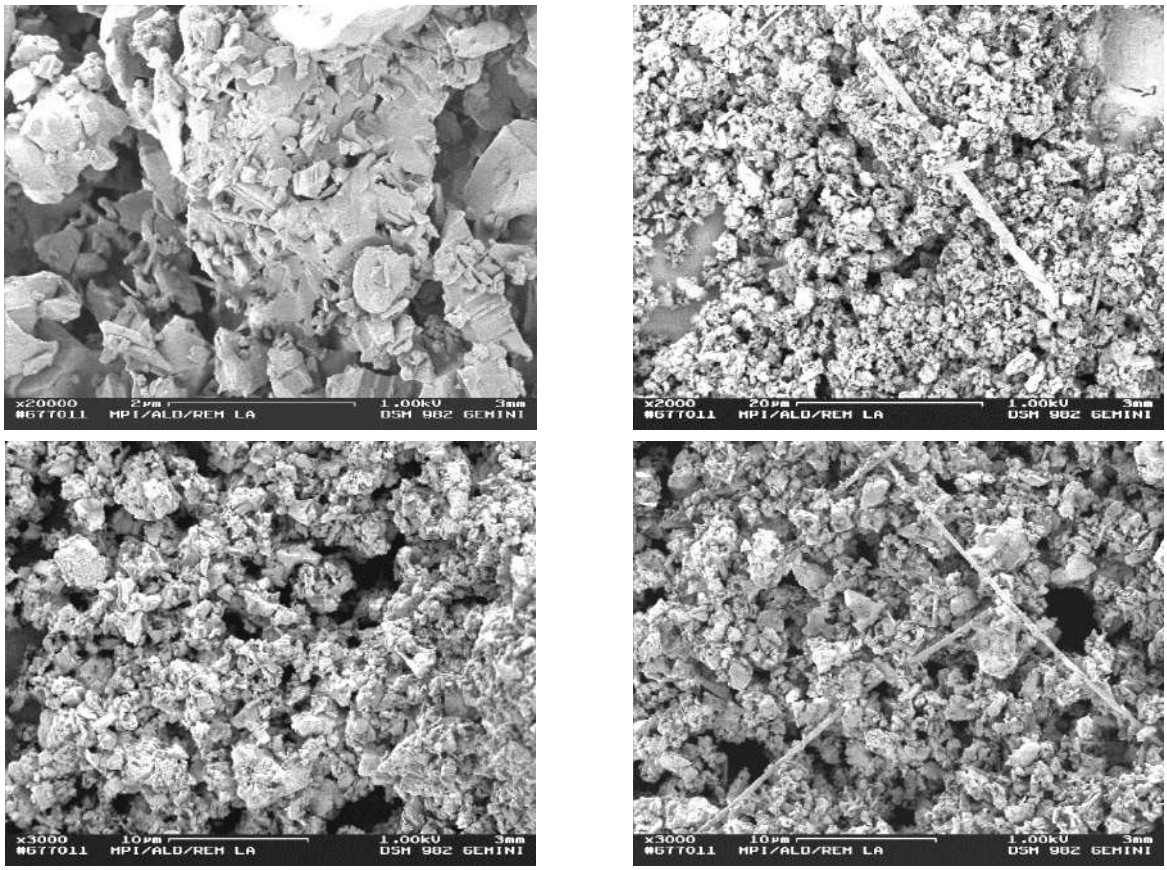

Figure 15. Typical SEM micrographs of as-received silicon nitride powder.

Table 8 shows the effects of milling time and method of dispersion on the properties of the Si_3N_4 powder. The specific surface area increases for all types of homogenization, but it is most pronounced in attrition-milled mixtures (Fig. 16).

Table 8. Effects of milling time and different types of homogenization procedures on the properties of Si_3N_4 mixtures

Homogenizatin	*Time (h)*	*Specific surface area (m^2/g)*	*Content of oxygen (wt.%)*	*Increase of oxygen content (wt.%)*
Planetary milling	1	5.46	2.82	1.01
Planetary milling	2	5.61	2.87	1.06
Planetary milling	4	6.35	3.31	1.50
Attrition milling	1	6.83	2.73	0.92
Attrition milling	2	8.99	2.89	1.08
Attrition milling	4	13.78	3.67	1.86
Vibratory milling (dry)	4	4.71	2.36	0.55
Vibratory milling (alcohol)	4	12.26	3.98	2.17

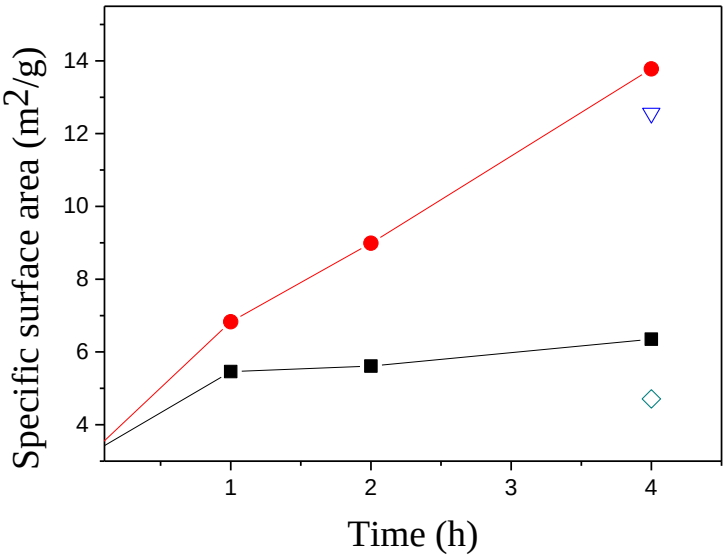

Figure 16. The effects of milling time on the specific surface area (■ - planetary milling; ∇- attrition milling; ● - dry vibratory milling; ◊ - alcohol vibratory milling)

For planetary-milled mixtures, the specific surface area was significantly increased after the first hour of milling, while upon prolonged milling it stays nearly constant. In the case of attrition-milled powders, the surface area continues to grow during prolonged milling and increases by more than 10 m^2/g after 4 h of processing, as compared with the as-received Si_3N_4 powder. Vibratory milling in alcohol shows very good results, but for dry vibratory milling the specific surface area increase in surface area is less than for all other processing methods.

Increasing of specific surface area is due to grinding of the crystallites. Fig. 17 illustrates the change in particle morphology after attrition milling in comparison with as-received powder. Rod-like and needle-shaped particles disappear, and all particles have an equi-axed shape. This has the positive effect of improved compressibility.

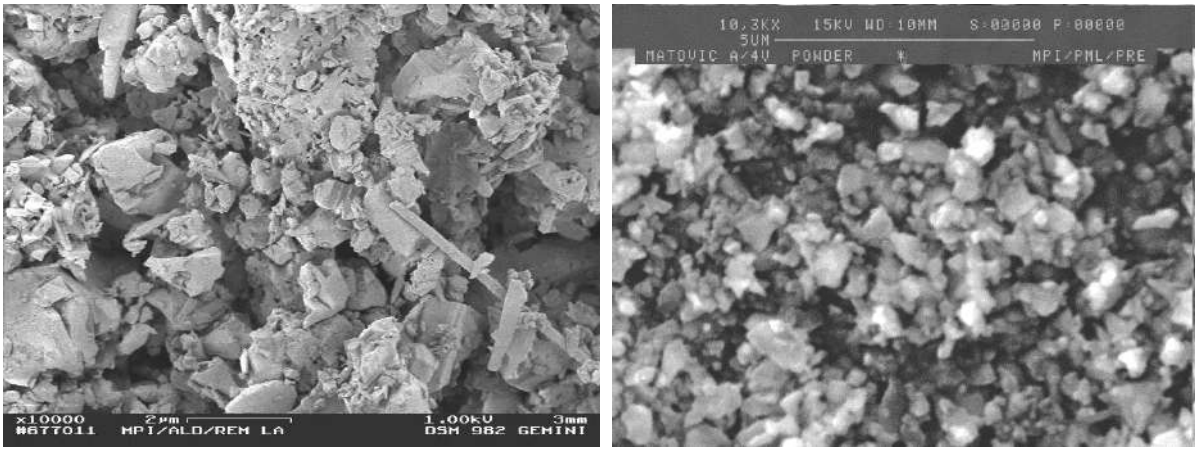

Figure 17. SEM photomicrographs of as-received and attrition milled (4 h) Si_3N_4 powders.

Table 9 shows that during all milling procedures, the oxygen content increased significantly with milling time. This is very important because the composition of the melt depends on type and amount of the additives and the oxygen content in the Si_3N_4 powder. Higher oxygen contents result in increased amount of liquid phase and thus in an enhancement of the rearrangement and diffusion processes. For the coarser-grained powders this effect is more significant. An oxygen content of at least 1.5% is necessary for high densification. Fig. 18. Shows the oxygen content as a function of the presence of the sintering additive and the milling procedure used. The overall oxygen content was calculated as the sum of oxygen from the sintering additive (5 wt.% $LiYO_2$) oxide layer on the surface of the Si_3N_4 powder. The highest increase was obtained for attrition milling (4 h) and vibratory milling (4 h in alcohol), which corresponds well with the increase specific surface area.

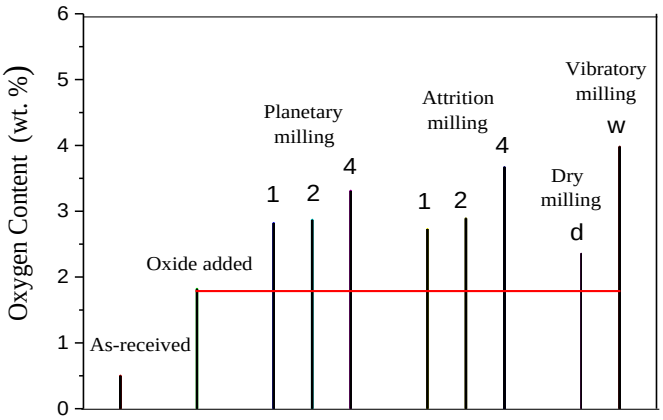

Figure 18. Oxygen content during processing with $LiYO_2$ additives (milled for 1,2,4-h ; d-dry milling; w-wet milling)

Fig. 19 shows the elemental mapping for yttrium in different green compacts. The light spots represent the $LiYO_2$ that is distributed in the green compacts. Large spots imply an agglomeration of the additive. The number of large spots was apparently greater in the samples prepared by planetary milling, especially for the samples milled for 1 or 2 h. Therefore, many agglomerates of the oxide additive exist in these compacts. The distribution of additives is obviously more homogenous in the compacts prepared by attrition milling than the compacts prepared by planetary milling. A confirmation for the higher quality of the additive distribution is density that is achieved after sintering (Table 9).

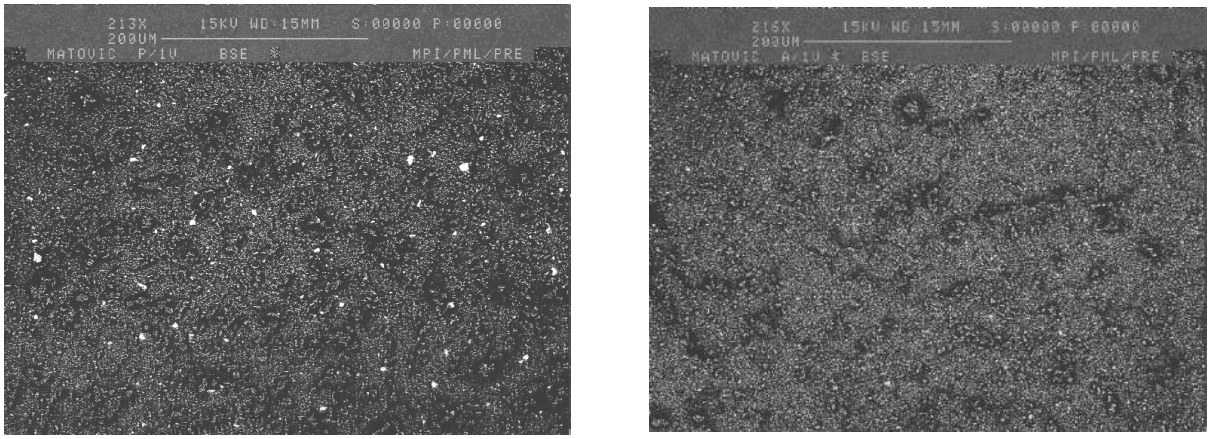

Planetary milling Attrition milling

Figure 19. (a): Backscattered electron images of green compacts of yttrium - ($LiYO_2$ containing Si_3N_4 mixtures prepared by planetary and attrition milling for 1h).

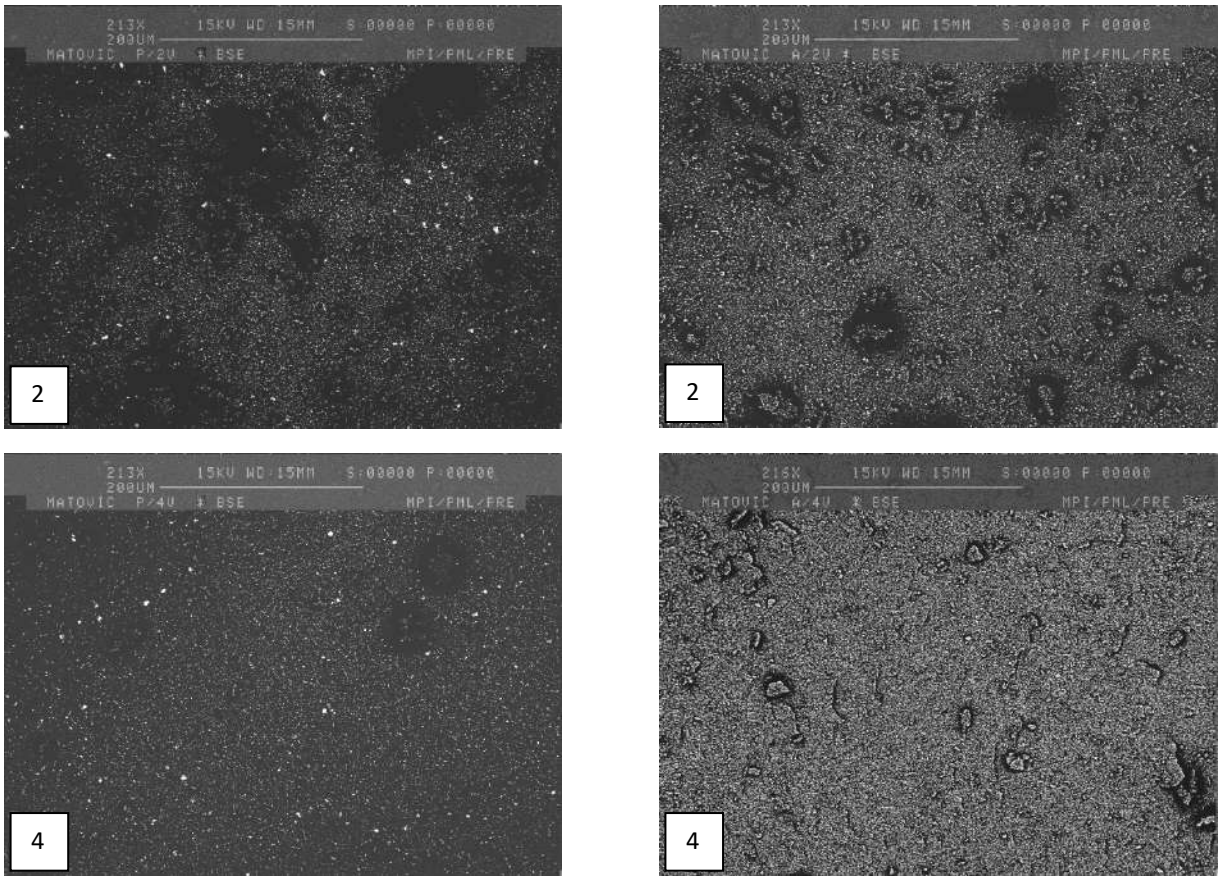

Planetary milling Attrition milling

Figure19. (b): Backscattered electron images of green compacts of yttrium-($LiYO_2$ containing Si_3N_4 mixtures prepared by planetary and attrition milling for 2 and 4 h)

Table 9. Densities after sintering at 1600 °C with 5% of $LiYO_2$ additive, (TD-theoretical density).

Time (h)	***Ball milling***		***Attrition milling***		***Vibratory milling****	
	Density (g/cm^3)	*TD (%)*	*Density (g/cm^3)*	*TD (%)*	*Density (g/cm^3)*	*TD (%)*
1	2,35	73,3	2,58	80,5	-	-
2	2,57	80,2	2,68	83,6	-	-
4	2,56	79,9	2,92	91,1	2,94	91,6

* wet milling

The sintered density after one hour of attrition milling is as high as after 2 and 4 h of planetary milling. With prolonged milling time attrition-milled samples increase their density. After 4 hours of milling, a sintered density of 91 % of the theoretical density is achieved. Comparable results are obtained for vibratory milled powders (wet milling). However, during vibratory milling, the powder mixture was contaminated by wear debris from the milling vial (tungsten carbide).

Different microstructures of sintered bodies are obtained for different homogenization methods (attrition and vibratory milling). The material produced from attrition-milled mixtures has a finer-grained microstructure with lower aspect ratios compared to the vibratory-milled mixtures (Fig. 20). In spite of the higher aspect ratio of vibratory milled mixtures, the presence of WC deteriorates the high-temperature strength due to its thermal decomposition and the oxidation of tungsten.

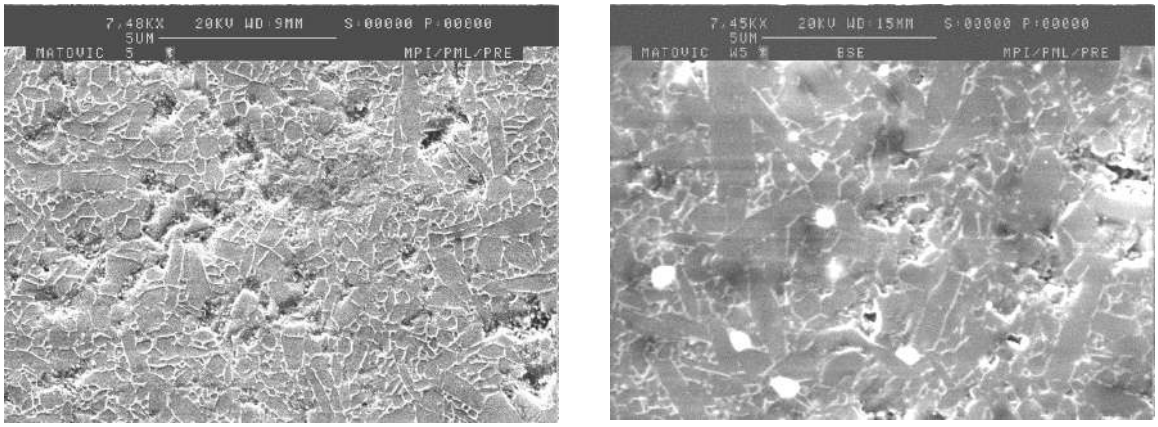

(a) (b)

Figure 20. SEM micrographs of polished and plasma etched sections of the sintered samples made by different homogenization procedures: (a) attrition milling, and (b) vibratory milling.

2.3.3 Summary

It was demonstrated the effects of different types of homogenization procedures on the best distribution of $LiYO_2$ additives in the matrix (Si_3N_4). Using tree different mechanical mixing processes (attrition milling, ball milling and vibratory milling) for the introduction of additives ($LiYO_2$) in Si_3N_4 powder, the best results are obtained for attrition milling. This method yields a good dispersion of the additive powder in fine unagglomerated Si_3N_4 without contamination. It also yields good sintering characteristics. Vibratory milling leads to a good dispersion of the additive, but the mixture is contaminated by WC wear debris which remains inside the materials during and after sintering and may affect the properties of the ceramics.

Generally, by optimizing the processing and sintering conditions it is possible to obtain materials from the low cost powder with similar phase composition and macrostructures in comparison to ones made from the reference powders.

2.4. Sintering additives

The desirable properties of Si_3N_4 ceramics are achieved only in a fully dense material. However, it is difficult to densify Si_3N_4 into a usable form without the use of sintering additives as discussed previously. Thus, using additives is a prerequisite for obtaining dense Si_3N_4 ceramics. The type and amount of sintering additives determine the liquid forming temperature, the onset of densification and its rate during sintering [11]. They also define the morphology of the β-grains and the characteristics of the grain-boundary phase, which in turn controls the high-temperature properties. The role of the additive can be expressed by the following reactions:

$(Si_3N_4 + SiO_2 + \text{impurities}) + \text{additive}$ [starting powder]

$\downarrow$ sintering temperature

β-Si_3N_4 + liquid (SiO_2 + additive + Si_3N_4) [sintering]
↓ cooling
β-Si_3N_4 + amorphous/crystalline phases (SiO_2 + additive) [final product]

Silica at the surface of Si_3N_4 powder particles reacts with the sintering additive producing a liquid phase. The melting temperature of the additive-SiO_2 composition and the amount and viscosity of the resulting liquid phase are closely connected with the SiO_2 concentration on the Si_3N_4 particle surfaces, the amount of dissolved α-Si_3N_4 in the liquid and the impurity content of the starting powder. The liquid promotes densification through a solution-reprecipitation mechanism. Upon cooling, the liquid solidifies and forms the residual intergranular glassy phase and possibly secondary crystalline phases [90].

Different types of additives have been employed for the pressureless and pressure-assisted sintering of Si_3N_4 ceramics [11, 49, 2, 91, 92] :

(a) Binary metal oxides or ternary oxides which do not form solid solutions with Si_3N_4. They remain as an amorphous or partially crystallized silicate grain-boundary phase. The more thoroughly investigated additives are MgO, Y_2O_3, Al_2O_3, La_2O_3, CeO_2, Yb_2O_3, ZrO_2, Li_2O, $MgAl_2O_4$, $ZrSiO_4$.

(b) Oxides or non-oxides or their mixtures which form solid solutions with Si_3N_4, like BeO, AlN, Al_2O_3 + AlN, Y_2O_3 + AlN, ZrN, ZrC, Mg_3N_2. They also form liquid phases with silica from the Si_3N_4 surface. α-Si_3N_4 is dissolved in the liquid and re-precipitated as β-Si_3N_4 solid solution which has incorporated a certain amount of the starting additive. During sintering, the amount and composition of the liquid phase changes gradually and it has been envisaged to be possible to produce a material without an amorphous intergranular phase [93, 94].

The eutectic temperatures of the commonly used oxide systems for the liquid-phase sintering of Si_3N_4 are listed in Table 10. However, it has been indicated that the presence of N lowers these eutectic temperatures further [95]. The alkali and alkaline earth oxides have a low melting point and the viscosity of the resulting liquid is also low. The solution-diffusion-precipitation processes are enhanced. In case of rare-earth oxides, the melting temperatures with SiO_2 are higher and densification rates are lower [96].

Table 10. Oxide additives used for the densification of Si_3N_4.

Additive M_xO_y	***Temperature of liquid formation, ℃***	
	Silicate M_xO_y-SiO_2	*Oxynitride* M_xO_y-SiO_2-Si_3N_4
Li_2O	1030	1030 [97]
MgO	1543	1390 [97]
Y_2O_3	1650	1480 [98]
CeO_2	1560	1460 [97]
ZrO_2	1640	1590 [97]
CaO	1435	1435 [97]
Al_2O_3	1595	1470 [98]

The viscosity of the liquid phase has a strong effect on the grain morphology which in turn affects the mechanical properties. Materials processed with additives that form liquid phases of higher viscosity consist of grains with a high aspect ratio [99], and as a consequence, exhibit better mechanical properties both at room temperature and at high temperatures. Good examples for different behavior of sintering additives are magnesia and yttria, respectively. The temperature of liquid formation for the MgO-SiO_2-Si_3N_4 system is lower by nearly 100°C in comparison with the Y_2O_3-SiO_2-Si_3N_4 system (Table 10). The MgO melt has also a lower viscosity than Y-SiAlON melts. The solubility of Si_3N_4 in a magnesium-containing melt is higher than in an yttrium-containing one. Therefore, the effect of MgO additive as a sintering aid is more beneficial. On the other hand, the higher viscosity and melting point of yttrium-containing liquid allow the sintered product to retain its thermomechanical properties at higher temperatures.

From Tables 10 and 11, it is clear that the sintering behavior is improved with increasing amount of additives. However, high additive amounts above 20 vol.% for certain thermodynamically less stable additives and/or high oxygen content of the starting powders can cause the formation of gas bubbles by increasing in the formation of gaseous SiO [101].

Table 11. Summary of sintering studies of Si_3N_4 at atmospheric pressure with magnesia and yttria additives and their compounds [100].

Additive	*Sintering temperature (℃)*	*Sintered density (% TD)*
5 mol% MgO	1500-1700	86
10 mol% spinel ($MgO{\cdot}Al_2O_3$)	1650-1900	96
5 wt% MgO + 0.15 wt% CaO + 0.8 wt% FeO + 4 wt% Y_2O_3 + 2 wt% Al_2O_3	1750	95
10 wt% $MgO{\cdot}Al_2O_3$	1600-1750	97
5 wt% MgO + BeO + CeO_2	1800	97
4 mol% Y_2O_3 + 2 mol% Al_2O_3	1725	Not mentioned
10 wt% Y_2O_3 + 3 wt% Al_2O_3	1600-1750	98
3.5-20 wt% Y_2O_3 + 20 wt% Al_2O_3	1750-1825	100
10 mol%Y_2O_3 + 20 mol% SiO_2	1750	90
4-17 wt% Y_2O_3 + 2-4 wt% Al_2O_3	1500-1750	95

Also, the ratio of the components in the additive has a major influence on the evolution of the microstructure. In case of yttria and alumina additives, with decreasing ratio of Y_2O_3 to Al_2O_3, the microstructure becomes finer with a lower aspect ratio [102].

During sintering, the amount and composition of the additives may be changed due to interaction with the atmosphere. Using nitrogen alumina can be partially reacted to AlN, which is very easily dissolved in the Si_3N_4 lattice causing a shift of the liquid phase composition and the structural properties of the Si_3N_4 ceramics. At high sintering temperatures, the alkali and alkaline-earth oxides are unstable and evaporate. On the other hand, rare-earth oxides are more stable than the other additives [103, 104], and even during long sintering times no change in their concentration has been found.

Often small deviations in compositions cause pronounced variations in effectiveness. For instances, two different Si_3N_4/additive mixtures was sintered, where additive formulated based on an addition of 15 wt.% of additives from the Li_2O-Y_2O_3 system (Table 12). The first additive was lithia + yttria (molar ratio 1:1) and the second was $LiYO_2$ as the sole additive.

Table 12. Chemical composition of the starting materials (wt.%).

Mixture	*Si_3N_4*	*Li_2O*	*Y_2O_3*	*$LiYO_2$*
M1	90	1.11	8.89	-
M2	90	-	-	10

The values of relative density and weight loss for selected compositions are shown in Fig. 21. The relative densities increase for all sintered samples and for all selected temperatures. Samples with $LiYO_2$ addition show higher densities than samples with Li_2O + Y_2O_3 additions. For sintered Si_3N_4 with addition a $YAlO_2$ and Y_2O_3 + Al_2O_3 has been reported similar behavior in the literature [9]. In contrast, the weight loss is lower for sintered bodies from additive with Li_2O + Y_2O_3.

The same trend is obtained for samples sintered at 1600 °C for different soaking time. The density increases for both types of additive, but it are more emphasized in case of M2 composition (Table 13). After 4 h of sintering, a sintered density of 95% and 91% of the theoretical density are achieved for M2 and M1 composition, respectively.

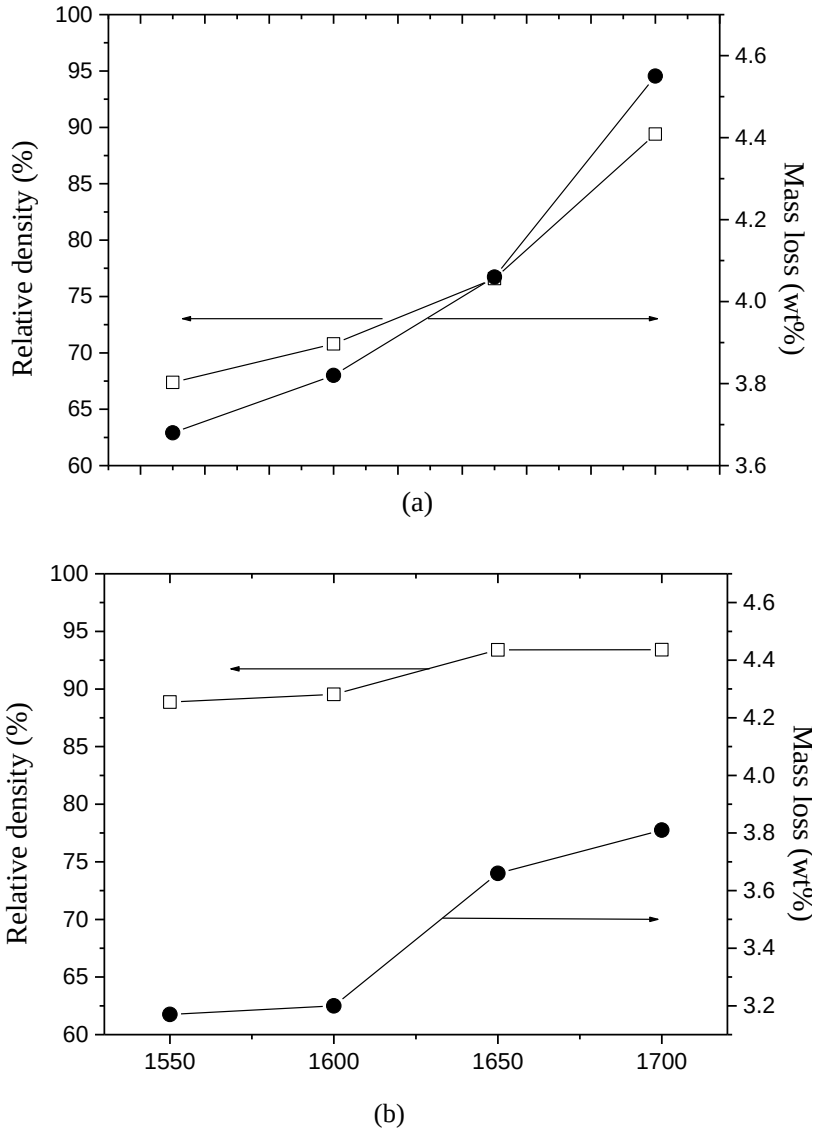

Figure 21. Plot of relative density and mass loss versus temperature for pressureless sintered Si_3N_4 with 10 wt% of: (a) LiO_2-Y_2O_3 and (b) $LiYO_2$. The soaking time at the temperature indicated was 5 min.

Table 13. Densities after sintering at 1600 °C with 10% of M1 and M2 composition (TD-theoretical density).

Time (min)	***M1 composition Li_2O + Y_2O_3 additive***	***M2 composition $LiYO_2$ additive***
	Density (TD)	*Density (TD)*
60	83	90
120	89	93
240	91	95

Fig. 22. shows the temperature dependence of shrinkage ($\Delta L/L_o$). The curves have nearly pan-parallel shape, which indicates that the same densification stages occur during heating, but the lengths change is more pronounced in samples from mixture M2.

The transformation of α-Si_3N_4 to β- Si_3N_4 evolves with sintering temperatures. The ratio β/(α+β) was determined by XRD and is shown in Fig. 23. At lower sintering temperatures, the amount of phase transformation is slightly higher for samples made from the M1 mixture. At 1700

°C, however, the α→β transformation is completed in the $LiYO_2$ system, while in case of the mixture ($Li_2O+Y_2O_3$), a small amount of α-Si_3N_4 (3 wt%) still remains.

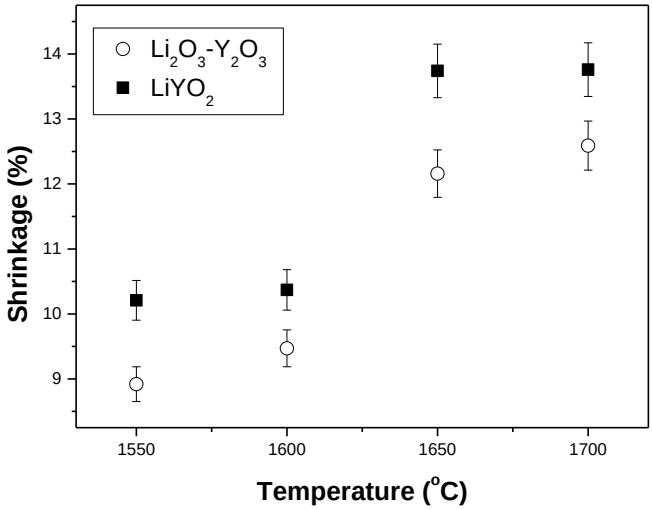

Figure 22. Linear shrinkage of Si_3N_4 green compacts with 10% of additive (■-$LiYO_2$, ○-Li_2O-Y_2O_3) after heat-treatment at 1550-1700 °C for 5 min.

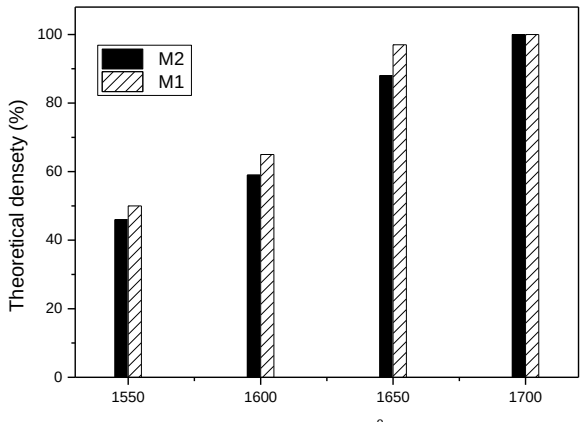

Figure 23. Evolution of β phase as a function of the sintering temperatures.

Different microstructures of the sintered bodies are obtained for the two different compositions (M1 and M2). The material produced from composition M2 has a finer-grained microstructure with lower aspect ratios compared to the sintered bodies prepared from composition M1 (Fig. 24).

As mentioned, sintering additives determine the temperature of the onset of liquid formation and rate of densification during pressureless sintering. They also have an influence on the morphology of Si_3N_4 grains and on the grain boundary phase. The additives used in this study cause eutectic temperatures of 1255 °C for the pure Li_2O-SiO_2 and 1650 °C for SiO_2-Y_2O_3 oxide system [10, 11] respectively. In the Li_2O-Y_2O_3 system, there is only one compound, $LiYO_2$, which is stable up to 1880 °C [12]. The lowest liquidus temperature in the $LiYO_2$-SiO_2 system is 1350 °C [12]. In this respect, there is a difference in using these two systems (M1, M2) during liquid phase sintering of Si_3N_4. In spite of the lower melting point in Si_3N_4/ additive M1, the degree of densification is higher in the system Si_3N_4/additive M2. This behavior is should to be related with the formation of liquids with different amounts of Li_2O and Y_2O_3 in composition M1. The Li_2O-rich liquid enhances the local densification, while the Y_2O_3-rich liquid hinders local densification. Deviation from the equimolarity of the additive components leads to a lower degree of densification. In case of the composition M2,

there is no deviation from the equimolarity of Li_2O and Y_2O_3 in the liquid phase which is consequently more homogeneous.

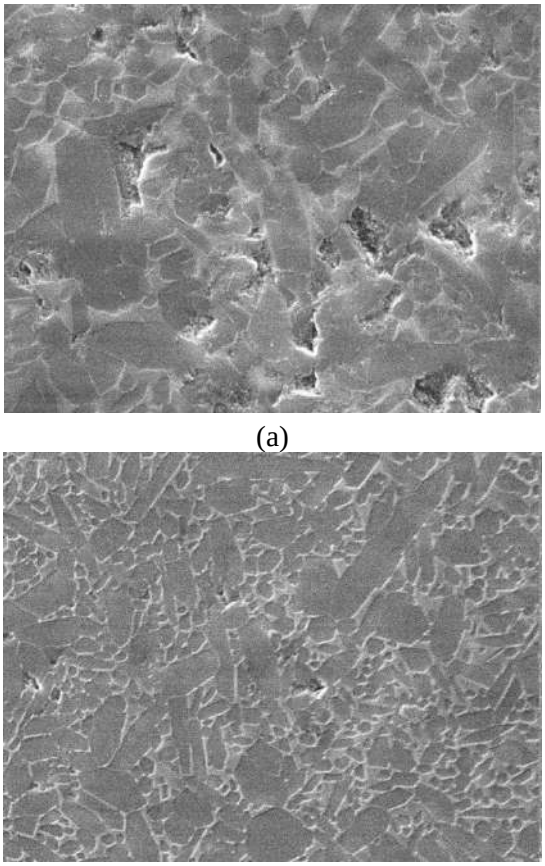

(a)

(b)

Figure 24. SEM micrographs of pressureless sintered material at 1600 °C for 4 h with additives of (a) composition M1, (b) composition M2.

The difference in densification behavior, as well as the higher weight loss of Si_3N_4 with the composition M1, as compared to composition M2, can be explained by referring to the different vapor pressures of the additive systems. The vapor pressure of Li_2O soon reaches high values upon increasing the temperature (10^{-1} Pa at 1300 °C, 1 Pa at 1500 °C and 10 Pa at 1600 °C) [13]. Li_2O is removed in gaseous form from the specimens at temperatures below 1600°C. Consequently, vaporization of Li_2O changes the composition of the liquid during heating in the Si_3N_4-Li_2O-Y_2O_3 system. Since the vapor pressure of $LiYO_2$ is lower in comparison to compared to Li_2O, differences in densification behavior and weight loss that are obvious from figure 1 become understandable.

However, in contrast to the densification behavior, the α–Si_3N_4 to β–Si_3N_4 phase transformation is more pronounced in the case of composition M1. With composition M1, Li_2O-rich liquid reduces local the viscosity which leads to the dissolution of some Si_3N_4 into the liquid and enhances the phase transformation. With increasing temperature the viscosity of the liquid phase is decreased resulting in a faster solution-diffusion-precipitation process. In case of composition M2, the improved homogeneity of the liquid leads to a sluggish but complete β- Si_3N_4 transformation.

Inhomogenity of liquid phase results in some residual porosity that is distributed within material sintered with the additive of composition M1 (Figure 2.6.4(a). This is due to evaporation of the Li_2O-rich liquid. In contrast, samples prepared from composition M2 have a homogeneaus distribution of elongated β-grains without porosity.

Results show that $LiYO_2$ has a more beneficial effect on sintering than the Li_2O + Y_2O_3 mixture. Using $LiYO_2$ as sintering additive leads to higher relative densities and to less weight loss, as compared to samples sintered with a Li_2O + Y_2O_3 mixture. Also, the α to β-Si_3N_4 phase

transformation is completely in the system $Si_3N_4/LiYO_2$ additive. It leads to a rod-like microstructure, which has potential for good high temperature properties.

The difference in sintering behavior occurs because of the heterogeneity of the liquid phase formed in the $Li_2O + Y_2O_3$ mixture-containg samples.

2.5 Liquid phase sintering of silicon nitride

Many manufacturing techniques such as pressureless sintering, gas-pressures sintering, hot-pressing and hot-isostatic pressing, which are employed for obtaining dense Si_3N_4 bodies, are related to liquid-phase sintering. The sintering behaviour of Si_3N_4 ceramics is affected directly by the characteristics of the liquid phase present. If the liquid fulfills the conditions of good wettability and solubility of Si_3N_4, densification can be described according to the standard mechanisms of liquid phase sintering: particle rearrangement, solution-precipitation and particle coalescence (or grain growth). During the sintering of α-Si_3N_4, the phase transformation to β-Si_3N_4 is an additional phenomenon interrelated with this sequence.

2.6 Densification

The densification of Si_3N_4 is negligible before the formation of the liquid. Once the liquid is formed, densification takes place through particle rearrangement, due to capillary forces as detailed above. The extent of particle rearrangement is mainly dependent on the size and shape of particles and amount and viscosity of the liquid phase. The rearrangement process ceases when interparticle contacts are formed that prevents the system from further densification. After formation of the particle bridges, however, the solution-precipitation process starts resulting in the collapse of the bridging. This leads to densification by secondary rearrangement and center-to-center approach [62]. The driving forces for the second stage are the higher solubility at the contact points of the particles and the differences in the chemical potentials between small and large particles, that lead to dissolution of small particles and precipitation of matter on the surface of larger particles.

There are two possible rate controlling steps during solution-precipitation, namely surface reaction and solute diffusion [77]. Which process would be dominant can be decided if the activation energies are obtained from the reaction kinetics. In case of the surface reaction, the activation energy ranges from 290 to 435 kJ/mol. This value matches the Si-N bond energy [78]. For the solute diffusion mechanism, the reaction activation energy lies in the range of 580-730 kJ/mol. These values correspond to the energies of Si diffusion in various silicate glasses [79]. In addition, the reaction is not sensitive to changes in either the liquid composition or the liquid content for the surface reaction controlled mechanism when compared to the solute diffusion mechanism.

2.6.1. Densification temperature

Identifying the liquid forming regions for powder compacts of the systems Si_3N_4-additive is quite complicated due to the presence of variable amounts of SiO_2, which is an inherent component of Si_3N_4 powders. In order to optimize the Si_3N_4-additive material system, a series of dilatometric tests has to be performed.

In this chapter it was demonstrated the densification of Si_3N_4 bodies in case of different additives.

According to the ternary diagrams for the Li_2O-Y_2O_3-SiO_2 [140] and Li_2O-Al_2O_3-SiO_2 [141], systems, the nominal eutectic temperature is 1350 °C in both cases. However, due to the dissolution of Si_3N_4 into the liquid phase, the overall liquid forming temperature is expected to be lower than the nominal eutectic temperature.

2.6.2 Si_3N_4-$LiYO_2$-SiO_2 system

The dilatometric data (Fig. 25) show that shrinkage first occurs at 1200 °C and becomes rapid at 1275 °C in the case of samples with 15 and 20 wt% of $LiYO_2$ additive. In case of samples with lower additive contents (5 and 10 wt%) the onset of shrinkage is retarded and its magnitude is much reduced. The onset of shrinkage can be related to liquid formation in the samples. This is in response

to the melting point in the Li_2O-SiO_2 system (1255 °C) [142]. The shrinkage accelerates when enough liquid phase for efficient densification by particle rearrangement has been formed.
Fig. 26 shows the effect of additive content on the linear shrinkage of the samples after heating to 1500 °C in dilatometer experiments. More liquid is formed as the amount of additive is increased. The maximum linear shrinkage of 11.9 % is obtained for 20 wt% of additive.

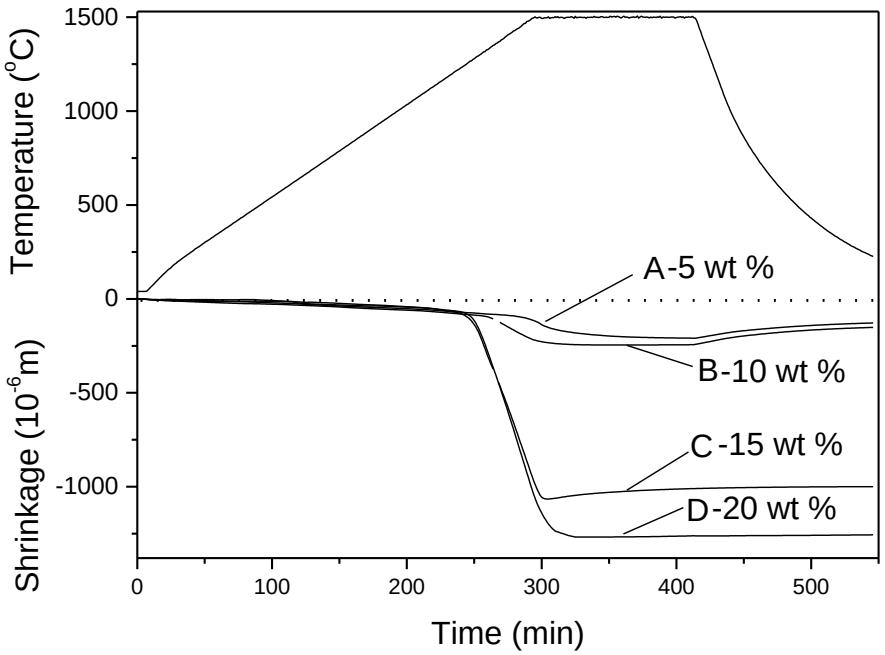

Figure 25. Length change of Si_3N_4 green bodies (A-5 wt.%, B-10 wt.%, C-15 wt.%, D-20 wt.% of $LiYO_2$) between room temperature and 1500 °C. A cylinder-shaped test body was examined by dilatometry in nitrogen atmosphere.

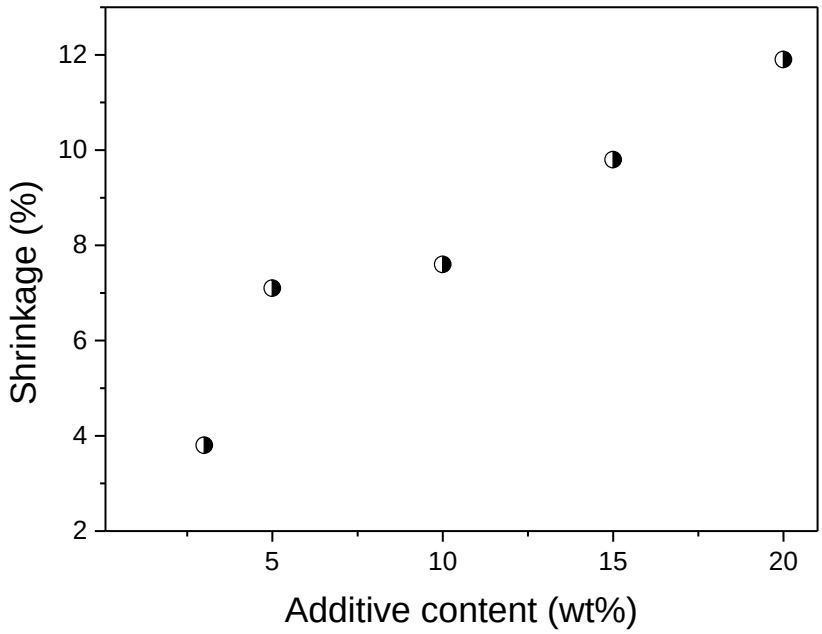

Figure 26. Linear shrinkage versus additive content in dilatometer experiments, after a holding time of 5 min at 1500 °C.

The presence of Li_2O in the liquid leads to lower melting point and a less viscous liquid phase at a given temperature, which allows faster transport of material through the melt. The redistribution

of the liquid and the filling of pores is also facilitated. This allows high density values to be reached at relatively low temperatures (Fig. 27). The density of samples with 15 wt% of additive is 2.84 g/cm^3 at 1300 °C and more than 2.95 g/cm^3 at 1350°C. With prolonged heating time, differences in the degree of densification become smaller. The increment in the sintered density likewise diminishes with increased quantity of additives (Fig. 28).

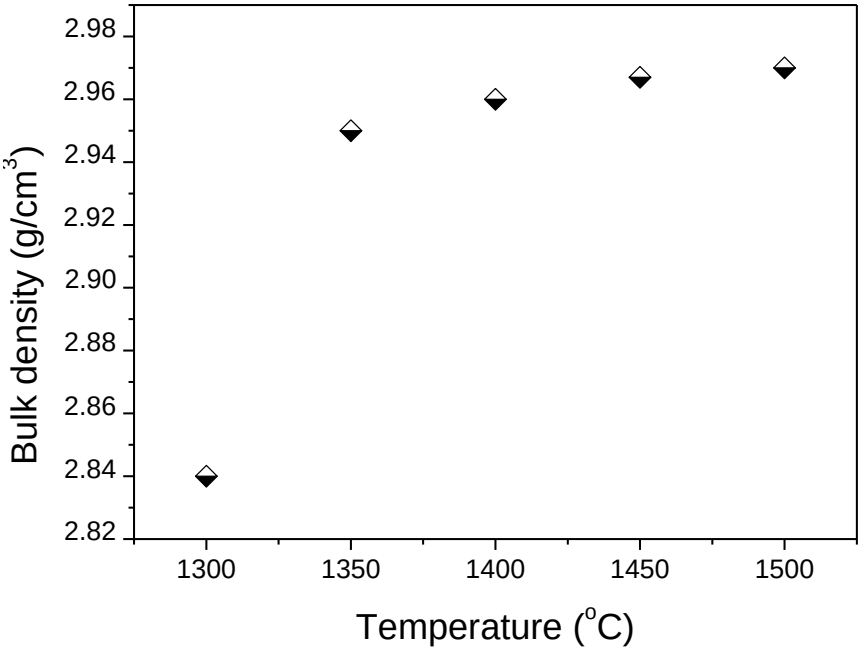

Figure 27. Density according to dilatometric measurements of Si_3N_4 with 15 wt% of $LiYO_2$ additive after a holding time of 5 min at the temperatures indicated.

The densification of Si_3N_4 ceramics is enhanced by increasing the liquid content and decreasing the liquid viscosity. The higher the $LiYO_2$ additive content in the liquid, the higher the oxygen content and therefore the lower the viscosity of liquid phase. On the other hand, dissolution of some Si_3N_4 into the liquid increases the viscosity of silicon-oxynitride glasses due to increasing nitrogen content. This also influences the shrinkage rate during densification.

The results show that all materials were not fully dense after dilatometric measurements up to 1500 °C. The best results were obtained for samples with 15 or 20 wt.% of additive. In view of the materials' properties that can be expected, 15 wt.% additive content may be considered as an auspicious compromise.

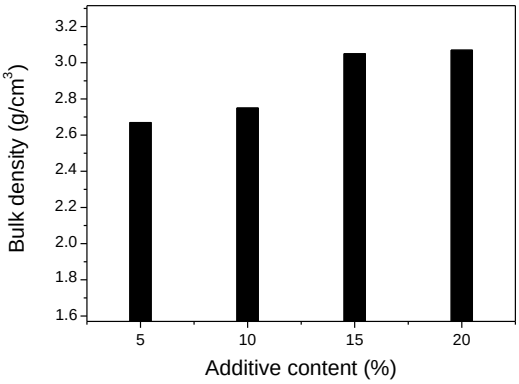

Fig. 28. Influence of the amount of $LiYO_2$ on the densification of Si_3N_4 samples fired at 1500 °C with a holding a time of 5 min.

The change in length and rate of shrinkage are shown in Fig. 74 (a) and (b) respectively. It can be seen that the shrinkage curve has a sigmoidal shape. As mentioned earlier, shrinkage starts at about 1200 °C and proceeds rapidly above 1275 °C. The shrinkage continues during the first 30 min of isothermal annealing at 1500°C, after which a plateau is reached. The total linear shrinkage is about 11% immediately after reaching 1500 °C and 12.5% after annealing for 2 h at this temperature.

The shrinkage velocity curve shows three maxima at 1275 °C, 1364 °C and 1453 °C (points 2 to 4). The appearance of the liquid in the sample starts at 1180 °C (point 1). Point 1 agrees with the melting temperature in the Li_2O-SiO_2 system [142]. The maximum at 1275 °C (point 2) is related to an increasing amount of liquid phase, which surrounds the silicon nitride particles completely, favoring grain rearrangement [143]. The XRD pattern of the sample quenched at this temperature shows crystalline yttrium-silicon oxynitride $Y_5(SiO_4)_3N$ ("N–apatite") and lithium-silicon oxynitride (LiSiNO) phases, which indicates the dissolution of some Si_3N_4 into the liquid (Table 20). This confirms that $LiYO_2$ acts as a very good flux and a solvent for Si_3N_4 that is also a prerequisite for a good sintering additive [144].

2.6.3 Sintering density

Nonisothermal sintering experiments up to 1500 °C shows that the relative densities reached are still too low for high mechanical strength and hardness. In order to further increase the density to above 95%, densification was conducted at different temperatures from 1550 °C to 1700 °C with 50 K intervals for different holding times.

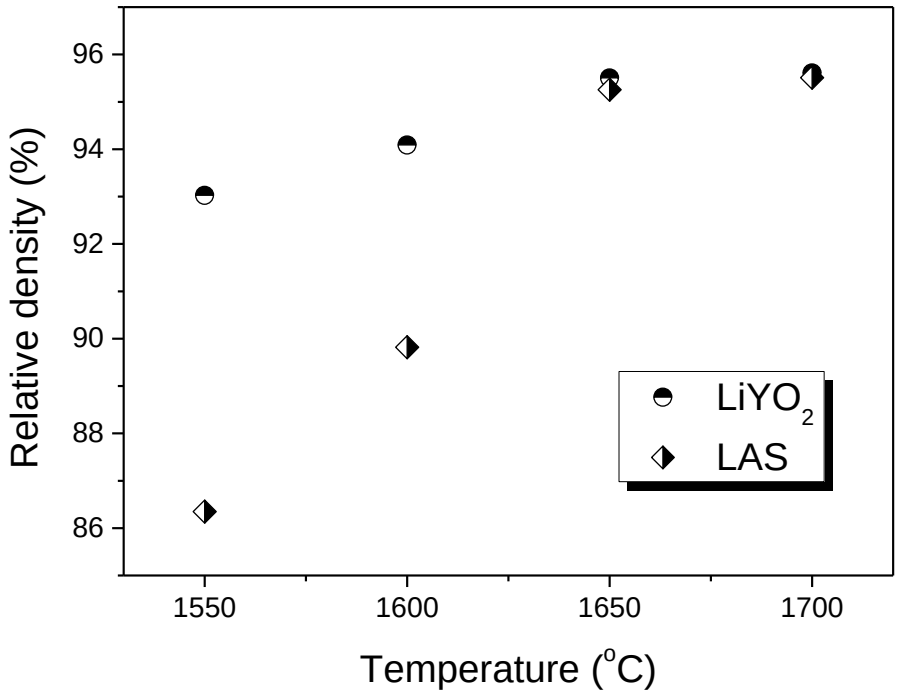

Figure 29. The difference in the densification behavior between Si_3N_4-$LiYO_2$ and Si_3N_4-$LiAlSiO_4$ ceramics with 15% of additive sintered at different temperatures from 1500°C up to 1700°C with a holding time of 5 min.

The influence of temperature on densification during sintering at higher temperatures for very short annealing time (5 min) is given in Fig. 29. At lower temperatures densification is more pronounced for bodies sintered with $LiYO_2$ additive. The densification increases monotonically with increasing temperature. In the case of $LiAlSiO_4$ additive, with increasing temperature the increment between the density values gets higher until 1650 °C. At 1700 °C, > 95% of the theoretical density are obtained with both additive systems.

The densification behavior at 1500 °C as a function of annealing time is shown for the Si_3N_4-$LiYO_2$ and Si_3N_4-$LiAlSiO_4$ systems in Fig. 30 and Fig. 31, respectively.

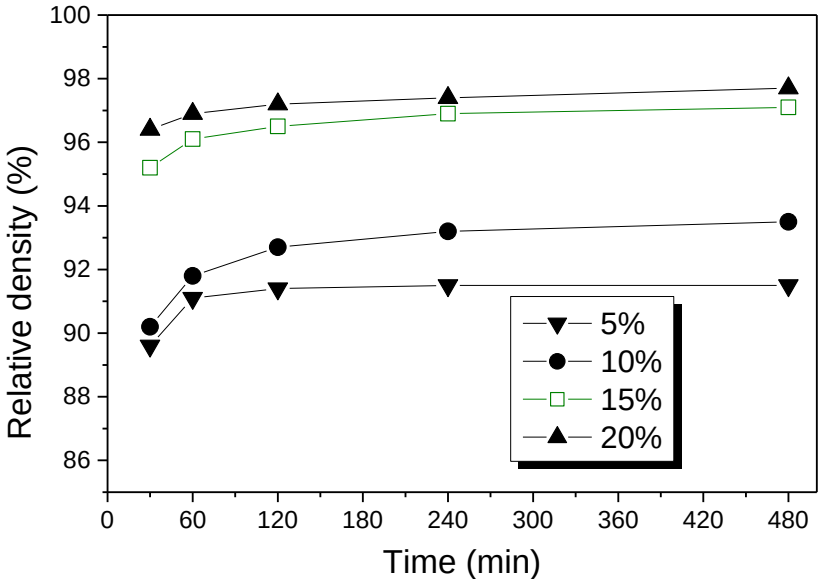

Figure 30. Relative densities at 1500 °C *vs.* annealing time for Si_3N_4 with $LiYO_2$ additives (5, 10, 15 and 20%).

At 1500 °C, densification is higher by nearly 2% with the $LiYO_2$ additive when compared to $LiASiO_4$. In the case of $LiYO_2$, the maximum density is obtained for bodies having higher additive content, while in the case of $LiAlSiO_4$ additive, the densification is nearly the same for bodies with 10 and 15% of additives. The difference in densification versus additive content is more pronounced in the $LiYO_2$ additive system.

The relationships between relative density and sintering temperature for the compositions with different amounts of additives are listed in Table 14 and Table 15, respectively.

In case of bodies with at least 15 wt% of $LiYO_2$ additive, high relative densities are obtained after just 2 h of sintering, while the densities remain nearly constant upon prolonged sintering. However, all samples sintered at higher temperature and longer annealing times show the same trend of decreasing density. The samples sintered at 1550 °C were found to exhibit higher densities in comparison with samples sintered at 1600 °C and 1650 °C.

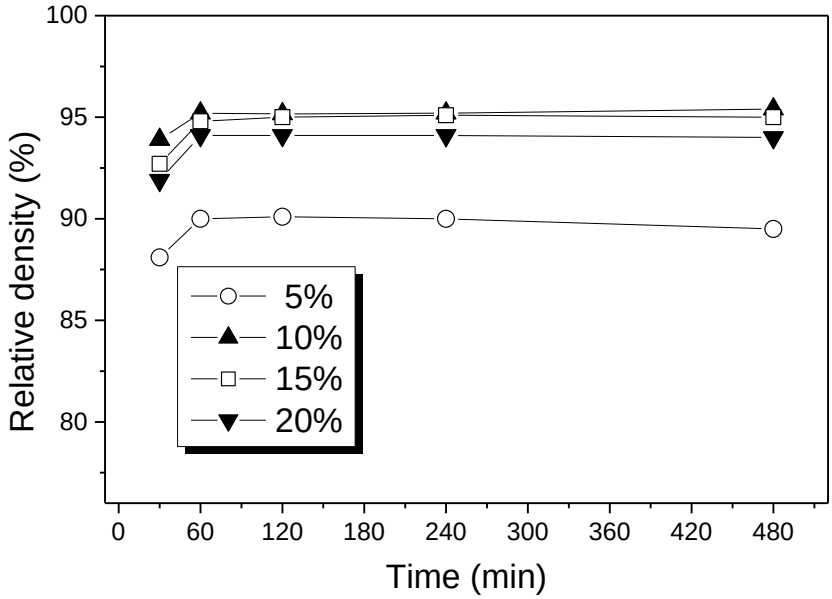

Figure 31. Relative densities at 1500 °C *vs.* anealing time for Si_3N_4 with $LiAlSiO_4$ additives (5, 10, 15 and 20%).

Higher relative density obtained at lower sintering temperatures may be attributed to the lower partial pressure of evaporating phases at these lower temperatures, especially with respect to lithia and silica. It has been noticed during dilatometric measurement that a significant mass loss occurred.

Table 14. Densities after sintering with different amounts of the $LiYO_2$ additive.

Additive content (wt.%)	*1550 ℃*			*1600 ℃*			*1650 ℃*		
	2 h	*4 h*	*8 h*	*2 h*	*4 h*	*8 h*	*2 h*	*4 h*	*8 h*
5	88.7	88.95	88.1	88.5	88.2	87.8	88.1	80.0	79.6
10	94.9	95.1	95.0	95.2	94.9	94.2	93.7	93.1	92.4
15	98.3	98.3	98.3	98.3	98.1	97.2	98.3	97.8	97.5
20	98.3	98.2	98.3	98.3	97.8	97.8	98.2	97.6	97.5

As shown in Fig. 32, Li_2O starts to evaporate from the samples at temperatures above 1300 °C and the Li concentration is drastically reduced after holding times of several hours at 1500 °C. After 8 h, the residual Li_2O content is as small as 0.08 wt%. This is in good agreement with published data [147] for the vapor pressure of Li_2O and its evaporation at higher temperatures. In contrast, Y_2O_3 is very stable based on thermodynamic calculations [148] and has no tendency for volatilization under the conditions investigated. Therefore, it can be concluded that Li_2O is removed in gaseous form during sintering, changing the liquid to a comparatively high-melting, Y_2O_3-rich composition. The lowest melting temperature in the system Y_2O_3-SiO_2 is 1650 °C [98]. Thus the liquid phase is mostly transient and this must have a marked influence on the kinetics of densification and phase transformations in the system studied.

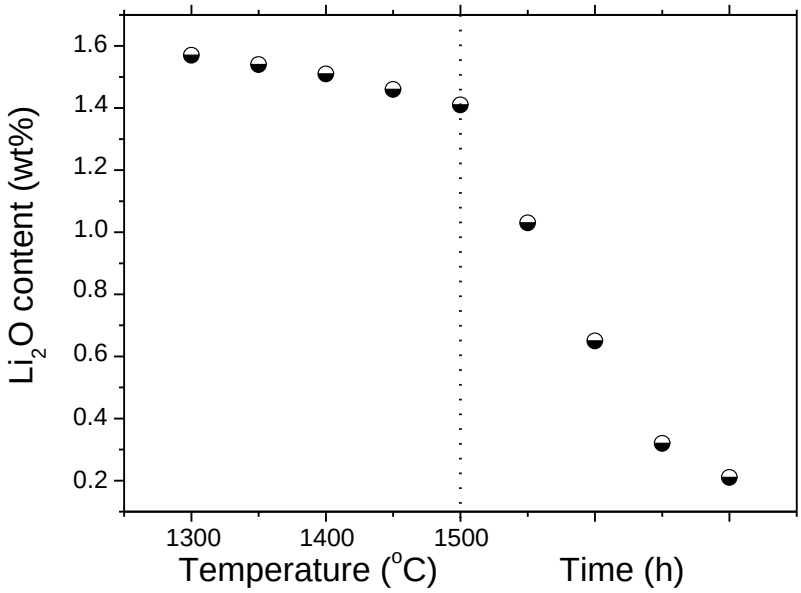

Figure 32. Lithia losses of Si_3N_4 compacts with 15 wt.% of $LiYO_2$ additive during dilatometric measurement and upon prolonged annealing time at 1500 °C.

In case of $LiAlSiO_4$ additive, the samples sintered with lower additive content exhibit higher densities in comparison with samples containing more additive. The highest value of 98.3% for the density is obtained for bodies with 10% additive content. The densities remain nearly constant on prolonged sintering at all sintering temperatures.

According to XRD patterns, at 1500 °C all of the $LiAlSiO_4$ additive is converted into liquid. The liquid phase formed in the $LiYO_2$ additive system contains less silica and hence, it is thermodynamically more stable than the liquid phase in the $LiAlSiO_4$ system which contains a substantial amount of silica.

Table 15. Densities after sintering with different amounts of the $LiAlSiO_4$ additive.

Additive content (wt.%)	*1550 ℃*			*1600 ℃*			*1650 ℃*		
	2 h	*4 h*	*8 h*	*2 h*	*4 h*	*8 h*	*2 h*	*4 h*	*8 h*
5	90.1	89.7	89.4	89.5	89.2	89.0	89.1	88.8	87.9
10	98.3	98.3	98.3	98.3	98.1	98.1	98.1	97.7	97.5
15	98.3	98.3	98.1	98.3	97.9	97.2	97.4	97.2	96.8
20	93.6	92.7	92.4	93.0	92.3	92.0	92.3	91.5	91.2

In other words, a larger amount of the liquid phase in the $LiAlSiO_4$ system leads to more evaporation according to the reaction:

$$Si_3N_4\ (s) + 3\ SiO_2\ (l) = 6\ SiO\ (g) + 2\ N_2\ (g) \qquad (2.4)$$

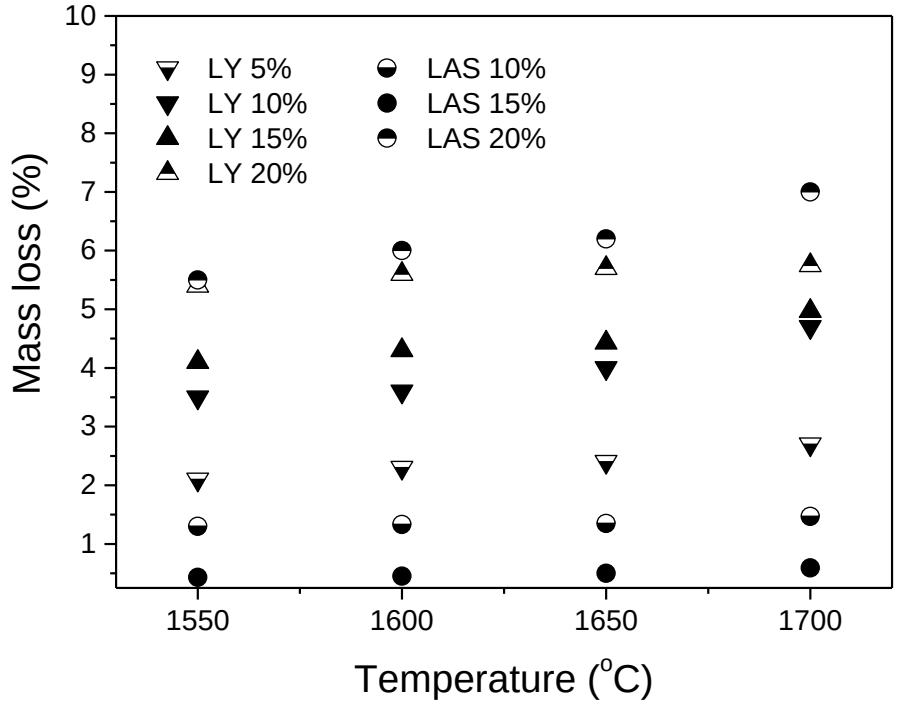

Figure 33. Mass loss as a function of temperature for Si_3N_4 compacts with different amounts of $LiYO_2$ and $LiAlSiO_4$ additives during sintering with a holding time of 5 min.

High mass loss is harmful to sintering, which is reflected in the observation that the density of samples having 20% of additive is always smaller than densities of bodies with 10 and 15% of additive.

The mass loss upon sintering with the $LiAlSiO_4$ additive system in comparison to the $LiYO_2$ system is shown in Fig. 33. The same trend is also observed during isothermal annealing (Fig. 34).

Reactions between Si_3N_4 and the glassy phases are responsible for the instability of Si_3N_4 ceramics at elevated temperature. However, Al_2O_3 and Y_2O_3 are stable based on thermodynamic calculations [148]. In contrast, the high vapor pressure of lithia causes its easy evaporation as mentioned earlier. It is expected on the basis of the vapor pressure data for Li_2O [147] that lithia should volatilize completely at higher temperatures. However, the results of the chemical analysis of the samples are in contradiction with this assumption, especially for $LiAlSiO_4$.

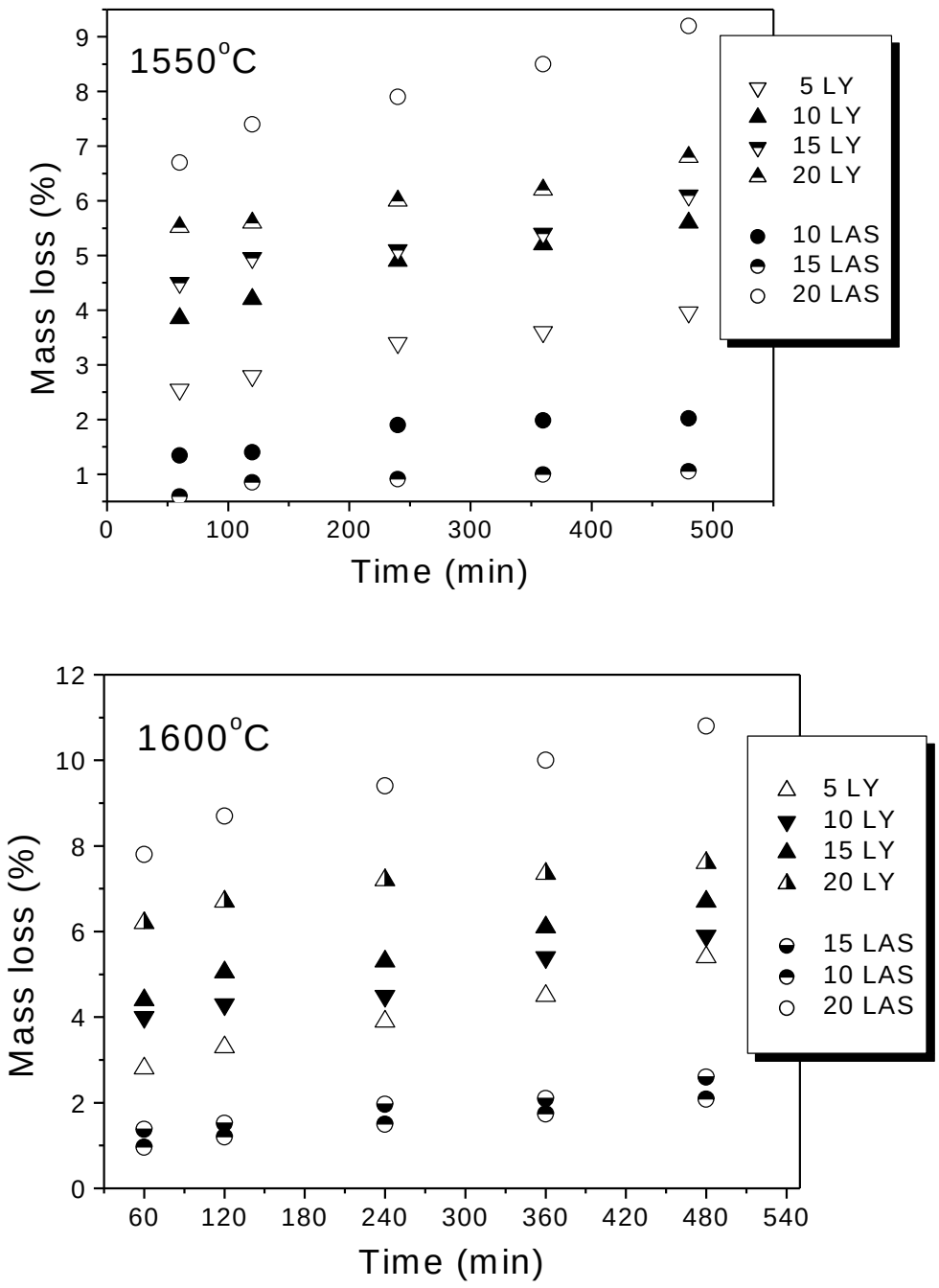

Figure 34. Mass loss of Si_3N_4 ceramics with the additive systems $LiYO_2$ (LY) and $LiAlSiO_4$ (LAS), heat-treated at 1550 °C and 1600 °C under 0.1 MPa N_2 as a function of soaking time.

The content of lithium in the Si_3N_4 ceramics sintered for 4 h at various temperatures is indicated in Fig. 35. The lithium content in the samples changes slightly in the case of the $LiAlSiO_4$ additive. However, with the $LiYO_2$ additive the lithium content decreases significantly with temperature.

On the basis of these findings, it can be concluded that the major part of the mass loss of the Si_3N_4 ceramics during sintering occurs according to the reaction (2.4), as mentioned before. This reaction is well known from thermodynamical and experimental work on the Si-N-O system [149, 150]. Since the silica content in the liquid phase is higher with the $LiAlSiO_4$ additive than with the $LiYO_2$ additive, the rate of the decomposition reaction (2.4) is faster and consequently the mass loss is high for samples having 20% of additives. Additionally for higher additive amounts, gas bubbling

occurs caused by an increased formation of gaseous SiO [101]. This is the case with the $LiAlSiO_4$ additive which has a higher oxygen content than the $LiYO_2$ additive.

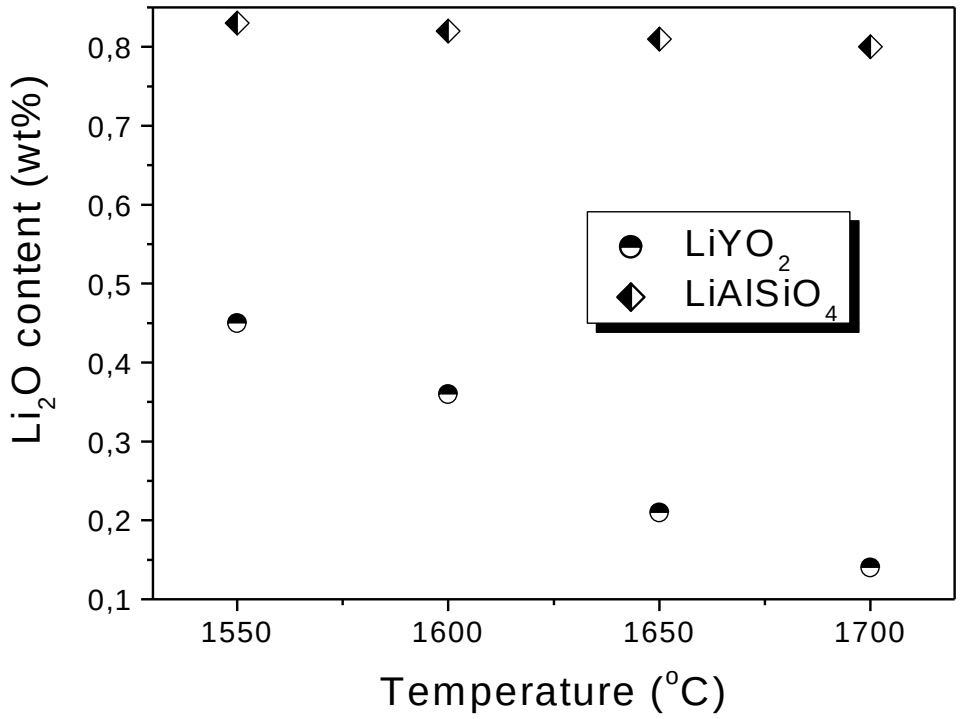

Figure 35. Mass loss of lithium in Si_3N_4 samples sintered at various temperatures.

2.6.4 Mg-exchange Zeolite Additive

The other example is magnesium alumosilicate (MgAS). Since melting temperatures are relatively low in the magnesium alumosilicate (MgAS) system, suitable sintering additives may be expected to exist in this system. Moreover, most $MgO–Al_2O_3–SiO_2$ glasses can be crystallized under proper heat treatment conditions [6], which may allow ceramics with favorable thermo-mechanical properties to be obtained in spite of the low sintering temperatures. Magnesium aluminum silicates (MgAS) have already been used for sintering of Si_3N_4 ceramics. The procedure described in [7] consisted of a mixture of MgO, Al_2O_3 and SiO_2, which then reacted with silica on the surface of Si_3N_4 to form MgAS liquid. In comparison, several advantages are expected if pre-reacted MgAS is used directly, such as smaller susceptibility to hydrolysis, lower vapor pressure of MgO at high temperature, and less problems with the homogeneity of the powder mixtures. MgAS compositions were successfully used as binders for silicon carbide fibers and in the matrix of silicon carbide-titania composites [8]. MgAS can be prepared from different sources, but the synthesis route used in the present study, which starts from ion-exchanged zeolites, has some benefits [9]. For example, it is a low-cost method leading to an amorphous phase with enhanced chemical reactivity as compared to crystalline phases. While one report on the use of an ion-exchanged barium- and lithium zeolite as a constituent of Si_3N_4 composite materials can be found in the literature [10,11], it seems that no work has been performed to-date on the pressureless sintering of Si_3N_4 with Mg-exchanged zeolite additives.

The onset of shrinkage is assumed to be related to liquid formation in the compacts. Dilatometric data (Fig. 36 and Fig. 37) show the shrinkage and shrinkage velocity. The maximum at 851 °C (point 1) is related to collapse of Mg-zeolite structure. The shrinkage first occurs at 1070 °C and accelerates somewhat at 1170 °C. However it increases dramatically at 1500 °C and levels off at 1500 °C after 55 and 40 min of isothermal annealing for samples with 10 and 30 wt.% of additives, respectively.

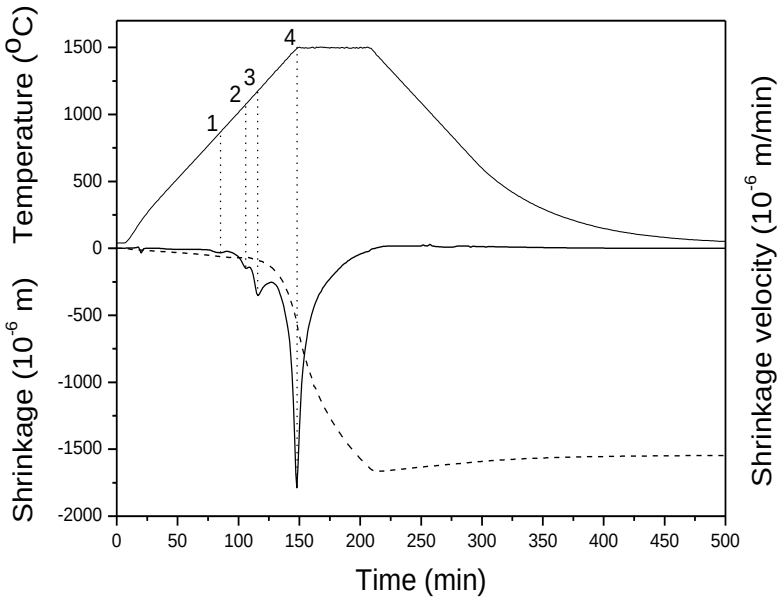

Figure 36. Shrinkage (full line) and shrinkage velocity (dashed line) of a silicon nitride green body with 10% MgAS additive showing characteristic features at (1) 851°C, (2) 1070 °C; (3) 1169 °C and (4) 1500 °C.

The phase evolution of samples with 10 wt.% of MgAS additive after heat treatments at temperatures between 900° and 1500°C for 5 min is shown in Fig. 38. The main crystalline phase is α–Si_3N_4 for all stages of annealing. At 900°C the initial MgAS sintering additive is present in an amorphous state due to collapse of Mg-zeolite structure at 850 °C. At 1300 °C the β–Si_3N_4 has completely disappeared indicating its dissolution into the liquid phase. Thus, resulting liquid belongs to Mg-Al-Si-N-O system. Also, the presence of a new phase (SiO_2) is associated with excess silica, which had crystallized from the liquid during cooling.

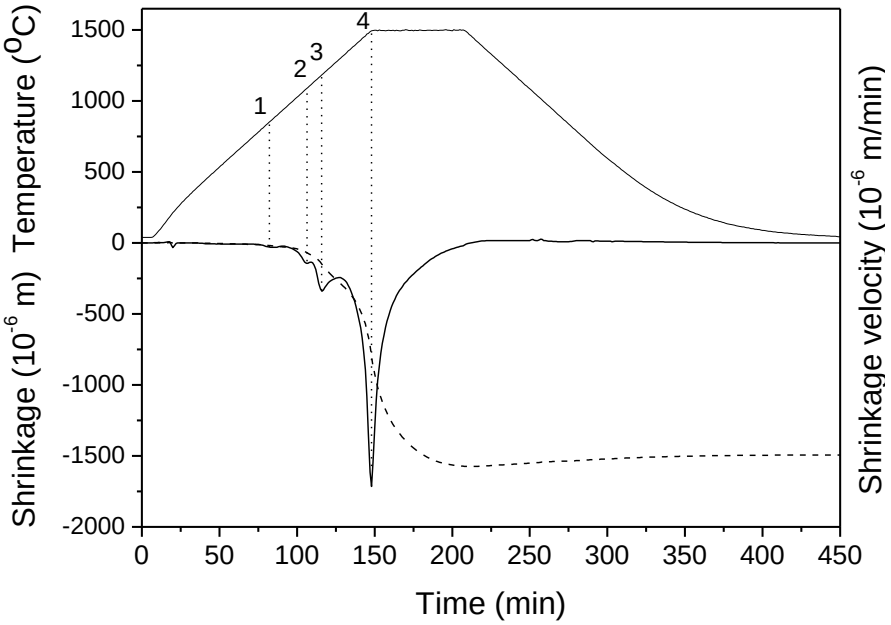

Figure 37. Shrinkage (full line) and shrinkage velocity (dashed line) of a silicon nitride green body with 30% MgAS additive showing characteristic features at (1) 850 °C, (2) 1070 °C; (3) 1171 °C and (4) 1500 °C.

According to the phase diagram $MgO-Al_2O_3-SiO_2$ the lowest eutectic temperature in the system is 1345 °C [14]. However, the overall liquid forming temperature is lower than the nominal eutectic temperature because of the present nitrogen in the liquid phase. This confirms that MgAS acts as a very good solvent for Si_3N_4, which is also a prerequisite for a good sintering additive.

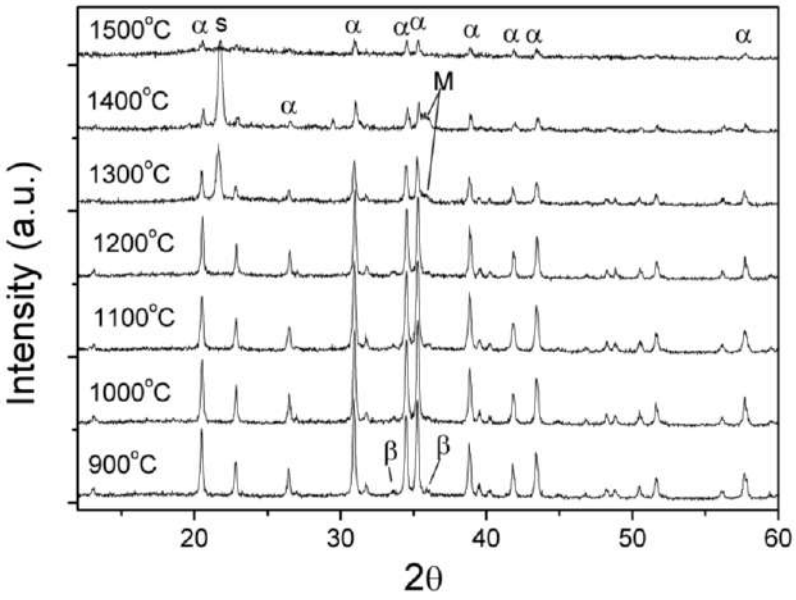

Figure 38. Phase evolution (α-Si_3N_3, β-Si_3N_3, S-SiO_2, M-Mg-Al-Si-N-O) during heating of mixture (Si_3N_4/MgAS) at different temperature for 5 min of soaking time.

XRD pattern shows remarkable decreasing of the diffraction lines intensities, which can be explained by the increasing of liquid amount. Therefore, the total liquid content increases substantially and at 1500 °C, which upon cooling formed amorphous glassy phase. At this temperature the crystalline α-Si_3N_4 phase, traces of silica as well as, oxynitride glassy phase are the only present phases. This phase compositions indicate that no significant transformation takes place up to 1500 °C. In the other side, having in mind that α–Si_3N_4 has a very high hardness as does magnesium silicon oxynitride glassy phase [2], the final ceramics might have promising mechanical properties in spite of the low sintering temperature.

2.6.5 General remarks

The three controlling stages: particle rearrangement, solution-precipitation and grain growth are observed in many Si_3N_4 systems [2]. The densification is controlled by particle rearrangement and by solution-diffusion-reprecipitation processes. Particle rearrangement contributes to densification at lower temperatures and solution-diffusion-reprecipitation is dominant at higher temperatures. For the $LiYO_2$ system, the densification depends largely on the sintering additive content. The larger amount of additive means a higher volume of liquid phase, which is favorable for efficient particle rearrangement resulting in the higher value of density. In case of the $LiAlSiO_4$ additive, it is found that the densification is less dependent on the additive content. Up to 1500 °C, densification is not accompanied by α→β Si_3N_4 transformation. Thus, the final density is thought to be reached largely without the intervention of the dissolution-diffusion-reprecipitation mechanism. This means that the overall sintering kinetics at low temperatures is less retarded when using the $LiYO_2$ additive in comparison to the $LiAlSiO_4$ additive, resulting in higher densities obtained at lower temperatures and short annealing times. With prolongated heating time, the differences in the degree of densification become smaller. It needs to be pointed out that the transport kinetics is also decisive for the phenomena of phase transformation and microstructural development.

In the case of MgAM additive onset of shrinkage first occurs at 1070 °C what is related to liquid formation in the mixture compacts. The used additive forms a liquid that acts as a very good

solvent for Si_3N_4 resulting in silicon oxynitride glassy phase which in turn allows decreasing the sintering temperatures at as low as 1500 °C.

2.6.6 Phase transformation

The α-Si_3N_4 phase is thermodynamically unstable during sintering (e.g. at 1400-2000 °C and 0.1 to 100 MPa N_2 pressure [2]) and shows a tendency to transform into the more stable β-Si_3N_4. The transformation is a reconstructive one [80]. This process involves the breaking and reforming of Si-N bonds. The nearest neighbour atoms remain the same in both the crystallographic forms [81]. The relations of α- and β-Si_3N_4 with α- and β-SiAlON are shown in Fig. 39. While the β→α-Si_3N_4 transformation has not been observed, the transformation between α- and β-Sialon is reversible [38].
Phase transformations play an important role for microstructural development. Different microstructures are possible depending on the location where reprecipitating of solute occurs. This location of reprecipitation can be either new β-nuclei generated by supersaturation [82] or the pre-existing β-grains, which coexist with the α-phase in the starting powders. If the raw powder contains a low concentration of β-grains, high supersaturation in the liquid phase

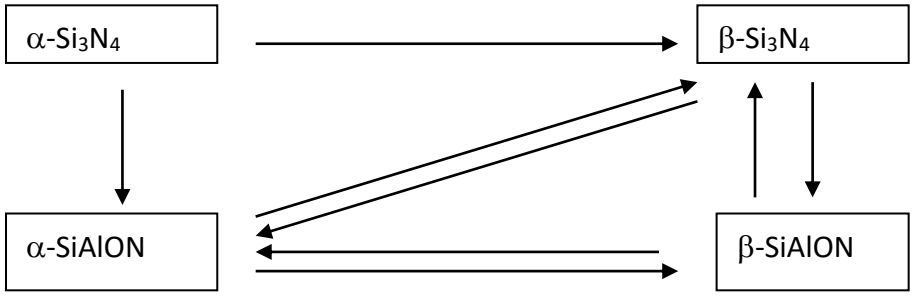

Figure 39. Phase transformation in Si_3N_4-Sialon-additive system.

The α→β phase transformation is a phenomenon which always occurs when α-Si_3N_4 containing powders will be liquid phase sintered. This process is substantially influenced not only by the amount but also by the chemistry of the liquid phase. It occurs by solution-diffusion-reprecipitation. Hence it is of great significance to describe this mechanism, which in turn has an impact on grain growth and microstructural development. It was shown that the various factors influencing the transformation, its kinetic and the relation of phase transformation to densification.

2.6.7 Temperature and time dependence

Fig. 40 shows the changes in β-Si_3N_4 phase content as a function of sintering temperature. With both additive systems, the time dependence of the α→β phase transformation displays a sigmoidal behaviour. However, the starting temperatures of the phase-transformation are significantly different for the two systems. With the $LiYO_2$ additive, the phase transformation already commences at 1300 °C although only a small amount of transformation is observed. For samples with 15 wt.% of additives, the transformation accelerates at 1500 °C and is terminated at 1700 °C after 5 min of annealing time.

In the case of the $LiAlSiO_4$ additive system the transformation starts at 1500 °C and increases only slightly with temperature (Fig. 40). The crystalline lithium aluminum silicate phase β-spodumene ($LiAlSiO_6$) remains stable as long as the temperature is lower than 1500 °C. In this stage, the liquid content is limited in the system. The β-spodumene phase, however, starts to dissolve into the liquid as the temperature exceeds 1500 °C. This increases the amount of liquid. The maximum degree of α→β-Si_3N_4 transformation for samples with 15 wt.% of additive was about 45% at 1700 °C after 5 min of sintering time.

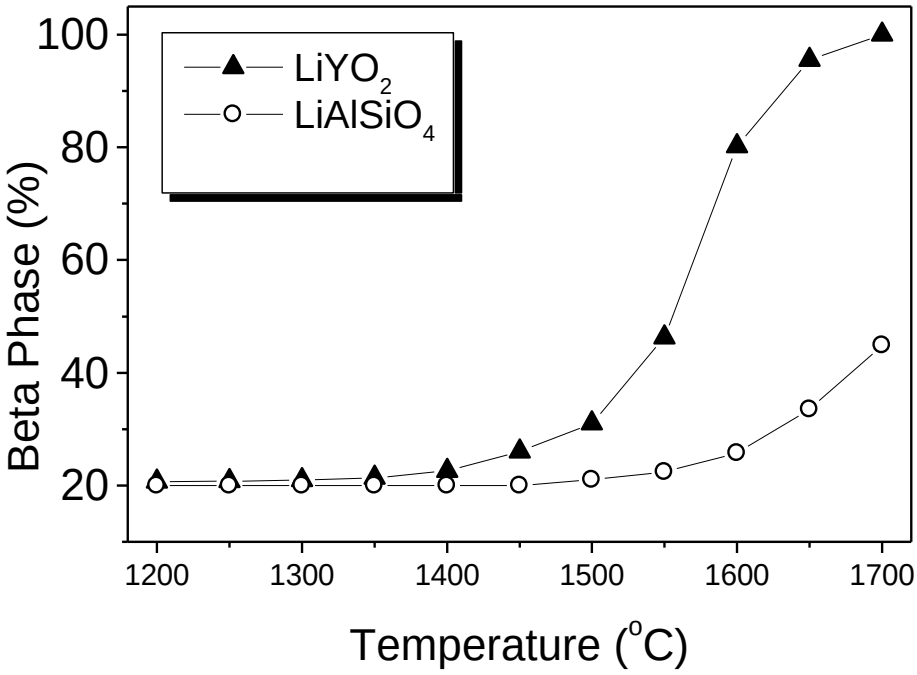

Figure 40. The α→β-Si_3N_4 phase transformation as a function of temperature in the Si_3N_4-$LiYO_2$ and Si_3N_4-$LiAlSiO_4$ systems for 5 min of annealing.

However, with prolongated annealing time the degree of phase transformation significantly increases in both cases (Fig. 41). With the $LiYO_2$ additive the phase transformation is finished at 1500 °C after 1 h of sintering, while the transformation from α-Si_3N_4 to β-Si_3N_4 is over after 8 h of annealing in the $LiAlSiO_4$-containing system (Fig. 42). It was found that a higher temperature of 1600 °C is necessary to convert all α-Si_3N_4 phase in case of using $LiAlSiO_4$ additive. The delayed phase transformation in the $LiAlSiO_4$-containing system suggests that phase transformation is sensitive to the liquid viscosity.

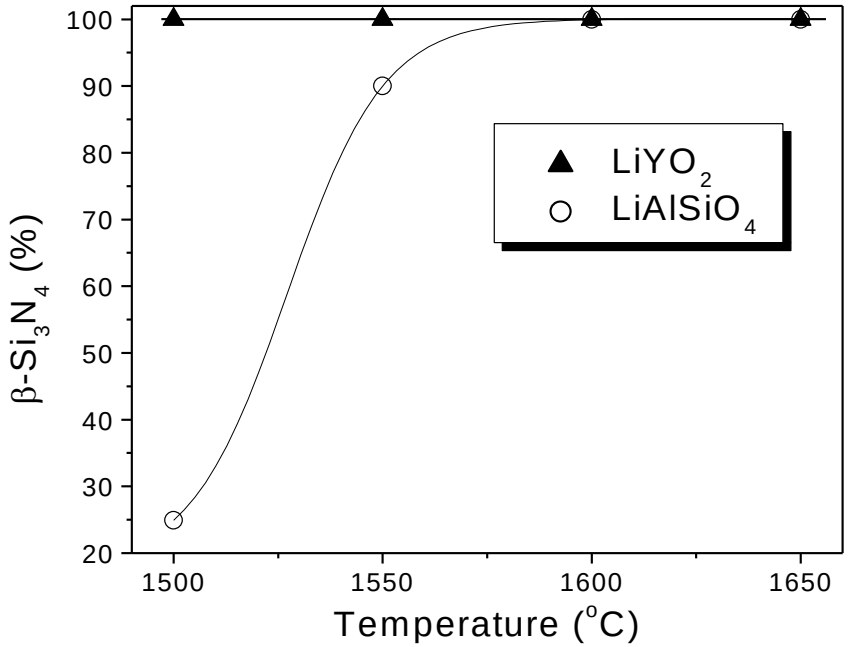

Figure 41. The phase transformation as a function of temperature in the Si_3N_4-$LiYO_2$ and the Si_3N_4-$LiAlSiO_4$ systems (15 wt.%) for 1 h of annealing.

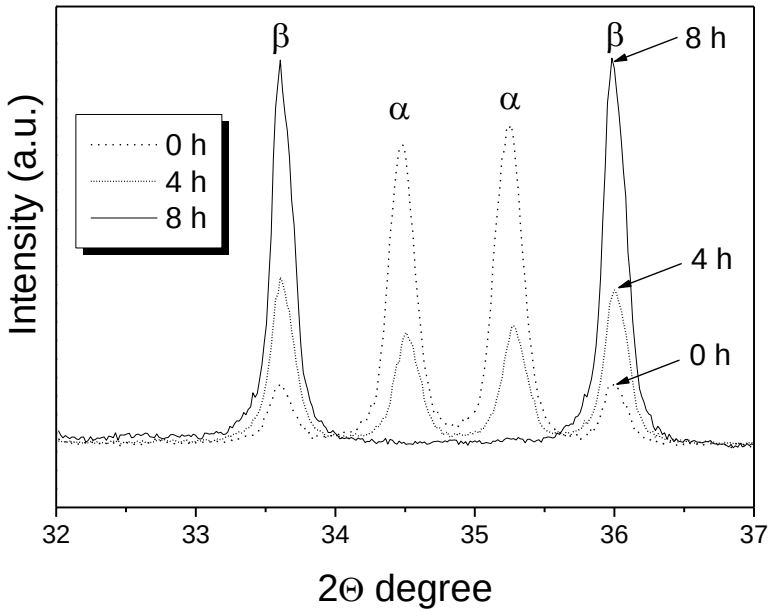

Figure 42. Evolution of phase transformation as a function of the dwell time temperature at 1500 °C.

2.6.8 Influence of additive content

The sintering experiments showed that the densification process is accompanied by the α→β Si_3N_4 phase transformation with $LiYO_2$ at low temperatures (below 1500 °C), while the action of the dissolution-diffusion-reprecipitation mechanism is retarded with the $LiAlSiO_4$ additive at the same temperatures. Thus the phase transformation is faster in the $LiYO_2$-SiO_2 system. Particularly, in the Si_3N_4-$LiYO_2$ system the degree of phase transformation increases with increasing additive content. This can be explained by the fact that increasing volume fraction of the liquid the amount of solute transported through the intergranular liquid film increases and a larger amount of phase transformation results.

Fig. 43 and Fig. 44. show the effect of additive content on phase transformation during sintering of Si_3N_4-$LiAlSiO_4$ ceramics as a function of temperature and the annealing time, respectively.

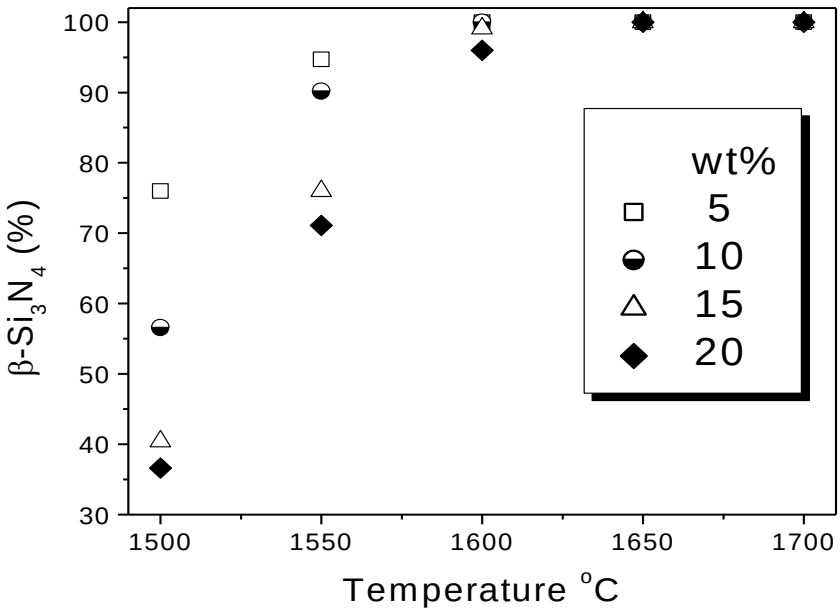

Figure 43. The effect of additive content on α→β-Si_3N_4 phase transformation during the sintering of Si_3N_4-$LiAlSiO_4$ ceramics for 1 h at different temperatures.

In case of the Si_3N_4-$LiAlSiO_4$ system increasing the additive content leads a decreasing degree of phase transformation. The large additive content increases resulting in the longer distance and larger difficulty for the diffusion of Si and N along the liquid phase and therefore the phase transformation is retarded with increasing additive content.

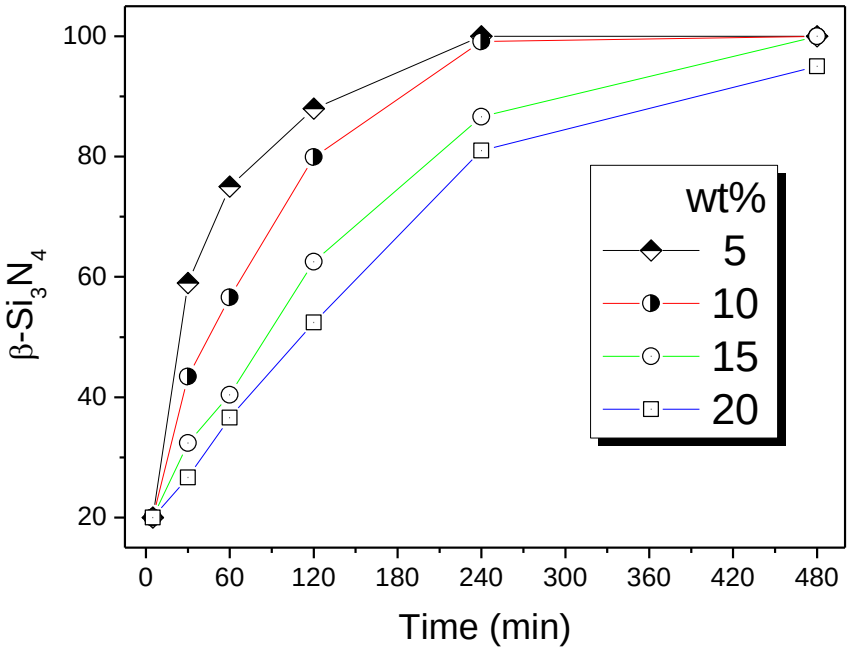

Figure 44. The effect of additive content on α→β-Si_3N_4 phase transformation during the sintering of Si_3N_4-$LiAlSiO_4$ ceramics at 1500 °C.

2.6.9 Kinetics of phase transformation

The curves for the time dependence of the α→β transformation suggest that the conversion kinetics is of first order. This can be described by the equation:

$$\frac{d\alpha}{dt} = -K\alpha \tag{2.5}$$

where K is a rate constant which accounts for the influence of temperature and α is the concentration of the α- Si_3N_4 phase in the sintered samples. The transformation rate depends not only on the concentration of the α-phase, but also on the composition and amount of liquid phase as given by the parameter K. The volume and viscosity of the vitreous phase will determine the extent to which compositional gradients and the nitrogen supersaturation in the α-Si_3N_4/liquid interface are maintained. The plots of log(α) against time are linear (Fig. 45 and Fig. 46) which supports the validity of Eq. (2.5).

In the $LiYO_2$ system, the transformation rate constant increases with increasing additive content while the opposite behavior is observed in the $LiAlSiO_4$ additive system, *i.e.* the rate constant decreases with higher additive content. The addition of Y_2O_3 to silica produces an important accelerating effect on both the phase transformation and the densification of Si_3N_4 ceramics. In this case, a higher additive content creates a higher volume of liquid phase, and as a result, faster α→β phase transformation and higher densities are obtained. In the $LiAlSiO_4$ additive system the more the liquid phase is present, the longer it will take to reach the total α→β conversion.

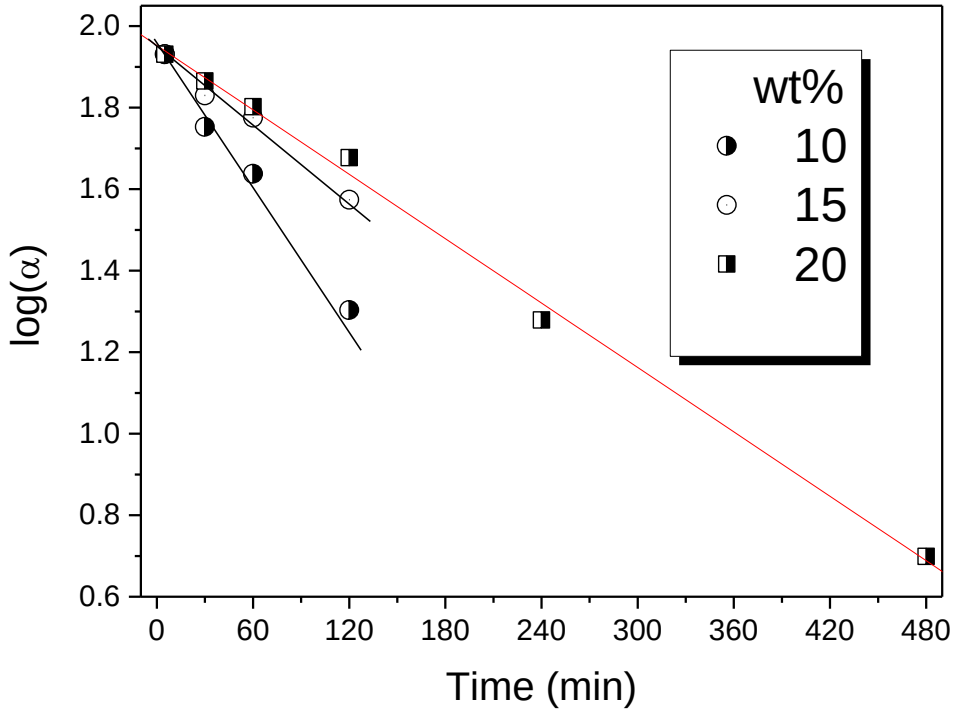

Figure 45. Linear dependence of log α-phase content on time for Si_3N_4 containing various amounts of the $LiAlSiO_4$ additive at 1500 °C.

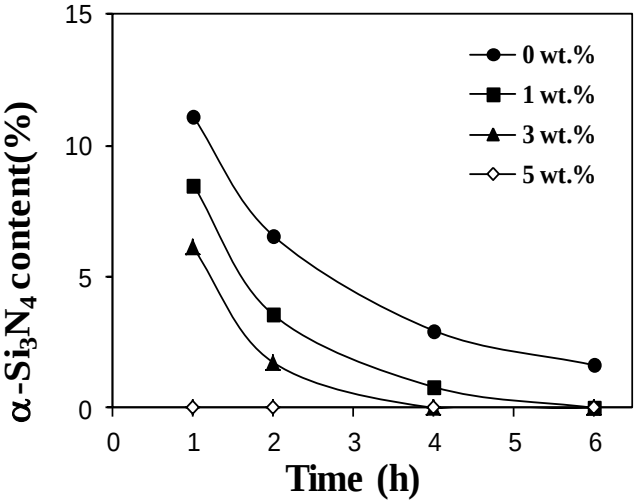

Fig. 46. α-phase content *vs.* isothermal heating time.

Kinetics of the α–β phase transformation can be emphasized in present of Si_3N_4 seeds. It was demonstrated that the phase transformation of α into β-Si_3N_4 is very sensitive of seeds content and heating time. The authors were calculated rate constants and activation energies for compositions with different β-Si_3N_4 seeds content in the presence of Y_2O_3-Al_2O_3 mixture as a sintering aid. The basic processes through which phase transformation is completed are: (i) dissolution of α-Si_3N_4 particles, (ii) diffusion through the liquid phase and (iii) precipitation of dissolved Si_3N_4 predominantly on preexisting β-seeds. Since the α–β Si_3N_4 transformation is influenced by the degree of local

supersaturation in the liquid phase [11] the reaction at α-Si_3N_4/liqiud surface and diffusion through the melt are basic steps of the phase transformation. After solution of α-grains in a liquid phase they transform into β-phase, which precipitates as mentioned, predominantly on the β-seeds. The degree of this reaction was calculated by determining the amount of unreacted α-Si_3N_4 phase. Fig. 46 summarizes the influence of heating time on phase transformation at 1700 °C for different seeds concentrations.

The rate of transformation, as seen from Fig. 46, increased with increasing seeds content in the samples. In samples without seeds, α-Si_3N_4 can still be detected even after 6 h of hot pressing at 1700 °C. However, in the samples with 5 wt.% seeds there was no evidence of α-Si_3N_4, even after the shortest heating time.

The phase transformation kinetics was studied in the temperature range from 1500 to 1600 °C, for all the compositions. After shorter heating time, ranged from 15 to 90 min, the amounts of retained α-phase are significant which enabled to follow the concentration decrease of the reactant.

Bowen [13] has shown that the α-β phase transformation in silicon nitride without seeds, in the temperature range from 1425-1750 °C, follows the first order equation:

$$\frac{d\alpha}{dt} = -k\alpha \tag{2.6}$$

that after integration becomes:

$$ln\ \alpha = -kt + 4.605 \tag{2.7}$$

in which α is α-Si_3N_4 content, k is the rate constant and t is a hot-pressing time. According to Eq. (2.7), the rate constant for corresponding temperature is obtained from the slope of the straight line. The relation between the rate constant and temperature is given by equation:

$$lnk = lnA - \frac{Ea}{R} \cdot \frac{1}{T} \tag{2.8}$$

where A and R are constants, T is absolute temperature and Ea is activation energy.

The rate constant k was calculated for each of our compositions at three different temperatures (Fig. 47 (a, b and c). The activation energies (Ea), for different seeds concentrations, were determined from the slope of *ln k vs. 1/T* function as given in Fig. 47 (d). The linear dependence of *ln α vs.* hot-pressing time *t*, presented by straight line for our results (Fig. 47), confirms that the assumption of the first order reaction was correct in our case, too.

From the obtained results it is obvious that the rate constant increases while the activation energy decreases with the increase of seeds concentration (Fig. 47). Large amount of seeds, which are favorable crystallization centers, beneficially affects the transformation that can be completed at lower temperature with lower energy consumption. In our system, for samples with 5 wt.% seeds, the activation energy is 348 KJ/mol (Fig. 48)

The results of the activation energy of the phase transformation differ in the literature. It is shown [13] that the value differs for different additives which form liquid phase. Bowen [13] calculated the activation energy for Si_3N_4 without seeds, in the presence of Y_2O_3/MgO sintering additive, as 500 KJ/mol. Hampshire and Jack [14] reported that the value of activation energy for transformation in the presence of Y_2O_3, was close to Si-N chemical bond energy, being 435±38 KJ/mol [5]. Our results for non-seeded Si_3N_4 of 397 KJ/ mol are close to this value and confirm the reconstructive nature of the transformation studied. Since the activation energy value for seeded samples is close to Si-N bond energy, the results point out that boundary reaction is the rate limiting step during the phase transformation. It may be added that the liquid phase on the basis of Y_2O_3-Al_2O_3 provides a good vehicle for mass transport being of relatively low viscosity. The results (Table 16) on the densification degree, being higher than transformation degree for the same samples, are in

accordance to the above made statement indicating, too, that the boundary reaction is the rate controlling step in the Si_3N_4 phase transformation.

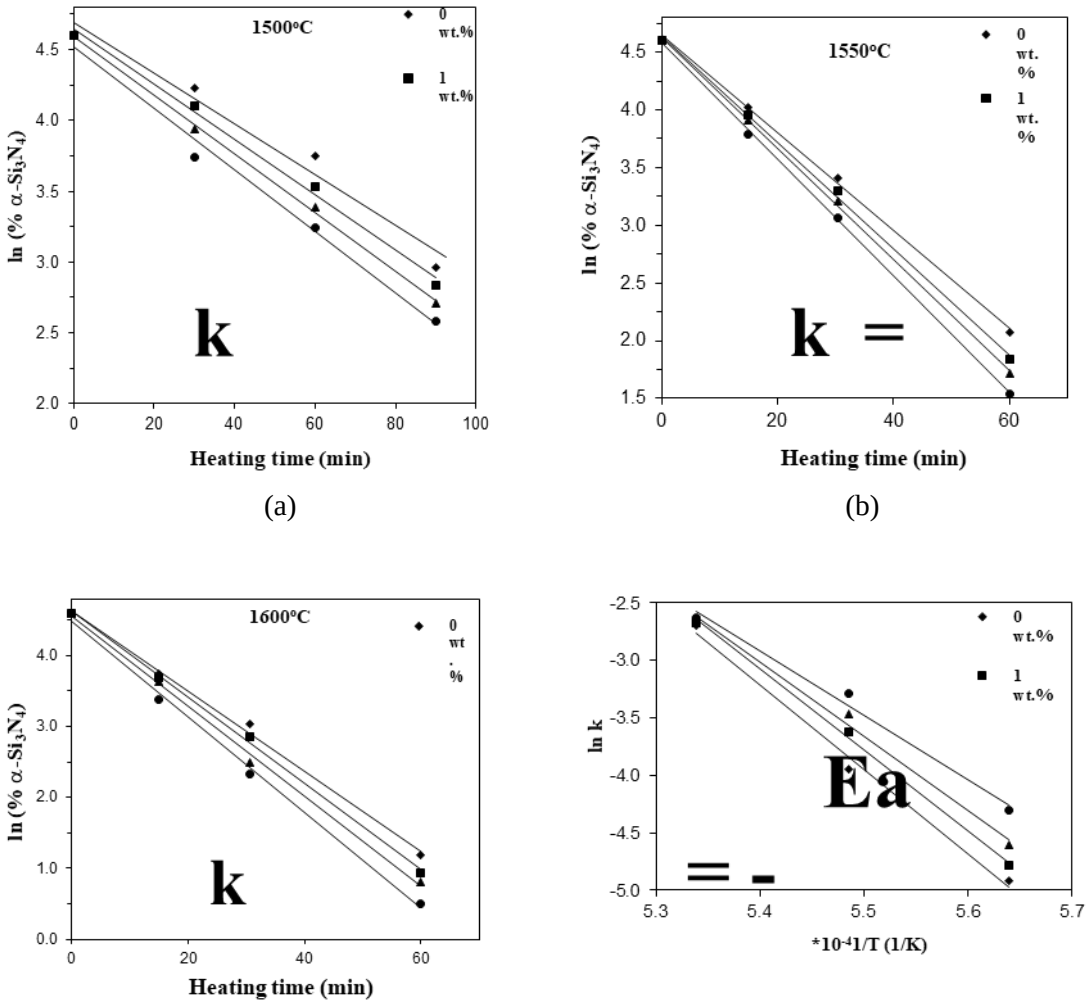

Figure 47. The rate constants for different amount of seeds at (a) 1500 °C, (b) 1550 °C (c) 1600 °C and (d) the activation energies.

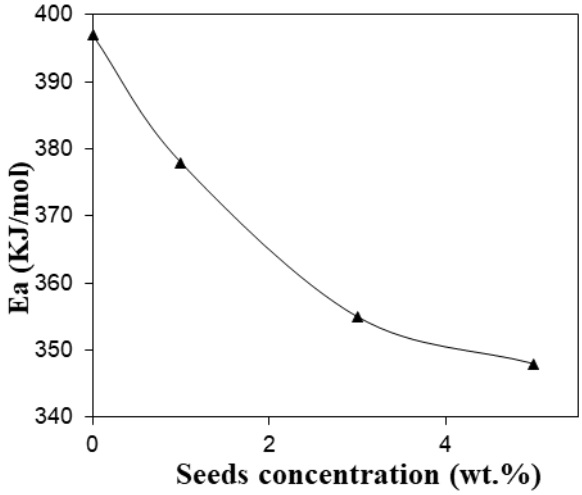

Figure 48. Activation energy as a function of seeds concentration.

Table 16. Content of α-phase (%) and densification degree %TD in seeded samples.

Temperature (°C)	***Time (min)***	***Seeds concentration (wt.%)***							
		0		*1*		*3*		*5*	
		%TD	α-phase (%)	%TD	α-phase (%)	%TD	α-phase (%)	%TD	α-phase (%)
1500	30	97.9	48	98.0	44	98.1	41	98.0	39
	60	98.2	29	98.4	26	98.7	22	98.6	19
	90	99.7	20	99.5	17	99.5	15	99.8	13
1550	15	98.0	55	98.3	55	98.2	50	98.2	45
	30	98.8	30	98.6	27	98.6	24	98.8	22
	60	99.4	18	99.5	16	99.4	14	99.6	11
1600	15	98.6	44	98.5	42	98.5	37	98.4	33
	30	99.1	24	99.0	20	99.2	18	99.1	17
	60	99.6	16	99.7	14	99.8	12	99.7	10

2.6.10 Transformation mechanism

The main factor that determines the kinetics of phase transformations is the diffusion of Si and N atoms in the liquid phase. The phase transformation is rate-controlled by interfacial reactions if the diffusion velocity is high and by material transport if the diffusion velocity is low. Sintering additives affect this behaviour by changing the viscosity and amount of the liquid phase. The rate transformation is strongly influenced by changing liquid phase content in the case of the diffusion mechanism. In contrast, it is independent of the liquid volume in the case of interface reaction control. In this study, the phase transformation is very much affected by changing the additive content for both systems. Thus, it can be concluded that the phase transformation with $LiYO_2$ additive as well as with the $LiAlSiO_4$ additive is mainly diffusion-controlled. The difference in transformation rate between the two additive systems can be explained by the fact that the yttrium ion is primarily a network modifier in a Y-Si-O-N glass, *i.e.* it perturbs Si-O bonds thus allowing rapid diffusion of ions through the liquid phase. On the other side Si has a different behaviour, *i.e.* it is a glass-former and the liquid phase is more rigid compared to the Y-Si-O-N glass. The nominal amount of Si in the material with $LiAlSiO_4$ additive is much higher than in the material with $LiYO_2$ resulting in slower mass transport.

2.6.11 Relation of transformation to densification

Densification and α→β phase transformation are two important phenomena which occur during the sintering of Si_3N_4 ceramics. However, it is difficult to determine the relationship between them. There have been reports in the literature that both occur nearly simultaneously, but the existence of a lag between the two reactions has also been observed.

The present study shows that the phase transformation and densification do not have a straightforward relationship with each other. This is illustrated in Fig. 49 where the extent of densification and α→β phase transformation is compared as a function of sintering temperature.

In both systems, there is a lag between densification and phase transformation showing that the major amount of transformation occurs in a later sintering stage. At 1400 °C, almost no transformation is observed, while more than 90% and 80% of the theoretical density have already been reached for the $LiYO_2$ and $LiAlSiO_4$ additives, respectively. At higher temperatures, the differences in the degree of densification and phase transformation become smaller in case of the $LiYO_2$ additive, while it is at 1700 °C still present in case of the $LiAlSiO_4$ additive.

Fig. 50 depicts the relationships between densification and phase transformation as a function of sintering time for both types of materials. In both cases, the differences in the degree of densification and phase transformation diminish with prorogated heating time. Both processes are particularly fast in the $LiYO_2$-Si_3N_4 system where the densification and phase transformation have gone to completion after 60 minutes already.

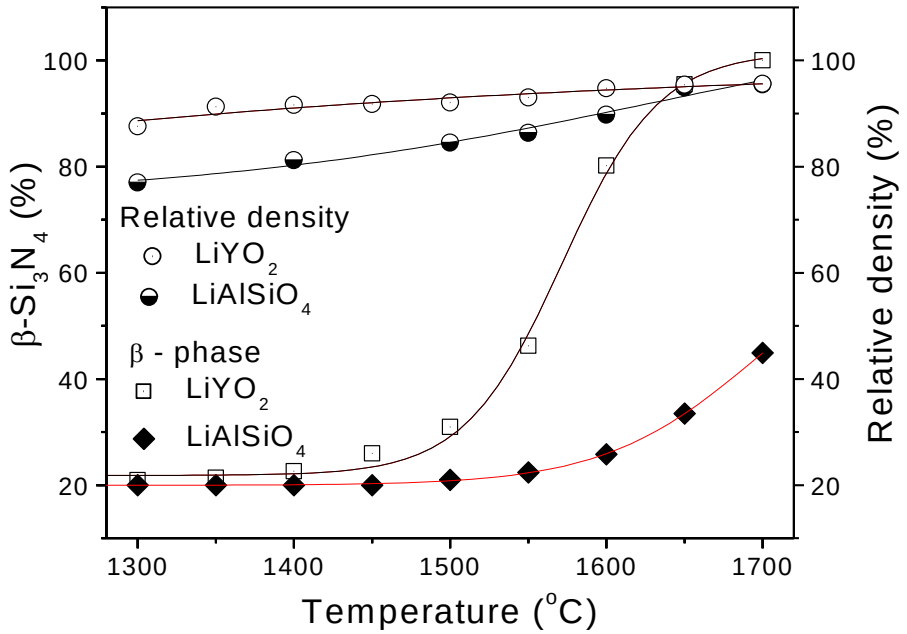

Figure 49. Densification and phase transformation as a function of sintering temperature for $LiYO_2$-Si_3N_4 and $LiAlSiO_4$-Si_3N_4 systems after a holding time of 5 min.

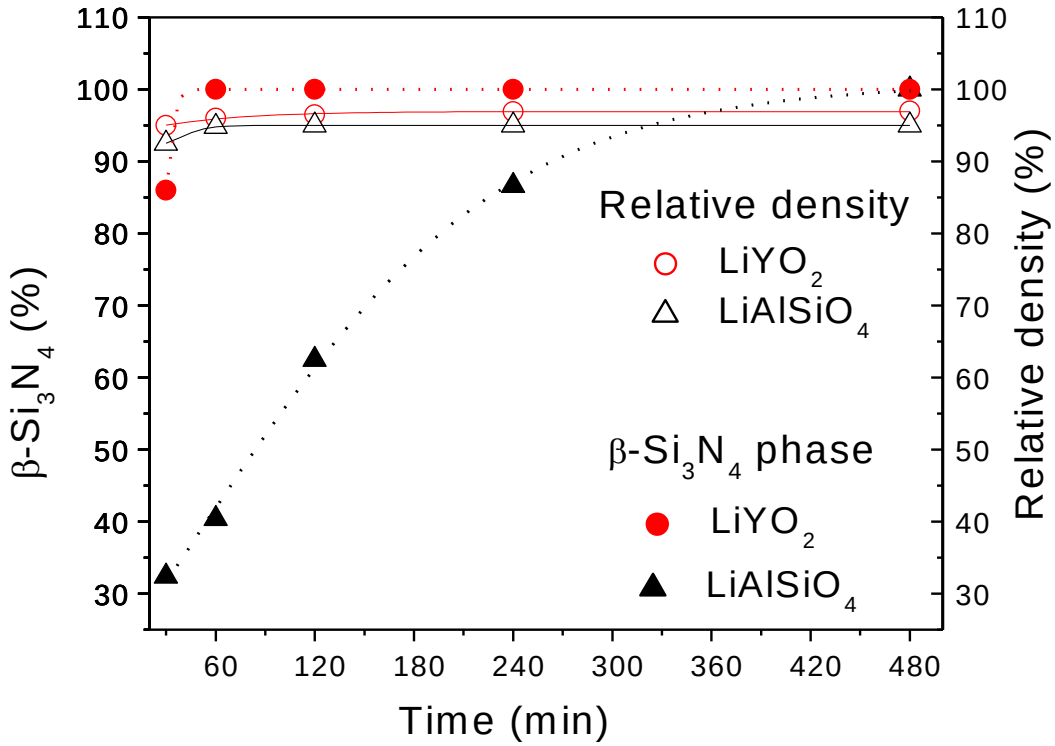

Figure 50. The relationship between densification and phase transformation as a function of sintering time for $LiYO_2$-Si_3N_4 and $LiAlSiO_4$-Si_3N_4 additive systems (with 15 wt.% of additive and at a sintering temperature of 1500°C).

The addition of Y_2O_3 to silica produces an important accelerating effect on both, transformation and densification of Si_3N_4 ceramics. In this case, higher additive content creates a less viscous liquid phase resulting in faster $\alpha \rightarrow \beta$ phase transformation and higher densities obtained. In the $LiAlSiO_4$ system the densification and transformation behavior is more complicated and it needs more work to clarify the details.

3. Microstructure

The microstructure has a crucial influence on the particular properties of a final material. Thus, the improvement of mechanical properties by microstructural control has been one of the main topics of interest in the development of Si_3N_4 ceramics. [159, 160]. The amount, size and morphology of the α- and β-Si_3N_4 grains are the key factors for the microstructure development. Generally, the microstructure is characterized by the three features: Si_3N_4 grains, the secondary crystalline phases and the amorphous grain boundary films. Their distribution and arrangement contribute to the quality of the actual microstructure and the reliability of the material.
During cooling, the liquid solidifies to amorphous or partially crystalline secondary phases, which are located either at the grain boundaries in the form of thin layers or at triple junctions (Fig. 51). This intergranular phase strongly affects the mechanical properties, especially at high temperatures. The thickness of the grain boundary film depends rather on the types of additives than on the amount of liquid phase. An increase in the amount of liquid leads only to an increasing volume of the triple points [87].

Figure 51. Typical microstructure of a liquid-phase sintered Si_3N_4 ceramics (schematic (a) and SEM micrograph (b)).
1- Si_3N_4 matrix grains, 2-crystalline secondary phase, 3-amorphous residue at triple junctions and grain boundaries.

A typical feature of sintered Si_3N_4 ceramics is the morphology of the Si_3N_4 grains. Residual α-grains are equiaxed. The β-phase exhibits an elongated grain structure with an aspect ratio (ratio of length to thickness) usually in the range of 5 to 10 [88, 89].
The microstructure development is controlled mainly by the Si_3N_4 starting powders, the additives used and the sintering parameters.In this chapter the various factors influencing the microstructure development, grain growth and the relation of phase transformation to microstructure are dealt with.

3.1 Microstructural observation in systems sintered with $LiYO_2$ additive

The microstructures of LPS-Si_3N_4 sintered with $LiYO_2$ additive at 1500 °C for different annealing time are shown in Fig. 52. Upon variation of the annealing time the grain size and morphology of the growing β-Si_3N_4 particles are significantly changed from equiaxed to elongated. Typically, the fraction of small grain sections is reduced, which indicates the dissolution of small particles parallel to the growth of the elongated Si_3N_4-matrix with increasing annealing time. According to these results it is suggested that the mechanism of Ostwald ripening is predominantly responsible for grain growth in the Si_3N_4 material. This is independent of whether this growth mechanism is reaction or diffusion controlled [161]. Since the phase transformation is completed after 1 h of annealing at 1500 °C (Fig. 40), the further grain growth of β-β-Si_3N_4 should be restricted,

resulting in a relatively stable microstructure [162]. However, in spite of the absence of α- to β-Si_3N_4 transformation during prolonged annealing, there is still substantial grain growth of the β-Si_3N_4 (Fig. 52 c). This indicates ongoing solution-precipitation reaction [163]. Ongoing solution-precipitation process may attributed to the fact that the $LiYO_2$ melt is such a good solvent for Si_3N_4. Fig. 53 taken at higher magnification shows that the precipitation takes place preferentially on pre-existing β-Si_3N_4 nuclei (of which the starting powder already contains 20 wt.%).

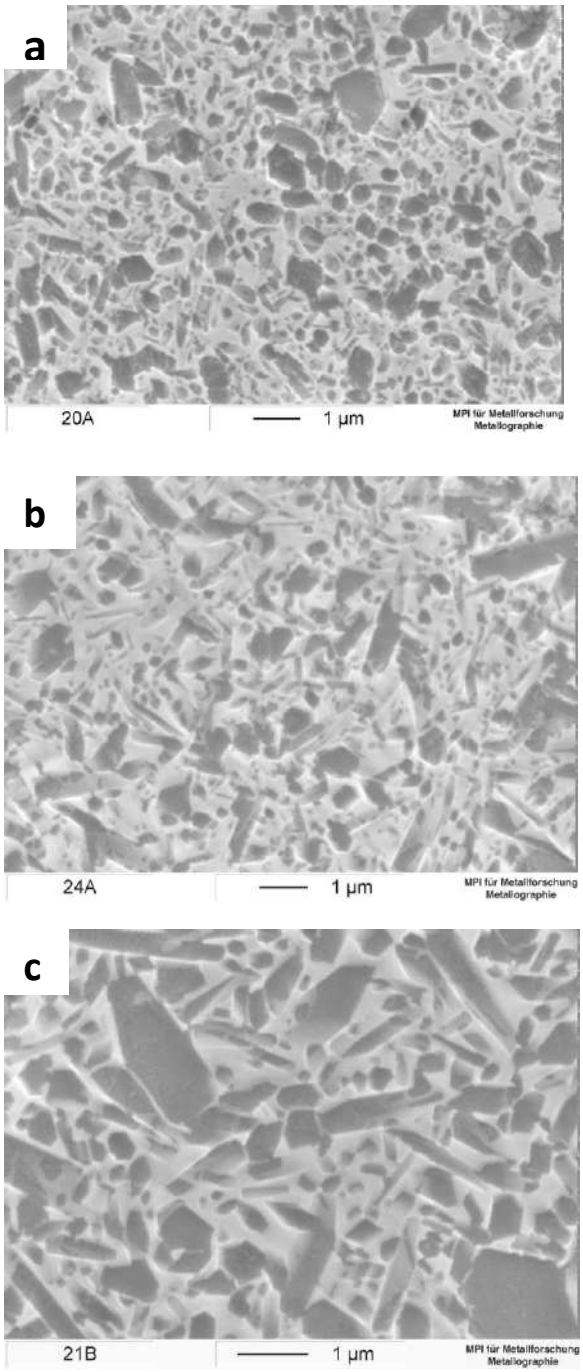

Figure 52. SEM micrograph of polished and plasma etched sections of samples with 15 wt.% additive sintered at 1500 °C for 0.5 h (a), 2 h (b) and 8 h (c).

The observation that β-Si_3N_4 undergoes a solution-precipitation mechanism similar to what was previously reported for α-Si_3N_4 is also in good agreement with model predictions for anisotropic Ostwald ripening process.

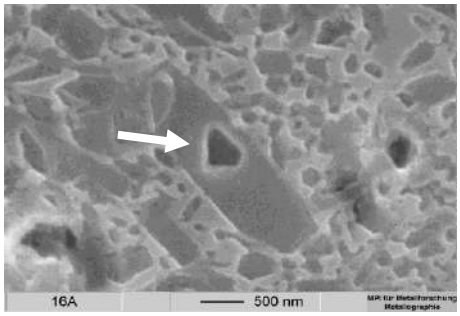

Figure 53. SEM image of polished and CF_4 plasma-etched cross section of the sintered Si_3N_4 material doped with $LiYO_2$ additive. The arrow shows β-Si_3N_4 material precipitated on a β-Si_3N_4 particle acting as a nucleus. The sample was sintered at 1500 °C for 2 h.

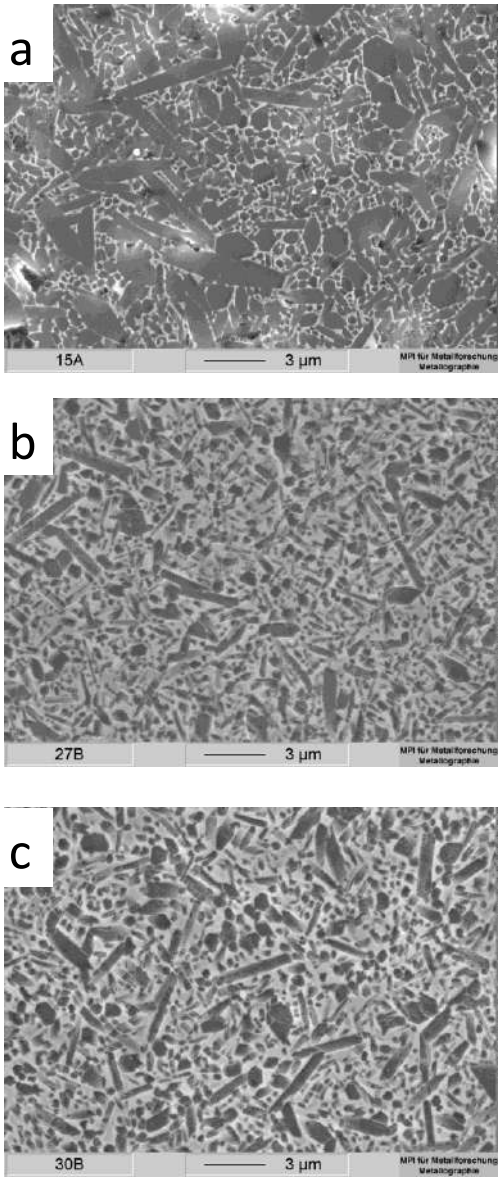

Figure 54. SEM microstructure of Si_3N_4 ceramics with total $LiYO_2$ additive content of (a) 5 wt.%, (b) 15 wt.%, (c) 20 wt.%, respectively. The samples were sintered at 1600 °C for 4 h.

Since the densification as well as the phase transformation is influenced by the additive content, the same has to be true for the microstructure development. Fig. 54 shows SEM micrographs with varying additive content. It can be seen that the number and aspect ratio of elongated β-grains increases with increasing $LiYO_2$ content. The material with a large additive content is mainly

composed of elongated grains. In contrast, with a small additive content, microstructure consists of coarse β-grains within a fine grain matrix. Thus, with increasing additive content, the aspect ratio distribution is shifted to higher values.

The microstructure of Si_3N_4 with 15 wt.% of additive sintered at 1600 °C for 8 h is characterized by a homogeneous distribution of elongated β–Si_3N_4 grains (dark) and glassy phase (light) located in thin layers at grain boundaries and triple points (Fig. 55). The β–Si_3N_4 grains are surrounded by a glassy phase at almost all grain contacts indicating a good wetting behavior. The different types of neighbour-neighbour contact situations can be attributed to the grain growth anisotropy of Si_3N_4 such as interlocking of a growing plane by the plane of a neighboring grain (a) and interlocking of a plane growing through the intergranular phase (b) and rounded edges due to edge-on-plane contact with an adjacent grain can also be seen (c).

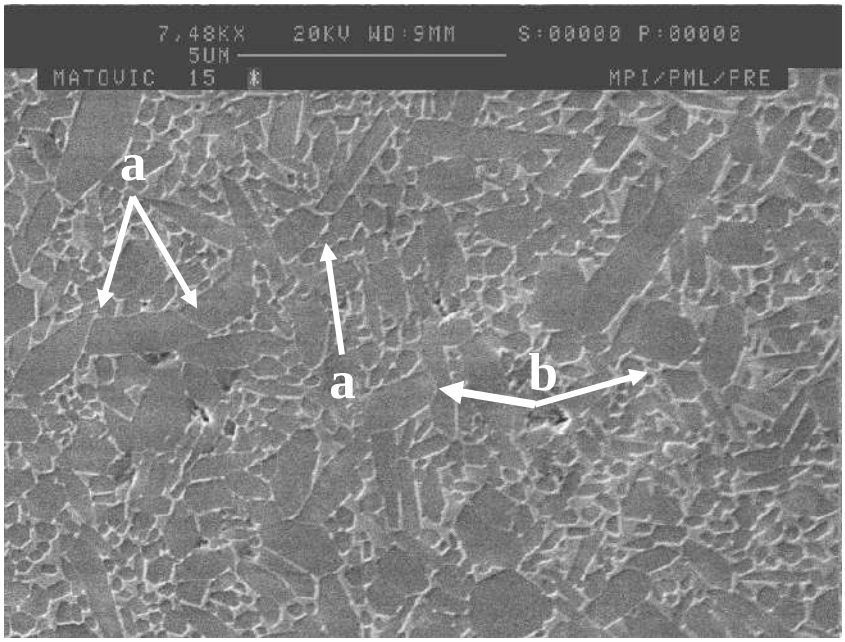

Figure 55. SEM micrograph of polished and plasma etched section of a sample with 15 wt.% additive sintered at 1600°C for 8 h. Motion of basal and prism planes: (a) interlocking of two prism planes, (b) rounded planes contacting each other.

X-ray diffraction patterns of samples sintered at 1600 °C for 8 h show only the presence of β–Si_3N_4 and no other crystalline phases (Fig. 56). This indicates that the remainder of the secondary phase, after evaporation of virtually all of the lithium originally present in the sample, has been completely converted into a glass and that total conversion of α–Si_3N_4 to β–Si_3N_4 has taken place.

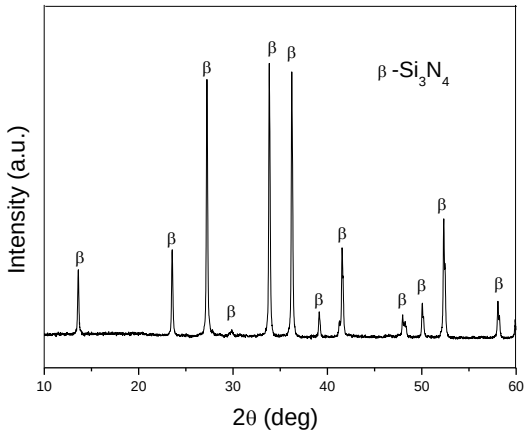

Figure 56: XRD pattern of a sample with 15 wt.% of additive sintered at 1600 °C for 8 h.

The amorphous phase in the Si_3N_4 materials is well-established to remain as a stable film at the grain boundaries [165], with an increasing additive content only causing an enlargement of the multi-grain junctions. For the present materials, the chemistry of the intergranular phase and β-grain was analysed by energy dispersive microanalysis (EDX) with the SEM (Fig. 57 and Fig. 58). Backscattered electron (BSE) images are shown for reference. EDX analysis on the basal plane of a β-Si_3N_4 grain (denoted by cross in the Fig. 57) shows Si and N, but no Y. This is because Y is insoluble in Si_3N_4 [132]. Consequently, Y_2O_3 is localized in the grain-boundary glassy phase. Lithium is not detected by this method because it is a light element. However, chemical analyzes show that almost all of the Li_2O from the samples evaporates during sintering for 8 h at 1500 °C (Fig. 32). Thus, at higher temperatures than 1500 °C there is no lithium and the intergranular phase consists of Y, Si, N and O. This is in good agreement with chemical analyses from the big pocket in the Fig. 58, after 1 h at 1650 °C

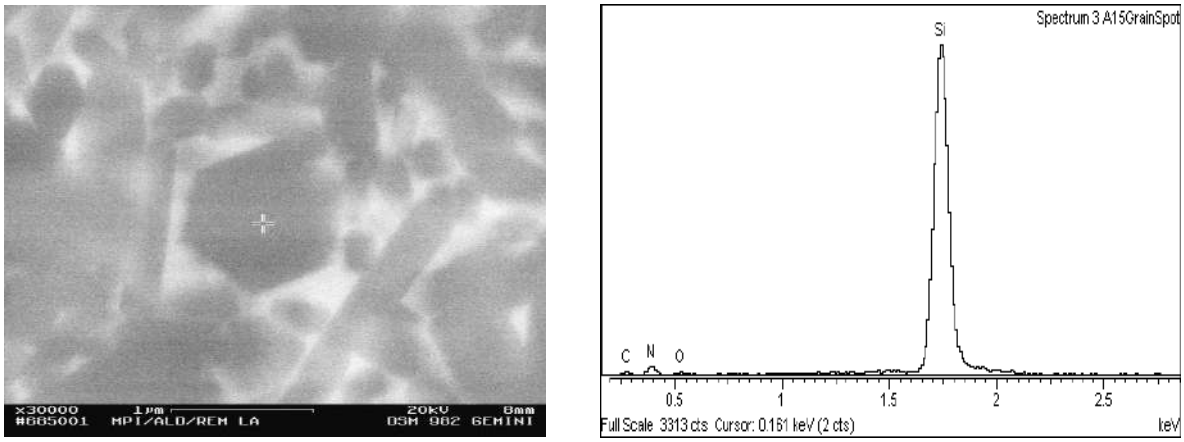

Figure 57: Backscattered electron image and EDX of β-Si_3N_4 grain (+). Sample sintered at 1650 °C for 1 h.

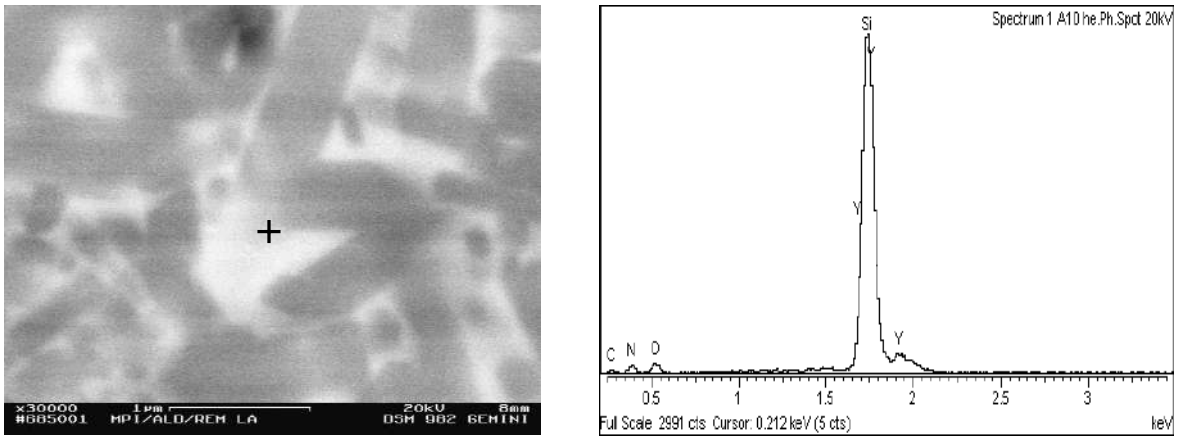

Figure 58. Backscattered electron image and EDX of intergranular phase (+). Sample sintered at 1650 °C for 1 h.

3.2 Microstructural observation in systems sintered with $LiAlSiO_4$ additives

Fig. 59 shows a SEM micrograph of a Si_3N_4 ceramic doped with 15 wt% of $LiAlSiO_4$ sintered at 1500°C for 8 h. The microstructure consists of Si_3N_4 grains separated by glassy phase. Although the α→β Si_3N_4 phase transformation is completed at 1500°C after 8 h of annealing time (Fig. 44), there are no bimodal grains. The morphology of the grains is mostly globular. Plasma etched samples reveal a typical core and rim structure which indicates the dissolution of small particles and reprecipitation on more stable bigger ones.

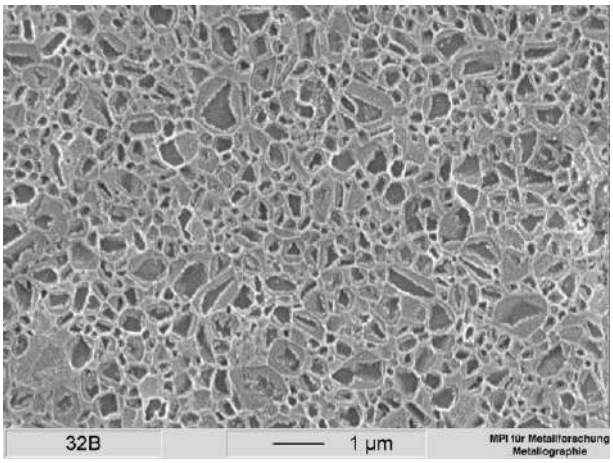

Figure 59. SEM micrograph of polished and plasma etched section of a sample with 15 wt.% of $LiAlSiO_4$ additive sintered at 1500 °C for 8 h.

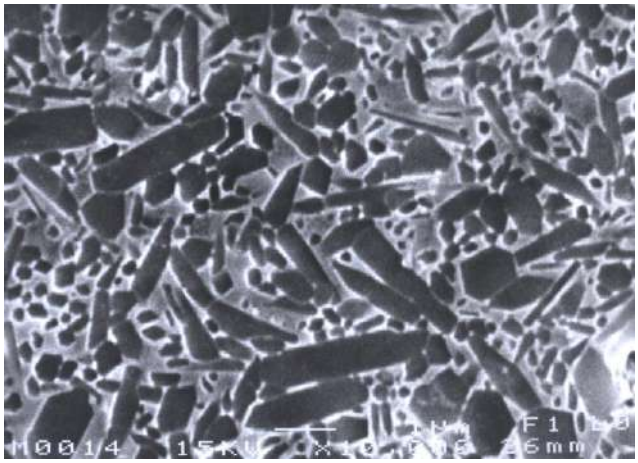

Figure 60. SEM micrograph of a polished and plasma etched section of a sample sintered with 10 wt.% of additive at 1600 °C for 8 h.

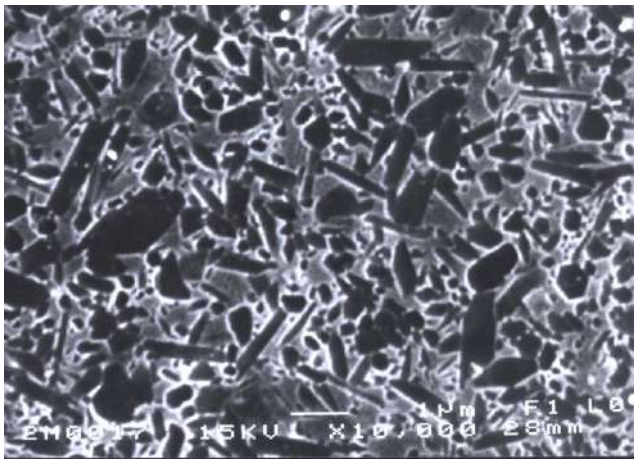

Figure 61. SEM micrograph of a polished and plasma etched section of a sample sintered with 15 wt.% of additive at 1600 °C for 8 h.

The microstructure of Si_3N_4 sintered at 1550 °C for 8 h is characterized by both equiaxed β-Si_3N_4 grains and elongated β-Si_3N_4 grains together with a glassy phase (white) located in thin layers at grain boundaries. During processing at 1600 °C significant differences in the microstructures of the ceramics were developed. Higher temperature enhances the grain growth resulting in a microstructure

with elongated β-Si_3N_4 grains (Figs. 60 and 61). Materials with larger additive content (15 wt.%) exhibit finer microstructure. The number of coarse elongated β-Si_3N_4 grains decreases with the increase in $LiAlSiO_4$ content. It seems that the growth of Si_3N_4 grains during sintering is restrained by the higher $LiAlSiO_4$ content.

At 1650 °C it is noticed that the amount of residual glass is become very low, indicating that aluminum and/or oxygen has been incorporated into the β-grains (Fig. 62).

EDX analysis of the sample sintered at 1650°C for 1 h showed that Al was dissolved in the β-Si_3N_4 grains. This process consumes the constituents of the liquid phase, thereby reducing the volume of the liquid phase as well as altering its composition. The liquid phase shifts to a more siliceous composition and hence to higher viscosity. Thus higher viscosity leads to a retardation of the grain-boundary diffusion processes, and therefore limits mass transport. This reduction in mass transport results in a retarded grain growth and the microstructure do not change in the case of the samples sintered at 1650 °C even for extended time intervals (Fig. 62).

To conclude, the material sintered with the $LiAlSiO_4$ additive forms a β-Sialon due to the incorporation of Al_2O_3 in the β-Si_3N_4 structure. This is expected to have a marked influence on the properties especially of the material sintered at higher temperatures (>1600 °C).

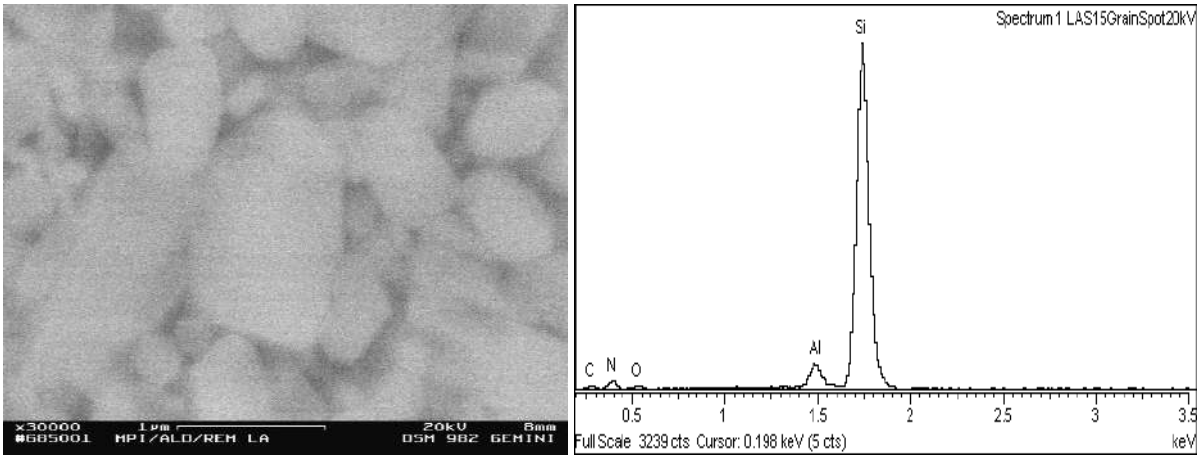

Figure 62. Backscattered electron images and EDX of β-Si_3N_4 grain. Sample is sintered at 1650°C for 1h.

4. Properties of Si_3N_4 materials

Si_3N_4 based ceramics have a broad variety of interesting properties such as low specific weight, good mechanical and thermomechanical behavior. They are also non-magnetic and good electrical insulation material. These unique properties allow fabrication of a wide range of materials with specified property combination.

4.1 Mechanical properties of Si_3N_4 materials

Table 17. Typical properties of advanced hot-pressed and pressureless sintered silicon nitrides at room temperature [106].

Property	***Hot pressed Si_3N_4***	***Pressureless sintered Si_3N_4***
Density (g/cm^3)	>3.20	3.20
Thermal conductivity (W/mK)	29.3	15.5
Flexural strength (MPa)	1200	
Compressive strength (MPa)	4500	4000
Thermal expansion (10^{-6}/K)	3.2	3.4
Young's modulus (GPa)	320	280
Toughness-K_{Ic} (MNm$^{3/2}$)	8.3	5.4

Typical data for the properties of hot-pressed and pressureless sintered Si_3N_4 are presented in Table 17. It can be inferred from the given data that Si_3N_4 possesses high strength, good thermal-shock resistance due to the low coefficient of thermal expansion and relatively good resistance to oxidation compared to other high-temperature structural materials [105]. The mechanical property of Si_3N_4 ceramics depend on pores present, cracks and inclusions. Among these factors, porosity has been demonstrated to have a pronounced effect on strength. Fig. 63 shows the relationship of the relative density and strength of pressureless sintered Si_3N_4 with yttria and alumina additives.

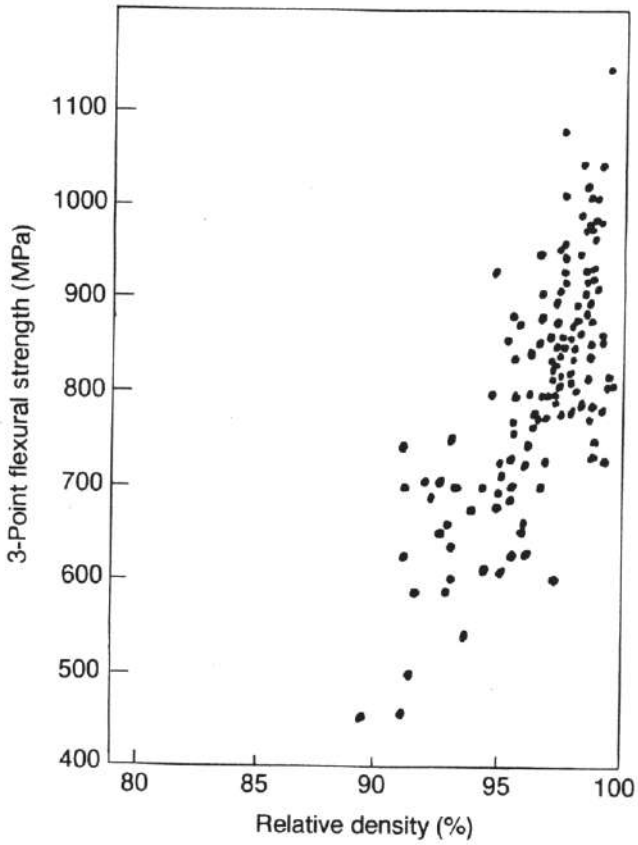

Figure 63. Dependence of the strength of pressureless sintered Si_3N_4 on the density [105].

Fracture toughness differs mainly with variations in the microstructure. The grain shape and the size and phase composition of the grain-boundary phase have a strong influence. High fracture toughness of Si_3N_4 based ceramics could be explained on the basis of similar toughening mechanisms as in whisker reinforced composite materials (grain bridging, pull-out, crack deflection, and crack branching [107, 108, 109]). However, these toughening mechanisms are only active when the dominant fracture mode is intergranular.

The ratio of transgranular to intergranular fracture depends on the strength of both intergranular-phase and Si_3N_4 grains. A material with higher toughness has a weaker grain boundary. On the other side, the strength of the grain-boundary phase is connected with the local residual stresses [110]. When the thermal expansion coefficient of the grain-boundary phase is higher than that of the Si_3N_4 grains, the grain-boundary phase is under tensile stress and the fraction of intergranular fracture is high. As a consequence, the fracture toughness increases. In contrast, ceramics with a grain boundary phase under compression have low fracture toughness because of a higher amount of transgranular fracture [111].

A comparison of the flexural strength values of pressureless sintered Si_3N_4 at ambient and high temperature is given in Table 18.

Table 18. Flexural strength data of pressureless sintered Si_3N_4.

Additive	*Flexural strength*	
	room temperature (MPa)	*high temperature (MPa)*
10 mol.% spinel	706	-
Y_2O_3, Al_2O_3	412	-
15 wt.% (MgO + Al_2O_3)	351	-
3.5-20 wt.% Y_2O_3 + 0-20 wt.% Al_2O_3	700	455 (at 1200 °C)
5 wt.% (MgO + BeO + CeO_2)	827	428 (at 1200 °C)
15 mol.% Y_2O_3	473	-
3-10 wt.% Y_2O_3	450	-
3-10 wt.% CeO_2	520	-
3.3-7.2 mol.% CeO_2 + 12.8-20 mol.% SiO_2	709	393 (at 1200 °C)
4.3 wt.% Y_2O_3 + 3.6 wt.% SiO_2	826	338 (at 1200 °C)
4 wt.% CeO_2 + 4 wt.% SiO_2	778	356 (at 1200 °C)
6.3 wt.% La_2O_3 + 3.6 wt.% SiO_2	729	412 (at 1200 °C)
5.9 wt.% Sm_2O_3 + 3.6 wt.% SiO_2	696	455 (at 1200 °C)
7.5 mol.% Y_2O_3 + 7.5 mol.% Pr_6O_{11}	800	>800 (at 1300 °C)
1 wt.% Al_2O_3 + 3 wt.% CeO_2	750	-
2 wt.% Al_2O_3 + 5 wt.% Y_2O_3	860	-
5-10 wt.% Y-Al-garnet	779	-
13.4 wt.% ZrO_2 + 2.2 wt.% Y_2O_3 + 4.1 wt.% Al_2O_3	422	463 (at 1200 °C)

The amount, composition and degree of crystallization of the grain boundary phase are the key factors for a successful development of Si_3N_4 ceramics for applications at elevated temperatures. Additives which result in amorphous silicate phases with a low softening point and low viscosity, such as alkali and alkaline earth oxides and Al_2O_3 and AlN, generally have a high strength at room temperature. However, due to a low softening point, they are not well suited for high temperature applications. Refractory intergranular phases with a higher degree of crystallinity were obtained by yttria or other rare earth oxides as sintering additives [112, 113]. The high temperature properties of Si_3N_4 with rare-earth oxides as sintering additive increase with decreasing ionic radii. The most superior high temperature properties are found with Lu_2O_3 as sintering additive due to the presence of $Lu_2Si_2O_7$ and $Lu_4Si_2O_7N_2$ as the grain boundary phases [2].

The presence of nitrogen in silicate glass helps to produce hard and refractory grain boundaries in the sintered product, thus improving its high temperature properties.

The hardness and indentation fracture toughness of both Si_3N_4 materials, *i.e.* materials sintered by $LiYO_2$ and $LiAlO_4$ additives, were measured and plotted against the annealing time (Fig. 64).

In both compositions, the fracture toughness and hardness initially increase with increasing annealing time, whereas decreasing hardness is observed in case of annealing for at least 4 h. Further prolongation of the sintering time leads to constant or decreasing hardness for both $LiAlSiO_4$ and $LiYO_2$ additives. On the other side, the fracture toughness continuously grows during prolonged annealing time for the $LiYO_2$ additive, while this behavior is less pronounced in case of $LiAlSiO_4$ additive. In this case it becomes constant after 4 hours of annealing.

Variations in the fracture toughness of Si_3N_4 materials sintered with $LiYO_2$ and $LiAlSiO_4$ additives should be related to the microstructures and glassy phase contents. Fracture toughness is improved when large elongated grains are formed in a fine matrix [166, 167]. In case of the $LiYO_2$ additive the fracture toughness increased with sintering time as a result of the continuous growth of elongated grains. On the other hand, materials sintered with $LiAlSiO_4$ additive at 1500 °C exhibit fine and predominantly equiaxed β-Si_3N_4 grains which do not change during long annealing times resulting in a constant value of fracture toughness.

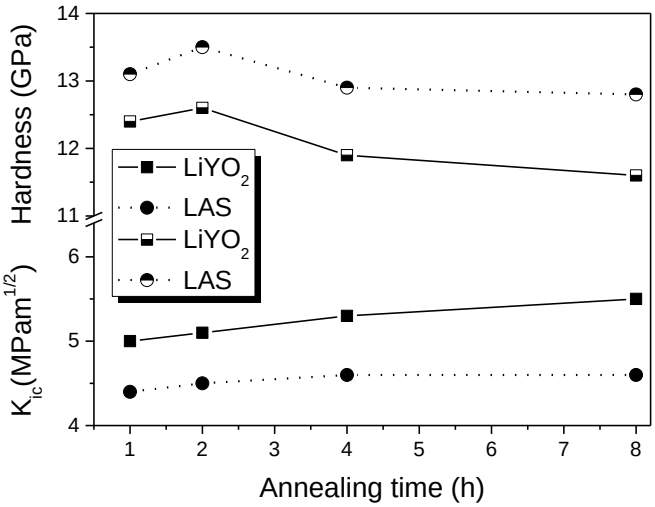

Figure 64. Variation of fracture toughness and hardness as a function of the annealing time in Si_3N_4 ceramics sintered with $LiYO_2$ and $LiAlSiO_4$ additive systems, respectively at 1500 °C.

The microstructural effects on the fracture toughness are well illustrated by crack paths generated by indentation, as shown in Figs. 65 and 66.

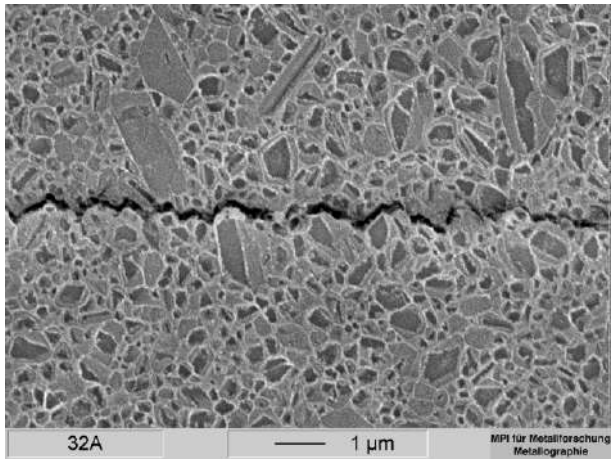

Figure 65. Microstructure and crack path in Si_3N_4 ceramic sintered with 15 wt.% of $LiAlSiO_4$ additive at 1500 °C for 8 h.

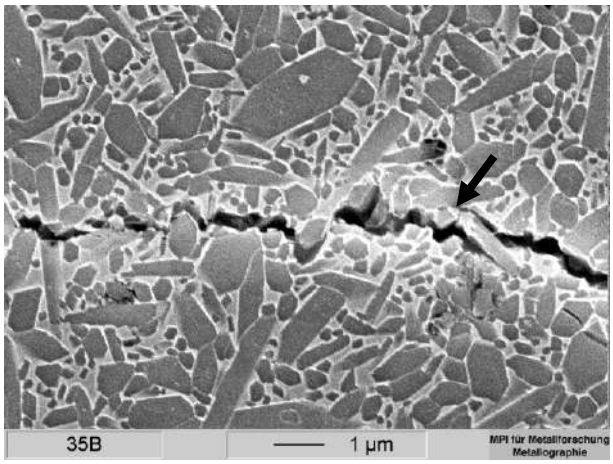

Fig. 66. Microstructure and crack path in Si_3N_4 ceramic sintered with 15 wt.% of $LiYO_2$ additive at 1600 °C for 8 h. The crack is bridged by an elongated grain (arrow,) which was pulled out of the matrix on the upper side of the crack as the crack opened.

Materials with globular grain structure reveal crack propagation with few signs of toughning mechanisms, such as crack deflection, grain pullout, debonding and bridging. On the other hand, microstructures with elongated grains that can act as a reinforcing phase promote crack bridging processes and consequently toughen the ceramics. Such mechanisms are operative in both the cases of $LiYO_2$ and $LiAlSiO_4$ additives, for samples sintered at 1600 °C, due to their similar microstructures.

The maximum values of fracture toughness obtained are 6.8 and 6.2 MN $m^{3/2}$ for the materials sintered with $LiYO_2$ and $LiAlSiO_4$ additives, respectively, at 1600 °C for 8 h.

4.2 Thermal properties

Thermal conductivity is one interesting property of Si_3N_4 which combined with the excellent mechanical properties make it a serious candidate for high-performance substrates [114]. Firstly, Haggerty and Lightfoot pointed out Si_3N_4 as a material with potentially high thermal conductivity at room temperature [115]. Calculation shows that the entrinsic thermal conductivity of β-Si_3N_4 single crystals is 320 W m^{-1} K^{-1} which is similar to the thermal conductivity of SiC and AlN that have been successfully fabricated for commercial uses as high thermal conductivity substrates and heatsinks [116]. However, relatively poor thermal conductivity values, ranging from 20 to 70 W m^{-1} K^{-1} have been reported for Si_3N_4 ceramics fabricated by reaction bonding [11], chemical vapor deposition [117], hot pressing and hot-isostatic-pressing methods [118]. Very recently, Watari et al. fabricated a Si_3N_4 with thermal conductivity value of 155 W m^{-1} K^{-1} by a novel processing technique termed grain-orientation technology [116].

It is postulated that heat flow in hexagonal β-Si_3N_4 is different depending on the crystal axis. In single crystal measurements it was shown that the conductivity along the c-axis is about three times higher than that along the a-axis [119].

The thermal conductivity of Si_3N_4 ceramics depends strongly on the amount of Al impurities and/or sintering additives because the incorporation of Al and O in the β-Si_3N_4 structure reduces the thermal conductivity of the grains due to the reduced free path of phonons. Thus, Al-free sintering additives are a precondition for the production of Si_3N_4 ceramics with high thermal conductivity [2]. Internal defects in the grains [120] and increasing grain boundary thickness were also found to decrease the thermal conductivity [121].

From a commercial point of view, it is very important to fabricate high thermal conductivity Si_3N_4 ceramics by conventional sintering technique such as pressureless sintering. Seeding combined with careful control of grain boundary composition can be one processing strategy for this purpose. In addition, microstructure design for harmonizing high thermal conductivity with good mechanical and electrical properties is also very important for the widespread use of Si_3N_4 ceramics as a high thermal conductivity material [114].

Controlling factors for the heat conductivity of Si_3N_4 based materials have been proposed by numerous researchers [168]. The factors are divided into two groups: (a) microstructure effects and (b) crystalline perfection. Since the $LiYO_2$ additive is not soluble in Si_3N_4, as it is the case with $LiAlSiO_4$ additive, ceramics sintered with these additives should be significantly different.

The influence of additive composition on thermal diffusivity of the sintered Si_3N_4 materials is shown in Fig. 67 (a) and (b). The thermal conductivity with the $LiYO_2$ additive is higher in comparison with the $LiAlSiO_4$ additive. Since the thermal conductivity of covalent materials is mainly due to phonons, it is controlled by the type and amount of crystal defects inside the grains.

EDX analyses of the sample sintered with $LiAlSiO_4$ at 1650 °C for 1 h showed that Al was dissolved in the β-Si_3N_4 grains. Dissolved Al and O act as point defects scattering phonons [169] and hence decrease the thermal conductivity. The thermal diffusivity significiently decreases with increasing temperature in both sintered materials (Fig. 67). The main reason is increasing phonon scattering due to the higher vibrational energy. However, the decrease in thermal diffusivity and conductivity is more pronounced in case of the $LiAlSiO_4$ additive due to a higher phonon density of states associated with partially occupied interstitial sites in β-Sialon.

The effect of additive content on the thermal conductivity of Si_3N_4 ceramics sintered with 5-20 wt% of $LiYO_2$ additive at 1650°C for 4 h is tabulated in Table 19.

Table 19. The effect of additive amount on the thermal conductivity of Si_3N_4 ceramics sintered with $LiYO_2$ additive.

Additive content (wt.%)	*Density (g/cm^3)*	*Thermal conductivity (W/m·K)*
5	2.85	38.6
10	3.12	29.1
15	3.21	29.7
20	3.20	26.8

In spite of the low density (high porosity), a higher value of thermal conductivity is obtained for materials sintered with only 5 wt% of additive. Increasing the additive content reduces the thermal conductivity. Since the phase composition and grain-boundary phase are the same, the difference in the thermal conductivity is attributed to the variation in the microstructure.

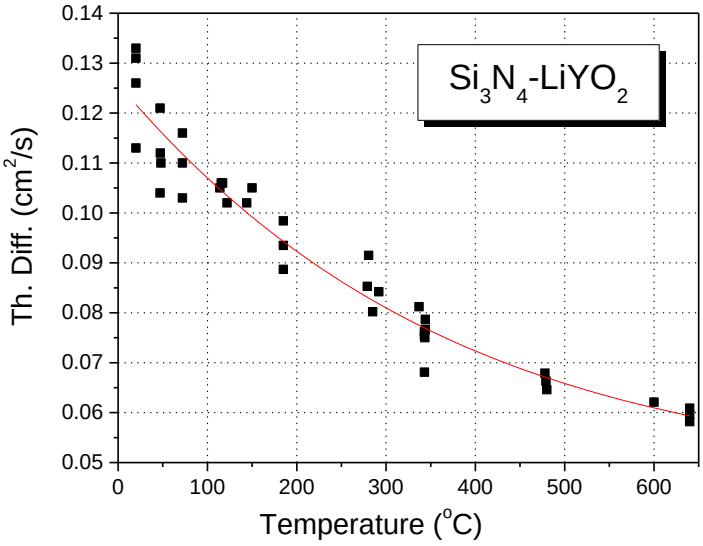

(a)

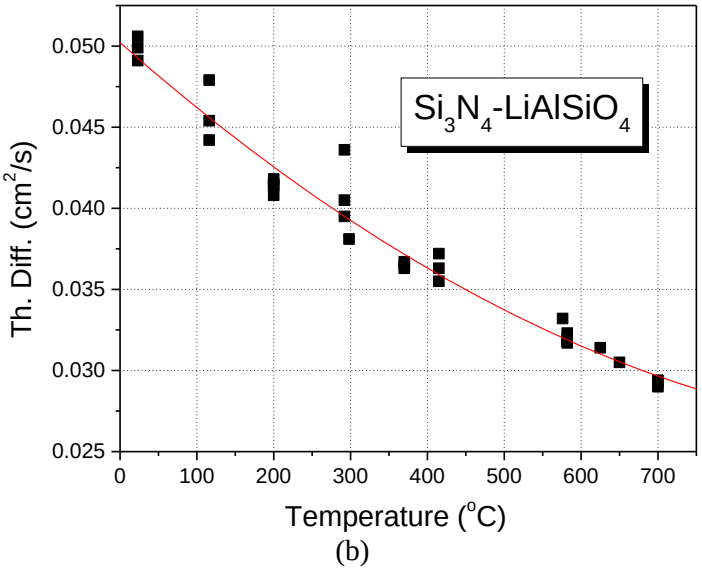

(b)

Figure 67. Temperature dependence of thermal diffusivity of Si_3N_4 ceramics sintered with 15 wt.% of $LiYO_2$ (a) and $SiAlSiO_4$ (b) additive.

Considering the thermal conductivity of SiO_2 based glasses, the thermal conductivity of the intergranular phase is much lower than that of Si_3N_4 grains, ranging from 0.1 to 0.7 W/m·K [170]. Thus, Si_3N_4 ceramics can be considered as two-phase materials composed of the Si_3N_4 grains with high thermal conductivity and the intergranular phase with low thermal conductivity. The thermal conductivity of two-phase materials depends on the individual thermal conductivity of the phases and on their distribution. In the case of higher additive contents, the amount of glassy phase in the grain-junction is higher which results in a decreasing overall thermal conductivity.

4.3 Oxidation resistance of Si_3N_4 materials

As silicon nitride materials are used in oxidising environments, a number of studies have been made on the oxidation of Si_3N_4 sintered with different additive systems [122, 123, 124, 125, 126, 127, 128].

Si_3N_4 is thermodynamically unstable in air. However, it is protected against further oxidation by a thin surface layer of amorphous silica. Generally, there are three oxidation reactions, which can cause oxidation of Si_3N_4:

$$Si_3N_4(s) + 3O_2 \rightarrow 3SiO_2(s) + 2N_2 \quad (4.1)$$

$$Si_3N_4(s) + 3SiO_2 \rightarrow 6SiO(g) + 2N_2 \quad (4.2a)$$

$$2\,Si_3N_4(s) + 3O_2 \rightarrow 6SiO(g) + 4N_2 \quad (4.2b)$$

Reaction 4.1 forms a dense oxide layer that inhibits further oxidation and is therefore called passive oxidation. Once an oxide layer is formed the rate of further reaction is controlled by the oxygen diffusion through this layer and shows a parabolic rate law:

$$(\Delta G/A)^2 = K_p t \quad (4.3)$$

where $(\Delta G/A)$ is the weight gain per unit area, t is the oxidation time and K_p is the parabolic rate constant. Reactions 4.2a and 4.2b occur at low oxygen partial pressures. The reactions proceed in a continuous manner. This is the so-called active oxidation which does not form a protective layer and thus proceeds as long as the oxygen (or SiO_2) is not completely consumed.

There are a number of other parameters which influence the oxidation. The presence of impurity elements increases the rate of oxidation if they are incorporated into the amorphous layer, where they are normally concentrated by segregation and increase the oxygen diffusivity [129]. An opposite effect is observed if these elements promote the crystallization of oxide phases on the surface, resulting in lower oxygen diffusivity and a decreased oxidation rate. Oxidation also increases if crystalline secondary oxynitride phases oxidize. This reaction involves a significant increase of volume as in the case of some silicon yttrium-oxynitrides. The volume increase can produce surface flaws thereby creating fresh surfaces [130].

5. Composites

Due to its importance as structural material, the effect of composition and microstructure on mechanical properties of Si_3N_4 ceramic was widely studied by many authors. Intention to increase further the reliability of Si_3N_4 has shifted the emphasis towards development a different types of composite ceramics (Table 20). By incorporating a controlled amount of elongated β-Si_3N_4 single crystal particles into the matrix (seeding) in an attempt to grow further the elongated uniformly distributed grains in a matrix of equiaxed or slightly elongated grains [2], toughening mechanisms such as crack deflection and/or bridging via interfacial debonding, are activated [107, 108, 109]. It is now well accepted that seeding is a useful method of providing an effective way to improve the

fracture resistance while retaining high strength, provided that the size, content and distribution of the elongated β-Si_3N_4 single-crystal particles are carefully controlled [131, 132].

Table 20. Summarized Si_3N_4 ceramic composites.

Composite	***Improved properties***
Si_3N_4/ Si_3N_4	Fracture toughness and strength, thermal conductivity
Si_3N_4/SiC	Mechanical properties at high temperature
Si_3N_4/TiN/TiC	Electrical conductivity and wear behaviour
Si_3N_4/TiB_2	Cutting behaviour and fracture toughness
Si_3N_4/BN	Wear behaviour, thermal shock resistance
Si_3N_4/TaN	Electrical conductivity
Si_3N_4/$MoSi_2$	Oxidation resistance
Si_3N_4/ silicides	Oxidation resistance
Si_3N_4/Al_2O_3/C	Chemical stability against metals used for refractories
Si_3N_4/ ZrO_2	Hardness and oxidation stability
Si_3N_4/ W	Heating elements

5.1 Si_3N_4/Si_3N_4 composites (Seeded Si_3N_4 ceramics)

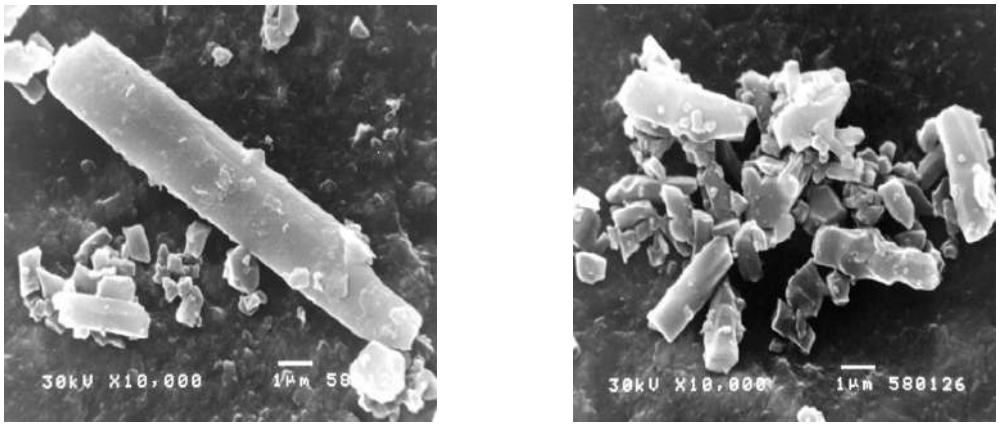

(a) (b)

Figure 68. SEM microphotographs showing the as-synthesized seeds.

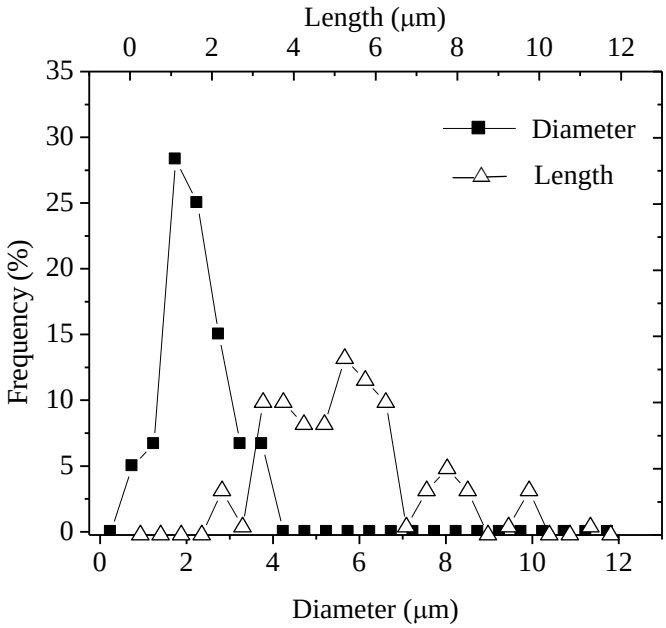

Figure 69. Distribution of width and length of synthesized rod-like seeds.

Silicon nitride seeds in beta form are usually obtained by gas pressure sintering procedure at 1850 °C [133]. Preparation of β-Si_3N_4 seeds under flowing nitrogen using powder bed method is also demonstrated [134]. Since, the additives are precondition for obtaining β-Si_3N_4 seeds, subsequent acid treatment to remove the additives is necessary. There is no difference in β-Si_3N_4 seeds prepared from this two method. Example of large elongated rod-like grains synthesized by pressureless sintering is shown in Fig. 68 (a) and (b). They were identified as β-Si_3N_4 single-crystal particles with mean diameter of 2.22 μm and mean length of 5.43 μm. The distribution of seeds in terms of their width and length are shown in Fig. 69. The lengths of seeds vary from 2.91 μm to 11.04 μm, while their width varies from 0.97 μm to 3.62 μm.

The amount of the seeds has to be moderate to avoid impingement of grains. As an example, the effect of seed particle concentration on relative density of specimens sintered with ceria as sintering additive for various times is shown in Fig. 70. It should be pointed out that the green densities do not differ to a great extent for sample with different seeds concentration in the range studied. As can be inferred from Fig. 70, full density was achieved in samples denoted as 0 (non-seeded), 3 (1 wt.% seeds) and 4 (3 wt.% seeds) after sintering at 1800 °C for 4 h [134]. This is significantly shorter sintering time than used in other works [134]. The results also show that the particle rearrangement process proceeds smoothly with non-seeded samples, in which particles are equiaxed with the size of less than 0.5 μm which was the starting powder particle size as provided by the supplier. With increasing seeds concentration (0-3 wt.%) sintered density decreases for shorter sintering times (up to 4 h) while for longer sintering times (4 to 6 h) sintered density kept on being constant independent of seeds content within the studied range. Clearly, elongated seeds do not rearrange smoothly during consolidation process due to their geometry and are an obstacle to particles rearrangement process. That is why samples with increasing seeds concentration (1, 3 and 5 wt.% seeds) show density decrease. Densities are lower than for unseeded samples. It can be seen from Fig. 70, that seeding with 5 wt.% seed particles, caused considerable density decrease, for all soaking times.

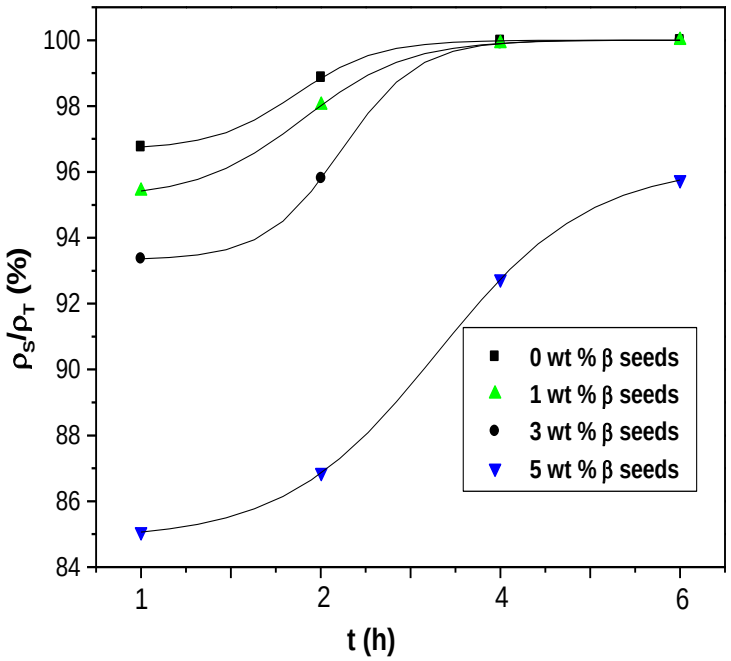

Figure 70. Effect of sintering time (at 1800 °C) and the amount of seed particles on relative density of silicon nitride. Theoretical density was calculated from the rule of mixtures.

The addition of seeds to samples sintered leads to an increase in fracture toughness with an increase in seeds concentration of up to some amount and thereafter it decreases (Fig. 71).

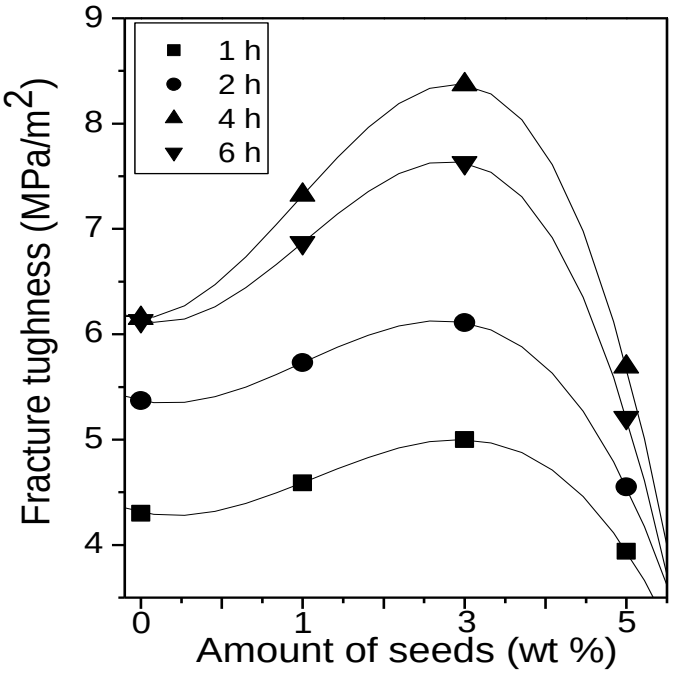

Figure 71. Effect of sintering time and amount of seed particles on fracture toughness of silicon nitride sintered at 1800 °C with CeO_2 additive.

However, an increase in fracture toughness with an increase in sintering time was observed for all samples. It is quite clear from the densification results in Fig. 70 and fracture toughness measurement in Fig. 71 that the addition of seeds had the dominant effect on fracture toughness and causes its increase despite the fact that density remained unchanged. The addition of seeds provided the conditions for activating grain bridging and pulls out mechanisms capable of enhancing fracture toughness.

The decrease in fracture toughness in samples containing seeds above approximately 3 wt.% suggests that the growth of elongated grains may be limited by their concentration. It seems that under the present experimental conditions, there is an optimum amount of seeds beyond which the growth of elongated grains is limited. This reasoning is in line with the kinetics of nucleation of the elongated grains. As the seed concentration (or their number) increases the number of nucleation sites also increases leading to grain growth inhibition.

Seeded samples of Si_3N_4 ceramics sintered by means of Y_2O_3-Al_2O_3 additive have similar behavior. The variations in microstructure for specimens sintered at 1600 and 1700 °C with 1, 3 and 5 wt.% seeds are shown in Figs. 72 and 73. In contrast to the non-seeded samples, which exhibits a relatively uniform microstructure with mostly small and equiaxed grains, the seeded specimens exhibit the bimodal microstructure with elongated Si_3N_4 grains embedded in a matrix of finer grains. It should be also noticed that in specimens sintered at 1600 °C the presence of rounded shape grains indicate, too the remaining α-phase as was confirmed by XRD.

The size of β-Si_3N_4 grains depends not only on the heating time, but also on the seeds content. If during transformation the large number of seeds were present this would mean the large number of centers of crystallization, which significantly accelerates phase transformation but not necessarily the grain growth (Fig. 72). With increasing number of crystallization centers, whole available amount of β-Si_3N_4 crystallizes on a larger number of centers inducing less β-Si_3N_4 deposited on each seed, which in turn, results in smaller final grain size (Fig. 72c).

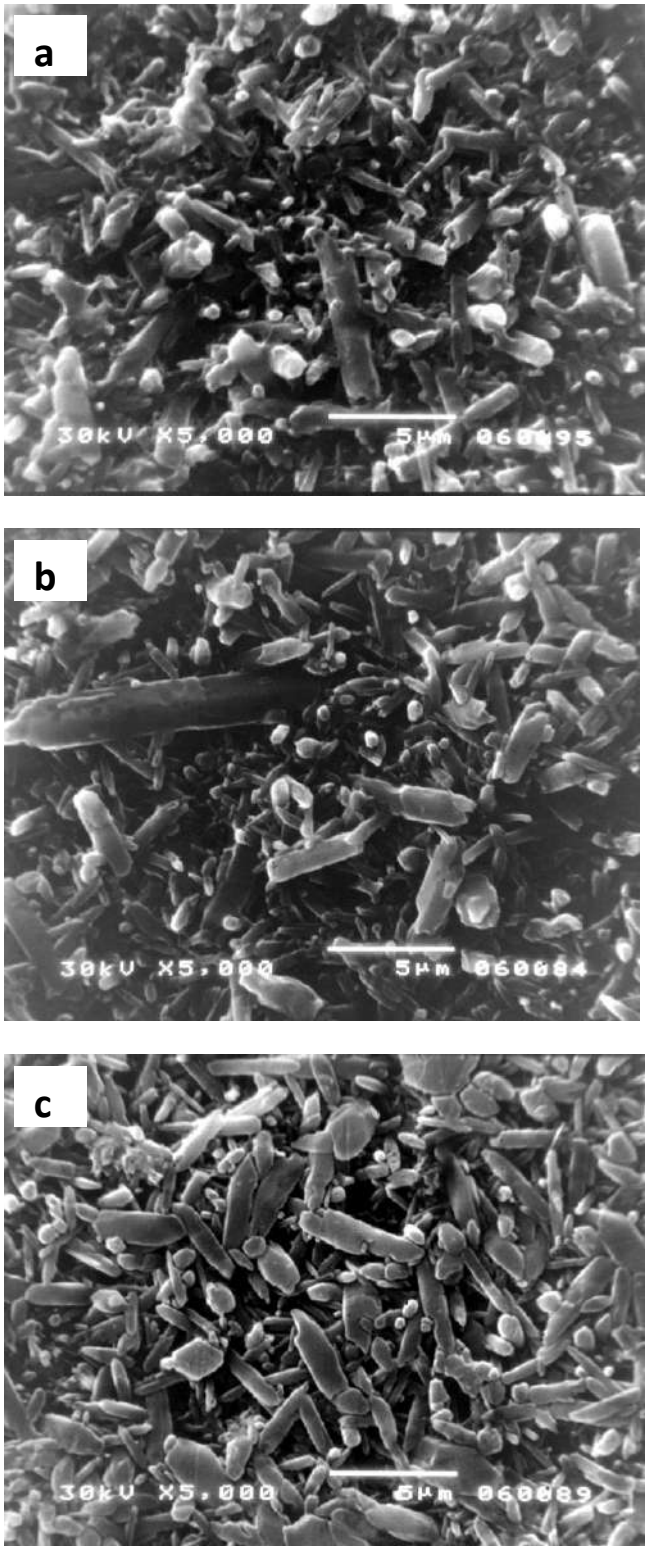

Figure 72. SEM images of seeded samples sintered at 1600 °C for 1 h, (a) 1 wt.%, (b) 3 wt.% and (c) 5 wt. % seeds.

With further increase of seeds amount (5 wt.%), the grain diameter is decreased due to impingement of seeds, as well, which is more pronounced in specimens sintered at 1700 °C as can be seen in Fig. 73c.

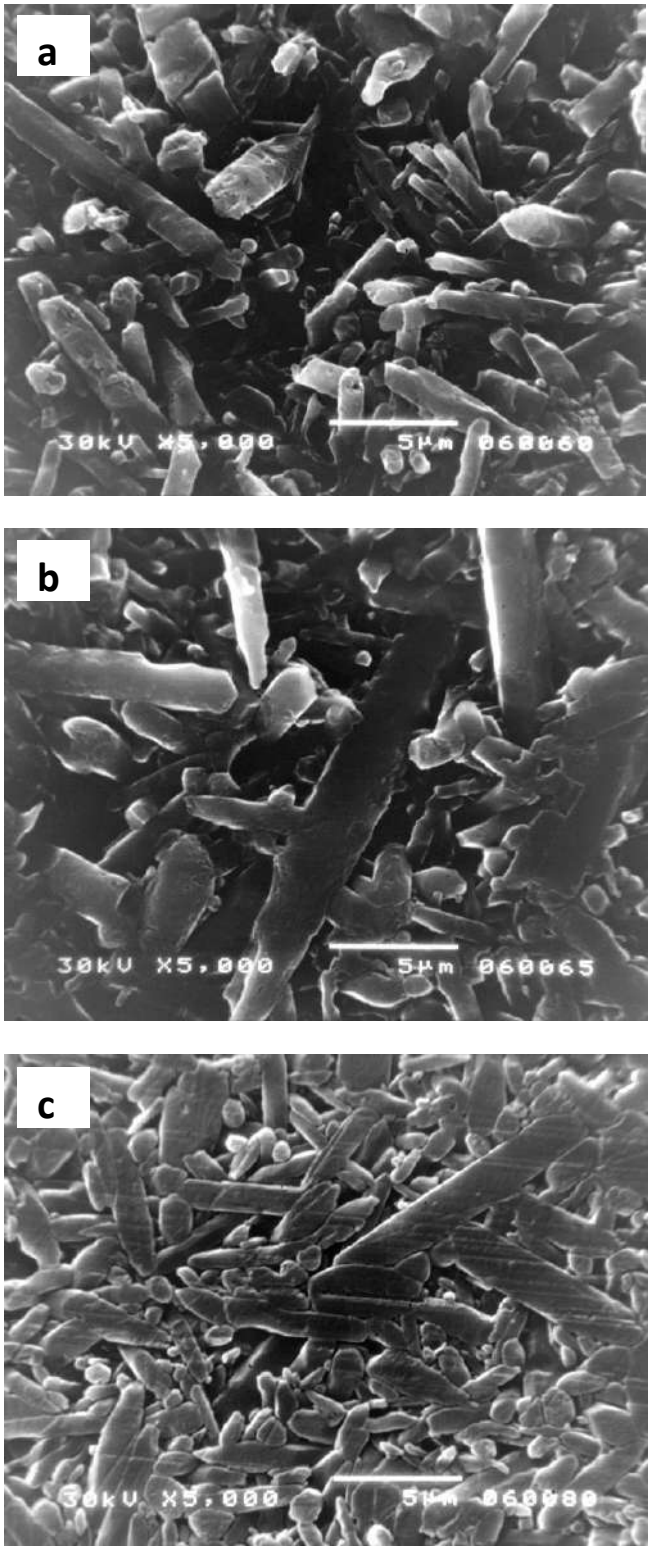

Figure 73. SEM images of seeded samples sintered at 1700°C for 1 h, with (a) 1 wt.%, (b) 3 wt.% and c) 5 wt.% seeds.

The appearance of β-grains with different aspect ratio in these compositions is also due to the broad size distribution of initial β-seeds. According to the observed microstructure it can be seen that the seeding allows the microstructural design and through the optimization of seeds content the concentrations of elongated grains can be tailored.

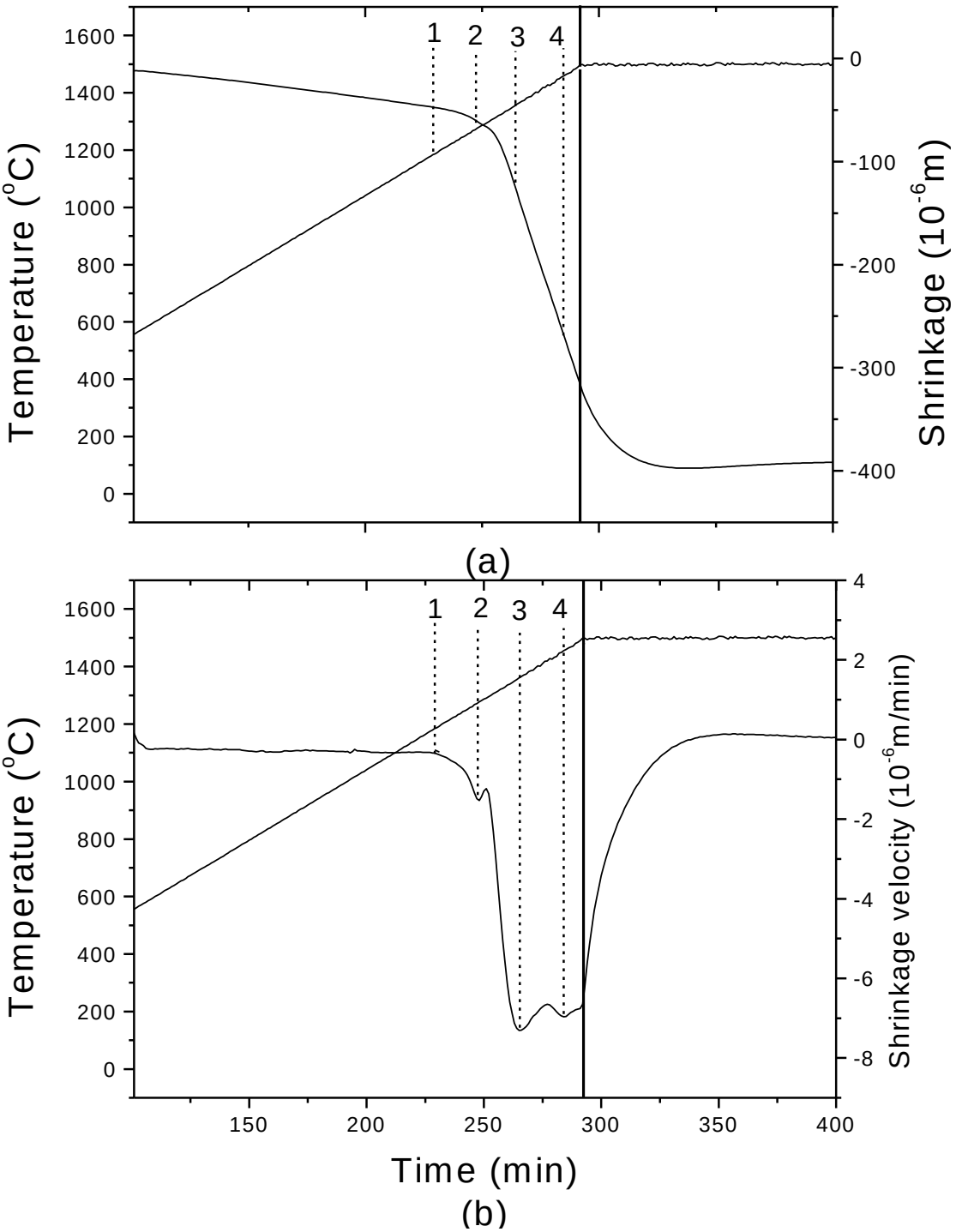

Figure 74. Shrinkage (a) and shrinkage velocity (b) of a silicon nitride green body with 15% $LiYO_2$ additive showing characteristic features at (1) 1180 °C; (2) 1275 °C; (3) 1364 °C and (4) 1453 °C.

The XRD pattern of the sample quenched at 1364 °C (point 3 on the Fig. 74) shows the disappearance of the LiSiNO phase resulting in an increasing amount of the liquid phase and consequently, an accelerated shrinkage. The maximum at 1453 °C corresponds to the onset of the phase transformation from α–Si_3N_4 to β–Si_3N_4. The densification rate decreases from this point, coinciding with a significant degree of $\alpha \rightarrow \beta$ transformation.

The phase contents of the samples quenched at different temperatures are presented in Table 20.

Table 20. Phase contents of the samples quenched at different temperatures.

Temperature (℃)	*Phase content (wt.%)*	*Remarks*
1180	β-Si_3N_4 21 %	onset of shrinkage
1275	β-Si_3N_4 22 % LiSiNO, $Y_5(SiO_4)_3N$	1st maximum of shrinkage velocity
1364	β-Si_3N_4 23 % $Y_5(SiO_4)_3N$	2nd maximum of shrinkage velocity
1453	β Si_3N_4 26 % $Y_5(SiO_4)_3N$	3rd maximum of shrinkage velocity
1500	β-Si_3N_4 32 % $Y_5(SiO_4)_3N$	after annealing for 5 min
1500	β-Si_3N_4 65 % $Y_5(SiO_4)_3N$	after annealing for 2 h

5.2. Si_3N_4-Li_2O-Al_2O_3-SiO_2 system

The dilatometric data (Fig. 75) show that shrinkage first occurs at 1080 °C and increases somewhat at 1270 °C for all samples, except for that with 5 wt.% of additive. The shrinkage continues during the isothermal annealing at 1500 °C. The onset of shrinkage is related to liquid formation in the sample compacts.

The effect of additive content on the linear shrinkage of the samples is shown in Fig. 76. Linear shrinkage increases significantly from 3 to 8% for the samples containing 5 and 10% of additives respectively. However, with further increasing additive content, linear shrinkage remains nearly constant. Linear shrinkage values ranging from 8.1 to 8.5% are obtained for samples containg 10, 15 and 20 wt.% of additives.

The remarkably low shrinkage of samples with 5 wt.% of additive could be attributed to an insufficient liquid formation. In general, more liquid is formed when the amount of additive is increased. In spite of growing additive content, it is found that the shrinkage reaches nearly the same value in the range of 10 to 20 wt.% of additives. This indicates that the liquid volume does not differ much with increasing additive content or the liquid content has not much pronounced influence on densification.

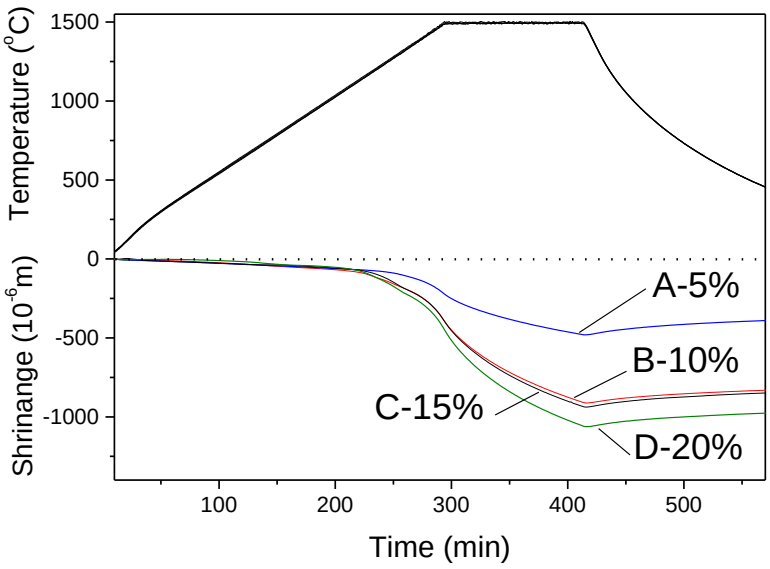

Figure 75. Length change of Si_3N_4 green bodies (A-5 wt.%, B-10 wt.%, C-15 wt.%, D-20 wt.% of $LiAlSiO_4$ between room temperature and 1500 °C. A cylinder-shaped test body was examined by dilatometry in nitrogen atmosphere.

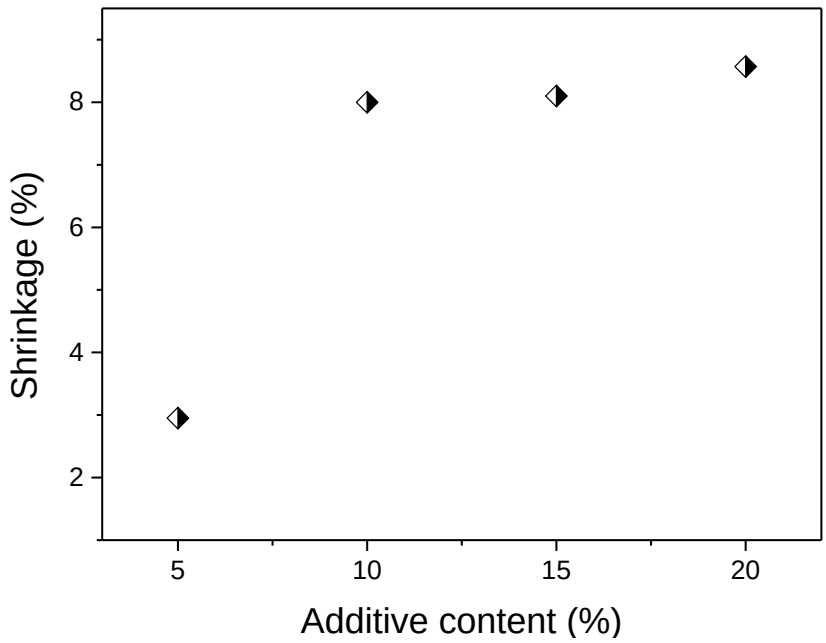

Figure 76. Linear shrinkage versus $LiAlSiO_4$ additive content in dilatometer experiments, after a holding time of 5 min at 1500 °C.

The maximum achieved density i.e. 2.65 g/cm^3 is obtained for 10 wt% of additive. Actually, the presence of Li_2O allows for the formation of a liquid phase at very low temperature. In case of samples with 10 wt% of additive the density has already increased to 2.03 g/cm^3 at 1080°C, that is nearly 10 % higher than the density of the starting mixture. With prolonged heating time, the density further increases to 2.65 g/cm^3 at 1500 °C (Fig. 77). In spite of the low sintering temperatures all the materials were not fully dense after dilatometric measurements up to 1500°C. This has to be attributed to the influence of the furnace atmosphere inside the dilatometer and the small size of the samples.

The influence of the amount of $LiAlSiO_4$ additive on the densification of Si_3N_4 is shown in Fig. 78. The best results were obtained for bodies with 10 or 15 % of additive, with attending of decreasing density upon further increase of the additive content.

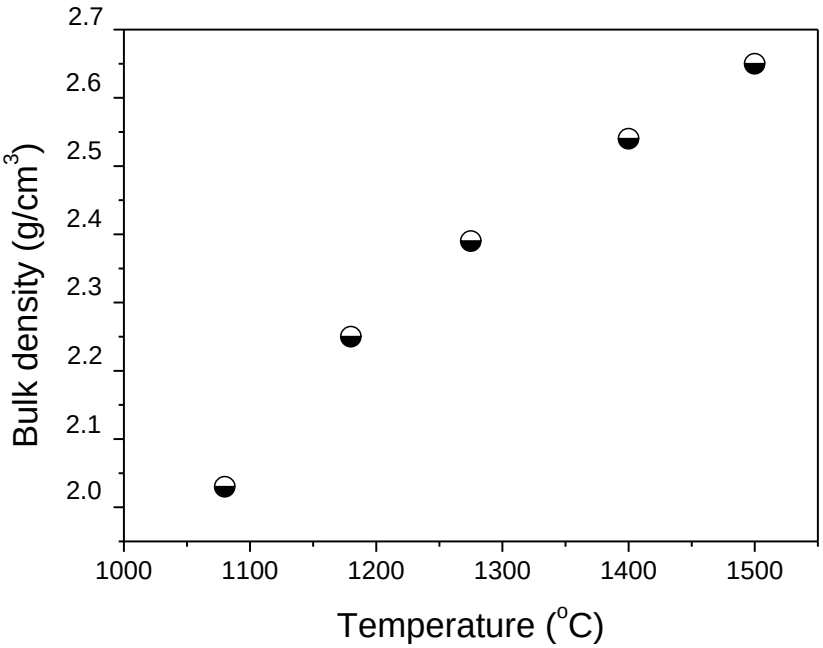

Figure 77. Density according to dilatometric measurements of Si_3N_4 with 10 wt.% of $LiAlSiO_4$ additive after a holding time of 5 min.

The shrinkage and shrinkage rate during densification of a sample with 10% of additive are shown in Fig. 79. The shrinkage rate curve shows three maxima at 1180 °C, 1275 °C and 1490°C indicated by three points 2 to 4.

The XRD patterns of the samples quenched at these temperatures show different phase compositions as listed in Table 21, indicating that the viscosity and volume of the liquid phase change significantly during heating.

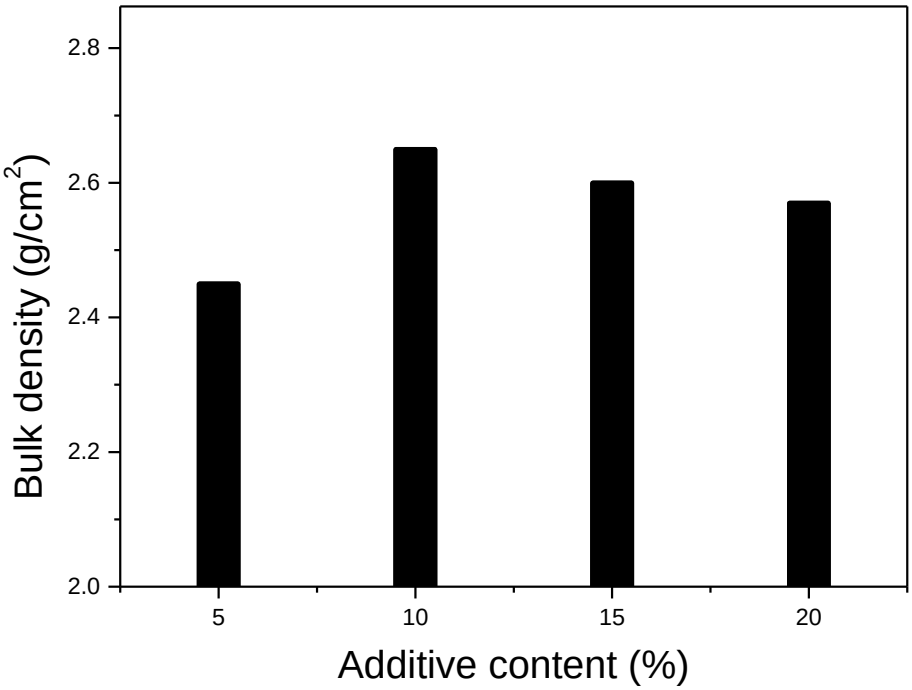

Figure 78. Influence of the amount of $LiAlSiO_4$ additive on the densification of Si_3N_4 samples fired at 1500°C with a holding a time of 5 min.

The appearance of the liquid in the sample starts at 1080 °C (point 1 in Fig. 79) corresponding to the eutectic melting point in the Li_2O-SiO_2 phase diagram. The maximum at 1180 °C (point 2 in Fig. 79) is related to an increasing amount of the liquid phase. Its phase composition shows lowering of the intensity of β-eucryptite i.e. $LiAlSiO_4$ phase due to its melting. The presence of coesite (SiO_2) is associated with excess silica which has crystallized from the liquid during cooling. The XRD pattern for the sample quenched at 1275 °C (point 3 in Fig. 79), shows the disappearance of the β-eucryptite phase but appearance of β-spodumen ($LiAlSiO_6$) which is a phase with the same cation ratio (Li:Al) as a $LiAlSiO_4$ but containing a higher amount of silica. In spite of the total conversion of $LiAlSiO_4$ additive into liquid phase the total amount of liquid phase does not increases significantly due to partial crystallization in to a new phase ($LiAlSiO_6$). This leads only to moderate increase of density.

The maximum at 1490 °C, which occurs together with a decrease in the XRD intensity of the $LiAlSiO_6$ phase and an increase in the intensity of SiO_2, corresponds to a increasing volume of the liquid phase (point 4 in Fig. 79).

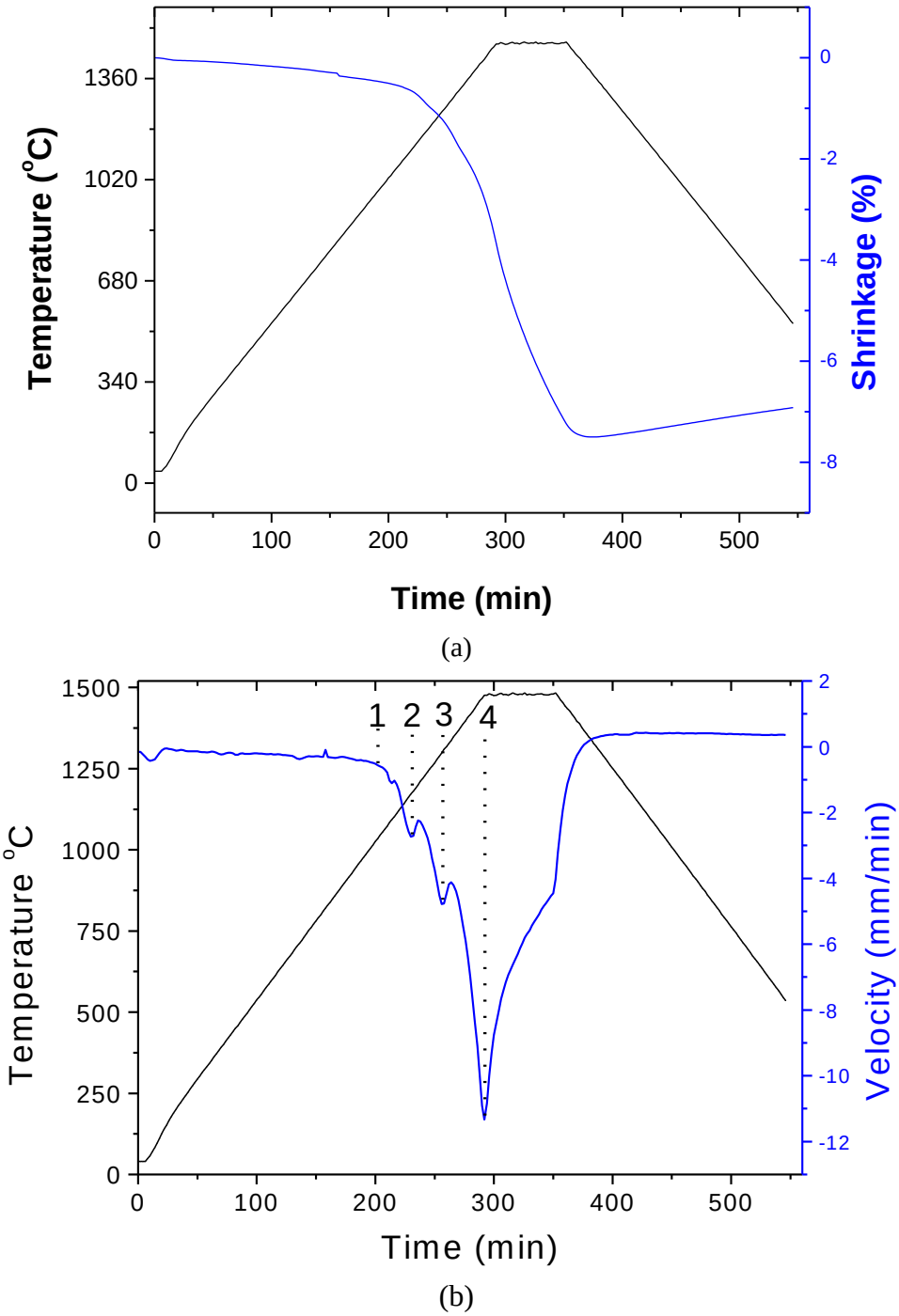

Figure 79. Shrinkage (a) and shrinkage velocity (b) of a silicon nitride green body with 15% $LiAlSiO_4$ additive showing characteristic features at (1) 1080 °C, (2) 1180 °C; (3) 1275 °C and (4) 1490 °C.

However, the α/β-Si_3N_4 ratio remains the same up to 1500 °C indicating that no significant transformation takes place during the first stage of sintering. This means that the initial stage is related with the formation of the liquid phase and to the reaction between the sintering additive and the surface silica from Si_3N_4 grains.

The results from the dilatometric measurements show that materials with both additive systems were not fully dense after heating up to 1500 °C. Densification is more effective with the $LiYO_2$ system than with the $LiAlSiO_4$ system under the same sintering conditions as shown in Fig. 28 and Fig. 78. This behavior cannot be explained exclusively by the difference in the volume fraction

and liquid viscosity of the two systems. Reaction with the reducing gas atmosphere inside the graphite-heated sintering furnace should also be taken into consideration.

Table 21. Phase contents of the samples quenched from different temperatures.

Temperature (°C)	*Phase content (wt.%)*	*Remarks*
1080	β-Si_3N_4 20 % β-$LiAlSiO_4$	onset of shrinkage
1180	β-Si_3N_4 20 % β-$LiAlSiO_4$, SiO_2	1st maximum of shrinkage velocity
1275	β-Si_3N_4 20 % β-$LiAlSi_2O_6$, SiO_2	2nd maximum of shrinkage velocity
1490	β Si_3N_4 20 % β-$LiAlSi_2O_6$, SiO_2	3rd maximum of shrinkage velocity
1500	β Si_3N_4 20 % β-$LiAlSi_2O_6$, SiO_2	after annealing for 5 min
1500	β-Si_3N_4 35 % SiO_2	after annealing for 2 h

It was found that the crystallization of the secondary phases from the melt can already occur during sintering especially for compositions on a tie line between one secondary phase and Si_3N_4. In this case, the volume fraction of the liquid phase is strongly reduced and complete densification is impossible. According to the XRD patterns and densities of the samples quenched at particular temperatures during dilatometric measurement, the amount of liquid due to the sequence of chemical reactions increases only slowly with temperature. Hence, the densification may be assumed to take place with less particle rearrangement than is usual in the liquid phase sintering. This explains why the variation in shrinkage and density that is obtained for samples having different additive contents is much smaller than in case of the $LiYO_2$ additive.

In the case of the $LiYO_2$ system, the density increases monotonically with increasing additive content according to Fig. 28. Higher additive content provides a higher volume of liquid needed to fill the porosity. In addition, an appreciable amount of Si_3N_4 can be dissolved in the liquid formed, which additionally leads to higher densification [56].

6. Conclusion

Si_3N_4 based materials, as described previously, have good mechanical and thermal properties, which are well-balanced compared to other ceramic materials. They are lighter and possess better heat resistance and wear resistance than metals. For example, SiC is an excellent heat conductor, however, its toughness and thermal shock resistance are behind that of Si_3N_4. Toughened zirconia can exhibit much higher strength and toughness as Si_3N_4, but its high temperature properties and thermal shock resistance are poor. Different types of Si_3N_4 materials can be produced by changing the starting powders, types and amounts of additives and manufacturing processes. These properties make them prime candidate materials for structural applications at ambient and high temperatures.

Acknowledgement
This research was financially supported by the Ministry of Science, Technological Development and Innovation of the Republic of Serbia (Grant No. 451-03-68/2022-14/200017).

References

[1] J. F. Collins and R. W. Gerby, Metals, **7** (1955) 612.
[2] G. Petzow and M. Herrmann, Structure and Bonding, **Vol. 102** (2002) p. 51.,Springer-Verlag, Berlin.

[3] G. Deeley, J. Herbert, Powder Metall., **8** (1961) 145.
[4] M. Mitomo and Y. Tayima, J. Jpn. Ceram. Soc., **99** (1991) 1014.
[5] G. R. Terwilliger, J Am. Ceram. Soc., **57** (1974) 48.
[6] M. Mitomo, J. Mater. Sci., **11** (1976) 1103.
[7] Y. Ojama and O. Kamigaito, Jpn. J. Appl. Phys., **10** (1971) 1637.
[8] K. H. Jack and W. J. Wilson, Nature (Phys. Sci), **238** (1972) 28.
[9] K. H. Jack, J. Mater. Sci., **11** (1976) 1135.
[10] F. Riley, J. Am. Ceram. Soc., **83** [2] 245-65 (2000).
[11] G. Ziegler, J. Heinrich, G. Wötting, J. Mater. Sci., **22,** 3041-86 (1987).
[12] D. Suttor, G. S. Fischman,. J. Am. Ceram. Soc., **75** (5) 1063-67 (1992).
[13] L. M. Sheppard, Ceram. Bull., **70** (1991) 692.
[14] M. Herrmann, J. Schulz and J. Hintermayer, 4th Euro-Ceramics **Vol. 2** (1995) 211.
[15] S. Kim, T. Sonders, J. Am. Ceram. Soc., **74** (1991) 1833.
[16] A. Zerr, G. Miehe, G. Serghiou, M. Schwarc, E. Kroke, R. Riedel, H. Fuess, P. Kroll and R. Boehler, Nature, **440** (1999) 340.
[17] C. Kirk, J. Appl. Phys., **50** (1979) 4190.
[18] P. Morgan, in Nitrogen Ceramics, ed. F. Riley, Noordhoff, Leyden (1977) p. 23.
[19] D. Thompson and P. Pratt, Mat. Sci. Forum, **47** (1989) 21.
[20] W. Dressler and R. Riedel, Int. J. Refrectory Metals and Hard Materials, **15** (1997) 13.
[21] S. Wild, P. Grievson and K. Jack, 'Special Ceramics' **Vol. 5** (1972) p. 385.
[22] H. Priest, F. Burns, G. Priest and E. Skaar, J. Am. Ceram. Soc., **7** (1973) 395.
[23] K. Kato, Z. Inoue, K. Kijima, I. Kawada, H. Tanaka and T. Yamane, J. Am. Ceram. Soc., **58** (1975) 90.
[24] T. Zoltai, Am. Mineral., **45** (1960) 960.
[25] C. Wang, X. Pan, M. Rühle, F. Riley and M. Mitomo, J. Mater. Sci., **31** (1996) 5281.
[26] D. Hardie and K. Jack, Nature, **180** (1957) 332.
[27] R. Green, Acta Crystallogr., **B35** (1979) 800.
[28] S. Hampshire and K. Jack, in Progress in Nitrogen Ceramics, ed. F. L. Riley, Martinus Nijhoff, Boston (1983) p. 225.
[29] J. Jiang, K. Stahl, R. Berg, D. Frost, T. Zhou and P. Shi, Europhys. Lett., **51** (2000) 62.
[30] J. Jiang, K. Kragh, D. Frost, K. Stahl and H. Lindelov, J. Phys. Condens. Matter, **13** (2001) L515-L520.
[31] R. Marchand, Y. Laurent, J. Guyader, P. L'Haridion and P. Verdier, J. Eur. Ceram. Soc., **8** (1991) 197.
[32] L. Gauckler, H. Lukas and G. Petzow, J. Am. Ceram. Soc., **58** (1975) 346.
[33] T. Ekström and M. Nygren, J. Am. Ceram. Soc.,**75** (1992) 259.
[34] M. Herrmann, H. Klemm and C. Schubert, in Silicon Nitride Based Hard Materials, Handbook of Ceramic Hard Materials, **Vol. 2.,** ed. Ralf Riedel, Darmstadt, Wiley-VCH, Weinheim (2000) p. 749.
[35] V. Izhevskiy, L. Genova, J. Bressiani and F. Aldinger, J. Eur. Ceram. Soc., **20** (2000) 2275.
[36] K. Jack, Nature, **274** (1978) 880.
[37] K. Jack, Prospects for nitrogen ceramics, Key Engng. Mat., **Vol. 89-91** (1994) 345.
[38] H. Mandal, D. Thompson and T. Ekström, J. Eur. Ceram. Soc., **12** (1993) 421.
[39] M. R. Lee, S. S. Russel, J. W. Arden, C. T. Pillinger, Meteoritics, **30** (1995) 387.
[40] W. Rhodes and S. Natansonh, Ceram. Bull., **68** (1989) 1804.
[41] D. Segal, Br. Ceram. Transaction, **85** (1986) 184.
[42] F. Riley, Mat. Sci. Forum, **47** (1989) 70.
[43] A. Merzhanov, Ceram. Int., **21** (1995) 371.
[44] M. Herrmann, I. Schulz, W. Hermel, Chr. Schubert and A. Wendt, Z. Metallkd., **92** (2001) 788.
[45] M. Ekelund and B. Forslund, J. Am. Ceram. Soc., **75** (1992) 532.
[46] T. Arakova, K. Ohno and K. Ueda, Ceramics, **22** (1987) 34.
[47] Z. Pan, H. Li and H. Zhang, J. Mater. Res., **13** (1998) 1996.
[48] Z. Dohcevic, B. Matovic, S. Boskovic and Z. Popovic, Philosophical Magazine A, **82** (2002) 93.

[49] G. Ziegler, Z. Werkstofftech. **14** (1983) 189.
[50] A. H. Heuer and V. L. Lou, J. Am. Ceram. Soc., **73** (1990) 2785.
[51] H. M. Jennings, J. Mater. Sci., **18** (1983) 951.
[52] C. Greskovich, J. Rosolovski, J. Am. Ceram. Soc., **59** (1976) 336.
[53] V. K. Lou, T. E. Mitchell and A. H. Heuer, J. Am. Ceram. Soc., **68** (1985) 49.
[54] W. D. Kingery, Solid State Phenomena, **25-26** (1992) 1.
[55] A. W. Adamson and A. P. Gast, Physical Chemistry of Surfaces, Wiley-Interscience, New York (1997) p. 6.
[56] W. D. Kingery, Introduction to Ceramics, John Wiley, New York (1960) p. 386.
[57] M. W. Barsoum, Fundamentals of Ceramics, McGraw-Hill, Singapore (1997) p. 334.
[58] W. D. Kingery, J. Appl. Phys., **30** (1959) 301.
[59] W. D. Kingery and M. D. Norasimhan, J. Appl. Phys., **30** (1959) 307.
[60] G. Petzow and W. J. Huppmann, Z. Metallkde., **67** (1976) 579.
[61] R. M. German, Liquid Phase Sintering, Plenum, New York (1985) p. 5.
[62] J. Weiss and W. Kaysser, 'Liquid phase sintering', in Progress in Nitrogen Ceramics, ed. F. L. Riley, Martinus Nijhoff Publishers, Boston (1983) p. 169.
[63] W. A. Kaysser and G. Petzow, Z. Metallkde., **76** (1985) 687.
[64] S. Kang, W. A. Kaysser, G. Petzow and D. N. Yoon, Powder Metall., **27** (1984) 97.
[65] S. Sarian and H. W. Weart, J. Appl. Phys., **37** (1966) 1675.
[66] J. Svoboda, H. Riedel and R. Gaebel, Acta Mater. **44** (1996) 3215.
[67] S. Lee and S. L. Kang, Z. Metallkde., **92** (2001) 669.
[68] J. K. Park, S. J. Kang, K. Y. Eun and D. N. Yoon, Metall. Trans., **20** (1989) 837.
[69] S. J. Kang and P. Azou, Powder Metall., **28** (1985) 90.
[70] J. K. Park, S. J. Cho, and D. N. Yoon, Metall. Trans., **15** (1984) 1075.
[71] J. K. Park, H. H. Kwon, and D. N. Yoon, Metall. Trans., **17** (1986) 1915.
[72] O. J. Kwon and D. N. Yoon, Int. J. Powder Metall., **17** (1981) 127.
[73] G. Petzow and W. A. Kaysser, Basic Mechanisms of liquid Phase Sintering, in Sintered Metal-Ceramic Composites, ed. G. S. Upadhyaya, Elsevier Science Publishers, Amsterdam, (1984) p. 595.
[74] G. Petzow and H. E. Exner, Z. Metallkde., **67** (1976) 611.
[75] N. J. Shaw, Powd. Metall. Int., **21** (1983) 25.
[76] M. N. Rahaman, Ceramic Processing and sintering, Dekker, New York, (19959 p. 524.
[77] P. Drew and M. H. Lewis, J. Mater. Sci., **9** (1974) 1833.
[78] K.Kijima and S. Shirasaki, J. Chem. Phys., **65** (1976) 2668.
[79] G. Brebec, R. Sella, J. Bevenot and J. C. Martin, Acta Metall., **28** (1980) 327.
[80] D. R. Messier, F. L. Riley and R. J. Brook, J. Mater. Sci., **13** (1978) 1199.
[81] P. Drew and M. H. Lewis, J. Mater. Sci., **9** (1974) 261.
[82] M. Krämer, M. J. Hoffmann and G. Petzow, Acta Metall. Mater., **41** (1993) 2939.
[83] Y. Okamoto, N. Hirosaki, Y. Akimüne and M. Mitomo, J. Ceram. Soc. Jpn., **105** (1997) 476.
[84] N. J. Shaw, Powder. Metall. Int., **21** (1989) 16.
[85] D . D. Lee, S. L. Kang and D. N. Yoon, J. Am. Ceram. Soc., **71** (1988) 803.
[86] M. A. Einarsrud and M. Mitomo, J. Am. Ceram. Soc., **76** (1993) 1624.
[87] H. J. Kleebe, J. Ceram. Soc. Jpn., **105** (1997) 453.
[88] J. Rödel, J. Eur. Ceram. Soc., **10** (1992) 143.
[89] K. T. Faber and A. G. Evans, Acta Metall., **31** (1983) 565.
[90] T. M. Shaw, O. L. Krivanek and G. Thomas, , J. Am. Ceram. Soc., **62** (1979) 305.
[91] I. C. Huseby and G. Petzow, Powder Metall.Int., **6** (1974) 17.
[92] S. Hausner, Sci. Ceram., **12** (1983) 229.
[93] K. H. Jack, in Nitrogen Ceramics, ed. F. L. Riley, Matinus-Nijhoff, (1983) p. 109.
[94] J. Briggs, Mater. Res. Bull., **12** (1997) p. 1047.
[95] S. Hampshire, R. A. Drew and K. H. Jack, Phys. Chem. Glasses, **26** (1985) 182.
[96] N. Hirosaki, A. Okada and K. Matoba, J. Am. Ceram. Soc., **71** (1988) C-144.
[97] O. Abe, Ceram. Int., **16** (1990) 53.
[98] O. Fabrichnaya, H. J. Seifert, R. Weiland, T. Ludwig, F. Aldinger and A. Navrotsky, Z. Metallkd. **92** (2001) 9.
[99] J.C. Bressiani, V. Izhevskyi, A. H. Bresiani, Mater. Res., **2** (1999) 165.

[100] S. Bandyopadhyay, in Sintered metallic and ceramic materials, John Wiley, Chichester (2000) p. 556.
[101] M. Herrmann, G. Putzky, S. Siegel and W. Hermel, cfi. Ber. DKG, **69** (1992) 375.
[102] H. Björklund, L. K. Falk, K. Rundgren and J. Wasen, J. Eur. Ceram. Soc., **17** (1997) 1285.
[103] M. Herrmann and O. Goeb, J. Eur. Ceram. Soc., **21** (2001) 304.
[104] K. Yokoyama and S. Wada, J. Ceram. Soc. Jpn., **108** (2000) 230.
[105] M. M. Schwartz, 'Handbook of structural ceramics', McGraw-Hill. (1992) p. 21
[106] K. Komeya, in Fine Ceramics, ed. S. Saito, Elsevier Science Publishing Co. New York (1988) p. 175.
[107] P.F. Becher, C. H. Hsueh, P. Angelini and T. N. Tieges, J. Am. Ceram. Soc., **71** (1988) 1050.
[108] H. Mandel and M. J. Hoffmann, in Nitrides and Oxynitrides, ed. S. Hampshire, Trans. Tech. Publications Ltd., Zelene, (2000) p. 219.
[109] P. Sajgalik, J. Dusza and M. Hoffmann, J. Am. Ceram. Soc., **78** (1995) 2619.
[110] I. Peterson and T. Tien, J. Am. Ceram. Soc., **78** (1995) 2345.
[111] I. Tanaka, G. Pezzotti, K. Okamoto, Y. Miyamoto and M. Koizumi, J. Am. Ceram. Soc., **74** (1992) 755.
[112] G. D. Quinn, J. Mater. Sci., **25** (1990) 4361.
[113] W. E. Luecke, S. M. Wiederhorn, J. Am. Ceram. Soc., **82** (1999) 2769.
[114] K. Hirao, K. Watari, H. Hayashi and M. Kitayama, MRS Bulletin **6** (2001) 451.
[115] S. Haggerty and A. Lightfoor, Ceram. Eng. Sci. Proc., **16** (1995) 475.
[116] K. Watari, J. Ceram. Sci. Jpn., **109** (2001) 57.
[117] T. Hirai, S. Hayashi and K. Niihara, Am. Ceram. Soc. Bull., **57** (1978) 1126.
[118] K. Tsukama, M. Shimada and M. Koizumi, , Am. Ceram. Soc. Bull., **60** (1981) 910.
[119] K. Watari, L. Pottier, B. Li, D. Fournier an M. Toryjama, in Grain Boundary Engineering in Ceramics, ed. T. Sakuma, L. Sheppard and Y. Ikuhara, Westerville, (2000) p. 341.
[120] K. Watari, K. Hirao, M. Toriyama and K. Ishizaki, J. Am. Ceram. Soc., **82**. (1999) 777.
[121] M. Kitayama, K. Hirao, M. Toriyama and S. Kanzaki, J. Am. Ceram. Soc., **82**. (1999) 3105.
[122] S. C. Singhal, J. Mater. Sci., **11** (1976) 500.
[123] D. Cubiccotti and K. H. Lau, J. Am. Ceram. Soc., **61** (1978) 512.
[124] C. N. Babini, A. Bellosi and P. Vincenzini, J. Mater. Sci., **19** (1984) 1029.
[125] A. Bouarroud, P. Goursat and J. L. Besson, J. Mater. Sci., **20** (1985) 1150.
[126] M. Mieskowski and W. A. Sanders, J. Am. Ceram. Soc., **68** (1985) C1-60.
[127] P. Andrews and F. L. Riley, J. Eur. Ceram. Soc., **5** (1989) 245.
[128] S. K. Biswas, J. Mukerji and P. K. Das, Key Engng. Mater., **89-91** (1994) 271.
[129] J. Schlichting, L. J. Gauckler, Powder Metall. Int. **9** (1977) 36.
[130] G. Petzow and J. Weiss, Bulletin de la societe chimique Beograd, **46** (1981) 123.
[131] H. Emito and M. Mimoto, J. Eur. Ceram. Soc., **17** (1997) 797.
[132] S. Kanzaki, M. Brito, M. Valecillos and K. Hirao, J. Eur. Ceram. Soc., **17** (1997) 1841.
[133] H. Imamura, K. Hirao, M. Brito, M. Tortiyama and S. Kanzaki, J. Am. Ceram. Soc., **83** (2000) 495.
[134] A. Vuckovic, Master Thesis (2005) University Belgrade.